Investigation of Rydberg States in Ensembles of Ultracold Bosonic and Fermionic Ytterbium Isotopes

Inaugural-Dissertation

zur

Erlangung des Doktorgrades der

Mathematisch-Naturwissenschaftlichen Fakultät

der Heinrich-Heine-Universität Düsseldorf

vorgelegt von

Alexander Miethke

aus Hilden

Düsseldorf, März 2026

Aus dem Institut für Experimentalphysik
der Heinrich-Heine-Universität Düsseldorf

Gedruckt mit der Genehmigung der
Mathematisch-Naturwissenschaftlichen Fakultät der
Heinrich-Heine-Universität Düsseldorf

Tag der mündlichen Prüfung: 10.03.2026

Referent:	Prof. Dr. Axel Görlitz
Koreferent:	PD Dr. Götz Lehmann

Summary

This dissertation investigates the Rydberg states of ultracold fermionic and bosonic ytterbium (Yb) atoms. Building upon the experimental setup developed by C. Halter[1] [1], which itself was originally established by B. Schepers [2], this work advances the foundation for ultracold ytterbium Rydberg experiments toward the study of interatomic interactions.

Rydberg atoms, characterized by their large electric dipole moments and high sensitivity to external electric fields, provide a powerful platform for exploring long-range interactions and quantum control. Ytterbium is well-suited for such studies: its two-valence-electron structure enables flexible excitation schemes and allows for the creation of trappable Rydberg atoms, making it an attractive species for applications in optical atomic clocks [3] and quantum information processing [4, 5].

In this work, ytterbium atoms are produced in an atomic-beam oven, decelerated using a Zeeman slower, and captured in a single-stage magneto-optical trap (MOT) under ultra-high-vacuum conditions. Following Rydberg excitation, the atoms are detected either via a charge-coupled device (CCD) camera or a microchannel plate (MCP) detector after field ionization.

This dissertation is structured in two major parts. The first part focuses on high-resolution spectroscopic studies in a single-stage MOT, including polarizability measurements of the isotope ^{174}Yb for S- and P-states with high principal quantum numbers (n) in the range $n = 70 - 90$, as well as black-body-radiation-limited lifetime measurements for states with $n = 35 - 80$. The measured lifetimes are compared to theoretical predictions obtained using multichannel quantum defect theory (MQDT) calculations from the *PairInteraction* software [6], showing good agreement.

Extensive spectroscopic data were obtained for the bosonic isotopes ^{172}Yb, ^{174}Yb, and ^{176}Yb, and for the fermionic isotopes ^{171}Yb and ^{173}Yb. The results for ^{171}Yb are directly compared to precise MQDT calculations by Peper et al. [7], revealing good consistency. Using single-channel quantum defect theory (SQDT), small isotope-dependent differences in the ionization energies of the bosonic isotopes were determined. The measurements on Rydberg states of ^{173}Yb represent, to the best of our knowledge, the first extensive experimental data reported for this isotope.

In the second part of this thesis, the extension of the experimental setup through the implementation of a two-stage MOT is described. This upgrade required the construction

[1] "Halter" now uses the name "Wallin".

and integration of a new laser system operating at 556 nm. The wavelength is generated by frequency doubling an amplified fiber laser at 1112 nm via second-harmonic generation (SHG). With this upgrade, the atomic density is increased by nearly two orders of magnitude – reaching several $10^{10}\,\mathrm{cm}^{-3}$ – while the temperature is reduced to a few tens of μK. At these conditions, the mean atomic separation of two Rydberg atoms is approximately 5 μm, such that Rydberg-Rydberg interactions are expected to become observable for high-lying Rydberg states.

To enable the observation of interaction between Rydberg atoms, a dedicated measurement scheme was developed, forming an ideal basis for future experiments on controlled Rydberg-Rydberg interactions. In this scheme, the Rydberg excitation beam is spatially scanned across the MOT volume, allowing for the measurement of density-dependent ion signals. The developed detection scheme together with the upgraded experimental apparatus represents a significant step toward the realization of strongly interacting ytterbium Rydberg systems.

Zusammenfassung

Diese Dissertation untersucht die Rydbergzustände ultrakalter fermionischer und bosonischer Ytterbiumatome. Aufbauend auf dem von C. Halter[1] [1] entwickelten experimentellen Aufbau, der ursprünglich von B. Schepers [2] etabliert wurde, erweitert diese Arbeit die Grundlage für Experimente mit ultrakalten Ytterbium-Rydbergatomen hin zur Untersuchung interatomarer Wechselwirkungen.

Rydbergatome zeichnen sich durch ihre großen elektrischen Dipolmomente und ihre hohe Empfindlichkeit gegenüber externen elektrischen Feldern aus. Damit stellen sie eine leistungsfähige Plattform zur Erforschung langreichweitiger Wechselwirkungen und quantenkontrollierter Prozesse dar. Ytterbium eignet sich hierfür gut, da die Zweivalenzelektronenstruktur flexible Anregungsschemata ermöglicht und die Erzeugung von Rydbergatomen erlaubt, welche für das Einfangen in einer magneto-optischen Falle (MOT) geeignet sind. Dadurch ist Ytterbium ein vielversprechendes Element für Anwendungen in optischen Atomuhren [3] und der Quanteninformationsverarbeitung [4, 5].

In dieser Arbeit werden Ytterbiumatome in einem Atomstrahl-Ofen erzeugt, mittels eines Zeeman-Slowers abgebremst und in einer einstufigen magneto-optischen Falle unter Ultrahochvakuumbedingungen gefangen. Nach der Anregung in einen Rydbergzustand erfolgt die Detektion der Atome entweder über eine CCD-Kamera (Kamera mit ladungsgekoppeltem Bauelement) oder über einen Multikanalplatten-Detektor (MCP) nach Feldionisation.

Diese Dissertation ist in zwei Hauptteile gegliedert. Der erste Teil behandelt hochauflösende spektroskopische Untersuchungen in einer einstufigen MOT. Dazu gehören Polarisierbarkeitsmessungen des Isotops ^{174}Yb für S- und P-Zustände mit hohen Hauptquantenzahlen im Bereich $n = 70 - 90$ sowie Messungen der durch Schwarzkörperstrahlung begrenzten Lebensdauern für Zustände mit $n = 35 - 80$. Die gemessenen Lebensdauern werden mit theoretischen Vorhersagen verglichen, die mittels Multikanal-Quantendefekttheorie-Berechnungen (MQDT) unter Verwendung der *PairInteraction*-Software [6] erhalten wurden und zeigen eine gute Übereinstimmung.

Umfangreiche spektroskopische Daten wurden für die bosonischen Isotope ^{172}Yb, ^{174}Yb und ^{176}Yb sowie für die fermionischen Isotope ^{171}Yb und ^{173}Yb aufgenommen. Die Ergebnisse für ^{171}Yb werden direkt mit präzisen MQDT-Berechnungen von Peper et al. [7] verglichen und zeigen eine gute Konsistenz. Unter Verwendung der Ein-Kanal-Quantendefekttheorie (SQDT) können zudem kleine isotopenspezifische Unter-

[1] "Halter" trägt heute den Namen "Wallin".

schiede in den Ionisationsenergien der bosonischen Isotope bestimmt werden. Die Messungen an Rydbergzuständen des Isotops ^{173}Yb stellen nach unserem Kenntnisstand die ersten umfangreichen experimentellen Daten für dieses Isotop dar.

Im zweiten Teil dieser Dissertation wird die Erweiterung des experimentellen Aufbaus durch die Implementierung einer zweistufigen MOT beschrieben. Dies erforderte den Aufbau und die Integration eines neuen Lasersystems bei 556 nm. Die entsprechende Wellenlänge wird durch Frequenzverdopplung eines verstärkten Faserlasers bei 1112 nm mittels Frequenzverdopplung (SHG) erzeugt. Durch diese Verbesserung erhöht sich die Atomdichte um nahezu zwei Größenordnungen auf mehrere $10^{10}\,\mathrm{cm}^{-3}$, gleichzeitig wird die Temperatur auf wenige zehn µK reduziert. Unter diesen Bedingungen beträgt der mittlere Abstand zweier Rydberg-Atome etwa 5 µm, sodass Rydberg-Rydberg-Wechselwirkungen voraussichtlich beobachtbar werden.

Zur Detektion von Wechselwirkungen zwischen Rydbergatomen wurde ein spezielles Messschema entwickelt, das eine ideale Grundlage für zukünftige Experimente zu kontrollierten Rydberg-Rydberg-Wechselwirkungen bildet. Dabei wird der Rydberganregungsstrahl schrittweise räumlich über das MOT-Volumen geführt, wodurch dichteabhängige Ionensignale erfasst werden können. Die entwickelte Detektionsmethode zusammen mit dem verbesserten experimentellen Aufbau stellen einen bedeutenden Schritt auf dem Weg zur Realisierung stark wechselwirkender Ytterbium-Rydbergsysteme dar.

Contents

List of Abbreviations

AOM	Acousto-Optic Modulator
ASE	Amplified Spontaneous Emission
BBR	Black-Body Radiation
CCD	Charge-Coupled Device
CTE	Coefficient of Thermal Expansion
ECDL	External Cavity Diode Laser
EOM	Electro-Optical Modulator
FBG	Fiber Bragg Grating
FWHM	Full Width at Half Maximum
FSR	Free Spectral Range
HV	High Voltage
LBO	Lithium Triborate Crystal
MC	Microcontroller
MCP	Microchannel Plate
MQDT	Multichannel Quantum Defect Theory
MOT	Magneto-Optical Trap
ODT	Optical Dipole Trap
PD	Photodiode
PDH	Pound-Drever-Hall
PI	Polarization-Independent
QE	Quantum Efficiency
QDT	Quantum Defect Theory
SC	Scanning Cavity
SHG	Second Harmonic Generation
SOI	State of Interest
SQDT	Single-Channel Quantum Defect Theory
STCL	Scannable Transfer Cavity Lock
TA	Tapered Amplifier
UHV	Ultra-High Vacuum
Yb	Ytterbium

1.

Introduction

Research in fundamental physics does not always appear directly connected to practical applications. Nevertheless, work in atomic physics has repeatedly shown that fundamental studies can provide the basis for technological and theoretical developments that extend well beyond their original scope.

A striking example is Albert Einstein's mass-energy equivalence relation formulated in 1905 [8], combined with Francis W. Aston's discovery of the helium mass defect [9]. These insights established the conceptual framework of nuclear fusion physics, ultimately enabling the first viable designs for controlled fusion reactors such as the tokamak [10] and the stellarator [11], which remain among the most promising candidates for sustainable energy generation.

Another important development arose from quantum mechanical insights into solid-state systems. Felix Bloch's (1928) theory of electrons in periodic potentials [12] and Clarence Zener's (1934) description of tunneling and band structure [13] laid the groundwork for the invention of the transistor by Bardeen, Brattain, and Shockley in 1948 [14]. This device revolutionized modern electronics and paved the way for the digital age.

In a similar manner, the field of Rydberg physics evolved from early fundamental discoveries into a rich platform for both basic and applied research. Johannes Rydberg's empirical formula for atomic spectral lines from 1888 [15], later theoretically explained by Bohr's atomic model [16] and Schrödinger's wave mechanics [17], provided a solid theoretical foundation. The advent of tunable laser systems enabled high-precision spectroscopy of Rydberg atoms, and pioneering experiments by Thomas F. Gallagher and others in the 1970s [18] marked the beginning of modern Rydberg physics.

Today, Rydberg atoms play a central role in a variety of modern applications. They are employed in precision measurements for atomic clocks [3, 19, 20], utilized as ultra-sensitive electric field sensors [21, 22], and extensively investigated for quantum computing [23–25]. The latter exemplifies how fundamental atomic physics can translate into transformative technology.

Furthermore, Rydberg atoms serve as a versatile interface in hybrid quantum systems, where they can couple strongly to photons, cavities, and superconducting circuits, con-

necting atomic and solid-state platforms [26]. They also enable the formation of exotic ultralong-range Rydberg molecules [27], providing unique insights into low-energy electron-atom scattering and molecular binding mechanisms at micrometer scales.

Taken together, these properties make Rydberg atoms a very interesting platform for both fundamental research and emerging quantum technologies, spanning fields from quantum optics and metrology to quantum simulation and hybrid quantum systems.

Although substantial progress has been made in this field, many aspects – such as detailed state energies, lifetimes, and interaction characteristics – remain only partially explored. This thesis aims to contribute to this ongoing effort by investigating an extensive range of Rydberg states across different bosonic and fermionic isotopes (see chapter 5), thereby providing additional data to support future developments in Rydberg physics.

1.1. Ytterbium

The selection of an appropriate atomic species plays an important role in realizing and controlling Rydberg states in practice. Early Rydberg experiments predominantly focused on alkali atoms such as rubidium [28–30] and cesium [28, 31, 32], chosen for their single-valence-electron simplicity and well-characterized spectra. In contrast, two-electron atoms, such as alkaline earth or ytterbium, offer distinct advantages that extend beyond these traditional systems.

Ytterbium's narrow optical clock transitions and long-lived metastable states make it attractive not only for quantum information processing, but also for precision metrology [33] and the quantum simulation of strongly correlated many-body systems [34]. The availability of different ytterbium isotopes, both with and without nuclear spin, combined with its favorable atomic structure, offers a wide range of possible excitation schemes, rendering ytterbium Rydberg states an attractive system to study.

Table 1.1.: List of the stable isotopes of ytterbium with their natural abundances and nuclear spin values [35].

Isotope	**Abundance [%]**	**Nuclear Spin (I)**
^{168}Yb	0.13	0
^{170}Yb	3.05	0
^{171}Yb	14.3	$\frac{1}{2}$
^{172}Yb	21.9	0
^{173}Yb	16.1	$\frac{5}{2}$
^{174}Yb	32.0	0
^{176}Yb	12.7	0

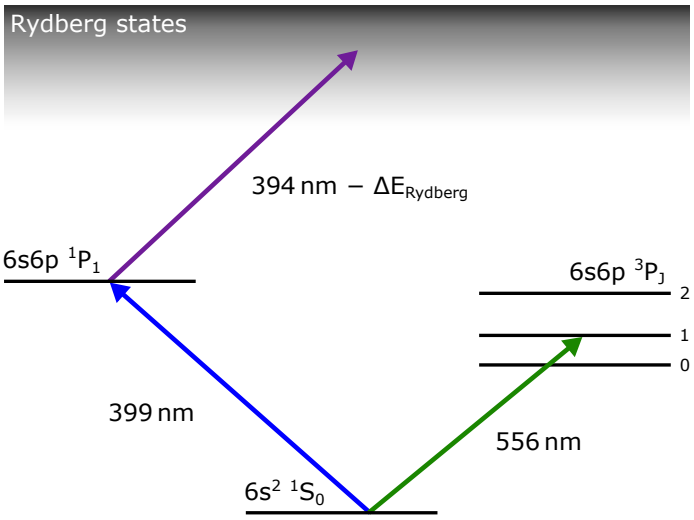

Figure 1.1.: Energy level scheme relevant for laser cooling, trapping, and excitation to Rydberg states. The broad ${}^1S_0 \rightarrow {}^1P_1$ transition is employed for the initial magneto-optical trap (MOT), the Zeeman slower, and as the intermediate state in the Rydberg excitation scheme, while the narrow ${}^1S_0 \rightarrow {}^3P_1$ intercombination line is used in the narrow-line MOT to achieve higher atomic densities.

In addition, mature laser-cooling and trapping techniques are available.

Ytterbium is a silvery rare-earth element with atomic number 70 and an electron configuration of $[\mathrm{Xe}]\, 4f^{14}\, 6s^2$, resulting in two valence electrons, making it similar in behavior to alkaline earth metals. This electronic structure gives rise to long-lived metastable triplet states and narrow optical transitions that enable high-precision spectroscopy. Naturally occurring ytterbium comprises seven stable isotopes, summarized in table 1.1.

The ${}^1S_0$ ground state has total angular momentum $J = 0$, and is therefore magnetically insensitive to first-order Zeeman shifts [36]. Consequently, its energy remains essentially unaffected by small magnetic-field fluctuations, leading to extended coherence times and enhanced stability of quantum states [4]. This magnetic robustness is a key asset for experiments that demand long-term stability, such as optical lattice clocks and coherent control of Rydberg excitations.

The different stable isotopes of ytterbium offer distinct advantages, making it worthwhile to investigate and compare their respective level structures and Rydberg state lifetimes. With the highest abundance, ^{174}Yb is particularly well-suited for initial studies and benchmarking against theoretical models. In fact, this isotope was solely used in previous stages of this experiment [1].

The bosonic isotopes ^{172}Yb and ^{176}Yb also have zero nuclear spin ($I = 0$) and are included in the present work. Since these three isotopes are all bosons and lack hyperfine structure, their excitation spectra and overall behavior in Rydberg states are expected to

be largely similar, allowing for consistent cross-comparisons.

In contrast, the fermionic isotopes ^{171}Yb and ^{173}Yb possess nuclear spins of $I = \frac{1}{2}$ and $I = \frac{5}{2}$, respectively. The presence of a finite nuclear spin introduces hyperfine splitting, which is particularly relevant for the description of Rydberg levels, as it significantly increases the number of accessible transitions and complicates the spectral structure [7, 37]. This, however, also enhances the relevance of these isotopes for applications in quantum information, where hyperfine-resolved states may serve as qubit levels.

Due to their relatively high natural abundances, ^{171}Yb and ^{173}Yb can be efficiently cooled and trapped from a thermal atomic beam with a natural composition of isotopes without additional effort. In contrast, the isotopes ^{170}Yb and especially ^{168}Yb have very low natural abundances, which complicates their use in precision experiments.

Consequently, this work focuses on the five isotopes ^{172}Yb, ^{174}Yb, ^{176}Yb, ^{171}Yb, and ^{173}Yb, which can be reliably cooled and trapped using standard laser cooling methods.

The energy level scheme in figure 1.1 includes the relevant transition scheme for laser cooling, magneto-optical trapping, and excitation to high-lying Rydberg states. Two cooling transitions can be used in our experiment: one proceeding via the intermediate singlet state $6s^2\,{}^1S_0 \rightarrow 6s6p\,{}^1P_1$ with a natural linewidth of $\Gamma_{\text{blue}} = 2\pi \times 29\,\text{MHz}$, and the other via the triplet state $6s^2\,{}^1S_0 \rightarrow 6s6p\,{}^3P_1$ with a narrow linewidth of $\Gamma_{\text{green}} = 2\pi \times 182\,\text{kHz}$. These two pathways offer flexibility in tailoring the excitation scheme to specific experimental requirements.

1.2. Cooling and Trapping

The investigation of fundamental properties of atoms – especially Rydberg atoms – requires an environment with minimal external perturbations. One way to achieve such conditions, is to spatially confine and cool the atoms to ultracold temperatures, typically in the millikelvin (mK) range or below. Reducing thermal motion is essential to extend interaction times, minimize Doppler broadening of spectral lines, and suppress decoherence effects due to collisions or external fields. These conditions are particularly important for high-resolution spectroscopy, such as those performed in this work, where Doppler broadening and motion-induced line shifts are effectively eliminated, allowing for precise determination of transition frequencies and line shapes.

A well-established technique to meet these requirements is laser cooling and trapping [38], which exploits the momentum exchange between atoms and photons. One of the most widely used configurations is the magneto-optical trap [39]. The MOT enables both spatial confinement and cooling of neutral atoms by combining the radiation pressure from red-detuned laser beams with the position-dependent Zeeman shifts induced by a magnetic field gradient (see figure 1.2 a)), described in detail in the standard references [38, 40].

To enhance the loading efficiency of the MOT, particularly from a thermal atomic beam,

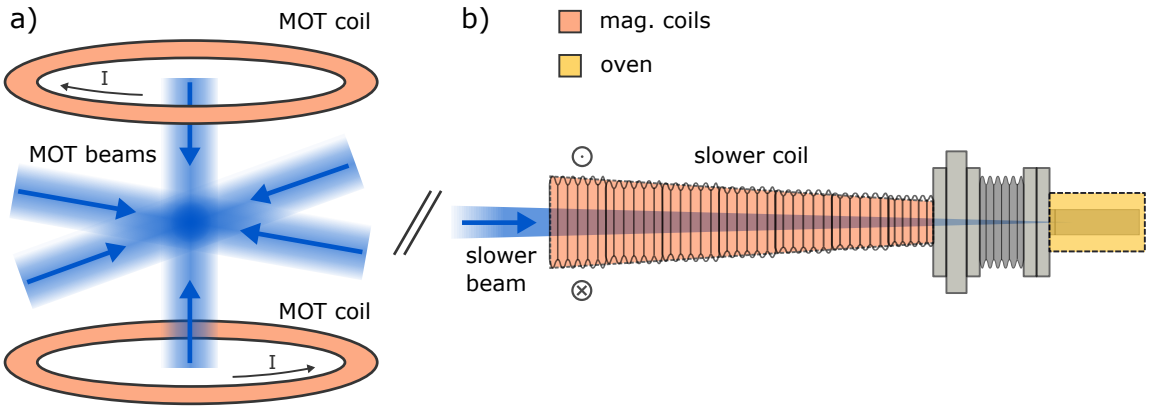

Figure 1.2.: Schematic of the MOT in a), illustrating the six pairwise orthogonal cooling beams and the anti-Helmholtz coil configuration. Panel b) shows the Zeeman slower with its increasing field geometry. Atoms from the oven are decelerated by the focused slower beam while traversing the magnetic field profile.

a Zeeman slower is often employed to load the MOT, as illustrated in figure 1.2 b). It consists of a spatially varying magnetic field along the atomic beam axis and a counter-propagating laser beam that is red-detuned relative to the atomic transition. The magnetic field causes a position-dependent Zeeman shift of the atomic energy levels, which compensates for the changing Doppler shift as the atoms decelerate. With an appropriate magnetic field profile the atoms remain resonant with the slowing laser over a long distance. The resulting continuous scattering of photons exerts a net force against the atomic motion, effectively reducing their velocity. Circular polarization of the slowing laser ensures that only atoms moving toward the beam experience resonant scattering. Once pre-decelerated in this way, the atoms enter velocity ranges compatible with the MOT´s capture conditions, allowing for efficient trapping.

As illustrated in figure 1.3, the magnetic field of the MOT causes a spatially dependent Zeeman splitting of the atomic energy levels. The magnetic field typically exhibits a linear gradient, with the trap center defined by the location of the field zero. Red-detuned, circularly polarized laser beams interact with the atoms such that those moving toward a beam experience a Doppler shift which brings them closer to resonance with that counter-propagating beam. This results in a velocity-dependent damping force that opposes the atomic motion. Simultaneously, the spatially varying magnetic field induces a position-dependent Zeeman shift of the atomic energy levels. In combination with the detuning of the laser δ_0 and the polarization of the beams, this gives rise to an imbalance in the scattering rates between the two counter-propagating beams, depending on the atom's position. As a result, a restoring force emerges that increases linearly with displacement from the trap center and directs atoms back toward the center.

The total force acting on an atom in the MOT can therefore be approximated by a

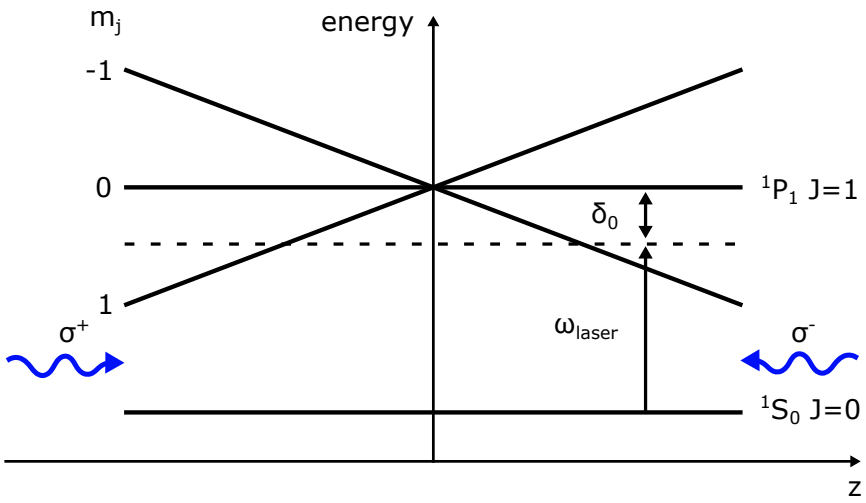

Figure 1.3.: Schematic illustration of the working principle of a magneto-optical trap. An applied magnetic field induces Zeeman splitting of the excited state into its m_j sublevels. Red-detuned, circularly polarized laser beams create a position-dependent restoring force: atoms displaced from the trap center experience a Zeeman shift into resonance with the counter-propagating beam and are pushed back toward the center. Adapted from [39].

combination of damping and restoring terms

$$\vec{F}_{\mathrm{MOT}} = -\beta\vec{v} - \kappa\vec{r}$$

Here, β denotes the damping coefficient associated with the velocity-dependent cooling force, and κ is the effective spring constant resulting from the position-dependent restoring force. This combination ensures both cooling and confinement of atoms near the trap center. The single-stage MOT of Yb, operated on the $6s^2\,{}^1S_0 \rightarrow 6s6p\,{}^1P_1$ transition at a wavelength of 399 nm, is commonly referred to as the blue MOT. Typically, about 10^7 atoms can be captured, with a Doppler limit for the bosonic isotopes of 690 µK setting the lower bound for the achievable temperature. The subsequent narrow-line MOT, operating on the $6s^2\,{}^1S_0 \rightarrow 6s6p\,{}^3P_1$ transition at 556 nm – referred to as the green MOT – has a corresponding Doppler limit of 4.4 µK (see section 7.3). In the experiment described in this thesis typically up to 10^6 atoms are captured in the green MOT. Notably, these cooling limits only yield for the bosonic isotopes of ytterbium. Fermionic isotopes can be cooled below this limit due to the presence of hyperfine structure arising from their non-zero nuclear spin. This allows sub-Doppler cooling mechanisms, such as Sisyphus cooling and polarization-gradient cooling to further reduce the atomic temperature, especially for the blue MOT [41]. Once cooled and localized, the atoms form a well-isolated and highly controllable platform for further investigations, such as the excitation and study of Rydberg states.

1.3. Rydberg Atoms

To introduce the fundamental concepts underlying Rydberg atoms, it is instructive to begin with the simplest atomic system: the hydrogen atom. Although atoms such as ytterbium are significantly more complex, the hydrogenic model – comprising a single electron orbiting a proton – offers an intuitive and analytically tractable starting point, as discussed in detail by T. F. Gallagher [18] and by Löw et al. [42]. It provides a conceptual basis for understanding the behavior of complex Rydberg systems, including those involving alkaline-earth-like atoms such as ytterbium.

While the Bohr model is only an approximation and fails to accurately describe low-lying states or multi-electron systems, it nonetheless captures the essential physics of states of high principal quantum number n and maximum angular momentum.

In particular, when the electron occupies a state with high n, the energy of an atom in such a Rydberg state is described by

$$E_n = -\frac{R_\infty hcZ^2}{n^2}. \tag{1.1}$$

Here R_∞ denotes the Rydberg constant, and Z is the atomic number of the atom. The size of such a Rydberg atom can exceed that of its ground-state counterpart by more than two orders of magnitude [18], leading to exaggerated physical properties (see table 1.2).

Within this semiclassical framework, the large spatial separation between the oppositely charged electron and the ionic core results in a significant effective electric dipole moment, which can be induced by external fields or interactions with nearby atoms. Assuming a purely classical dipole model, the electric dipole moment $\vec{d}$ scales linearly with the electron-nucleus separation

$$\vec{d} = e \cdot \vec{r}.$$

This large dipole moment is of particular interest, as it enables strong long-range interactions between Rydberg atoms, which are central to many applications in quantum optics [43].

Several key physical properties of Rydberg atoms and their scaling behavior with the principal quantum number n are summarized in table 1.2. The electron-nucleus separation scales as n^2, which in turn leads to an effective dipole moment that also approximately scales as n^2. The binding energies, discussed in section 5.2, scale as n^{-2}, while the radiative lifetimes, analyzed in section 5.3, scale as n^3. Additionally, the polarizability of the Rydberg states, presented in section 5.1, follows an n^7 scaling.

In an neutral multi-electron atom with a single highly excited electron, the remaining electrons largely screen the nuclear charge. As a result, the Rydberg electron interacts predominantly with a singly charged ionic core, composed of a nucleus with Z protons (and N neutrons) surrounded by $Z - 1$ unexcited electrons. In this picture, the atom becomes

Physical Quantity	**Symbol**	**Scaling** n
Electron-nucleus distance	$\langle r \rangle$	n^2
Binding energy	E	n^{-2}
Transition frequency $n \to n{+}1$	ν	n^{-3}
Electric dipole moment	d	n^2
Radiative lifetime	τ	n^3
Static polarizability	α	n^7
van der Waals coefficient	C_6	n^{11}

Table 1.2.: Approximate scaling laws of key physical quantities for Rydberg atoms as functions of the principal quantum number n. Adapted from [18].

effectively hydrogen-like, consisting of two main constituents: one electron orbiting a singly charged core. As long as the electron remains sufficiently far from the core, this hydrogenic approximation remains valid. This approach enables the use of hydrogenic models as a first-order description, even for non-hydrogenic atoms such as ytterbium.

However, deviations from the ideal Coulomb potential arise when the Rydberg electron's wavefunction penetrates the ionic core region, particularly in states with low orbital angular momentum ℓ. These deviations reflect the finite size, polarizability, and complex internal structure of the core, and are captured quantitatively by the so-called quantum defect $\delta_{n,\ell,j}$. This quantity effectively shifts the principal quantum number and is used to define the effective principal quantum number [18]

$$n^* = n - \delta_{n,\ell,j}.$$

This correction modifies the energy spectrum, thereby enabling the retention of a hydrogen-like description of Rydberg atoms even in multi-electron systems, as discussed in detail in chapter 2. In particular, the quantum defect becomes negligible for high-ℓ states, where the electron remains largely outside the ionic core due to the centrifugal barrier, rendering core-penetration effects insignificant.

As a result, the characteristic scaling laws of hydrogenic Rydberg states can be generalized to complex atoms by replacing n with n^*. Several key properties depend strongly on this effective quantum number. For instance, the radiative lifetime scales approximately as $(n^*)^3$, while the static polarizability scales as $(n^*)^7$.

1.4. Rydberg-Rydberg Interaction

Rydberg atoms are intrinsically fascinating and allready offer some practical applications, such as electromagnetic field sensing [44, 45]. Moreover, when interactions between Rydberg atoms are considered, they provide a gateway to a wide range of novel and potentially useful phenomena.

Inspired by Richard Feynman's vision of quantum simulation [46], the use of Rydberg atoms as a platform for quantum logic operations was proposed around 2000. Jaksch et al. [47] and Lukin et al. [48] introduced the concept of Rydberg blockade effects – strong dipole-dipole interactions between highly excited atoms – that enable fast and coherent two-qubit gates with neutral atoms. This theoretical description established Rydberg atoms as a promising candidate for scalable quantum computing architectures and quantum simulation [42, 49–51], with ytterbium being a particularly attractive candidate [52]. As a prominent example, Rydberg atom arrays have been proposed and realized as quantum simulators for solid-state-like systems: for instance, bilayers of Rydberg atoms can mimic electron-phonon coupling in unconventional superconductors [53].

Notably, the isotope ^{171}Yb, due to the finite nuclear spin, allows for the implementation of nuclear spin qubits with exceptional robustness. These qubits exhibit extraordinarily long coherence times owing to their minimal magnetic sensitivity and weak coupling to environmental noise [54].

These applications make use of the strong van der Waals interaction strength, characterized by the C_6 coefficient, which scales approximately as $(n^*)^{11}$, as presented in table 1.2. The non-resonant dipole-dipole interaction (see section 6.1.2) is proportional to this coefficient via $V_{\mathrm{vdW}} \propto C_6/R^6$ and dominates the long-range interaction between Rydberg atoms [55]. Typical atomic densities required to observe this effect are on the order of $10^{10}\,\mathrm{cm}^{-3}$ for Rydberg states with principal quantum numbers $n > 80$. The steep dependence on the effective principle quantum number highlights the importance of high-n states for the investigation of these interactions.

1.5. Outline of this Thesis

The experimental work described in this thesis can be divided into two parts. In the first part, a single-stage MOT is used to measure Rydberg transition energies, polarizabilities, and lifetimes [56]. The main experimental apparatus required for these measurements was originally built by C. Halter [1]. With minor adaptations, these measurements were performed and are presented here.

In the second part, the focus is on preparing for the investigation of Rydberg-Rydberg interactions, which requires a higher atomic density. For this purpose, a second cooling stage was implemented to operate a two-stage MOT. This thesis reports the successful

implementation of this second stage and the resulting measurements of Rydberg atoms at higher density. This forms the basis for the investigation of Rydberg-Rydberg interactions.

Chapters 2 to 5 of this thesis are dedicated to the first part of the experimental work. The theoretical foundations necessary to understand the underlying Rydberg physics – ranging from hydrogenic models to single- and multichannel quantum defect theory, as well as the behavior of Rydberg atoms in electric fields – are presented in chapter 2.

In chapter 3, the experimental apparatus used for the single-stage MOT is described, including the vacuum system, laser setup, and experimental control. The required experimental sequence is detailed in chapter 4. The measurement results for Rydberg energy levels, polarizabilities, and lifetimes are presented in chapter 5.

The second part of the thesis begins in chapter 6, which introduces the theoretical concepts of Rydberg-Rydberg interactions. The experimental modifications necessary for the two-stage MOT are described in chapter 7, including a characterization of its successful implementation. In chapter 8, the first measurements of Rydberg atoms in the high-density two-stage MOT are presented, along with a new detection technique for probing Rydberg-Rydberg interactions.

Finally, chapter 9 outlines possible improvements to the current experiment and discusses both short- and long-term perspectives toward investigating interacting Rydberg systems.

2.

Theory of Ultracold Rydberg Atoms

A solid theoretical understanding is essential for interpreting and designing experiments involving highly excited Rydberg atoms. This chapter summarizes established concepts and models that describe their structure, dynamics, and interaction with external fields. This overview reproduces existing knowledge and serves solely to provide the theoretical foundation for the experimental work. It begins with the quantum mechanics of simple atomic systems and gradually extends to more realistic descriptions that account for multi-electron effects and field-induced phenomena.

The treatment of the hydrogen atom (section 2.1.1) follows the presentations in [57] and [58] and serves as the canonical starting point, since its analytic solution provides fundamental insight into quantization, angular-momentum coupling, and the characteristic $1/n^2$ energy scaling that defines Rydberg series. Building on this foundation, section 2.1.2 introduces quantum defect theory, following the treatments in [18, 59, 60], to account for deviations from the hydrogenic model in real atoms with a single valence electron, such as rubidium and caesium. This framework is further extended in section 2.1.3 through multi-channel quantum defect theory, which adds channel couplings to complex level structures characteristic of multi-electron systems, following the descriptions in [60–62].

Subsequently, section 2.2 examines the influence of external electric fields on Rydberg atoms. The discussion of the Stark effect (section 2.2.1) follows [18, 63, 64], while the treatment of field-ionization processes (section 2.2.2), based on [65–67], highlights their role as key mechanisms for manipulating and detecting Rydberg states in experimental settings. Collectively, these theoretical foundations provide the framework for understanding the energy structure, interaction dynamics, and spectroscopic signatures discussed in the subsequent experimental chapters.

2.1. Rydberg States

This section introduces the fundamental concepts of Rydberg states, laying the theoretical foundation for their application to multi-electron systems such as ytterbium. After defining the key characteristics of Rydberg states, we will gradually develop the theoretical tools

necessary to describe their behavior in increasingly complex atomic systems.

Rydberg states are highly excited electronic states of atoms, characterized by a principal quantum number $n \gg 1$. In these states, the valence electron occupies an orbital located far from the atomic core.

Since the structure of Rydberg states in multi-electron atoms is significantly more complex than in hydrogen, suitable approximations are required for their theoretical treatment. A common approach is to compare these systems to hydrogenic Rydberg states, as the hydrogen atom permits analytic solutions due to its simple, single-electron structure. In the Rydberg regime, this comparison becomes particularly meaningful, as the outermost electron is located far from the atomic core and is only weakly influenced by the inner electrons, rendering the system approximately hydrogen-like.

The primary deviations arise when the electron penetrates the core region. Since the core of a non-hydrogen atom has a finite size, the electron´s probability density within the core is non-zero. These issues are addressed throughout this chapter.

2.1.1. Quantum Mechanics of Hydrogen

In this section, the wavefunctions and energy levels of hydrogenic states are derived within the framework of quantum mechanics, as outlined in [57]. Here, the hydrogen atom is considered to consists of a point-like nucleus – a heavy proton with charge $+e$ – and a single light electron with charge $-e$, which moves under the influence of the Coulomb potential generated by the proton. In addition, the electron is spinless for the following treatment. The quantum mechanical behavior of such systems is governed by the Schrödinger equation

$$i\hbar\frac{\partial\psi}{\partial t} = -\frac{\hbar^2}{2m}\nabla^2\psi + V\psi. \tag{2.1}$$

For time-independent potentials, a complete set of stationary states exists

$$\psi_n(\mathbf{r},t) = \psi_n(\mathbf{r})\, e^{-i\mathcal{E}_n t/\hbar}, \tag{2.2}$$

where $\mathbf{r} = (x,y,z)$, and the spatial wavefunction $\psi_n(\mathbf{r})$ satisfies the time-independent Schrödinger equation

$$-\frac{\hbar^2}{2m}\nabla^2\psi + V\psi = \mathcal{E}\psi. \tag{2.3}$$

Since the potential acting on the electron is given by the central Coulomb potential,

$$V(r) = -\frac{e^2}{4\pi\varepsilon_0}\,\frac{1}{r}, \tag{2.4}$$

which depends only on the radial distance r, it is natural to express the wavefunction in spherical coordinates. The time-independent Schrödinger equation in these coordinates becomes

$$-\frac{\hbar^2}{2m}\left[\frac{1}{r^2}\frac{\partial}{\partial r}\left(r^2\frac{\partial\psi}{\partial r}\right)+\frac{1}{r^2\sin\theta}\frac{\partial}{\partial\theta}\left(\sin\theta\frac{\partial\psi}{\partial\theta}\right)+\frac{1}{r^2\sin^2\theta}\frac{\partial^2\psi}{\partial\phi^2}\right]+V\psi=\mathcal{E}\psi. \tag{2.5}$$

To solve this equation, we use the method of separation of variables and assume a product solution

$$\psi(r,\theta,\phi)=R(r)\,Y(\theta,\phi). \tag{2.6}$$

Substituting this ansatz into equation (2.5) and performing algebraic manipulation yields

$$\frac{1}{R}\frac{d}{dr}\left(r^2\frac{dR}{dr}\right)-\frac{2mr^2}{\hbar^2}\left[V(r)-\mathcal{E}\right]+\frac{1}{Y}\left[\frac{1}{\sin\theta}\frac{\partial}{\partial\theta}\left(\sin\theta\frac{\partial Y}{\partial\theta}\right)+\frac{1}{\sin^2\theta}\frac{\partial^2 Y}{\partial\phi^2}\right]=0. \tag{2.7}$$

Since the first term depends only on r and the second only on the angles, both terms must equal a constant. Without loss of generality, this separation constant is denoted by $\ell(\ell+1)$.

Next, we separate the angular function as

$$Y(\theta,\phi)=\Theta(\theta)\,\Phi(\phi), \tag{2.8}$$

leading to the angular equation

$$\left[\frac{1}{\Theta}\left(\sin\theta\frac{d}{d\theta}\left(\sin\theta\frac{d\Theta}{d\theta}\right)\right)+\ell(\ell+1)\sin^2\theta\right]+\frac{1}{\Phi}\frac{d^2\Phi}{d\phi^2}=0. \tag{2.9}$$

Again, the terms must each equal a constant. Conventionally, this constant is denoted as m^2. The azimuthal part is then easily solvable

$$\frac{d^2\Phi}{d\phi^2}=-m^2\Phi \quad\Rightarrow\quad \Phi(\phi)=e^{im\phi}, \tag{2.10}$$

with the periodicity condition $\Phi(\phi+2\pi)=\Phi(\phi)$ implying that m must be an integer.

The solution[1] for the polar angle function is

$$\Theta(\theta)=A\,P_\ell^m(\cos\theta), \tag{2.11}$$

where A is a normalization constant and $P_\ell^m(x)$ is the associated Legendre function

$$P_\ell^m(x)\equiv(-1)^m\left(1-x^2\right)^{m/2}\frac{d^m}{dx^m}P_\ell(x), \tag{2.12}$$

with the Legendre polynomials $P_\ell(x)$ defined via Rodrigues' formula [57]

$$P_\ell(x)\equiv\frac{1}{2^\ell\ell!}\frac{d^\ell}{dx^\ell}\left(x^2-1\right)^\ell. \tag{2.13}$$

[1] Although other mathematical solutions can be found, they exhibit divergences at $\theta=0$ and/or $\theta=\pi$ and are therefore not considered physically acceptable.

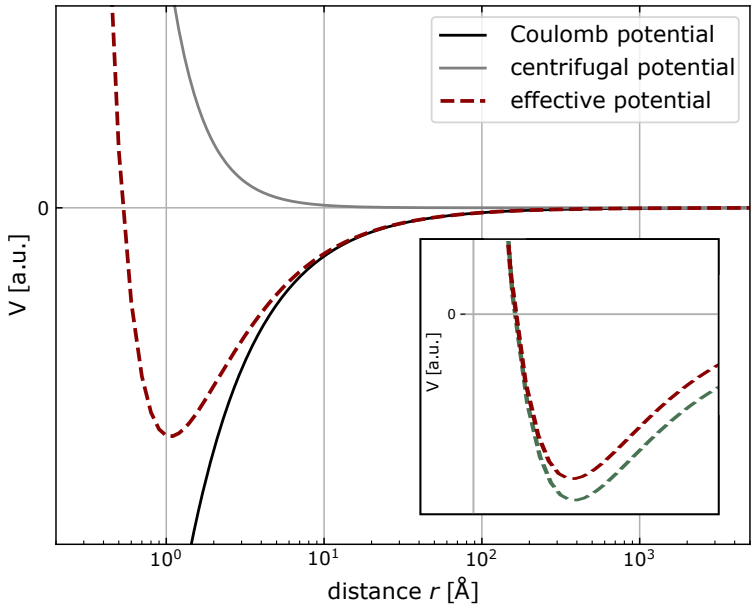

Figure 2.1.: Effective potential for the hydrogen atom with angular momentum $\ell = 1$. The Coulomb potential is shown in black, and the centrifugal potential in grey; their sum, the effective potential, is plotted in red. The inset schematically compares the effective potential to a non-hydrogenic atom, which is deeper near the core. This modification leads to a phase shift in the corresponding radial wavefunction. Inspired by [18].

Combining the solutions and applying normalization yields the spherical harmonics

$$Y_\ell^m(\theta,\phi) = \sqrt{\frac{2\ell+1}{4\pi}\frac{(\ell-m)!}{(\ell+m)!}}\, e^{im\phi}\, P_\ell^m(\cos\theta). \tag{2.14}$$

We now turn to the radial part. From equation (2.7), we get

$$\frac{d}{dr}\left(r^2\frac{dR}{dr}\right) - \frac{2mr^2}{\hbar^2}[V(r)-\mathcal{E}]R = \ell(\ell+1)R. \tag{2.15}$$

Introducing $u(r) \equiv rR(r)$, this transforms into

$$-\frac{\hbar^2}{2m}\frac{d^2u}{dr^2} + \left[V(r) + \frac{\hbar^2}{2m}\frac{\ell(\ell+1)}{r^2}\right]u(r) = \mathcal{E}u(r), \tag{2.16}$$

where the effective potential is

$$V_{\text{eff}}(r) = V(r) + \frac{\hbar^2}{2m}\frac{\ell(\ell+1)}{r^2}. \tag{2.17}$$

This sum of the Coulomb potential $V(r)$ and the centrifugal potential, represented by the second term, is shown in figure 2.1.

Substituting the Coulomb potential from equation (2.4), we arrive at the radial equation for hydrogen

$$-\frac{\hbar^2}{2m_e}\frac{d^2u}{dr^2}+\left(-\frac{e^2}{4\pi\varepsilon_0}\frac{1}{r}+\frac{\hbar^2}{2m_e}\frac{\ell(\ell+1)}{r^2}\right)u(r)=\mathcal{E}u(r). \tag{2.18}$$

By defining the new variables

$$\kappa\equiv\sqrt{-\frac{2m_e\mathcal{E}}{\hbar^2}},\quad \rho\equiv\kappa r,\quad \rho_0\equiv\frac{m_e e^2}{2\pi\varepsilon_0\hbar^2\kappa}, \tag{2.19}$$

we obtain the dimensionless radial equation

$$\frac{d^2u}{d\rho^2}=\left[1-\frac{\rho_0}{\rho}+\frac{\ell(\ell+1)}{\rho^2}\right]u(\rho). \tag{2.20}$$

To simplify the asymptotic behavior, we use the ansatz

$$u(\rho)=\rho^{\ell+1}e^{-\rho}v(\rho), \tag{2.21}$$

which transforms equation (2.20) into

$$\rho\frac{d^2v}{d\rho^2}+2(\ell+1-\rho)\frac{dv}{d\rho}+\left[\rho_0-2(\ell+1)\right]v(\rho)=0. \tag{2.22}$$

Using a power series expansion

$$v(\rho)=\sum_{j=0}^{\infty}c_j\,\rho^j, \tag{2.23}$$

insertion into the differential equation gives the recursion relation

$$c_{j+1}=\left[\frac{2(j+\ell+1)-\rho_0}{(j+1)(j+2\ell+2)}\right]c_j. \tag{2.24}$$

To ensure convergence at infinity, the series must terminate. Let $c_{N-1}\neq 0$ but $c_N=0$, implying

$$\rho_0=2(N+\ell). \tag{2.25}$$

Setting $n\equiv N+\ell$ and using equation (2.19) the energy levels are given by the Bohr formula

$$\mathcal{E}_n=-\frac{m_e}{2\hbar^2}\left(\frac{e^2}{4\pi\varepsilon_0}\right)^2\frac{1}{n^2}=\frac{\mathcal{E}_1}{n^2}. \tag{2.26}$$

The allowed values of ℓ and m follow from the quantization condition: $\ell=0,1,...,n-1$ and $m=-\ell,...,+\ell$, giving a total degeneracy

$$d(n)=\sum_{\ell=0}^{n-1}(2\ell+1)=n^2. \tag{2.27}$$

The polynomial $v(\rho)$ is then given by the associated Laguerre polynomial

$$v(\rho) = L_{n-\ell-1}^{2\ell+1}(2\rho), \tag{2.28}$$

defined via

$$L_p^q(x) \equiv (-1)^p \left(\frac{d}{dx}\right)^p L_{p+q}(x), \qquad L_q(x) \equiv \frac{e^x}{q!}\left(\frac{d}{dx}\right)^q \left(e^{-x}x^q\right). \tag{2.29}$$

Putting everything together and normalizing, the radial part of the wavefunction is given by

$$R(r) = \sqrt{\left(\frac{2}{na}\right)^3 \frac{(n-\ell-1)!}{2n(n+\ell)!}}\, e^{-\frac{r}{na}} \left(\frac{2r}{na}\right)^\ell L_{n-\ell-1}^{2\ell+1}\left(\frac{2r}{na}\right). \tag{2.30}$$

where $a = \frac{4\pi\varepsilon_0\hbar^2}{m_e e^2}$ is the Bohr radius. The total hydrogen wavefunctions then take the form

$$\psi_{n\ell m} = \sqrt{\left(\frac{2}{na}\right)^3 \frac{(n-\ell-1)!}{2n(n+\ell)!}}\, e^{-\frac{r}{na}} \left(\frac{2r}{na}\right)^\ell L_{n-\ell-1}^{2\ell+1}\left(\frac{2r}{na}\right) Y_\ell^m(\theta,\phi). \tag{2.31}$$

The energy a state with principal quantum number n is then

$$\mathcal{E}_n = -\frac{R_\infty\, h\, c}{n^2}. \tag{2.32}$$

Thus the energy difference between two levels is

$$\mathcal{E}_\gamma = \mathcal{E}_i - \mathcal{E}_f = -R_\infty\, h\, c\left(\frac{1}{n_i^2} - \frac{1}{n_f^2}\right). \tag{2.33}$$

Expressed in terms of wavelength $\lambda = c/\nu$, this becomes

$$\frac{1}{\lambda} = \frac{\mathcal{E}_\gamma}{h\, c} = R_\infty\left(\frac{1}{n_f^2} - \frac{1}{n_i^2}\right), \tag{2.34}$$

where R_∞ is the Rydberg constant, given by

$$R_\infty \equiv \frac{m_e}{4\pi c\hbar^3}\left(\frac{e^2}{4\pi\varepsilon_0}\right)^2. \tag{2.35}$$

The Rydberg energy is commonly known as

$$R_\infty\, h\, c = 13.6\,\mathrm{eV}. \tag{2.36}$$

To be precise, this Rydberg constant R_∞ is defined under the assumption of an infinitely heavy nucleus compared to the orbiting electron. The mass-corrected Rydberg constant is obtained by introducing the reduced mass

$$m_r = \frac{m_e M}{m_e + M}, \tag{2.37}$$

which for hydrogen leads to

$$R_H = R_\infty \frac{m_r}{m_e}. \tag{2.38}$$

2.1.1.1. Hydrogen-like Systems

Note that the previous discussion was limited to hydrogen. For hydrogen-like systems – atoms with a single electron but more than a single proton in the nucleus, such as deuterium, tritium, or hydrogenic ions (e.g., He^+, Li^{2+}, etc.) – the angular part of the wavefunction remains unchanged due to the preserved spherical symmetry. The Coulomb potential generalizes to

$$V(r) = -\frac{Ze^2}{4\pi\varepsilon_0 r}, \tag{2.39}$$

where Z denotes the nuclear charge. The corresponding energy levels are modified by incorporating the modified potential. The resulting expression for the allowed energy levels reads [58]

$$\mathcal{E}_n = -\frac{R_Z\, h\, c}{n^2}, \tag{2.40}$$

using the definition of an effective Rydberg constant for the system

$$R_Z = R_\infty \frac{m_r}{m_e} Z^2. \tag{2.41}$$

2.1.2. Single-Valence-Electron Atoms and Quantum Defect Theory

To extend the model beyond hydrogen, we now consider atoms with a single valence electron outside a closed-shell core. When this outermost electron is excited to a Rydberg state, the inner-shell electrons effectively screen the nuclear charge. As a result, the Rydberg electron experiences an effective potential corresponding approximately to a single positive charge, thus reducing the system to a hydrogen-like one – especially when the electron is far from the atomic core.

In this regime of large electron-nucleus separation, the similarity to the hydrogen atom becomes particularly pronounced. However, deviations from hydrogenic behavior arise when the electron penetrates the core region. Unlike the approximately point-like proton in the hydrogen atom, the core of a multi-electron atom has finite spatial extent. This leads to modifications in the effective potential experienced by the Rydberg electron and hence to observable shifts in the energy levels.

To determine the allowed energy states in such systems, it is necessary to revisit the effective potential. For large r, the potential remains Coulomb-like, $V(r) \sim -\frac{e^2}{4\pi\varepsilon_0 r}$. Assuming that the inner electrons are not affected by the outermost electron and that they are distributed spherically symmetrically around the nucleus, although the excited electron may still penetrate this charge cloud. When the excited electron is located within this cloud, the effective potential becomes significantly deeper than the bare Coulomb potential due to the reduced shielding of the nuclear charge. We further assume the existence of a

characteristic radius r_c, below which the potential is lower than $V(r)$ and above which it coincides with $V(r)$.

However, quantum defect theory (QDT) provides a framework in which solutions of the Schrödinger equation are constructed separately in the inner and outer regions and matched at an intermediate radius.

Assuming spherical symmetry, the angular part of the wavefunction remains unchanged (see equation (2.14)). The radial part, however, must be solved using the modified potential. In the outer region ($r > r_c$), where the potential is Coulombic, the solution is known. In the inner region, where the electron can penetrate the core, the potential becomes deeper than that of hydrogen, as schematically shown in the inset of figure 2.1.

The radial equation becomes

$$\frac{d}{dr}\left(r^2\frac{dR}{dr}\right) - \frac{2mr^2}{\hbar^2}[V_{\text{non-H}}(r) - \mathcal{E}]R = \ell(\ell+1)R, \tag{2.42}$$

where $V_{\text{non-H}}(r)$ denotes the effective potential including deviations from the hydrogenic form.

In QDT, it is common to express the radial wavefunction in terms of the regular and irregular Coulomb wavefunctions $f(\ell, \mathcal{E}, r)$ and $g(\ell, \mathcal{E}, r)$, which are linearly independent solutions to the radial equation for hydrogen

$$R_f(r) = \frac{f(\ell, \mathcal{E}, r)}{r}, \tag{2.43}$$

$$R_g(r) = \frac{g(\ell, \mathcal{E}, r)}{r}. \tag{2.44}$$

In the limit $r \to 0$, these solutions behave as [59]

$$f(\ell, \mathcal{E}, r) \propto r^{\ell+1}, \tag{2.45}$$

$$g(\ell, \mathcal{E}, r) \propto r^{-\ell}, \tag{2.46}$$

with g being unphysical for bound states due to its divergencer at the origin for $\ell > 0$. This implies that the contribution of g to the total wavefunction must vanish in the limit $r \to 0$.

In the asymptotic region ($r \to \infty$) for $\mathcal{E} < 0$, the functions take the form

$$f = u(\ell, \nu, r)\sin(\pi\nu) - v(\ell, \nu, r)e^{i\pi\nu}, \tag{2.47}$$

$$g = u(\ell, \nu, r)\cos(\pi\nu) + v(\ell, \nu, r)e^{i(\pi\nu+\frac{1}{2}\pi)}, \tag{2.48}$$

where ν is related to the energy via

$$\mathcal{E} = -\frac{m_e}{2\hbar^2}\left(\frac{e^2}{4\pi\varepsilon_0}\right)^2\frac{1}{\nu^2}. \tag{2.49}$$

Following [18], the boundary conditions require that as $r \to \infty$, $u \to \infty$ and $v \to 0$.

As $r \to 0$, only the f solution remains physical. Imposing these boundary conditions implies $\sin(\pi\nu) = 0$, so $\nu \in N$, leading to the known hydrogenic energy levels.

Transitioning to non-hydrogenic, single-valence-electron atoms, we introduce a phase shift τ_ℓ due to the modified inner potential. For $r > r_c$, the radial wavefunction can then be written as [18, 60]

$$R(r) = \frac{1}{r}\left[f(\ell,\nu,r)\cos\tau_\ell - g(\ell,\nu,r)\sin\tau_\ell\right]. \tag{2.50}$$

These wavefunctions can be computed numerically using standard methods such as the Numerov algorithm [68] or Runge-Kutta integration [69, 70].

We assume that τ_ℓ depends primarily on the angular momentum quantum number ℓ, as the centrifugal barrier $\ell(\ell+1)/r^2$ affects the electron's ability to penetrate the core. For larger ℓ, the electron is increasingly excluded from the core, and the system becomes more hydrogen-like.

To fulfill the asymptotic boundary condition: as $r \to \infty$, $\Psi \to 0$ the coefficients of u (see equation (2.47) and equation (2.48))) must vanish, since $u \to \infty$ in this limit. This leads to

$$\cos\tau_\ell \sin(\pi\nu) + \sin\tau_\ell \cos(\pi\nu) = 0, \tag{2.51}$$

which can be rewritten using trigonometric identities yielding

$$\sin(\pi\nu + \tau_\ell) = 0, \tag{2.52}$$

and consequently

$$\nu = n - \frac{\tau_\ell}{\pi}. \tag{2.53}$$

By defining the quantum defect as $\delta_\ell := \frac{\tau_\ell}{\pi}$, the energies of Rydberg states can now be expressed as

$$\mathcal{E}_{n,\ell} = -\frac{R_Z\, h\, c}{(n-\delta_\ell)^2}, \tag{2.54}$$

where R_Z denotes the reduced-mass-corrected Rydberg constant of the atom and $n^* = n - \delta_\ell$ is the effective principal quantum number.

Generally, the quantum defect δ_ℓ decreases with increasing ℓ, as the overlap of the electron wavefunction with the core diminishes. Since the effective principal quantum numbers is reduced relative to the hydrogenic value n by the quantum defect, the energy levels are shifted to higher values. This shift arises from the previously mentioned finite spatial extension of the core, which allows the outermost electron to penetrate the core region.

Importantly, the quantum defect itself is not strictly constant but exhibits an energy dependence. This can be described by the Rydberg-Ritz formula [60]

$$\delta_{n,\ell} = \delta_0(\ell) + \frac{\delta_1(\ell)}{(n-\delta_0(\ell))^2} + \frac{\delta_2(\ell)}{(n-\delta_0(\ell))^4} + \dots \tag{2.55}$$

This series expansion allows for improved accuracy in predicting energy levels, especially for low n.

2.1.3. Multi-Electron Atoms and Multichannel Quantum Defect Theory

A natural generalization for describing multi-electron atoms, such as ytterbium with more than one valence electron, is provided by multichannel quantum defect theory (MQDT). As the name suggests, MQDT describes systems in which multiple configurations of the ionic core must be considered, giving rise to several channels that contribute to the dynamics. For non-hydrogenic Rydberg atoms, a channel corresponds to a specific asymptotic configuration defined by the quantum numbers of the residual ion and the Rydberg electron, their angular momentum coupling, and the associated ionization threshold. The ionic core is characterized by its internal quantum numbers, which can differ due to excitations of the inner electrons, fine- and hyperfine structure, or alternative electron configurations; each distinct core state defines a separate channel with its own ionization threshold. The outer electron is described by its orbital angular momentum ℓ and, in combination with the spin s, its total angular momentum j. Together, they determine the total angular momentum of the system. Each channel therefore specifies the state of the ionic core when the electron is far away, the partial wave of the Rydberg electron, and the corresponding threshold energy.

In the present discussion, we focus on dissociation channels, which are formed by an electron with angular momentum ℓ and a residual ionic core. These channels describe the system when the outermost electron is considered infinitely far from the nucleus. The treatment presented here follows [60–62].

As is standard in this field, energies are expressed in terms of wavenumbers, as described by the definition

$$E \equiv \mathcal{E}/hc, \quad I_i \equiv \mathcal{I}_i/hc. \tag{2.56}$$

We assume the electron can reside in a total number of N_{ch} channels, each associated with an ionization limit $\mathcal{I}_i$ (with $i = 1, \dots, N_{\mathrm{ch}}$). For a time-independent calculation at total energy $\mathcal{E}$, a channel i is said to be open if $\mathcal{E} > \mathcal{I}_i$, and closed otherwise. In an open channel, the electron can escape to infinity with positive kinetic energy, while in a closed channel, this is energetically forbidden. Therefore, the wavefunction in a closed channel must decay exponentially at large distances.

In MQDT, two different antisymmetrized ansätze for the total wavefunction are used. The first is

$$\Psi(X,r) = \mathcal{A}\sum_i C_i\,\chi_i(X)\,\phi_i(r), \tag{2.57}$$

where r denotes the radial coordinate of the outer electron, while X represents all other relevant coordinates (e.g., angular variables, core electrons, and spins). The coefficients C_i determine the admixture of the individual channel wave functions, and $\mathcal{A}$ is the anti-symmetrization operator. The function $\phi_i(r)$ corresponds to the radial wave function of channel i, whereas $\chi_i(X)$ describes both the angular and spin dependence of the outermost electron, as well as the radial, angular and spin dependence of all other electrons. This ansatz is closely related to individual dissociation channels, in the sense that each term in the sum predominantly corresponds to a single channel, while inter-channel coupling is treated as a small perturbation.

The second ansatz, which better describes the inner region (near the core), is

$$\Psi(X,r) = \mathcal{A}\sum_\alpha A_\alpha\left[\mathcal{F}_\alpha(X,r)\cos(\pi\delta_\alpha) - \mathcal{G}_\alpha(X,r)\sin(\pi\delta_\alpha)\right] \tag{2.58}$$

where δ_α are the eigenquantum defects[2] associated with eigenchannels α, and A_α are constant coefficients. In the case of divalent atoms, such as Yb, these coefficients describe the three-body interactions of the doubly charged core and the two remaining electrons. Note that the coupling schemes corresponding to the indices i and α in the two different ansätze do not need to be the same.

Assuming the electron moves in a Coulomb potential (far) outside the core, the radial part of the Schrödinger equation becomes

$$\left[-\frac{\hbar^2}{2m_r}\frac{d^2}{dr^2} - \frac{\hbar^2}{2m_r}\frac{l_i(l_i+1)}{r^2} - \frac{e^2}{4\pi\epsilon_0 r}\right]u_i(r) = \epsilon_i u_i(r), \tag{2.59}$$

with the reduced mass m_r, $u_i(r) = r\phi_i(r)$ and $\epsilon_i = \mathcal{E} - \mathcal{I}_i$.

As in standard QDT, the general solution is a superposition of regular and irregular Coulomb functions

$$u_i(r) = f(\epsilon_i,\ell_i;r)\cos(\pi\nu_i) + g(\epsilon_i,\ell_i;r)\sin(\pi\nu_i), \tag{2.60}$$

where f and g are the regular and irregular Coulomb solutions that can be calculated numerically [71], and ν_i is a channel-specific phase parameter.

In the limit of large electron-core separations, it is assumed that the functions $\mathcal{F}_\alpha$ and $\mathcal{G}_\alpha$ can be written as linear combinations of $\chi_i(X)\,\frac{f(\epsilon_i,\ell_i;r)}{r}$ and $\chi_i(X)\,\frac{g(\epsilon_i,\ell_i;r)}{r}$, respectively. Thus, for $r\to\infty$, we find

$$\mathcal{F}_\alpha(X,r) = \sum_i U_{i\alpha}\,\chi_i(X)\,\frac{f(\epsilon_i,\ell_i;r)}{r} \tag{2.61}$$

[2] In single-channel situations, δ_α is directly analogous to the quantum defect δ_ℓ in standard QDT. In multi-channel cases, it generalizes δ_ℓ to eigenchannel quantum defects that account for inter-channel coupling. In the literature, this eigenchannel quantum defect it is often denoted by μ_α.

and

$$\mathcal{G}_\alpha(X,r) = \sum_i U_{i\alpha}\,\chi_i(X)\,\frac{g(\epsilon_i,\ell_i;r)}{r}. \tag{2.62}$$

The $U_{i\alpha}$ coefficients are real and independent of the electron coordinates. The two ansätze described above yield physically admissible bound-state wavefunctions only if (i) the parameters ν_i, C_i, δ_α, and A_α are chosen such that the radial functions satisfy $\phi_i(r) \to 0$ as $r \to \infty$, (ii) both equation (2.57) and equation (2.58) represent bound states as well as states with energies above the lowest ionization threshold[3], and (iii)

$$\sum_i C_i\chi_i(X)\phi_i(r) \equiv \sum_\alpha A_\alpha\left[\mathcal{F}_\alpha(X,r)\cos(\pi\delta_\alpha) - \mathcal{G}_\alpha(X,r)\sin(\pi\delta_\alpha)\right] \tag{2.63}$$

holds at large distances.

Constraint (i) gives [72]

$$\epsilon_i = -\frac{m_r e^4}{(4\pi\epsilon_0)^2\hbar^2}\cdot\frac{1}{2\nu_i^2}, \quad i = 1,\ldots,N_{\mathrm{ch}} \tag{2.64}$$

relating ν_i to the channel energies ϵ_i. Here, the quantities ν_i can be interpreted – analogously to previous descriptions of single-channel non-hydrogenic Rydberg atoms – as effective principal quantum numbers. Introducing the reduced-mass-corrected Rydberg constant[4] R_Z, the energy in wavenumbers becomes

$$E = I_i - \frac{R_Z}{\nu_i^2}\,. \tag{2.65}$$

In MQDT, a scattering matrix $[U_{i\alpha}]$ is introduced to describe how asymptotic channel states are transformed by the short-range interaction region. It encodes all inter-channel couplings, determines phase shifts and resonance structures, and links the short-range physics to the asymptotic Coulomb solutions for both bound and continuum states.

An indirect consequence of the unitarity of the scattering matrix is requirement (ii): the square matrix $[U_{i\alpha}]$, composed of the elements $U_{i\alpha}$, must be orthogonal.

In the limit of large r, requirement (iii), namely equation (2.63), provides relations between the coefficients A_α and C_i

$$\sum_i U_{i\alpha}\sin\left[\pi(\nu_i+\delta_\alpha)\right]C_i = 0, \quad \alpha = 1,\ldots,N_{\mathrm{ch}}, \tag{2.66}$$

$$\sum_\alpha U_{i\alpha}\sin\left[\pi(\nu_i+\delta_\alpha)\right]A_\alpha = 0, \quad \alpha = 1,\ldots,N_{\mathrm{ch}}, \tag{2.67}$$

$$A_\alpha = \sum_i U_{i\alpha}\cos\left[\pi(\nu_i+\delta_\alpha)\right]C_i, \tag{2.68}$$

[3]Notably, energies above the lowest ionization threshold in one channel can still be bound states in other channels, due to the differing ionization thresholds. Such states can still exhibit inter-channel coupling.

[4]In some literature the reduced-mass-corrected Rydberg constant is denoted by $\tilde{R}$.

$$C_i = \sum_\alpha U_{i\alpha} \cos\left[\pi(\nu_i + \delta_\alpha)\right] A_\alpha. \tag{2.69}$$

A non-trivial solution for equation (2.66) and equation (2.67) exists only if

$$\det\left|U_{i\alpha} \sin\left[\pi(\nu_i + \delta_\alpha)\right]\right| = 0. \tag{2.70}$$

For a given set of eigenquantum defects δ_α and a matrix $[U_{i\alpha}]$, this determines the values of the effective quantum numbers ν_i. Using the relation in equation (2.64), the corresponding energies can then be obtained.

An alternative way to describe the coupling is provided by the reactance matrix $[K_{ij}]$, defined by

$$[K_{ij}] = [U_{i\alpha}]\ \delta^{\mathrm{Kr}}_{\alpha\alpha'} \tan(\pi\delta_\alpha)\ \left[U_{j\alpha'}\right]^\dagger\ , \tag{2.71}$$

where $\delta^{\mathrm{Kr}}_{\alpha\alpha'}$ denotes the Kronecker-symbol. The corresponding coefficients can be obtained by using the related system of linear equations, defined by

$$\sum_j \left[K_{ij} + \delta^{\mathrm{Kr}}_{ij} \tan(\pi\nu_i)\right] c_j = 0, \quad i = 1, ..., N_{\mathrm{ch}}. \tag{2.72}$$

Relating the coefficients c_j and C_j yields

$$C_j = \frac{c_j}{\cos(\pi\nu_j)}. \tag{2.73}$$

The associated quantization condition is then

$$\det\left|K_{ij} + \delta^{\mathrm{Kr}}_{ij} \tan(\pi\nu_i)\right| = 0. \tag{2.74}$$

For numerical computations of the calculation of bound-state energies and the determination of matrix elements through fitting to experimental data, this formulation is particularly convenient.

The two different schemes via $[U_{i\alpha}], \delta_\alpha$ and via $[K_{ij}]$ are equivalent, since the eigenvalues of K are $\tan(\pi\delta_\alpha)$, and its eigenvectors are the columns of $[U_{i\alpha}]$.

The ionization thresholds I_i together with the reaction matrix $[K_{ij}]$ (or, equivalently, the quantum defects δ_α and the transformation matrix $U_{i\alpha}$) define the complete Rydberg series. These quantities can either be computed ab initio or determined empirically by fitting to spectroscopic data [62]. While the values of I_i can be obtained directly from experiments, the matrices K or U and the quantum defects δ_α are typically extracted via fitting procedures, forming the foundation of empirical MQDT.

Typically, the jj coupling scheme provides a natural basis at long ranges, whereas LS coupling dominates at short ranges. The matrix $[U_{i\alpha}]$ can be simplified by introducing an intermediate basis $\bar{\alpha}$ of pure LS-coupled channels, factorizing it into the product of a jj–LS transformation matrix $[U_{i\bar{\alpha}}]$ and a rotation matrix $[V_{\bar{\alpha}\alpha}]$ that describes the mixing among the LS-coupled channels [73, 74]

$$[U_{i\alpha}] = [U_{i\bar{\alpha}}][V_{\bar{\alpha}\alpha}], \tag{2.75}$$

where the transformation matrix is given by the Wigner-9j symbols

$$U_{i\bar{\alpha}} = \sqrt{(2j_{c_i}+1)(2j_{e_i}+1)(2L_{\bar{\alpha}}+1)(2S_{\bar{\alpha}}+1)} \begin{Bmatrix} l_{c_i} & s_{c_i} & j_{c_i} \\ l_{e_i} & s_{e_i} & j_{e_i} \\ L_{\bar{\alpha}} & S_{\bar{\alpha}} & J_{\bar{\alpha}} \end{Bmatrix}. \tag{2.76}$$

The quantum numbers of the ionic core in channel i are denoted by l_{ci}, s_{ci}, and j_{ci}, while those of the outer electron are given by l_{ei}, s_{ei}, and j_{ei}. The quantum numbers of the LS-coupled system are $L_{\bar{\alpha}}$, $S_{\bar{\alpha}}$, and $J_{\bar{\alpha}}$.

The rotation matrix can itself be factorized into a product of N rotation matrices $[R_{\bar{\alpha}\alpha}(m)]$, yielding

$$[U_{i\alpha}] = [U_{i\bar{\alpha}}][V_{\bar{\alpha}\alpha}] = [U_{i\bar{\alpha}}][R_{\bar{\alpha}\alpha}(1)][R_{\bar{\alpha}\alpha}(2)]...[R_{\bar{\alpha}\alpha}(N)]\,. \tag{2.77}$$

These rotation matrices are defined as [62]

$$R_{\bar{\alpha}\alpha}(m) = \begin{cases} \cos\theta_m, & \bar{\alpha} = \alpha = p_m, \\ -\sin\theta_m, & \bar{\alpha} = p_m \text{ and } \alpha = q_m, \\ \sin\theta_m, & \bar{\alpha} = q_m \text{ and } \alpha = p_m, \\ \cos\theta_m, & \bar{\alpha} = \alpha = q_m, \\ 1, & \bar{\alpha} = \alpha \neq p_m, q_m, \\ 0, & \text{otherwise}, \end{cases} \tag{2.78}$$

where each m corresponds to a specific angle θ_m and an associated pair of indices (p_m, q_m). Since $[V_{\bar{\alpha}\alpha}]$ is an $N \times N$ matrix, a complete factorization requires at most $N(N-1)/2$ rotations. In empirical MQDT models, the angles θ_m typically act as fitting parameters. In many cases, fewer factorization steps are sufficient to obtain a satisfactory fit, which reduces the overall number of parameters.

The matrix elements of $[K_{ij}]$, the rotation matrix $[V_{\bar{\alpha}\alpha}]$, and the eigenquantum defects δ_α are generally energy-dependent across the entire Rydberg series. Depending on the chosen formulation, this energy dependence of the MQDT parameters can be expressed as

$$\delta_\alpha = \delta_\alpha^{(0)} + \delta_\alpha^{(1)} \frac{(I_s - E)}{R_Z} \tag{2.79}$$

or alternatively

$$K_{ii} = K_{ii}^{(0)} + K_{ii}^{(1)} \frac{(I_s - E)}{R_Z}, \tag{2.80}$$

where $K_{ii}^{(0)}$ and $K_{ii}^{(1)}$ are energy-independent constants. Similarly, the quantum defects $\delta_\alpha^{(0)}$ and $\delta_\alpha^{(1)}$ are treated as constants, and all off-diagonal elements are assumed to be energy-independent.

In a first approximation, the energy dependence of the matrix elements of $[K_{ij}]$ and $[V_{\bar{\alpha}\alpha}]$, as well as of the eigenquantum defects δ_α, is often negligible, particularly over small ranges of Rydberg energies.

Notably, no energy shift occurs when the ionization threshold of the different channels coincide.

2.1.3.1. Calculation of Energies

To determine the energies of the bound states, the free parameters θ_m and δ_α are treated as fitting parameters within the framework of empirical MQDT. The bound-state energies are then obtained for a given K-matrix, or equivalently, for specified eigenquantum defects and rotation angles, provided that both equation (2.65) and either equation (2.70) or equation (2.74) are simultaneously satisfied.

In practice, it is common to select a dominant channel j associated with the Rydberg series of interest. The resulting effective principal quantum number ν_j, then determines the corresponding value of ν_i via

$$\nu_i = F_i(j;\, \nu_j) \tag{2.81}$$

where

$$F_i(j;\, \nu_j) = \left(\frac{I_i - I_j}{R_Z} + \frac{1}{\nu_j^2} \right)^{-1/2} . \tag{2.82}$$

The bound-state energies are determined by identifying a value of ν_j that satisfies equation (2.65) as well as one of the conditions in equation (2.70) or equation (2.74), while the remaining values ν_i are obtained using equation (2.81).

2.2. Rydberg Atoms in Electric Fields

As is well established, Rydberg atoms exhibit an extreme sensitivity to external electric fields due to their large transition dipole moments and the extended spatial distribution of the outer electron wavefunction. This pronounced field susceptibility can be both a powerful advantage and a significant source of perturbation. On the one hand, it enables their application as highly sensitive electric-field sensors [75, 76]. On the other hand, in fundamental spectroscopy – where the unperturbed energies of Rydberg states are to be determined – residual static or fluctuating background fields induce Stark shifts and splittings of the energy levels. If unaccounted for, these effects lead to systematic errors

and degraded spectral resolution. Consequently, accurate field compensation is essential, as implemented in the present work and described in detail in [1].

The following section provides an overview of the interaction of Rydberg states with static electric fields (DC)[5], as well as of field ionization in the strong-field regime, the latter forming the physical basis for the field-ionization detection schemes employed in this work.

2.2.1. Stark Effect

The shift of atomic energy levels in the presence of an external electric field is referred to as the Stark effect. The perturbation of the unperturbed Hamiltonian H_0 can be described by the interaction Hamiltonian

$$H' = -\mathbf{d} \cdot \mathbf{F} = -e\,\mathbf{r} \cdot \mathbf{F}, \tag{2.83}$$

where $\mathbf{d} = e\,\mathbf{r}$ is the electric dipole operator and $\mathbf{F}$ is the static electric field vector.

The shift of an eigenstate $|n^{(0)}\rangle$ of H_0 with eigenenergy $\mathcal{E}_n^{(0)}$ can be evaluated using time-independent perturbation theory. The first-order correction is given by

$$\Delta\mathcal{E}_n^{(1)} = \langle n^{(0)} \,|\, H' \,|\, n^{(0)} \rangle, \tag{2.84}$$

while the second-order correction reads

$$\Delta\mathcal{E}_n^{(2)} = \sum_{k \neq n} \frac{\left|\langle k^{(0)} \,|\, H' \,|\, n^{(0)} \rangle\right|^2}{\mathcal{E}_n^{(0)} - \mathcal{E}_k^{(0)}}. \tag{2.85}$$

2.2.1.1. Linear Stark Effect

The linear Stark effect arises when the first-order term in equation (2.84) does not vanish. This occurs in systems where the considered state is degenerate and the dipole matrix element between degenerate states is non-zero. In the hydrogen atom, states with the same principal quantum number n and angular momentum quantum numbers differing by ± 1 fulfill this condition. An applied electric field mixes these states, producing stationary states with a permanent dipole moment. As a result, the degeneracy is lifted, and the energy levels shift linearly with $F = |\mathbf{F}|$, as described by equation (2.84) [18]. This lifting of degeneracy manifests itself as a splitting of the energy levels, with the shift magnitude scaling approximately as n^2 for Rydberg states.

To describe the splitting and the shift caused by the Stark effect in an applied electric field it is useful to replace spherical coordinates by parabolic coordinates. They are related to the carthesian and spherical coordinates as

[5] A distinction can be made between DC and AC Stark shifts; the latter primarily occur in optical fields and are not considered here.

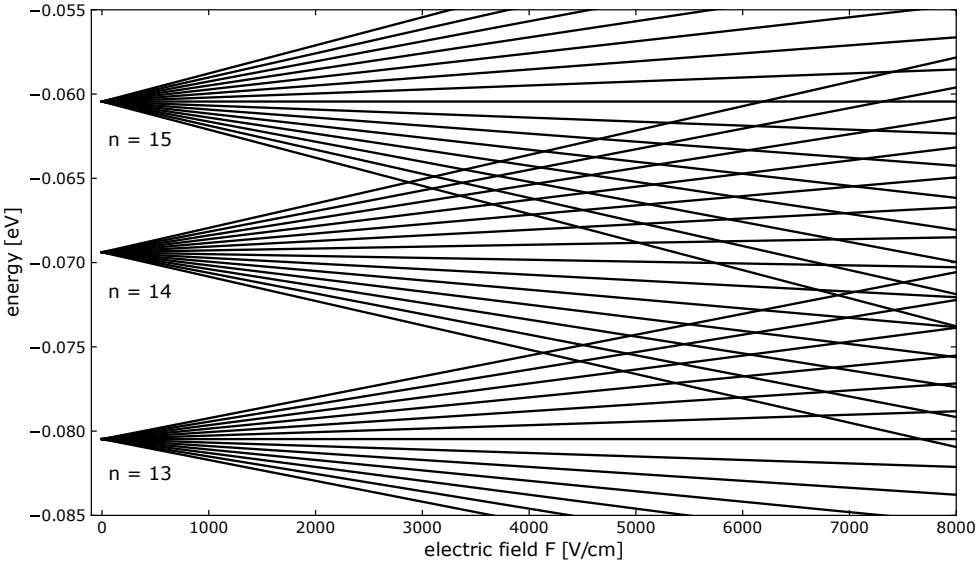

Figure 2.2.: Stark map of hydrogen calculated for $n = 13$ to $n = 15$ for $m = 0$. As described by equation (2.89) the energy levels are split into $n - |m|$ Stark levels. For increasing applied electric fields, the levels cross.

$$\begin{aligned} \xi &= r + z, \\ \eta &= r - z, \\ \phi &= \arctan \frac{y}{x}. \end{aligned} \tag{2.86}$$

In these coordinates, the Schrödinger equation takes the form

$$\left[-\frac{\hbar^2}{2m}\nabla^2 - \frac{2e^2}{4\pi\varepsilon_0(\xi+\eta)} + \frac{eF}{2}(\xi - \eta) \right] \psi(\xi, \eta, \phi) = \mathcal{E}\psi(\xi, \eta, \phi). \tag{2.87}$$

Parabolic coordinates naturally align with the symmetry imposed by the external electric field, ensuring that the Schrödinger equation remains separable in the corresponding variables even in the presence of the field [63]. As a result, the wavefunction can be expressed in the separable form

$$\psi(\xi, \eta, \phi) = u_1(\xi)\, u_2(\eta)\, e^{im\phi}. \tag{2.88}$$

Typically, the energy levels in the presence of an external electric field are obtained by first solving the Schrödinger equation in parabolic coordinates for the field-free case, followed by the application of perturbation theory to account for the effect of the electric field [18].

In this framework, the familiar spherical quantum numbers[6] (n, ℓ, m) are transformed into the parabolic quantum numbers (n, n_1, n_2, m), with the relations

$$n = n_1 + n_2 + |m| + 1, \qquad k \equiv n_1 - n_2, \tag{2.89}$$

[6]Here, m is a quantum number and should not be confused with the m introduced in the previous section.

where k characterizes the asymmetry between the two parabolic coordinates. In a pictorial sense, the quantum numbers n_1 and n_2 represent the number of nodes of the u_1 and u_2 wavefunctions in the ξ and η direction, respectively. As shown in [18], the nodes of the wavefunctions are located along parabolas. As a result of the applied electric field the eigenenergies to lowest order in F become [64]

$$\mathcal{E}_{n,n_1,n_2,m} = -\frac{R_H hc}{n^2} + \frac{3}{2} nkea_0 F, \tag{2.90}$$

where the second term is the linear Stark associated shift, with $k = n_1 - n_2$. The allowed values of k range from $-(n-|m|-1)$ to $+(n-|m|-1)$ in steps of two, resulting in a total of $n-|m|$ Stark levels. Example calculations for $n = 13$ to $n = 15$ with $m = 0$ are shown in figure 2.2. As illustrated in the figure, the Stark levels corresponding to different principal quantum numbers n intersect as the applied electric field increases. In the regime of low electric fields considered here, the Stark shift exhibits a strictly linear behavior.

2.2.1.2. Quadratic Stark Effect

For non-hydrogenic Rydberg atoms in electric fields, the presence of the finite-sized ionic core prevents the wavefunctions from being separable in parabolic coordinates. Consequently, n_1 ceases to be a good quantum number. The resulting level structure is too complex to be described by a simple set of parameters or eigenenergies. As demonstrated in [64], an effective way to represent the combined atom-field system is to compute and visualize Stark maps obtained by diagonalizing the energy matrix. Although no exact analytical description is available, many essential features can nevertheless be understood from the numerical simulations.

In the case of non-degenerate states, no permanent dipole moment exists in the absence of an external field, and the leading contribution arises from an induced dipole moment. This yields the quadratic Stark effect in the low field region, where the shift is proportional to F^2 and can be expressed in terms of the static scalar polarizability α_n

$$\Delta\mathcal{E}_n^{(2)} = -\frac{1}{2}\alpha_n F^2. \tag{2.91}$$

The polarizability itself is given by

$$\alpha_n = -2e^2 \sum_{k\neq n} \frac{\left|\langle k^{(0)} \,|\, z \,|\, n^{(0)}\rangle\right|^2}{\mathcal{E}_n^{(0)} - \mathcal{E}_k^{(0)}}. \tag{2.92}$$

Here, the field induces a dipole moment in the atom, and the corresponding interaction energy scales with F^2. For Rydberg states, α_n scales approximately as n^7, which explains their extreme sensitivity to weak stray electric fields.

A detailed discussion of polarizabilities in the context of Rydberg states in ytterbium is provided in section 5.1.

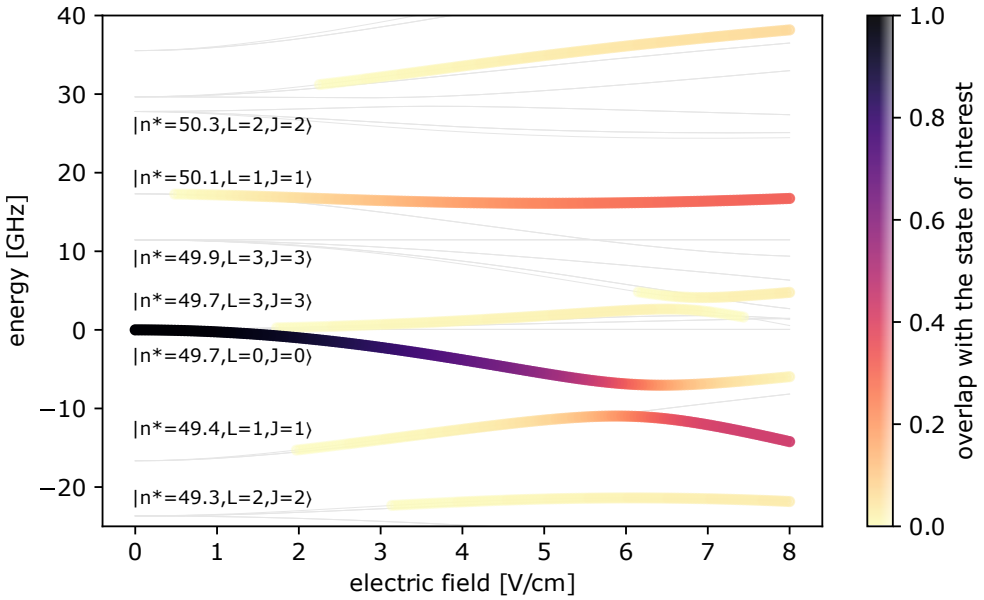

Figure 2.3.: Stark map of the $^1S_0$ Yb Rydberg state with $n^* = 49.7$, calculated using the *PairInteraction* software [6]. As the external electric field is increased, the energy levels shift and split, exhibiting characteristic avoided crossings with neighboring states. These interacting neighboring states are labeled in the figure. The basis around the target state is defined using $\Delta n^* = \pm 1$, $\Delta s = \pm 0.5$, and $\Delta j = \pm 3$.

In contrast to the behavior of Stark states in the hydrogen atom, where genuine level crossings can occur due to the high degree of degeneracy with respect to the orbital quantum number ℓ, the situation in non-hydrogenic atoms is markedly different. Here, the presence of the ionic core potential breaks the degeneracy in ℓ, such that states with the same principal quantum number n but different orbital angular momenta are already split in energy at zero external field. When an external electric field is applied and gradually increased, these states are shifted by the Stark effect and may energetically approach each other.

The energy regions in which this effect dominates are referred to as avoided crossing zones, where the eigenstates undergo a continuous admixture and gradually exchange character, rather than exhibiting sharp crossings. This behavior is illustrated in figure 2.3 for the $^1S_0$ Yb Rydberg state with $n^* = 49.7$, calculated using the *PairInteraction* software [6]. For this calculation, a basis around the target state with $\Delta n^* = \pm 1$, $\Delta s = \pm 0.5$, and $\Delta j = \pm 3$ was employed, ensuring that all relevant neighboring states contributing to the avoided crossings are included. The figure clearly shows the characteristic energy shifts and splittings of the involved states as the external electric field is increased. These avoided crossings play a central role in determining the dynamics of Rydberg states in non-hydrogenic atoms, influencing processes such as field ionization, state mixing, and population redistribution among nearby levels. Understanding their structure is crucial for

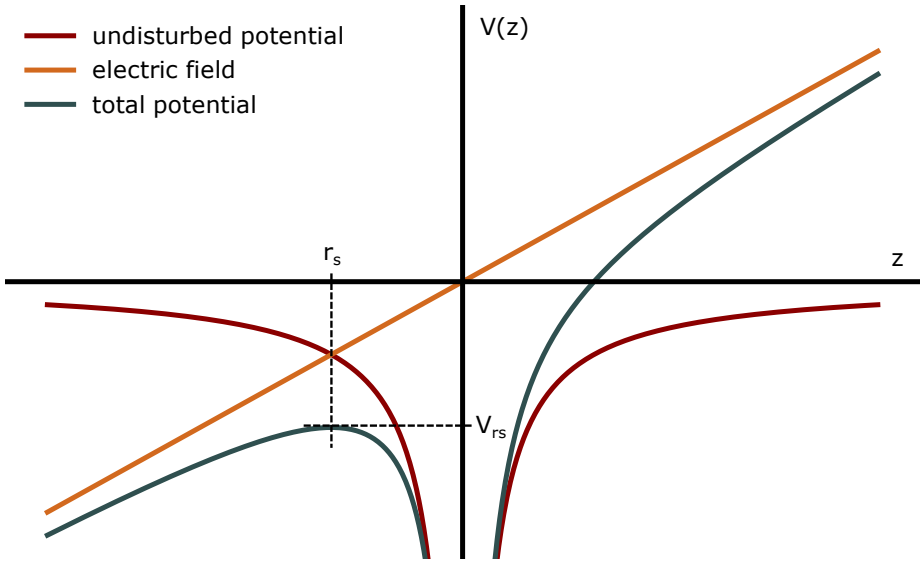

Figure 2.4.: Total potential experienced by a bound electron in the presence of an external electric field. The applied field superimposes a linear term on the undisturbed Coulomb potential, resulting in a tilted overall potential landscape. This distortion lowers the potential barrier on one side of the atom and facilitates electron escape, thereby enabling field ionization. Inspired by [77].

interpreting spectroscopic measurements, controlling excitation pathways, and designing experiments that exploit or avoid strong state mixing.

2.2.2. Field Ionization of Rydberg States

Rydberg atoms, with principal quantum numbers $n \gg 1$, possess extremely small binding energies, due to the characteristic n^2 scaling. The weak binding makes these states highly susceptible to static electric fields, which can distort the Coulomb potential to the point of ionization.

2.2.2.1. Hydrogen

Let us first consider the hydrogenic case. In the presence of a static electric field $\mathbf{F}$, neglecting the Stark shift, the core potential experienced by the electron can be written as

$$V(r,\theta) = -\frac{e}{4\pi\varepsilon_0 r} + Fr\cos\theta, \tag{2.93}$$

where θ is the angle between $\mathbf{r}$ and $\mathbf{F}$. The resulting potential, obtained as the superposition of the unperturbed Coulomb potential and the contribution from the static electric field, is depicted in figure 2.4. As illustrated, the external field induces a tilt of the Coulomb potential landscape, thereby modifying the barrier for electron escape. In the field direction

($\theta = 0$), the second term lowers the Coulomb barrier and creates a saddle point at

$$r_s = -\sqrt{\frac{e}{4\pi\varepsilon_0 F}}. \tag{2.94}$$

The potential at this saddle point is

$$V(r_s) = -2\sqrt{\frac{eF}{4\pi\varepsilon_0}}. \tag{2.95}$$

This can be expressed in terms of an energy via $\mathcal{E}_0 = e \cdot V(r_s)$. Classical field ionization starts to occur when the saddle-point energy equals the binding energy of the Rydberg state

$$\frac{R_H\, hc}{n^2} = e \cdot 2\sqrt{\frac{eF_{\text{class}}}{4\pi\varepsilon_0}}. \tag{2.96}$$

Solving for F_{class} yields the classical ionization threshold

$$F_{\text{class}} = \frac{\pi\epsilon_0}{e^3}\,\frac{(R_H\, hc)^2}{n^4}. \tag{2.97}$$

This scaling shows that the electric field required for ionization decreases rapidly with increasing n as n^{-4}. From a quantum-mechanical perspective, ionization may also proceed via tunneling, which also becomes possible in the presence of an external electric field. In this scenario, the field-induced distortion of the potential barrier reduces its width, allowing the electron wavefunction to penetrate and eventually escape through quantum tunneling, even at field strengths below the classical ionization threshold.

So far, Stark shifts have been neglected in the treatment of field ionization. When they are taken into account, the sublevels are shifted differently in energy (see figure 2.2), which leads to multiple distinct ionization thresholds, as analyzed for example in [65].

2.2.2.2. Non-Hydrogen

As discussed earlier, in multi-electron systems electron-electron interactions and core penetration break the degeneracy and symmetry of the hydrogenic spectrum. When an external electric field is applied, these nearly degenerate states couple, leading to avoided crossings (see section 2.2.1.2). Such couplings strongly modify the ionization behavior.

In this case, the ionization field of a given state is no longer directly determined by its apparent binding energy. Through state mixing near avoided crossings, a more strongly bound state can acquire the character of a more weakly bound one, thereby ionizing at different fields. Another effect of state mixing is that a state with little amplitude near the saddle point of the tilted Coulomb potential may suddenly gain significant probability density there, enhancing its tunneling rate. Conversely, tunneling can also be suppressed. As a consequence, a state that is well-defined at zero external field may exhibit several effective ionization thresholds.

The ionization dynamics in the vicinity of avoided crossings are described by Landau-Zener transitions [66, 67]. The outcome depends sensitively on the rate at which the external field is ramped. For slow ramps, the passage is adiabatic: the electron follows the adiabatic branch and inherits its character. As visible in figure 2.4 the pathway is deflected by adjacent states. In this scenario, ionization may occur at reduced fields, since an electron initially localized away from the saddle point can acquire amplitude near it. In contrast, for a fast ramp, the system crosses the avoided region on a timescale much shorter than that required for the coupling to induce a significant admixture of the other state. The interaction is therefore effectively too weak to alter the wavefunction within the available time, and the system retains the character of its original diabatic state.

This behavior is quantified by the Landau-Zener transition probability [67]

$$P_{\mathrm{LZ}} = \exp\left(-\frac{\pi\Delta^2}{2\hbar\, a\beta}\right), \tag{2.98}$$

where Δ is the minimum energy gap at the avoided crossing, a is the relative slope of the two diabatic levels, and $\beta = dF/dt$ is the ramp rate of the external field. In the limit of large β (fast ramp), the exponent becomes small, and $P_{\mathrm{LZ}} \to 1$. Thus, the system overwhelmingly remains in its initial diabatic state.

In realistic experimental conditions, the dynamics are typically intermediate, resulting in coherent superpositions of the two pathways. This explains why in non-hydrogenic systems the effective field required for field ionization is often found to be lower than the classical limit. An analysis of ionization thresholds relative to the classical ionization limit of ytterbium was performed by C. Halter [1]. In the case of a fully diabatic passage, the atoms would ionize at the classical ionization threshold. For higher principal quantum numbers, the experimental ionization process is predominantly diabatic, since the minimum energy gap at the avoided crossing scales with n as

$$\Delta \propto \frac{\delta_\ell}{n^4}. \tag{2.99}$$

As described by the Landau–Zener model, the effective ionization threshold in the case of high n is shifted closer to the classical limit, which was found in the experiment. Both diabatic and adiabatic passages were found for lower n. This is explained by the ionization characteristics as a function of the principal quantum number.

The ionization limits for the analyzed states of Yb [1] form the basis for the detection scheme for Rydberg atoms outlined in this work in section 4.3.

3.

Experimental Apparatus – Single-Stage MOT

In this chapter, the experimental components used for the investigation of ultracold Yb Rydberg atoms are presented. The setup is based on the experimental apparatus developed and described in the PhD thesis of C. Halter [1]. The apparatus has been partially redesigned and extended for the purposes of this thesis. Several components have been upgraded or replaced, and additional laser systems and optical elements have been integrated to enable advanced control and manipulation of the atomic system. More specifically, several improvements were implemented to speed up the measurements by approximately a factor of 20 and increase the stability of the system. To ensure a complete description of the setup all relevant components are explained in the following. Major improvements made in the course of this thesis are indicated in the text.

The chapter begins with an overview of the vacuum system (section 3.1), which includes the electrode assembly for electric field generation as well as magnetic field coils for the magnetic field control. This is followed by a detailed description of the laser system used for the blue magneto-optical trap (section 3.2). The section on the Rydberg excitation laser system (section 3.3), which includes a frequency doubling stage, has been expanded to incorporate a newly developed laser system (section 3.3.3) for frequency stabilization, ensuring improved short and long-term stability of the Rydberg excitation source.

3.1. Vacuum System

Since the experiment requires extremely low background gas pressures, the system operates under ultra-high vacuum (UHV) conditions, with a pressure on the order of 10^{-10} mbar. The vacuum system consists of three main parts, as illustrated in figure 3.1: the atomic oven chamber, the Zeeman slower and the main chamber where an ultracold ensemble of Yb atoms is prepared for the investigation of Rydberg states. The atomic oven section is connected to the main chamber via the Zeeman slower. The main chamber houses the electrode assembly for electric field control and several magnetic field coils for field manipulation are arranged around it. A total of nine viewports attached to the main

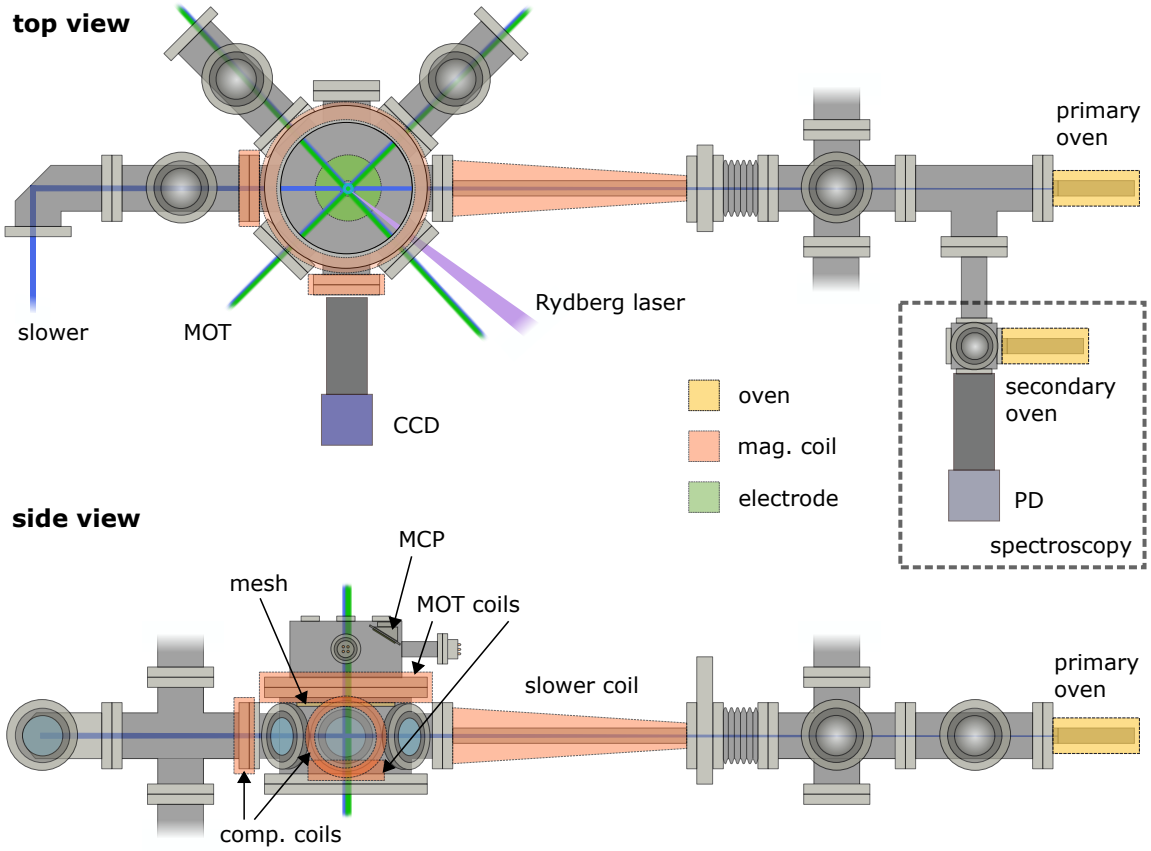

Figure 3.1.: Overview of the vacuum system. The main chamber is connected to the atomic oven source via a Zeeman slower. The top and side views illustrate the various optical access points for the MOT laser beams, the Zeeman slower beam, the Rydberg excitation laser, and the charge-coupled device (CCD) camera. The magnetic field coils and the electrode assembly used for electric field control and field ionization are also depicted. Additionally, the microchannel plate detector – used as the primary detector for Rydberg atoms – is shown. Adapted from C. Halter [1].

chamber provide optical access for the Zeeman slower beam, six MOT beams, the Rydberg excitation beam, and a CCD camera. To enable future studies involving Yb atoms trapped in optical lattices, four additional small viewports were incorporated at the top of the main chamber.

3.1.1. Atomic Oven Section

Two ovens are employed in this experiment, both shown in figure 3.1. The primary oven generates the atomic beam used for the MOT, while the secondary oven is dedicated to ytterbium spectroscopy for frequency stabilization of the blue MOT laser system, see section 3.2. Both ovens are operated at 420 °C to ensure a sufficient atom flux. This

section of the chamber is equipped with an ion pump for maintaining UHV conditions, and a viewports allowing for fluorescence detection in the spectroscopy chamber using a photodiode. To facilitate maintenance procedures and allow for the refilling of the atomic ovens without venting the entire system, a gate valve separates the oven section from the main chamber, enabling isolated access to individual chamber sections.

3.1.2. Zeeman Slower

To capture atoms in a magneto-optical trap, their initial velocities – on the order of few hundred meters per second – must be reduced to below 20 m/s. This deceleration is achieved using a counter-propagating laser beam in combination with a spatially varying magnetic field [78] generated by a tapered coil, designed by Sven Tassy [79]. As the atoms slow down, the Doppler shift alters the effective laser frequency in the atoms' frame. To compensate for this shift and maintain resonance with the slowing transition, the Zeeman effect is utilized in a field-increasing configuration. The magnetic field is shaped by varying the number of windings along the propagation axis of the atomic beam[1]. The slower has a total length of 33.9 cm. To prevent excessive heating of the wrapped pipe, the coil is wound around a double-walled pipe through which cooling water is circulated.

3.1.3. Magnetic Coils

In addition to the coil used for the Zeeman slower, additional magnetic coils are mounted on the main chamber to create a MOT and to compensate stray background fields (see figure 3.1). In order to trap atoms in a MOT, a pair of coils in an anti-Helmholtz configuration – referred to as the MOT coils – is employed. Due to the geometry of the chamber, the upper coil is larger than the lower one. It has an inner diameter of 15.25 cm and a total of 76 windings[2]. The lower coil is mounted within a recessed flange, positioning it closer to the MOT center, thereby allowing sufficiently large magnetic field gradients to be achieved with moderate currents. It has an inner diameter of 2.5 cm and 16 windings.

To ensure full three-dimensional control of the magnetic field, two additional compensation coils are integrated into the setup. Each of these coils has an inner diameter of 7.25 cm and consists of 60 windings. A slower compensation coil is positioned opposite to the Zeeman slower, and another coil is installed to control the third spatial dimension. Water cooling is applied to the edges of the coils via two boreholes to prevent thermal overload.

By adjusting the current in the individual coils, the magnetic field distribution within the chamber can be tailored to the experimental requirements. In particular, it is crucial for certain measurements – such as time-of-flight experiments – to minimize the magnetic

[1] The coil winding scheme can be found in [2]

[2] The total of 76 windings for the big coil and the 60 windings for the compensation coils result from 10 and 8 layers, respectively, with the number of turns alternating between 8 and 7 per layer.

trapping field. To this end, the MOT coil current control is designed to be rapidly switchable, allowing for a fast and controlled shutdown of these magnetic fields.

3.1.4. Electrode Setup

Rydberg atoms exhibit an extreme sensitivity to external electric fields due to their large dipole moment. Consequently, accurate measurements require the compensation of residual background fields to minimize frequency shifts and spectral broadening effects.

Furthermore, the detection scheme employed in our experiment requires Rydberg atoms to be ionized and subsequently guided toward the detector by means of electric fields. To allow both field control and efficient ion detection, a dedicated electrode configuration is implemented, as depicted in figure 3.2. This comprises a lower electrode plate with a central aperture to allow optical access to the atoms, and an upper segmented ring electrode divided into four individually addressable quadrants, enabling precise shaping of the electric potential in the MOT region. A picture and a schematic representation with the spatial dimensions of this configuration is provided in figure 3.2. To illustrate how it is integrated into the main chamber, an exploded view of the central assembly is shown in a). The upper ring electrode has a thickness of 3.0 mm and a radius of 18.5 mm with the individual segments spaced 2.0 mm apart. The lower plate has a thickness of 3.5 mm and contains a central aperture with a radius of 5.0 mm. The vertical separation between the lower and the upper electrodes is 7.5 mm. In addition to the electrodes the intra-vacuum resonator for the future creation of an optical lattice is visible. Details can be found in chapter 9.

Low and high voltages are applied to the various segments of the electrode assembly to generate controllable electric fields. For this purpose, self-built high-voltage amplifiers are employed.

The ionization pulse, as well as the first acceleration pulse, is applied to the lower electrode plate. Voltages in the range of 30 V and 450 V are achievable. Based on simulation results from [1], this upper limit corresponds to an ionization electric field of approximately 200 V/cm. The compensation voltages used to counteract residual background fields are significantly lower, typically around 15 V. To deflect the ions toward the MCP, a single segment of the upper ring electrode – positioned opposite the detector – is used. A voltage of 750 V is applied in this case, corresponding to an electric field of approximately 320 V/cm.

Since short electric field pulses are required to ionize the Rydberg atoms and to accelerate the ions toward the MCP detector, a pulse generator is employed. It is capable of generating pulses with durations on the order of hundreds of nanoseconds, thereby minimizing the perturbation time of the atoms. Further details on the applied pulse shapes and timing schemes can be found in chapter 4.

The MCP operates under high voltage conditions to exploit the avalanche multiplication mechanism, thereby allowing single-ion detection via the generation of secondary electrons

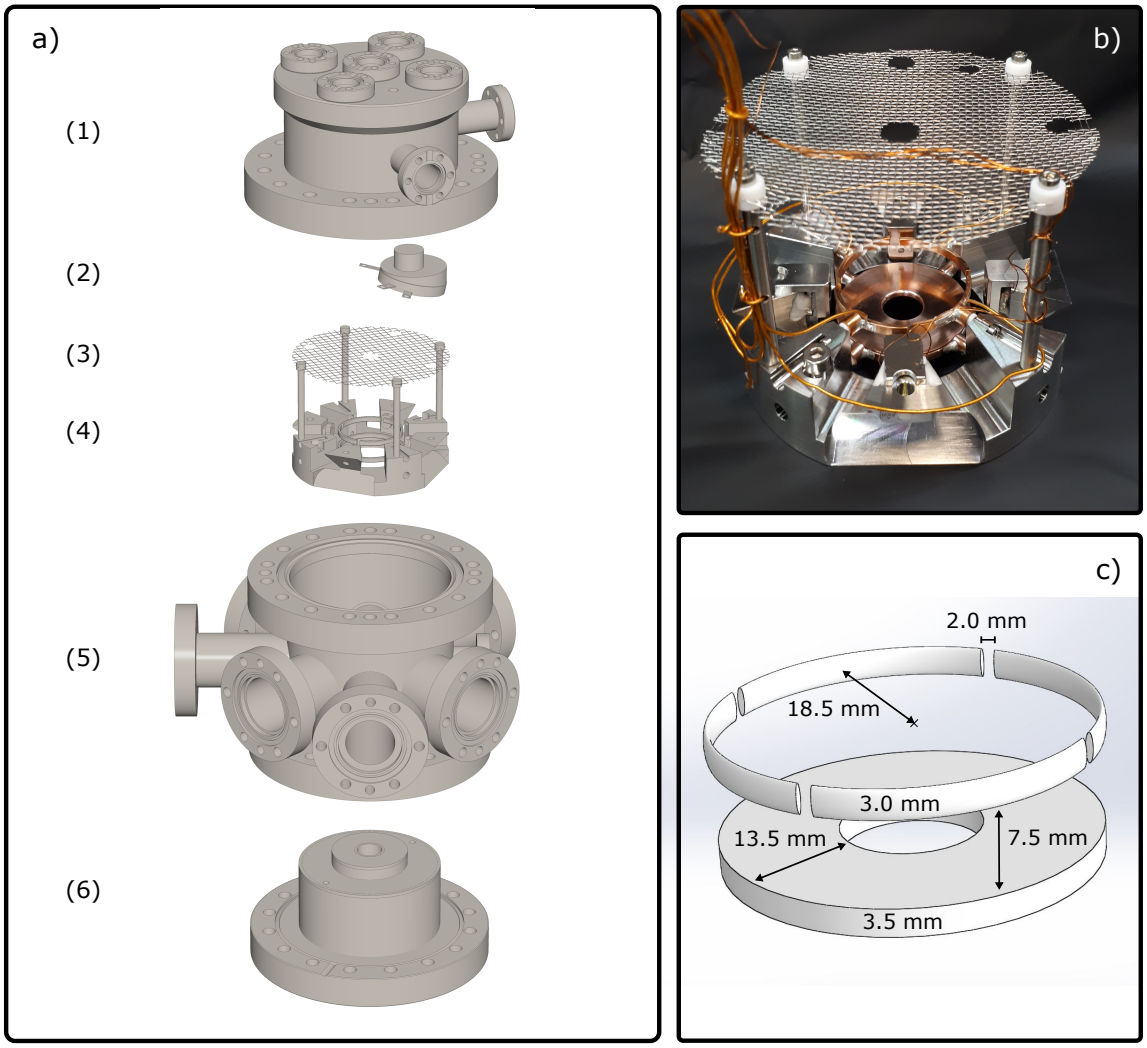

Figure 3.2.: a) Explosion sketch of the main chamber and the electrode setup. In (1), small windows at the top, indended for future implementation of lattice beams, are visible. Part (2) displays the MCP. The central region contains the optical resonator setup with the mounted shielding mesh (3) and the electrode assembly (4). In (5) the main part of the chamber with the viewports for optical access – used for the slowing and trapping beams, the Rydberg excitation laser, and the CCD camera – is shown. The larger MOT coil is wound around the upper flange connecting (1) and (5), while the smaller MOT coil is located inside the bottom part of the chamber (6). b) Photograph of the complete setup including the intra-vacuum resonator and the mesh for shielding the detector's high voltage. c) Close-up sketch of the electrode system indicating the dimensions. Visible are the lower plate, which includes a central aperture for optical access, and the upper segmented ring electrode. b) and c) adapted from [1].

(see section 3.1.5). However, the associated electric field, must be shielded to prevent unwanted perturbations of the atomic ensemble. For this purpose, a steel mesh is positioned between the electrode structure and the MCP, effectively isolating the detection field from the MOT. A low voltage can be applied to this mesh to optimize the shielding performance. As shown in figure 3.2 a)(1), an electrical feedthrough (10-pin) is used to connect the electrodes and the mesh to the voltage sources. To supply the high voltage to the MCP and extract the output signal from the detector a second 4-pin electrical feedthrough is employed.

3.1.5. Atom and Ion Detectors

Since both the laser-cooled and trapped Yb atoms, as well as the excited Rydberg atoms, need to be detected, the two primary detectors employed in this work are described in the following. The first one is the CCD camera for fluorescence imaging of the MOT and the second one is the MCP for the detection of ionized Rydberg atoms.

3.1.5.1. CCD Camera for Fluorescence Imaging

As previously mentioned an imaging system using a CCD camera[3] is connected to the main chamber. The camera has a pixel size of 8.3 µm × 8.3 µm and a total number of 768 × 576 pixels. The camera has a minimal exposure time of 50 µs. To perform imaging an 2:1 telescope is used with an aperture of 25.4 mm and a distance to the MOT of about 21.4 cm from the first lens of the telescope. The pictures taken with the camera are displayed using a LabView graphical user interface [80]. Both, a continuous and a triggered mode can be processed. The timing and typical exposure times are discussed in chapter 4.

3.1.5.2. Microchannel Plate for Ion Detection

In earlier stages of this experiment, Rydberg atoms were primarily detected using the depletion spectroscopy method [1, 56], where the excitation of Rydberg states is detected as a loss of atoms in a MOT. However, this technique has limitations: atom losses in the MOT can arise not only from Rydberg excitation but also from external perturbations of the system. Therefore, an alternative direct detection method is now used. By applying high-voltage pulses, the excited Rydberg atoms can be ionized and subsequently accelerated toward an ion detector for direct detection (see section 3.1.4). As previously described in [1], a high voltage of −2.5 kV is applied to the input electrode of a two-stage microchannel plate. The single tubes inside of the detector are tilted. Two MCPs are arranged in a chevron configuration, where two plates rotated by 180° with respect to each other are mounted in series. This geometry prevents ions from traversing the detector[4] directly. The

[3] ABS UK1117-M, *ABS Optronics Jena*

[4] MCP detector Chevron Model S3018-10-D60-MA, *Scientific Instruments*

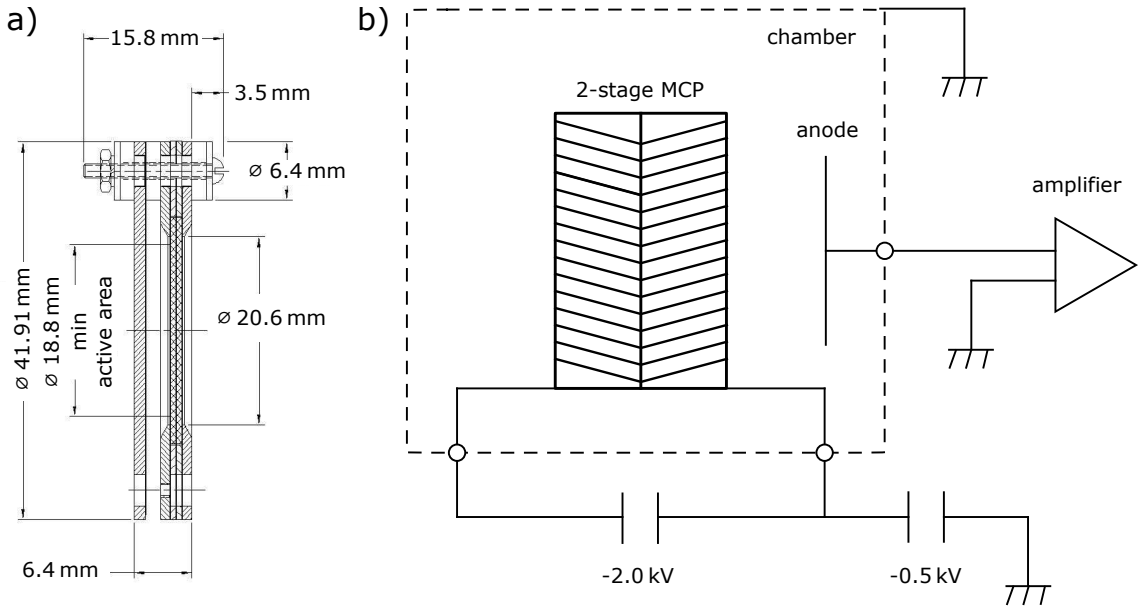

Figure 3.3.: a) Side view of the MCP with dimensional annotations. The two MCP stages, the anode, and the minimum active area are visible. Adapted from the datasheet (S3018-10-D60-MA, SI Scientific Instruments GmbH, supplied with the product; not publicly available). b) Schematic wiring diagram of the two-stage MCP. The input electrode is set to $-2.5\,\mathrm{kV}$, the output of the second stage to $-0.5\,\mathrm{kV}$, and the anode is grounded. Adapted from [1].

active area has a diameter of minimum 19 mm, as depicted in figure 3.3 a). A metal anode is positioned behind the MCP stack to collect the electron signal; it is held at ground potential. The associated wiring diagram is presented in figure 3.3 b). Upon impacting the MCP surface, ions generate primary electrons, which are subsequently accelerated, producing secondary electrons with each successive collision with the channel walls. This avalanche multiplication results in a measurable current, provided that the intrinsic dark count rate of the MCP ($0.6\,\mathrm{cts/s/cm^2}$) is exceeded, thereby defining the lower detection threshold.

The resulting current pulses must be processed by an electronic unit to determine the number of incident ions (the electronic circuit is shown in the appendix in figure A.1). For this purpose, the output of the MCP is connected to an I-U-amplifier[5], which converts the current pulses into amplified voltage pulses. Due to the short time intervals between individual ion arrivals, the counting electronics must operate at high speed. A fast (4 GHz) divide-by-two prescaler in combination with a 12-bit counter yields an effective 13-bit counting system. The limiting factor is the 12-bit counter's maximum bandwidth of 82 MHz, resulting in a temporal resolution of approximately 13 ns. All 13 bits are read out

[5]This deviates from the setup described in [1].

by an Arduino microcontroller, which also generates timing gates to restrict detection to time windows in which ion signals are expected. This is necessary to exclude interference signals caused by high-voltage switching pulses, which precede the actual ion arrival time. The data acquired by the Arduino is transmitted via USB to a computer and analyzed using a software tool described in [1].

3.2. Blue MOT Laser System

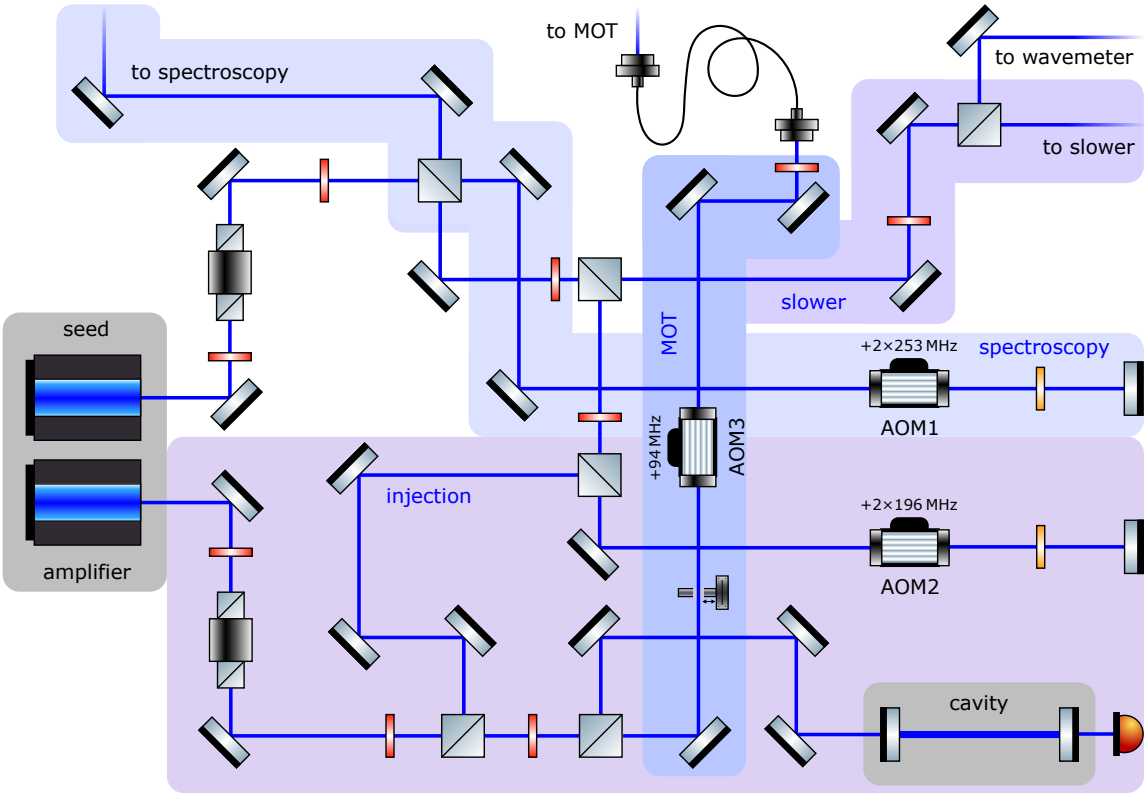

Figure 3.4.: Schematic drawing of the laser system at 399 nm for the Zeeman slower and the blue MOT. The seed laser beam is split into three paths: for frequency stabilization via Yb spectroscopy, for the slower beam, and for injection into the amplifier laser. The amplified output provides the light for the MOT beams.

The blue laser system forms the basis for cooling and trapping the ytterbium atoms. It enables the preparation of a dense cloud of cold Yb atoms. This is achieved via the ${}^1S_0 \rightarrow {}^1P_1$ transition at 398.9 nm (see figure 1.1).

The laser system shown in figure 3.4 consists of two lasers: a narrow-bandwidth seed laser and a high-power amplifier laser. This combination allows the system to benefit from both high spectral purity and sufficiently high output power. The seed laser[6] operated

[6]Nichia NDHV310ACAEI; 10 mW

in a Littrow configuration [81], uses a reflection grating where the first diffraction order provides optical feedback and the zeroth order forms the output beam. The stability of the output frequency is enhanced through the use of Peltier elements, which provide precise and reliable temperature control. The laser exhibits a linewidth in the low-MHz range and operates at approximately 7 mW output power. The seed laser beam is split into three main paths: spectroscopy, injection, and the Zeeman slower, as illustrated in section 3.2. A portion of the seed laser output is directly used for the slower, which requires a detuning of approximately −500 MHz relative to the singlet transition (see chapter 1) to compensate the Doppler shift of the fast-moving atoms. Slightly more than 1 mW is allocated for this purpose, with a small fraction additionally used as a frequency reference for a home-built wavemeter (see section 3.3.1). A shutter is integrated into the slower path to be able to switch off the slower light. After being directed to the vacuum chamber free-space via mirrors, the beam is focused onto the nozzle of the Yb oven.

The spectroscopy path is used to frequency-lock the laser. For this purpose, the laser frequency must match the atomic resonance. Since the seed laser frequency is also used directly for the slower, which requires a detuning of approximately 500 MHz, this frequency offset must be compensated. This is achieved using an acousto-optic modulator (AOM) in a double-pass configuration (2×253 MHz), which also minimizes intensity fluctuations arising from spatial modulation of the beam. The modulated beam, now at the resonance frequency of the desired Yb isotope, is directed to the oven chamber (section 3.1.1), where it crosses the atomic beam orthogonally. The resulting fluorescence is detected by a photodiode, and the error signal for laser locking is obtained by demodulating the spectroscopy signal with a lock-in amplifier.

The third part of the seed laser is used for injection of the amplifier laser[7]. Through optical injection locking, the seed imposes its frequency characteristics onto the output of the amplifier. To compensate for the frequency offset of the seed from atomic resonance, the seed light is frequency-shifted by means of a double-pass AOM (2×196 MHz). The amplifier diode[8] typically delivers an injection-locked output power of about 30 mW, thereby providing high optical power combined with a narrow spectral linewidth. The quality of the injection lock is continuously monitored using an optical resonator. The amplified light passes through an additional AOM (94 MHz), setting it to the required red detuning of approximately −20 MHz for the MOT operation. This AOM, together with a mechanical shutter, also enables fast switching of the MOT beams. Since high beam quality is essential for optimal MOT operation the beam is guided to the chamber via an optical fiber[9]. Although the diode laser output deviates significantly from a Gaussian beam, leading to large coupling losses, this trade-off is accepted to achieve sufficient spatial mode quality.

[7] This laser has been installed in place of the former amplifier laser, as it provides higher output power.
[8] *Mitsubishi ML320G2*; 120 mW
[9] This fiber coupling was introduced during my experimental work to improve the beam quality.

Ultimately, we obtain approximately 2 mW of usable power for all the MOT laser beams.

3.3. Rydberg Laser System

Excitation to the Rydberg states is achieved via the intermediate blue MOT state $^1P_1$(see figure 1.1). The Rydberg laser system used for this purpose is depicted in figure 3.5. A commercial external cavity diode laser (ECDL)[10] operating near 788 nm serves as the seed source for the system. Its output is amplified using a tapered amplifier (TA)[11], and subsequently frequency-doubled to reach the target wavelength.

3.3.1. 788 nm Laser System

The DL pro diode laser, equipped with a built-in optical isolator providing 35 dB of isolation, delivers an output power of approximately 40 mW and provides a tuning range of several THz. This wide tuning capability is essential for addressing different Rydberg states via excitation from the intermediate MOT state. For a typical spectroscopy sequence targeting a specific principal quantum number n, the laser is scanned over several gigahertz (see section 5.2).

The seed laser output is split into two separate paths. One path is used for frequency stabilization (see section 3.3.3) and for wavelength monitoring, as depicted in figure 3.5. A home-built wavemeter based on a Michelson-Morley interferometer configuration is employed to measure the laser wavelength relative to a well-known reference – in this case, the frequency-locked blue seed laser. The interference signal between the two interferometer arms is monitored while the length of one arm is continuously varied. The number of zero crossings observed in the interference signal allows for determining the unknown wavelength by comparison with the known reference. This approach is based on the method described in [82].

In order to generate sufficient power for frequency doubling, the laser beam is first amplified using a so-called tapered amplifier. With an input power of 30 mW, an output power[12] exceeding 500 mW can be achieved. Since back-reflections from both the TA and the second-harmonic generation (SHG) ring cavity can lead to instability or damage, optical isolators are placed before and after the TA to suppress unwanted feedback.

Optimal mode matching to the amplifier and subsequently to the frequency-doubling cavity is realized using a lens system. As the SHG cavity is particularly sensitive to the longitudinal position of focal point, one of the lenses is mounted on a translation stage to

[10] *TOPTICA Photonics*, DL pro, 780 nm

[11] *Coherent Corp.*, TA-0785-2000-DHP

[12] To avoid damage to the SHG cavity, especially to the mirrors and nonlinear crystal, the TA is not operated at maximum power, although higher output would be possible.

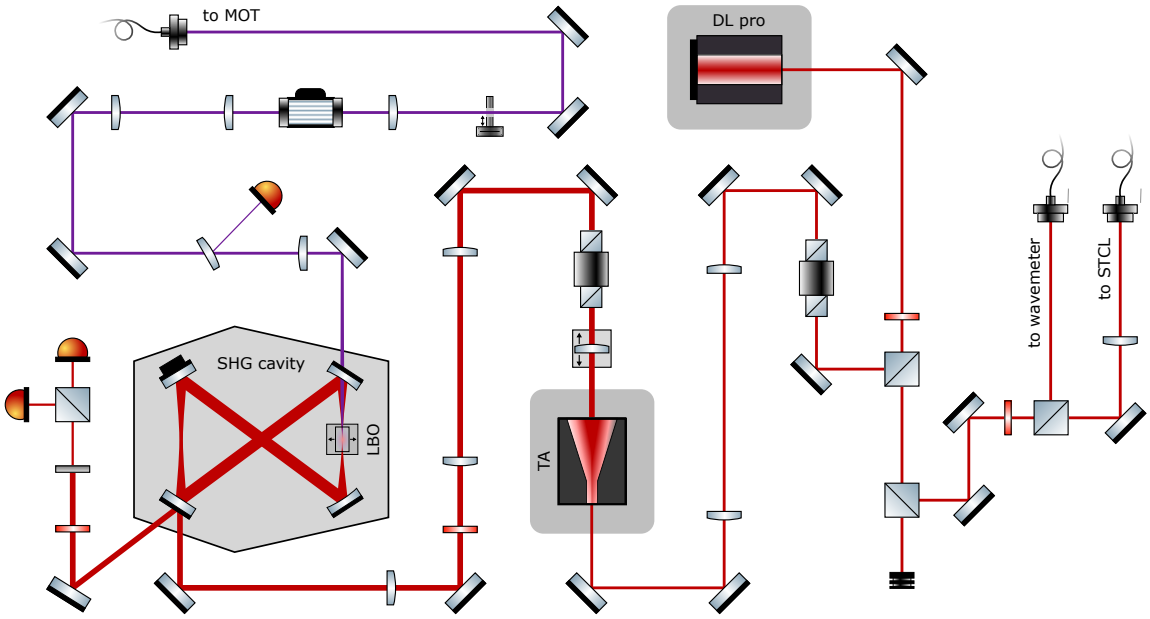

Figure 3.5.: Schematic of the Rydberg laser system. A commercial diode laser (DLPro) is amplified using a tapered amplifier (TA) and frequency-doubled to the target wavelength via an LBO crystal inside a bow-tie cavity. The resulting light is delivered to the MOT via an optical fiber and can be rapidly switched using an AOM. Two additional optical paths are implemented to facilitate wavelength measurement and frequency stabilization of the laser. Adapted and extended from [1].

allow fine adjustment. Additionally, polarization and beam diameter are adjusted using a waveplate and a telescope to ensure efficient coupling into the cavity.

3.3.2. SHG using an LBO Crystal in a Bow-Tie Cavity

Frequency doubling to the required wavelength of 394.1 nm – corresponding to the Rydberg excitation from the intermediate blue MOT state – is accomplished using a home-built resonant SHG ring cavity in a bow-tie configuration (see figure 3.5), as described in [41]. The nonlinear medium is a lithium triborate (LBO) crystal[13] with dimensions of $3 \times 4 \times 15\,\mathrm{mm}^3$. The end faces of the crystal are anti-reflection coated for both 788 nm and 394 nm to maximize transmission.

The cavity alignment can be optimized using adjustable mirrors, while the crystal itself is mounted on a precision-adjustable holder to enhance conversion efficiency. Under typical operating conditions, an output power of up to 20 mW at 394.1 nm is achieved.

Reflections from the cavity and the input coupling mirror are used to generate an error signal for active stabilization of the cavity length. The cavity is stabilized using the Hänsch-Couillaud locking technique [83], where the error signal is fed to a piezoelectric actuator

[13] *Raicol Crystals Ltd.*, LBO $3 \times 4 \times 15\,\mathrm{mm}^3$

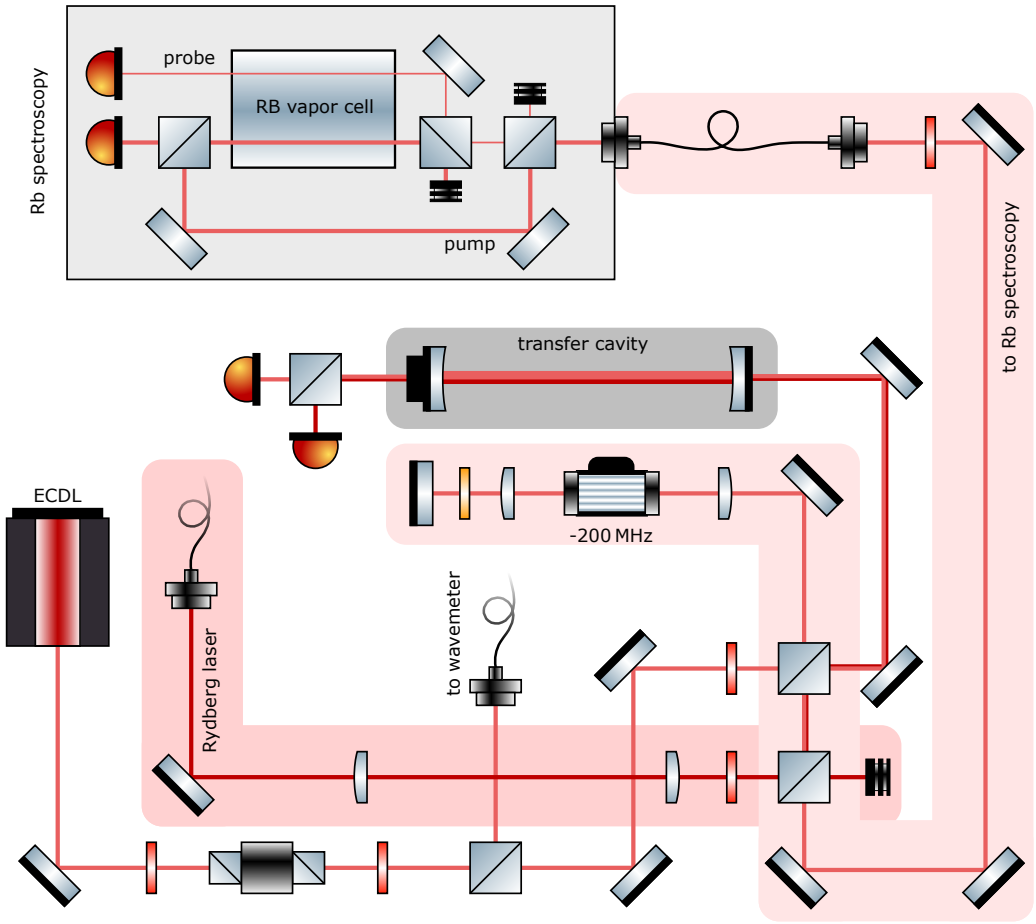

Figure 3.6.: Schematic drawing of the experimental setup used for the scanning transfer cavity lock (STCL). The frequency-stabilized ECDL is locked to a rubidium spectroscopy signal and serves as the reference for transferring frequency stability to the Rydberg laser. To aid visualization, different optical paths in the schematic are color-coded.

attached to one of the cavity mirrors. This feedback ensures resonance of the cavity with the input frequency even during dynamic tuning.

The generated UV light is monitored using a photodiode and can be rapidly switched by means of an AOM. Finally, the frequency-doubled beam is coupled into an optical fiber and guided to the MOT chamber, with up to 5 mW of UV power available at the atoms.

3.3.3. Frequency Stabilization using a STCL System

In our previous work described in [1], measurements of Rydberg transitions were performed by scanning the Rydberg excitation laser and recording the signal at the corresponding resonance peaks, while simultaneously measuring the wavelength of the laser using a wavemeter. While effective, this method is time-consuming, as each data point requires a full frequency scan over a transition of a Rydberg state.

To overcome this limitation, the present setup, employs frequency stabilization of the seed laser – and consequently of the UV light – allowing for continuous data acquisition without repeated scanning. For this purpose, an external cavity diode laser, referred to as the reference laser[14], was implemented, including a transfer cavity system, which has been built in a master thesis [84], as shown in figure 3.6. The reference laser is frequency-stabilized via Doppler-free rubidium spectroscopy (see figure 3.7 b) implemented in a compact, fiber-coupled setup. This setup contains a rubidium vapor cell as well as glued prisms and beam splitters that divide the beam into pump and probe paths for Doppler-free saturation spectroscopy [15]. The implementation of this setup is based on the approach in [85], as shown in figure 3.6.

The frequency stability of the reference laser is transferred to the Rydberg laser using a scanning transfer cavity lock (STCL) technique [86]. In this approach, a scanning optical cavity is used to compare and lock the frequencies of the two lasers, enabling precise and stable excitation of Rydberg states without the need for repeated scans.

The output of the reference laser first passes through an optical isolator and then a portion of the beam is sent through an acousto-optic modulator, for the required frequency modulation for the spectroscopy signal. Frequency stabilization is achieved using a lock-in technique similar to that described in section 3.2.

A second portion of the reference laser beam, along with the beam from the Rydberg laser (the darker red beam in figure 3.6) is sent to the scanning cavity (SC), which operates under vacuum and is temperature-stabilized using water-cooling to minimize pressure and temperature fluctuations. Inside the cavity, both beams generate different resonance maxima as depicted in panel a_2 and a_3 in figure 3.7, which are detected by two photodiodes. Due to their orthogonal polarization, the two beams can be separated behind the cavity using a polarizing beam splitter.

The photodiode signals are processed by a microcontroller (MC) based on an Arduino platform. A pulse from the reference-laser photodiode (panel a_2) switches the microcontroller input from LOW to HIGH, whereas a pulse from the Rydberg-laser photodiode (panel a_3) switches it from HIGH to LOW. Due to the frequency difference between the two lasers, their cavity-transmission peaks arrive at different times on the respective photodiodes, resulting in a change of the time interval $\Delta\nu$, as illustrated in figure 3.7 a_4. In this way, the frequency difference between the lasers is mapped onto the measured time interval.

The MC determines these intervals by comparison with its internal clock. By feeding the resulting time signal into a time-to-amplitude converter, the time – and thus the frequency

[14] In the laboratory, this laser is referred to as the "Aaron laser", named after its builder.

[15] Rubidium spectroscopy is used here primarily because cost-effective, self-built lasers are readily available at this wavelength, and a rubidium vapor cell, along with the necessary optical components, was already present in the laboratory. Moreover, the rubidium transition at 780 nm lies close to the initial wavelength of the DL Pro laser (788 nm), facilitating implementation of the STCL scheme.

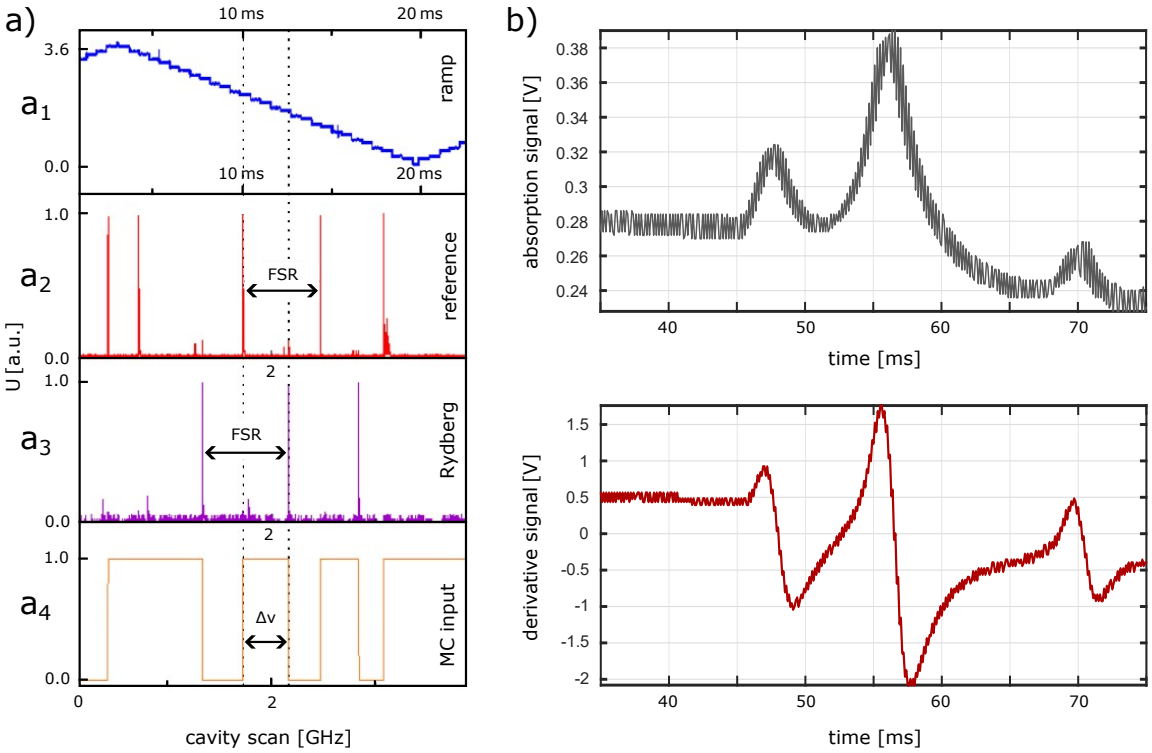

Figure 3.7.: a) Output signals of the scanning cavity (SC) recorded on two photodiodes. Panel a_1 shows the scan ramp. The signal of the stabilized reference laser is displayed in a_2, and the Rydberg-laser signal is shown in a_3. The microcontroller input, representing the time interval between two cavity peaks of the respective lasers, is shown in a_4. In b), a typical rubidium spectroscopy signal at $\lambda_{D2,4} = 780.250\,\text{nm}$ is presented, along with the corresponding derivative error signal used for frequency stabilization. Adapted from [84].

difference – is converted into a voltage. This voltage is supplied to a lock box, where it is compared to a predefined setpoint. In this manner, the measured interval $\Delta\nu$ is used to stabilize the frequency of the Rydberg laser relative to the stable reference laser. Provided that the Rydberg laser is tuned to the correct wavelength[16], the measured interval remains constant once the lock is engaged. A detailed description of this principle can be found in [84].

Any drift of the Rydberg laser results in a deviation from the reference interval, prompting a correction to restore the target frequency. To minimize hysteresis effects, the interval is consistently measured on the falling edge of the ramp (see panel a_1 in figure 3.7). In this way, the frequency stability of the reference laser is reliably transferred to the Rydberg laser. As demonstrated in [84], a frequency stability of the Rydberg laser better than 1 MHz can be achieved. Given that the linewidth of a typical Rydberg transition lies in

[16] In practice, the infrared light is used for locking. The Rydberg laser is frequency-stabilized in the infrared before being frequency-doubled to the target UV wavelength.

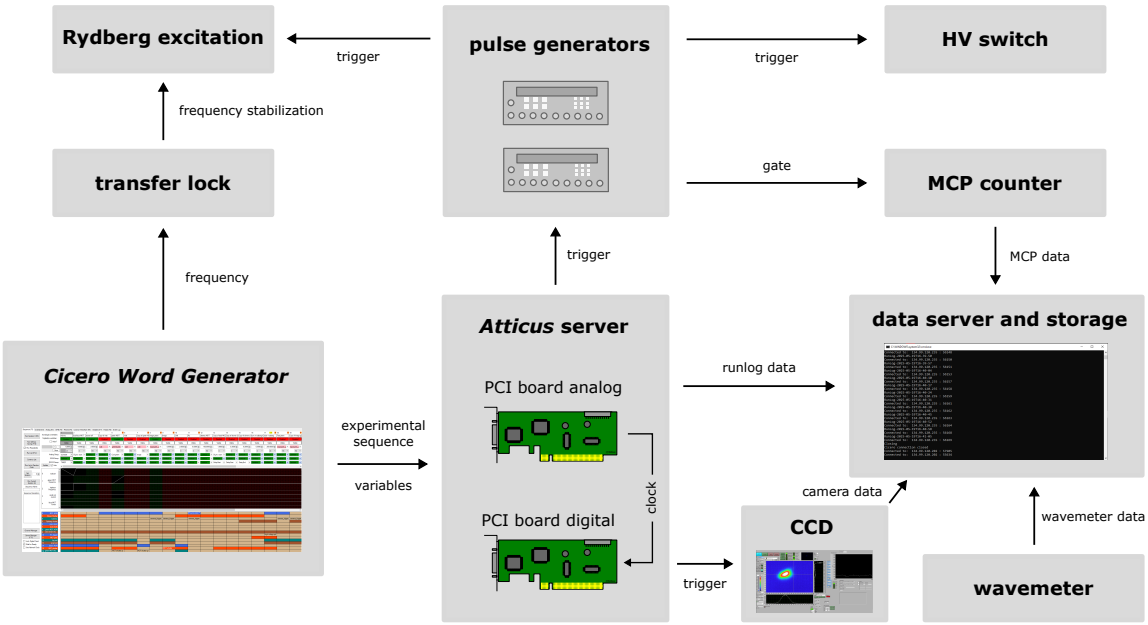

Figure 3.8.: Overview of the experimental control system, including analog and digital signal generation, triggering, data handling, and timing synchronization. Data from the CCD camera, wavemeter, MCP and the runlogs are temporally aligned, as the corresponding device programs run on different computers and must be matched and processed by the data server.

the range of several tens of MHz, this level of stability is sufficient for our experimental purposes.

3.4. Experiment Control System

The core of the experimental control system is the graphical user interface (GUI) software *Cicero Word Generator* [87], used in conjunction with an *Atticus* server. This server mediates communication between *Cicero* and the experiment by generating digital and analog control signals, as depicted in figure 3.8. These signals are transmitted to devices such as laser drivers, AOMs, power supplies, and shutters via two National Instruments interface cards[17]. Analog signals can be generated with 13-bit resolution over a voltage range of $-10\,\mathrm{V}$ to $+10\,\mathrm{V}$. Digital outputs are TTL signals with voltage levels of either $0\,\mathrm{V}$ or $+5\,\mathrm{V}$. Experimental sequences are created within *Cicero* and executed with a user-defined clock rate[18], which sets the temporal resolution of the sequence and is limited to about $10\,\mu\mathrm{s}$. Typically, these sequences provide triggers for shutters of the various laser

[17] *National Instruments*, analog PCI-6229 and digital PCI-6723

[18] The clock rate cannot be increased arbitrarily, as rendering time increases significantly at higher rates. A suitable trade-off was found at a clock rate of 100 kHz.

beams, for the CCD camera, for power or frequency ramps of lasers, and power supplies of the magnetic coils. For example, the frequency of the Rydberg excitation laser can be controlled via *Cicero*. This is achieved by applying a voltage to the laser driver, which adjusts the position of the diffraction grating mounted on a piezo actuator. In addition, constant values that do not need to be adjusted during a run can be set independently of any sequence.

Certain processes in Rydberg atom experiments require faster timing precision, particularly the switching of the Rydberg excitation beam, the application of HV pulses and the timing of the MCP counter gates, as shown in the upper part of figure 3.8. To meet these requirements without temporal limitations, two pulse generators[19] are employed. These provide delay resolutions of 5 ps and exhibit a typical channel-to-channel jitter of 50 ps. For further details on the precise timing schemes, see section 4.3.

Various devices in the setup acquire experimental data. To combine these data streams, which originate from different computers, a Python-based data server is used within the network. Its primary task is to collect data from the CCD camera, the wavemeter, the MCP detector, and the run logs, and to temporally align all incoming data streams. Since sequences executed in *Cicero* generate multiple triggers and thereby produce measurement results from different devices at different times, the data server ensures that corresponding events are correctly matched. This enables, for example, the extraction of ion counts as a function of the excitation wavelength, where the individual values must be associated reliably.

[19] *Stanford Research Systems DG535*

4.

Experimental Sequence

This chapter outlines the current experimental sequence for the production and detection of Yb Rydberg atoms, beginning with a thermal atomic beam and proceeding to the excitation of Rydberg states in an ultracold ensemble. While parts of this sequence were previously developed in the work of C. Halter [1], significant additions and optimizations have been introduced in the present study.

While we have used the trap-loss spectroscopy in our initial studies (see section 5.1), the current detection method uses field ionization to detect the excitation of Yb Rydberg states. Therefore, only this method is described in this chapter and a description of the trap-loss method is included in section 5.1.

The individual steps of the experimental sequence – implemented using *Cicero* and the *Atticus* server, as introduced in section 3.4 and illustrated in figure 4.1 – are described in the following sections. The preparation of ultracold atoms in a blue MOT is outlined in section 4.1. This is followed either by fluorescence imaging to analyze the MOT parameters (see section 4.2) or by the excitation of the trapped atoms to Rydberg states and their subsequent detection via MCP (see section 4.3).

4.1. Blue MOT

As described in chapter 3, the atoms must be precooled by a Zeeman slower to a velocity below approximately 20 m/s in order to be captured in the MOT. To achieve this, the slower beam, with a power of $\approx 1\,\mathrm{mW}$, and the three MOT beams, with a combined power of $\approx 2\,\mathrm{mW}$, are applied to the atoms for 3.5 s (see figure 4.1). This is done by switching both the mechanical shutters and the blue MOT AOM (see section 3.2). The MOT beams are red detuned by $-0.7\,\Gamma_{\mathrm{blue}}$ from resonance, and the optical power is approximately evenly distributed over all three beam pairs. Under these conditions, approximately 10^7 atoms can be trapped, corresponding to a peak atomic density of around $9 \times 10^8\,\mathrm{cm}^{-3}$ and a temperature well above the Doppler cooling limit, at roughly 4 mK. After the 3.5 s loading phase, the MOT reaches its saturation point, and no additional atoms can be accumulated for longer loading times. The required magnetic field gradient of about $40\,\mathrm{G\,cm}^{-1}$ is realized

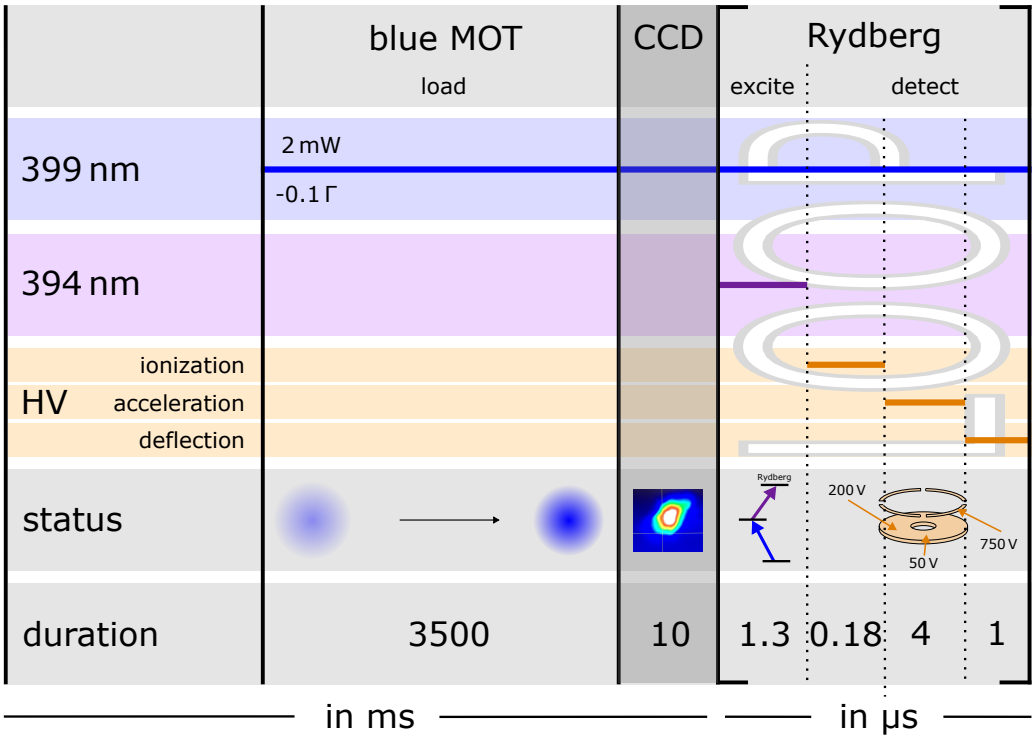

Figure 4.1.: Simplified schematic of the experimental sequence implemented via the *Cicero* GUI, highlighting the main stages. The sequence begins with loading the blue MOT, followed by an optional fluorescence imaging using the CCD camera. During the Rydberg excitation and detection phase, the blue light remains continuously on, while the Rydberg excitation beams are pulsed. Subsequently, a series of HV pulses is applied for ionization and ion guiding. This excitation and detection step can be repeated in a loop to improve the signal-to-noise ratio.

by applying currents to the different coils, as presented in table 4.1. The values of the currents are obtained by empirically maximizing the atom number in the blue MOT.

4.2. Fluorescence Imaging via CCD Camera

For specific purposes – such as the characterization and optimization of various MOT parameters – it is necessary to acquire fluorescence images of the atomic cloud. In such cases, the sequence step labeled CCD in figure 4.1 is activated. The CCD camera is triggered within the *Cicero* control sequence and operated with a variable exposure time, typically set to 10 ms.

For the characterization of the blue MOT, the cooling and trapping beams at the blue transition wavelength remain switched on during the imaging process, enabling the detection of blue fluorescence emitted by the trapped atoms. This can help optimizing the MOT

Table 4.1.: Currents applied to various coils in the experimental setup illustrated in figure 3.1.

Coil	Current [A]
Small MOT coil	19.4
Big MOT coil	12.0
Slower coil	10.7
Slower compensation	6.7
Horizontal compensation	1.0

parameters. For measurements with Rydberg atoms this CCD sequence step is omitted. In figure 4.1 the shading of this step indicates that it is optional and not part of the excitation sequence.

4.3. Rydberg Excitation and Detection

As described in section 1.1, the Rydberg excitation proceeds via an intermediate blue state. The realization of the Rydberg excitation and subsequent detection is highly demanding in terms of timing. Both the laser beams and the required electric fields must be precisely controlled. To ensure precise timing and synchronization, fast pulse generators trigger both the AOM for optical switching and the high-voltage pulses used for ionizing the atoms.

As shown in figure 4.1, the actual excitation process where the Rydberg excitation lasers are applied lasts for only 1.3 µs. This duration represents a compromise between achieving sufficient Rydberg excitation and avoiding saturation of the ion detector.

During the "Rydberg" phase the electric field has to be switched several times. The electrode configuration described in section 3.1.4 is used not only for ionizing and guiding the atoms, but also for compensating background electric fields during the actual excitation process. This compensation is essential for enabling precise spectroscopy of Rydberg states without perturbations due to Stark shifts. The optimal voltage settings were determined step by step by using the experimentally determined Stark maps, as discussed in detail in section 5.1. For these Stark maps, the transition energy of a single Rydberg state is measured at different electric field strengths. The resulting Stark shift exhibits the expected quadratic dependence of the transition frequency on the field, allowing the zero-field value to be identified at the parabola's turning point. A detailed description of this method was first presented in [1] and is also found in section 5.1. The left panel of figure 4.2 summarizes the voltages applied to the various segments of the electrode assembly during the excitation phase. The right panel shows simulation results of the electric field in the MOT region within the chamber for these values: in side view (a) and in top view (b).

Segment	Voltage [V]
U_1	13.02
U_2	10.38
U_3	12.58
U_4	15.22
U_{Plate}	-2.24
U_{mesh}	-5.00

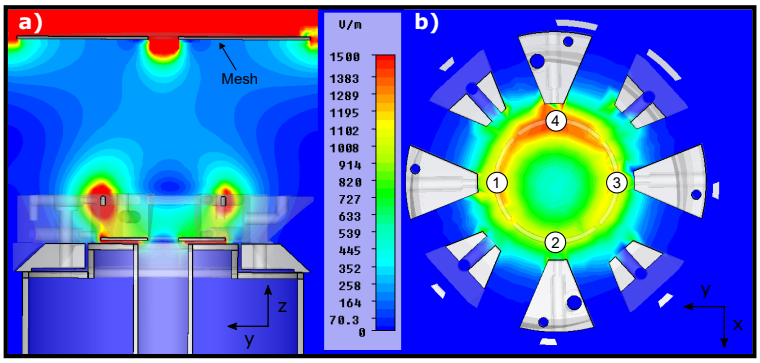

Figure 4.2.: Overview of the electrode configuration: the left table shows the applied voltages to the individual segments for optimal background field compensation, while the right panel depicts a simulation of the electric field within the MOT region of the chamber. The simulation includes a side view (a) and a top view (b). Adapted from [1].

After the excitation phase, HV pulses are applied to selected segments of the electrode setup to allow for detection of Yb atoms excited to Rydberg states. The Rydberg excitation is followed by an ionization pulse (see section 2.2.2) that is applied to the lower

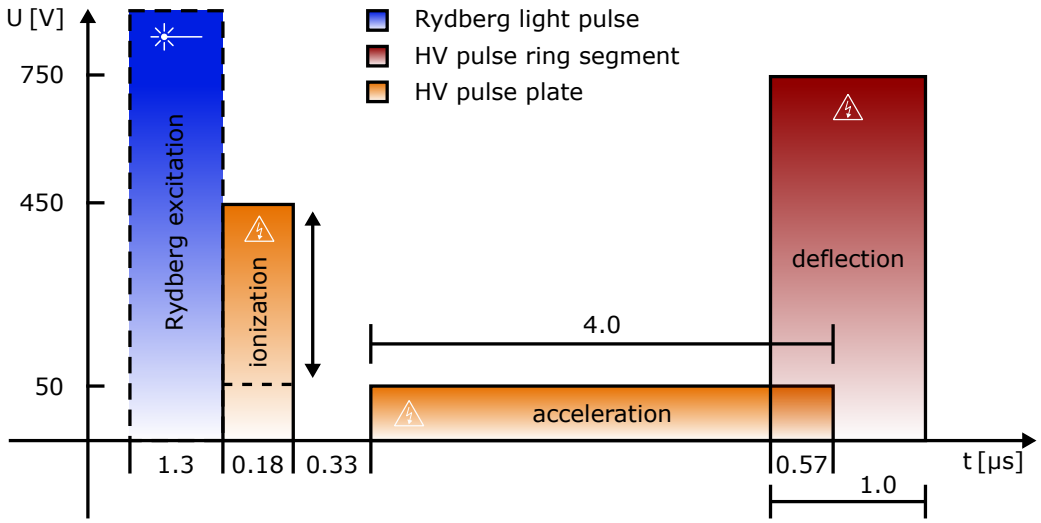

Figure 4.3.: Timing diagram of the pulse sequence during the "Rydberg" phase (figure 4.1). The timing on the µs scale is achieved using the fast pulse generator. The optical excitation pulse (blue) is followed by a series of HV pulses. The yellow pulses correspond to the ionization and subsequent acceleration, applied to the lower electrode plate (figure 3.2 and figure 4.4) with a delay of 330 ns. The guidance of the ions to the detector is improved by applying a so-called deflection pulse to one part of the segmented ring with a temporal overlap of 570 ns with the acceleration pulse. Adapted and extended from [1].

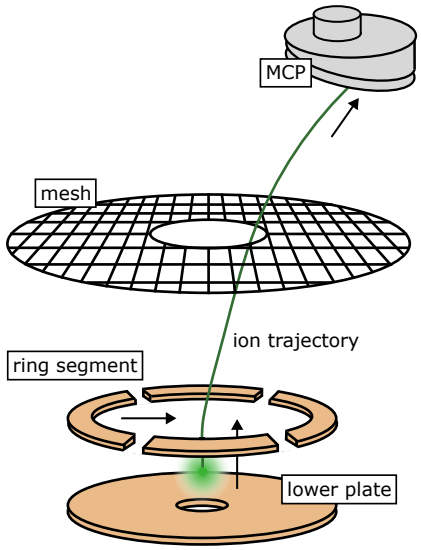

Figure 4.4.: Schematic illustration of the ion trajectory after the Rydberg atoms have been field-ionized. The ions are first accelerated by the lower plate, then deflected by a voltage pulse applied to one segment of the segmented electrode ring. After passing through the grounded mesh, they are finally accelerated by the MCP high voltage. For clarity, the geometric proportions in the figure are not drawn to scale and have been adjusted to emphasize the relevant features.

electrode plate. The required voltage varies depending on the specific Rydberg state, between 50 V and 450 V, which is sufficient to reach the ionization threshold for all states of interest.Specially, the upper voltage limit allows us to reach the classical ionization threshold of the $35\,S$ Rydberg state, which represents the lowest ionizable state in our current experiment.

To separate the ionization from the subsequent guidance of the atoms to the detector, the initial HV pulse is kept as short as possible. In our setup, the limiting factor is the self-built HV switch which limits the pulse duration to 180 ns.

The detection sequence is concluded with two additional HV pulses, designed to guide the ionized Rydberg atoms to the detector (see figure 4.3). First, a low-voltage acceleration pulse of 50 V is applied to the lower electrode plate for a duration of 4 µs, starting 330 ns after the ionization pulse. This pulse accelerates the ions upwards along a straight trajectory (see figure 4.4). As the MCP detector is laterally displaced to allow unobstructed laser access, a deflection pulse is applied to one of the ring segments opposite the detector. This pulse introduces a transverse electric field that tilts the ion trajectories toward the MCP, thereby enhancing the overall detection efficiency. The deflection pulse consists of a 750 V potential applied for 1 µs. It is important to note that a temporal overlap of 570 ns (see figure 4.3) between the acceleration and the deflection pulses yields optimal ion guidance.

In addition to controlling the timing of laser and electric fields, the pulse generators are

used to define a gate for the ion counting unit. As the HV pulses applied to the electrodes can cause false counts due to electromagnetic crosstalk with the counter electronics, the first 5 µs after the trigger from *Cicero* to the pulse generator – including the duration of all HV pulses – are excluded from detection. The gate is closed after 50 µs, as all ions arrive at the detector within this time window. This gating scheme effectively minimizes the number of spurious counts and improves data reliability.

To improve the signal-to-noise ratio, the Rydberg excitation and detection sequence can be repeated multiple times per experimental cycle. In early measurements with the blue MOT, up to 100 repetitions were performed to increase statistical accuracy. Typically, about 20 ions per repetition of the excitation and detection step is the maximum that is detected with the MCP.

5.

Spectroscopy of Rydberg States in the Single-Stage Blue MOT

In this chamber the main experimental results of this thesis on the spectroscopy of Rydberg state in Yb are presented and discussed.

In section 5.1, we introduce our initial spectroscopy experiments based on trap-loss spectroscopy of Rydberg states in Yb [56]. This work includes the investigation of the Stark effect of S- and P- states of ^{174}Yb. The trap-loss method itself, which was omitted in the previous chapter, is also described here in detail.

A detailed experimental study of isotope effects in the Rydberg spectroscopy of Yb [37] is presented in section 5.2. In particular it focuses on the effects of hyperfine interaction in the fermionic isotopes ^{171}Yb and ^{173}Yb.

Finally, section 5.3 is dedicated to so far unpublished experimental measurements of the lifetimes of Rydberg states in Yb. The experimental results are complemented by model calculations using the *PairInteraction* software package [6].

5.1. Trap-Loss Spectroscopy of Rydberg States in Ytterbium

This section is based on the previously published article:
Trap-loss spectroscopy of Rydberg states in ytterbium. C Halter, A Miethke, C Sillus, A Hegde and A Görlitz. Journal of Physics B: Atomic, Molecular and Optical Physics, Volume 56, Number 5. (2023).
Published by IOP Publishing Ltd.

Minor modifications have been made to adapt to the context of this work.

5.1.1. Experimental Setup

In our experiment, trap-loss spectroscopy is performed in a standard six-beam magneto-optical trap using the isotope ^{174}Yb. The MOT operates on the broad $6s^2\,{}^1S_0 \rightarrow 6s6p\,{}^1P_1$ transition at 399 nm and is continuously loaded from a Zeeman slower.

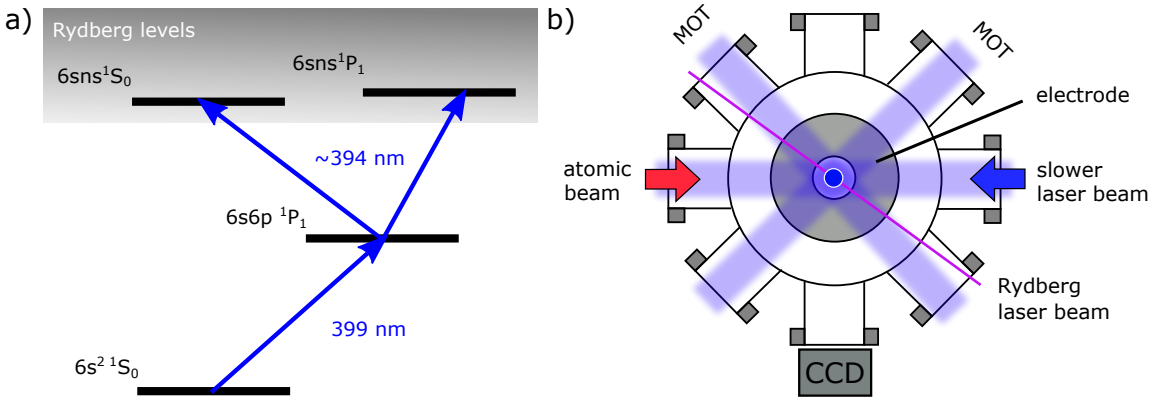

Figure 5.1.: (a) Relevant level scheme for Rydberg excitation of Yb: The MOT is operated on the $6s^2\,{}^1S_0 \rightarrow 6s6p\,{}^1P_1$ transition. Rydberg atoms are produced using radiation at 394 nm which connects the excited $6s6p\,{}^1P_1$ MOT state to the Rydberg manifold. (b) Top view of the experimental setup: The MOT is loaded from a Zeeman slower and operates in a standard six-beam configuration. For Rydberg excitation, the Rydberg laser beam is focused onto the MOT through one of the MOT beam windows. The fluorescence of the MOT is monitored using a CCD camera. An electrode is placed on the top viewport of the vacuum chamber to control the electric field.

The laser light for both the MOT and the Zeeman slower is provided by a home-built diode laser system in seed/amplifier[1] configuration (*Nichia NDHV310ACAEI / Nichia NDV4313E*), see figure 5.1 b). The seed laser is frequency-stabilized via Doppler-free spectroscopy of ytterbium. For precise control of the laser frequencies, acousto-optical modulators (AOMs) are employed.

Rydberg atoms can be produced in the MOT by a two-photon excitation scheme, as illustrated in figure 5.1 a). The first photon, with a wavelength of $\lambda_{\mathrm{MOT}} \approx 399\,\mathrm{nm}$, corresponds to the $6s^2\,{}^1S_0 \rightarrow 6s6p\,{}^1P_1$ MOT transition and is provided by the MOT laser.

To transfer the atoms from the $6s6p\,{}^1P_1$ state into a Rydberg state of the $6sns\,{}^1S_0$ or $6snp\,{}^1P_1$ series, the MOT is illuminated with an additional so-called Rydberg laser at a wavelength of $\lambda_{\mathrm{R}} \approx 394\,\mathrm{nm}$. The nominally forbidden transitions $6s6p\,{}^1P_1 \rightarrow 6snp\,{}^1P_1$ can be excited if an external electric field is applied, which leads to an admixing of even-parity states to the odd-parity $6snp\,{}^1P_1$ states.

The Rydberg laser light is generated using a commercial diode laser system (*Toptica* DL pro), which is frequency-doubled to λ_{R} using a Lithium Triborate (LBO) crystal integrated into a home-built bow-tie resonator (see section 3.3.1). The output of the frequency-doubling stage is delivered to the experiment via an optical fiber and is focused onto the

[1]This configuration has historically been referred to as a "master/slave" setup (as also used in our publication). To better reflect inclusive and respectful language, we instead refer to the lasers as "seed" and "amplifier".

MOT with a beam waist of $(100 \pm 10)\,\mu$m and a typical power of 1 mW.

The wavelength of the Rydberg laser is measured using a home-built Michelson wavemeter, which is referenced daily to a rubidium spectroscopy. The reference laser for the wavemeter is provided by the seed laser used for Yb cooling. Like the MOT and the slower light, the Rydberg laser can be switched using mechanical shutters and acousto-optical modulators.

A top view of the experimental setup is shown in figure 5.1 b). The MOT is located in a cylinder-shaped vacuum chamber with an inner diameter of 100 mm operating at a base pressure below 10^{-10} mbar. In the horizontal plane, the vacuum chamber possesses eight flange connections, two of which are used for the atomic beam and the counterpropagating slower laser beam, four for the horizontal MOT beams and two for imaging purposes. The vertical MOT beams are sent into the chamber through two additional viewports. The MOT magnetic field is generated by two water-cooled solenoids of different size which are mounted outside the vacuum chamber. The smaller coil with a diameter of 25 mm is mounted in a recessed flange on the bottom of the chamber while the larger coil with a diameter of 155 mm is mounted on top at a distance of 76 mm from the smaller one. In this configuration, the MOT is positioned very close to the smaller coil and the (grounded) walls of the vacuum chamber nearby. The Zeeman-slowed atomic beam which loads the MOT is generated by a single nozzle oven heated up to 420 °C. Under typical experimental conditions, 10^7 atoms are captured in the MOT at a temperature of several mK. The peak density in the MOT is on the order of $\rho_{\max} \approx 10^9\,\mathrm{cm}^{-3}$.

A relatively homogeneous electric field at the MOT position can be created by simply placing an electrode on the top viewport of the grounded vacuum chamber at a distance of 75 mm from the MOT position[2]. The electrode is a copper disk with a diameter of 150 mm and a 25 mm bore in the center which is used for the vertical MOT beam. Typically, a voltage of a few V is applied to the electrode leading to electric fields up to a few $10\,\mathrm{V m}^{-1}$ at the position of the MOT.

5.1.2. Measurement Procedure

A cycle of the sequence, which we use for the spectroscopic determination of the excitation energy of Rydberg levels of ^{174}Yb, is illustrated in figure 2(a). The cycle is initialized by turning off the slower and MOT light for 100 ms to remove all remaining atoms from the previous cycle. In the loading phase, the slower and the MOT light are switched on with the MOT light detuned by ≈ 22 MHz from the atomic resonance. The MOT is loaded for 3.5 s, to ensure saturation of the number of atoms in the MOT. Subsequently, the slower light is switched off and the Rydberg laser is switched on during the spectroscopy phase. If the Rydberg laser is resonant with a transition from the $6s6p\,^1P_1$ state to a Rydberg state,

[2] At the time these measurements were performed, this single electrode was used. For subsequent measurements, the electrode configuration described in section 3.1.4 was employed.

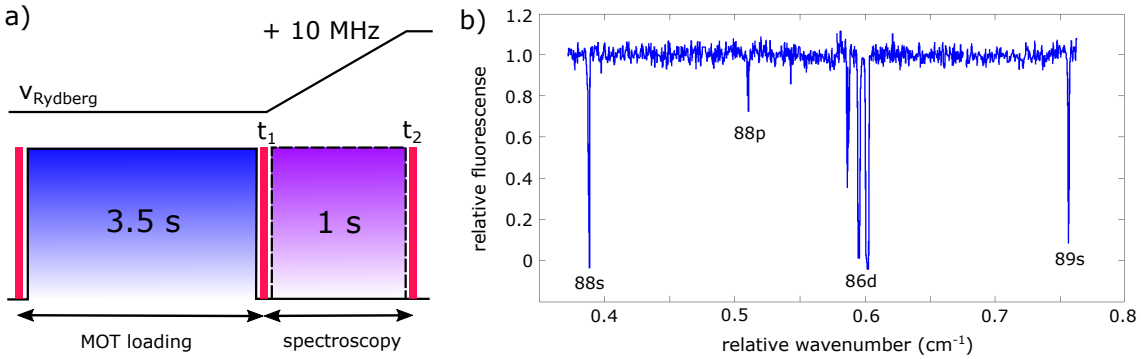

Figure 5.2.: (a) Experimental cycle for trap-loss spectroscopy. Each cycle is divided into an initialization phase, a MOT loading phase and a spectroscopy phase. The cycle is repeated between 50 and 100 times to record a spectrum. (b) Typical trap-loss spectrum of ^{174}Yb Rydberg states. Besides the 6s88s $^1S_0$-, 6s89s $^1S_0$- and the 6s88p $^1P_1$-state also D-levels can be seen in the spectrum. The offset of the x-axis is 50 427 cm^{-1}.

atoms are removed from the MOT and correspondingly the MOT fluorescence is reduced. To determine the relative loss induced by the Rydberg laser, fluorescence images of the MOT are taken right before the Rydberg laser is turned on and after 1 s of illumination. During this time, the frequency of the Rydberg laser is ramped over 10 MHz. The whole cycle is repeated between 50 and 100 times with varying frequency of the Rydberg laser in order to take a spectrum over a specific frequency range. Every fifth cycle is a calibration cycle, where the Rydberg laser is not switched on in the spectroscopy phase. This calibration is required to account for long-time fluctuations of the number of atoms trapped in the MOT.

A typical trap-loss spectrum is depicted in figure 5.2 b). The excitation frequencies (given in wavenumbers) are calculated by summing the excitation frequency of the intermediate $6s6p\,^1P_1$ state and the measured frequency of the Rydberg laser, which has an error of $\approx 0.005\,\mathrm{cm}^{-1}$ due to the uncertainty of the wavemeter. This includes the error of the wavemeter calibration using a frequency-locked laser, the wavelength measurement itself, and the wavemeter drift over a day.

Because of frequent calibrations, the day-to-day drift is canceled out. Other sources of error such as the Zeeman shift due to the MOT magnetic field are determined to be significantly smaller. With a magnetic field gradient of $\approx 40\,\mathrm{G\,cm}^{-1}$ and a MOT size of $\approx 2\,\mathrm{mm}$, the variation of the magnetic field in the MOT volume is $\approx 8\,\mathrm{G}$, leading to an uncertainty of $\approx 11\,\mathrm{MHz}$, which is much smaller than the wavemeter error and can thus be neglected. To determine the polarizability of a specific Rydberg state, line spectra are taken at various values of an externally applied electric field $\vec{F}$. The external field is generated by applying a voltage to the electric field plate which is located on top of the vacuum chamber. Due to the complex geometry of our chamber and the uncertainty in the

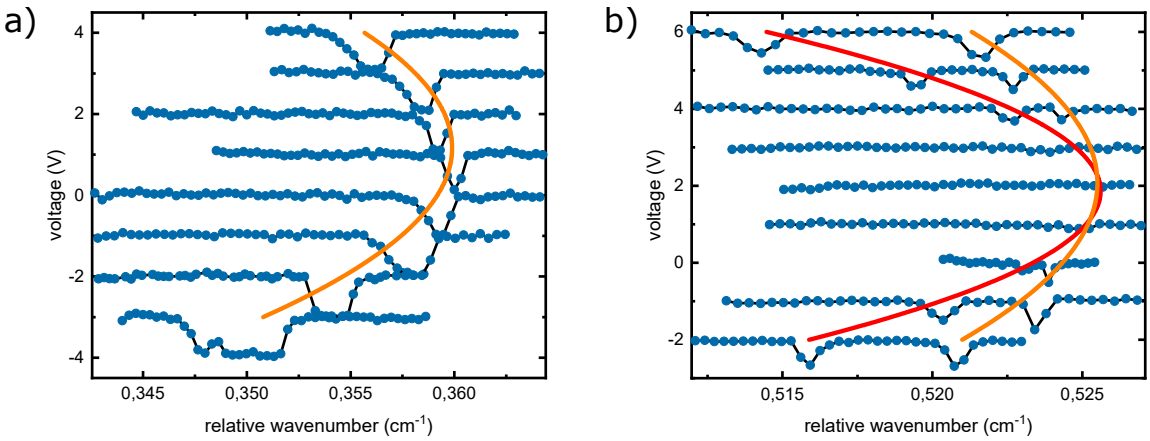

Figure 5.3.: Line spectra of the $6s83s\,^1S_0$ (a) and the $6s83p\,^1P_1$ state (b) for various values of an externally applied electric field. The solid orange and red lines are quadratic fits to the Stark shifted line centers corresponding to equation (5.3). The black lines of the spectra are shown as a guide for the eye. Due to a non-zero electric background field, the apex of the fits is shifted with respect to the zero value of the external electric field. In the case of the $6s83p\,^1P_1$ state, the Rydberg line disappears at zero field due to selection rules. At non-vanishing electric field, it splits into two lines corresponding to $|m_J| = 0$ and $|m_J| = 1$. The x-axis has an offset of $50425\,\mathrm{cm}^{-1}$ for both graphs.

exact position of the MOT relative to grounded surfaces, the corresponding electric field has a large uncertainty which is estimated to be more than 50 %. Therefore, we only give the value of the externally applied voltage in figure 5.3. Nevertheless, the experimental geometry ensures that the electric field $\vec{F}$ points predominantly in the vertical direction at the position of the atoms.

In figure 5.3, typical spectra are shown for the $6s83s\,^1S_0$ state (a) and the $6s83p\,^1P_1$ state (b), where spectra for different values of the applied voltage are combined into a single graph and the maxima are fitted to a function which is quadratic in the applied voltage (see equation (5.3)). For the relatively small values of the applied voltage, only Rydberg states experience a noticeable electric-field (Stark) shift and hence an observed line shift corresponds directly to an energy shift of the Rydberg state. Hence, we will refer to plots as shown in figure 5.3 as Stark maps.

A notable feature of the obtained Stark maps is that the $6s83s\,^1S_0$ line is only shifted by the external electric field while the $6s83p\,^1P_1$ line is additionally split into two components. This reflects the fact that the Stark shift depends on the absolute value $|m_J|$ of the magnetic quantum number, which can take the values $|m_J| = 0, 1$ for the $6s83p\,^1P_1$ state, while for the $6s83s\,^1S_0$ state only $|m_J| = 0$ is possible. At the apex of the $6s83p\,^1P_1$ Stark map, we observe almost no excitation of the atoms into the Rydberg state, in agreement with selection rules that forbid transitions between the two odd-parity states $6s6p\,^1P_1$ and

$6s83p\,^1P_1$. At finite electric field, even-parity states are admixed to the $6s83p\,^1P_1$ state and transitions become possible. In addition, the apex of the Stark maps is not at zero external field and is not even at an identical position for different Stark maps. We attribute this to background electric fields in the chamber which are most likely originating from patch charges on the top window. Those patch charges may vary on the time scale of days. To remove these charges, at least partially, we regularly illuminate the top window with a 340 nm LED [88] in between experimental runs. Vanishing of the $6s83p\,^1P_1$ line at the apex of the Stark map indicates that the applied external electric field which is oriented vertically compensates the background field to a large extent and we may assume that the background field is also oriented vertically.

The broadening of the spectra if an electric field is applied in figure 5.3 is attributed to a saturation of the trap loss due to a Rydberg excitation probability which is increasing with applied electric field. This saturation effect is significantly larger for the allowed transitions to the $^1S_0$ states. However, this broadening mechanism has little effect on the determination of the position of the line centers which is relevant for the determination of polarizabilities as described below.

5.1.3. Results and Discussion

Our results on the excitation energies and polarizabilities of the $6sns\,^1S_0$ and the $6snp\,^1P_1$ series of ^{174}Yb in the range from $n = 70$ to $n = 90$ are summarized in table 5.1. For each line a complete Stark map was recorded to determine the polarizability and the zero-field excitation energy. The excitation energies for the $6snp\,^1P_1$ series are extrapolated from quadratic fits to the Stark maps (see figure 5.3).

In a system with two valence electrons like Yb a full theoretical description of the Rydberg series can be obtained using Multi-Channel Quantum Defect Theory [89, 90]. However, for large principal quantum numbers and in the absence of perturbations by doubly excited states, the excitation energies of a Rydberg series are to a good approximation described by a single quantum defect according to

$$E_{\mathrm{exc}} = E_{\mathrm{ion}} - \frac{Ry}{(n-\delta_{L,J})^2} = E_{\mathrm{ion}} - \frac{Ry}{n^{*2}}. \tag{5.1}$$

Here $Ry = 10973696.959\,\mathrm{m}^{-1}$ is the mass corrected Rydberg constant and $E_{\mathrm{ion}} = 50443.07041(25)\,\mathrm{cm}^{-1}$ the first ionization energy [89]. The effective principal quantum number $n^* = n - \delta_{L,J}$ is determined by the quantum defect $\delta_{L,J}$, which describes the deviation from the hydrogenic case. It is due to the incomplete shielding of the charge of the nucleus by the inner electrons, which is particularly important for small L [18].

In figure 5.4, the measured excitation energies are plotted as a function of the principal quantum number. The values for the $6sns\,^1S_0$ series that we have obtained using the simple trap-loss method are in good agreement with previously reported values by the group at

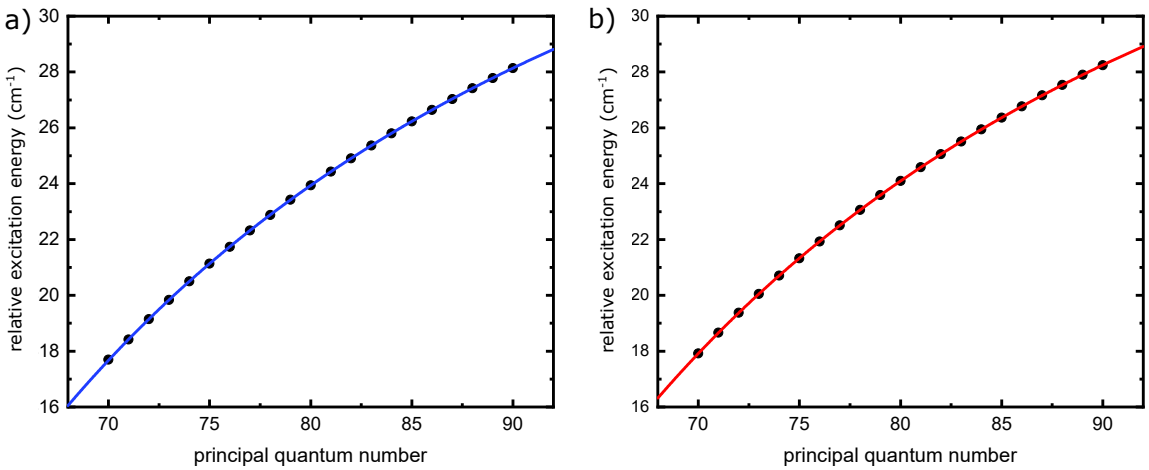

Figure 5.4.: Excitation energies for the $6sns\,{}^1S_0$ (a) and the $6snp\,{}^1P_1$ (b) Rydberg-series of ^{174}Yb. The solid lines correspond to fits according to equation (5.1) with $\delta_{L,J}$ being the only free fitting parameter. The obtained values for the quantum defect are $\delta_{0,0} = 4.2721(25)$ and $\delta_{1,1} = 3.9535(9)$. The y-axis has an offset of $50400\,\mathrm{cm}^{-1}$.

Laboratoire Aimé-Cotton [89] that have been measured using field-ionization of Rydberg states, which are also shown in the table. From fits of the measured excitation energies to equation (5.1) we get the quantum defects $\delta_{0,0} = 4.2721(25)$ and $\delta_{1,1} = 3.9535(9)$, where the value for the $6sns\,{}^1S_0$ series is again in good agreement with [89].

If Rydberg spectroscopy is performed in a small external electric field $\vec{F}$ a quadratic Stark shift

$$\Delta E = -\frac{1}{2}\alpha|\vec{F}|^2 \tag{5.2}$$

has to be taken into account where α is the state-dependent atomic polarizability. The total excitation energy is then given by

$$E_{\mathrm{exc}}(F) = E_{\mathrm{ion}} - \frac{Ry}{n^{*2}} - \frac{1}{2}\alpha|\vec{F}|^2. \tag{5.3}$$

The polarizability α of a Rydberg state with principal quantum number n, total angular momentum J and magnetic quantum number m_J can generally be written as [91]

$$\alpha(n, J, |m_J|) = \alpha_0(n, J) + \alpha_2(n, J)\frac{3m_J^2 - J(J+1)}{J(2J-1)}, \tag{5.4}$$

with the scalar polarizability $\alpha_0(n, J)$ and the tensor polarizability $\alpha_2(n, J)$. Thus, the external electric field splits a Rydberg line into $J + 1$ components which can be assigned to different absolute values $|m_J|$. For the $6sns\,{}^1S_0$ series, $J = 0$ and thus no splitting is observed. The polarizability which is determined as described in section 5.1.2 then corresponds directly to the scalar polarizability $\alpha_0(n, 0)$. For the $6sns\,{}^1P_1$ series with $J = 1$, scalar and tensor polarizability may be derived from the experimentally determined

State	E_{exc}	E_{ref}	α_0	State	E_{exc}	α_a	α_b	α_0	α_2
$6s70s\,^1S_0$	50417.693	50417.6654	1.00	$6s70p\,^1P_1$	50417.915	0.85	0.38	0.54	-0.16
$6s71s\,^1S_0$	50418.420	50418.4212	0.88	$6s71p\,^1P_1$	50418.661	1.00	0.37	0.58	-0.21
$6s72s\,^1S_0$	50419.142	50419.1438	1.02	$6s72p\,^1P_1$	50419.372	1.00	0.43	0.62	-0.19
$6s73s\,^1S_0$	50419.835	50419.8350	1.18	$6s73p\,^1P_1$	50420.051	1.59	0.56	0.90	-0.34
$6s74s\,^1S_0$	50420.497	50420.4966	1.37	$6s74p\,^1P_1$	50420.705	1.20	0.54	0.76	-0.22
$6s75s\,^1S_0$	50421.136	50421.1305	1.80	$6s75p\,^1P_1$	50421.328	1.27	0.42	0.70	-0.28
$6s76s\,^1S_0$	50421.737	50421.7379	1.77	$6s76p\,^1P_1$	50421.928	1.59	0.56	0.90	-0.34
$6s77s\,^1S_0$	50422.326	50422.3208	1.55	$6s77p\,^1P_1$	50422.505	1.60	0.65	0.97	-0.32
$6s78s\,^1S_0$	50422.881	50422.8797	1.53	$6s78p\,^1P_1$	50423.058	1.78	0.63	1.01	-0.38
$6s79s\,^1S_0$	50423.422	50423.4164	2.09	$6s79p\,^1P_1$	50423.588	2.10	0.72	1.64	-0.46
$6s80s\,^1S_0$	50423.935	50423.9322	2.83	$6s80p\,^1P_1$	50424.095	2.19	0.76	1.24	-0.48
$6s81s\,^1S_0$	50424.432	—	2.45	$6s81p\,^1P_1$	50424.585	2.65	0.79	1.41	-0.62
$6s82s\,^1S_0$	50424.907	—	2.64	$6s82p\,^1P_1$	50425.053	3.05	1.01	1.69	-0.68
$6s83s\,^1S_0$	50425.365	—	2.84	$6s83p\,^1P_1$	50425.510	3.13	1.03	1.73	-0.70
$6s84s\,^1S_0$	50425.805	—	3.54	$6s84p\,^1P_1$	50425.945	3.22	1.02	1.75	-0.73
$6s85s\,^1S_0$	50426.228	—	3.17	$6s85p\,^1P_1$	50426.364	3.69	1.45	2.20	-0.75
$6s86s\,^1S_0$	50426.638	—	3.70	$6s86p\,^1P_1$	50426.765	3.78	1.51	2.02	-0.76
$6s87s\,^1S_0$	50427.031	—	3.92	$6s87p\,^1P_1$	50427.160	4.41	1.45	2.43	-0.99
$6s88s\,^1S_0$	50427.413	—	4.92	$6s88p\,^1P_1$	50427.532	4.41	1.57	2.52	-0.95
$6s89s\,^1S_0$	50427.781	—	4.69	$6s89p\,^1P_1$	50427.898	4.67	1.56	2.60	-1.04
$6s90s\,^1S_0$	50428.137	—	5.60	$6s90p\,^1P_1$	50428.244	3.80	1.07	1.98	-0.91

Table 5.1.: Experimental excitation energies of the $6sns\,^1S_0$ and the $6sns\,^1P_1$ Rydberg series of ^{174}Yb and polarizabilities relative to the measured polarizability of the $6s70s\,^1S_0$ state. The stated values for E_{exc} are the measured energy differences between the $6s^2\,^1S_0$ ground state and the respective Rydberg state in cm^{-1}. E_{ref} are the corresponding energies measured in Ref. [89]. For the $6sns\,^1S_0$ series, α_0 is the experimentally determined relative scalar polarizability. For the $6snp\,^1P_1$ series α_a and α_b are the experimentally determined relative polarizabilities corresponding to $|m_J| = 0, 1$ and α_0 and α_2 are the derived values of the scalar and tensor polarizabilities according to equation (5.4). The accuracy of the excitation energies is limited by the accuracy of our home-built wavemeter and is estimated to be 150 MHz or correspondingly $0.005\,\mathrm{cm}^{-1}$. For the measured polarizabilities the main error results from the quadratic fit and is around 10 %.

values $\alpha(n,1,1)$ and $\alpha(n,1,0)$ of the two observed components (see figure 5.3 b)) according to

$$\alpha_0(n,1) = \frac{1}{3}\left(2\alpha(n,1,1) + \alpha(n,1,0)\right) \quad \text{and} \tag{5.5}$$

$$\alpha_2(n,1) = \frac{1}{3}\left(\alpha(n,1,1) - \alpha(n,1,0)\right). \tag{5.6}$$

Using these formulas, the values for $\alpha_0(n,1)$ and $\alpha_2(n,1)$ given in table 5.1 are calculated under the assumption that the tensor polarizability $\alpha_2(n,1)$ is negative implying that the measured component with the larger polarizability $\alpha_a(n,1)$ for a given state of the $6sns\,^1\mathrm{P}_1$

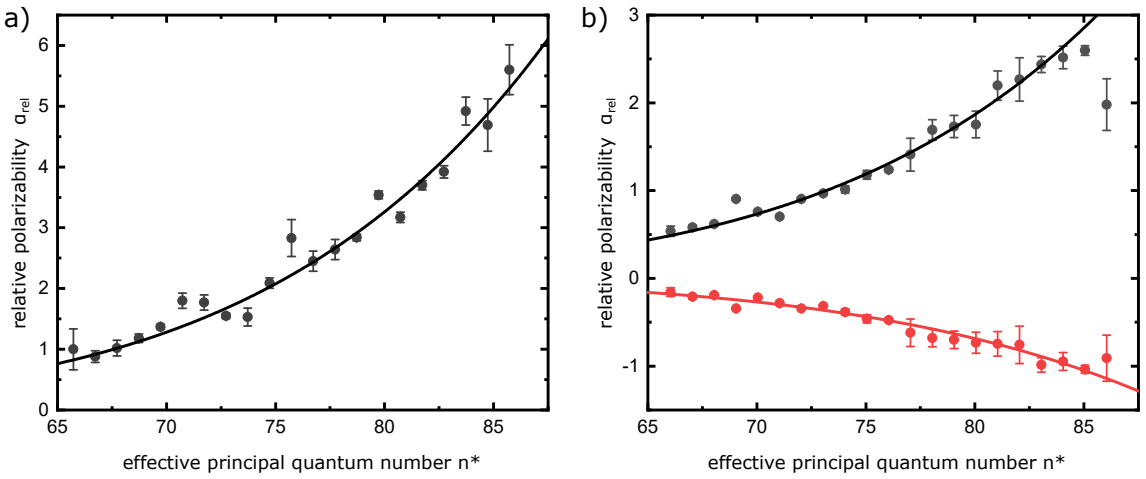

Figure 5.5.: Relative scalar and tensor polarizabilities of the 6sns ^{1}S$_0$ (a) and the 6sns ^{1}P$_1$ (b) Rydberg-series of ^{174}Yb. The scalar polarizability $\alpha_0(n,0)$ of a state 6sns ^{1}S$_0$ is directly determined from a quadratic fit to the external electric field (see figure 5.3 a)). The scalar polarizabilities $\alpha_0(n,1)$ (black dots) and the tensor polarizabilities $\alpha_2(n,1)$ (red dots) of the 6sns ^{1}P$_1$-states are determined using quadratic fits and making use of equation (5.4). All polarizabilities are normalized to the measured scalar polarizability of the 6s70s ^{1}S$_0$ state. Solid lines are fits of the polarizabilities to functions of the type $(a(n-\delta_{L,J}))^7 = (a\,n^*)^7$.

series corresponds to $J = 1$, $|m_J| = 0$. This assumption seems justified as it resembles the behavior of the polarizabilities in highly excited $^2P_{3/2}$- Rydberg states of rubidium [92, 93].

In figure 5.5, the determined scalar and tensor polarizabilities for all states of the 6sns ^{1}S$_0$ (a) and the 6sns ^{1}P$_1$ series of ^{174}Yb in the range of $n = 70$ to $n = 90$ are shown. The error bars result from quadratic fits to the line center of each spectrum and are on the order of 10 %. The error of the relative electric field values can be neglected compared to the fit errors, since the voltage supply has an accuracy of better than 1 %, leading to a maximum error contribution of 2 % to the polarizability. The solid lines in the figure are fits of the polarizabilities to functions of the type $(a(n-\delta_{L,J}))^7 = (a\,n^*)^7$, which reflect the expected scaling with n^{*7} of the polarizabilities of highly excited Rydberg states [18]. Due to the large uncertainty of the value of the external electric field at the position of the atoms, all polarizabilities are normalized to the measured polarizability of the 6s70s ^{1}S$_0$ - state.

5.1.4. Conclusion

In this manuscript, we have presented a spectroscopic measurement of the 6sns ^{1}S$_0$ and the 6sns ^{1}P$_1$ Rydberg-series of ^{174}Yb which is based on simple trap-loss spectroscopy in a magneto-optical trap. Using this method, we have obtained excitation energies for Rydberg states in the range of $n = 70$ to $n = 90$ which are in agreement with previously reported results on the 6sns ^{1}S$_0$ series and extend those results to larger principal quantum numbers

and the $6sns\,{}^1\mathrm{P}_1$ series. In addition, we have performed an investigation of the Stark effect in low electric fields allowing us to infer scalar and tensor polarizabilities which exhibit the expected n^{*7} scaling behavior. These results will be valuable for further experiments using Yb Rydberg atoms. The method described in this manuscript can also be used to study other Yb isotopes. Specifically, we plan to investigate the fermionic isotopes ^{171}Yb and ^{173}Yb where interesting effects due to the hyperfine coupling are expected [94].

While trap-loss spectroscopy is a very useful and simple method for the spectroscopy of Rydberg states it is not suitable for experiments involving time-resolved measurements or coherent manipulation of Rydberg states. Such experiments will require conservative trapping of the atoms to get rid of the perturbing influence of the MOT light. In addition, other detection methods such as field-ionization or detection by electromagnetically induced transparency [95] will have to be applied (see section 3.1.5). In order to be able to perform such exciting experimental studies we are upgrading our apparatus accordingly.

5.2. Isotope Dependence of Ytterbium Rydberg States

This section is based on the manuscript:
Isotope dependence of ytterbium Rydberg states. A. Miethke, L. P. Kozhiparambil Sajith, and A. Görlitz. *Manuscript has been submitted to the Journal of Physics B: Atomic, Molecular and Optical Physics.*
Minor modifications have been made to adapt to the context of this dissertation.

Here, we present detailed experimental results on the Rydberg spectra of $6sns\,{}^1S_0$ and $6snd\,{}^{1,3}D_2$ states with principal quantum numbers $35 \leqslant n \leqslant 80$ for three bosonic (^{172}Yb, ^{174}Yb, ^{176}Yb) and two fermionic (^{171}Yb, ^{173}Yb) isotopes. The spectra are obtained using two-photon excitation via the intermediate $6s6p\,{}^1P_1$ state in a magneto-optical trap. For ^{171}Yb and ^{174}Yb, our measurements are directly compared to the results of Ref. [7] while for ^{173}Yb our experimental results lay the groundwork for further theoretical modeling.

5.2.1. Theoretical Considerations

5.2.1.1. Single-channel Quantum Defect Theory

The most straightforward model to describe Rydberg states of ytterbium is single-channel quantum defect theory (SQDT) [72]. In this approach, each Rydberg series is associated with a so-called channel which is defined by the ionic core configuration and a set of "good" quantum numbers (L, S, J, F). In SQDT, the excitation energy of a Rydberg level

of isotope ^{X}Yb can be approximated by [7, 18]

$$E_i(^X\mathrm{Yb}) = I_{6s}(^X\mathrm{Yb}) - \frac{R_X}{(n-\mu_i)^2}\,. \tag{5.7}$$

Here $I_{6s}(^X\mathrm{Yb})$ denotes the ionization energy from the $6s^2\,{}^1S_0$ ground state of neutral ^{X}Yb to the $^2S_{1/2}$ ground state of singly-ionized $^X\mathrm{Yb}^+$, $R_X = R_\infty \frac{m_X}{m_e+m_X}$ is the reduced Rydberg constant, and μ_i is the quantum defect of the respective series.

The quantum defects μ_i (which are assumed to first approximation to be isotope independent) account for the deviation of the energy spectrum of a multi-electron Rydberg atom from the hydrogen case which is caused by the complex interaction of the ionic core with the Rydberg electron. For high angular momentum states, $\mu_i \to 0$ while for low-l states such as S- and D-states it remains significant. In general, quantum defects are energy-dependent even if SQDT is applicable [7, 89]. However, for the highly-excited S- and D-Rydberg states of ytterbium which are investigated in the present study, the assumption of energy-independence is a very good approximation and thus the dependence of μ_i on the principal quantum number n is small. Therefore, we will use the energy-independent values determined in the experimental study of Lehec et. al. [89] to interpret our results. These are $\mu_{1S} = 4.278312$ for the $^1S_0$-series, $\mu_{1D} = 2.713011$ for the $^1D_2$-series and $\mu_{3D} = 2.748627$ for the $^3D_2$-series.

Strictly speaking, high-lying Rydberg states of ytterbium where the Rydberg electron is far away from the nucleus are not appropriately captured by L-S-coupling but should rather be treated using (jj)-coupling. This implies that high-lying Rydberg states no longer have a pure singlet or triplet character and that mixing between singlet and triplet channels has to be taken into account. The associated change of the Rydberg state wave functions can be captured using a multi-channel quantum defect theory (see section 5.2.1.2). However, it can be shown that the energies of Rydberg states are still described by equation 5.7 if all channels converge to the same energy threshold [61] as is the case for high-lying states of the bosonic isotopes of ytterbium. Thus, it is still possible to attribute a singlet or triplet character to each observed state and to determine the singlet-triplet splitting which is expected to exhibit an $(n^*)^{-3}$ dependence [94] where the effective principal quantum number $n^* = n - \mu_i$ has been introduced.

5.2.1.2. Multi-channel Quantum Defect Theory

Equation 5.7 fails to describe the energies of Rydberg states properly when Rydberg series corresponding to different configurations of the ionic core and thus different ionization thresholds are no longer energetically well separated [7, 61]. In this case mixing of channels not only leads to a modification of wave functions but also to energy shifts. As already mentioned, the mathematical model used to account for channel mixing is multi-channel quantum defect theory which is applied in various contexts in atomic physics [72]. When

MQDT is applied to Rydberg states, the complex short-range interactions between the Rydberg electron and the ionic core are characterized by a set of channel-specific quantum defect parameters μ_α, while the long-range Coulomb potential is treated analytically [61]. Detailed discussions of the MQDT treatment of two-electron atoms and specifically ytterbium can be found in Ref. [7, 89] and we will only sketch the basic principles here.

In two-electron atoms with a $^1S_0$ ground state such as ytterbium, there are two principal mechanisms which lead to an energy shift due to channel mixing. The first one involves configuration interaction between singly- and doubly-excited Rydberg channels and the second one hyperfine mixing of Rydberg channels corresponding to ionic cores with different total angular momenta F_c and thus different energy thresholds.

Configuration interaction is generally relevant for all isotopes and in the case of the most abundant isotope ^{174}Yb it has been shown to affect Rydberg states with principal quantum numbers $n \lesssim 30$ [89]. For states with $n \gtrsim 30$ deviations remain sufficiently small to justify the use of SQDT for the description of high-lying states of the bosonic isotopes of ytterbium.

On the contrary, hyperfine mixing is only relevant for fermionic isotopes of ytterbium, which possess a non-zero nuclear spin I leading to two distinct hyperfine-split ionization thresholds corresponding to total angular momenta $F_c = I \pm 1/2$ of the ground state of singly-excited Yb^+. The hyperfine interaction mixes Rydberg channels of the same parity and total angular momentum F, converging to different ionization thresholds [7]. In the case of ^{171}Yb, the allowed total angular momenta of the ionic core are $F_c = 0$ and $F_c = 1$, while S-Rydberg states can have total angular momenta $F = 1/2$ or $F = 3/2$ and D-Rydberg states $F = 1/2$, $F = 3/2$, $F = 5/2$ or $F = 7/2$. In the case of ^{173}Yb, the allowed total angular momenta of the ionic core are $F_c = 2$ and $F_c = 3$, while S-Rydberg states can have total angular momenta $F = 3/2$, $F = 5/2$ or $F = 7/2$ and D-Rydberg states $F = 1/2$, $F = 3/2$, $F = 5/2$, $F = 7/2$, $F = 9/2$ or $F = 11/2$. Strong mixing occurs when the hyperfine interaction energy becomes comparable to the energy difference between Rydberg states with adjacent principal quantum numbers n, as is the case within the range of Rydberg states studied here.

The models discussed above form the basis for interpreting the measured spectra presented in section 5.2.3. In particular, deviations from the SQDT predictions will serve as indicators of hyperfine mixing between Rydberg series of the fermionic isotopes.

5.2.2. Experimental Setup

To test the applicability of the theoretical models sketched in section 5.2.1, we performed high-resolution two-photon spectroscopy of Rydberg states in ultracold Yb. The experimental apparatus used in this work is based on the setup described in Ref. [56], with the main modification that Rydberg-state detection is performed via field ionization instead of trap-loss spectroscopy. An overview of the apparatus is shown in figure 5.6. A beam

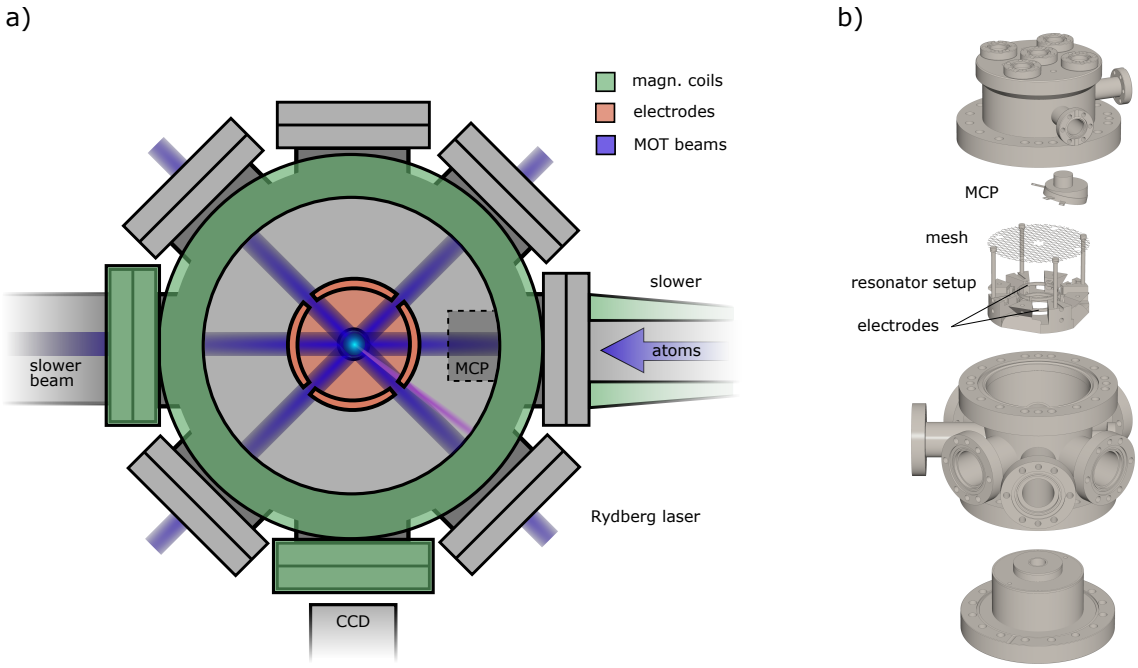

Figure 5.6.: (a) Top view of the experimental chamber showing the cooling laser beams at 389.9 nm, the Rydberg excitation laser beam near 394 nm, and the microchannel plate detector for ionized Rydberg atoms. Electrodes used for background field compensation and ionization are indicated in orange. (b) Exploded view of the electrode and detection assembly. The electrode structure consists of a base electrode below the atom cloud and segmented ring electrodes above. The distance between the base and the ring electrodes is 8 mm, with a ring diameter of 37 mm. A grounded mesh is placed 60 mm above the atom cloud to shield it from the MCP's electric field, located 120 mm above the atoms. A buildup resonator has been integrated into the setup for future experiments with optically trapped Rydberg atoms.

of ytterbium atoms produced by an effusive oven is first decelerated in a Zeeman slower and subsequently cooled and trapped in a magneto-optical trap. Both the Zeeman slower and the MOT operate on the strong $6s^2\,{}^1S_0 \rightarrow 6s6p\,{}^1P_1$ transition at 389.9 nm. For the fermionic isotopes ^{173}Yb (^{171}Yb), transitions to the hyperfine levels $F = 7/2$ ($F = 3/2$) of the $6s6p\,{}^1P_1$ state are used for cooling and trapping (see figure 5.7).

To prepare an ensemble of 10^6 to 10^7 Yb atoms with a temperature in the millikelvin range, atoms are loaded into the MOT for approximately 3.5 s. The peak atomic density in the MOT is well below $10^{10}\,\mathrm{cm}^{-3}$ for all isotopes, ensuring that interatomic interactions do not influence the Rydberg excitation process.

Spectroscopy of Rydberg states is performed in the MOT using a two-photon excitation scheme from the $6s^2\,{}^1S_0$ ground state via the intermediate $6s6p\,{}^1P_1$ level. The first photon is provided by the MOT laser at 389.9 nm, while the second photon originates from a

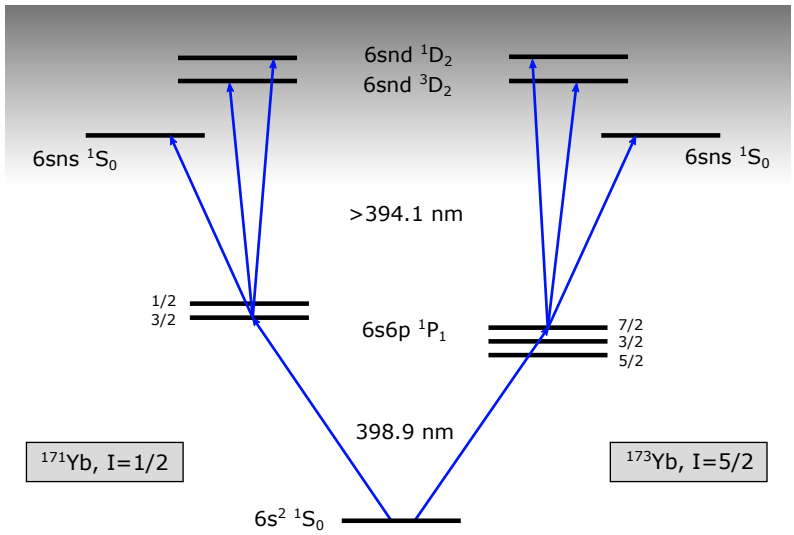

Figure 5.7.: Rydberg excitation scheme for the fermionic isotopes ^{173}Yb and ^{171}Yb. The cooling transition from $6s^2\,{}^1S_0$ to $6s6p\,{}^1P_1$ and the two-photon transitions to the Rydberg $6sns\,{}^1S_0$ and $6snd\,{}^{1,3}D_2$ states are indicated with their respective wavelengths. For bosonic isotopes, the same scheme applies but without hyperfine structure in the $6s6p\,{}^1P_1$ state.

separate laser beam used for Rydberg excitation. This laser is an amplified and frequency-doubled *Toptica DLpro* operating near 394 nm, which can be tuned to access different $6sns\,{}^1S_0$ and $6snd\,{}^{1,3}D_2$ states starting from principal quantum numbers around $n = 30$. The excitation scheme for the fermionic isotopes is shown in figure 5.7.

After loading the MOT for 3.5 s, the atoms are exposed to 100 pulses of the Rydberg excitation laser, each 500 ns long with a pulse separation of 200 µs. Following each laser pulse, a sequence of high-voltage pulses is applied to the electrodes for field ionization and ion collection. A first pulse of 400 V and 180 ns duration, applied to the base electrode, ionizes the Rydberg atoms. A second pulse of 50 V and 4 µs duration accelerates the resulting ions toward the MCP, and a third pulse of 750 V and 1 µs duration is applied to the segment of the ring electrode opposite the MCP to deflect the ions for optimal collection. The timing sequence is adjusted for maximal signal yielding a delay between ionization and acceleration of 330 ns, and a start of the deflection pulse 570 ns before the end of the acceleration phase.

The MCP is held at a constant voltage of −2.5 kV. A mesh with a 10 mm aperture positioned between the MCP and the atom cloud shields the atoms from stray electric fields while allowing ions to pass. The segmented ring and plate electrodes also enable active compensation of residual background fields in the interaction region, verified periodically by Stark-shift measurements [56]. Even for high-lying states ($n > 80$), the residual electric field corresponds to a Stark shift of only a few MHz.

Spectra of Rydberg transitions are obtained by scanning the frequency of the Rydberg excitation laser at a rate of typically 10 MHz per MOT cycle, while the MOT laser is held at a detuning of −20 MHz from the $6s^2\,{}^1S_0 \rightarrow 6s6p\,{}^1P_1$ transition. The absolute frequency of the Rydberg laser is calibrated to previously determined Rydberg transitions [56, 89] with an uncertainty better than 1 MHz per scan cycle, while the MOT laser frequency is stable within 5 MHz. When the sum of the two laser frequencies matches the energy of a Rydberg state, field-ionized atoms are detected by the MCP with typical count rates of a few ions per pulse, corresponding to several hundred counts per MOT cycle.

Changing the isotope under study is achieved by locking the MOT laser to the $6s^2\,{}^1S_0 \rightarrow 6s6p\,{}^1P_1$ transition of the desired isotope and updating the isotope reference in the wavemeter software. Prior to each measurement, the wavemeter is calibrated against the $6sns\,{}^1S_0$ Rydberg transition of ^{174}Yb using the reference data from Ref. [89], improving absolute frequency accuracy across isotopes.

5.2.3. Results and Discussion

In this section, we present and analyze experimental results on the excitation energies of singly-excited S- and D-type Rydberg states of the bosonic isotopes ^{172}Yb, ^{174}Yb, and ^{176}Yb, as well as of the fermionic isotopes ^{171}Yb and ^{173}Yb, covering principal quantum numbers in the range $35 \leqslant n \leqslant 80$. Our investigations focus on isotope-dependent effects and deviations from SQDT predictions. To obtain a general overview of the spectral evolution, frequency intervals corresponding to steps of approximately $\Delta n \approx 5$ were scanned.

5.2.3.1. Bosonic Isotopes

Spectra of transitions to $6sns\,{}^1S_0$ of the bosonic isotopes (which all have a vanishing nuclear spin $I = 0$) are shown in figure 5.8. Excitation frequencies are given relative to those of the corresponding states of the most abundant isotope, ^{174}Yb. During all measurements, the wavemeter was referenced to the $6s^2\,{}^1S_0 \rightarrow 6s6p\,{}^1P_1$ transition of the investigated isotope, yielding an estimated absolute frequency uncertainty for the two-photon transition of ≈ 70 MHz. To improve relative accuracy between the isotopes, the ^{174}Yb $6sns\,{}^1S_0$ transition frequencies were used as secondary references and compared to the high-precision data reported by Lehec et al. [89] leading to an error for the frequency differences of ≈ 30 MHz.

In each of the S-spectra (figure 5.8) only a single transition to a $^1S_0$ state is observed for each isotope though also $^3S_1$ states exist. This is due to the fact that our two photon excitation scheme via the intermediate $6s6p\,{}^1P_1$ state prevents the observation of transitions to $^3S_1$ since transitions between pure singlet and triplet states are forbidden. In the framework of a MQDT model this corresponds to the fact that there is no mixing between $^1S_0$ and $^3S_1$ channels due to unequal total angular momentum J.

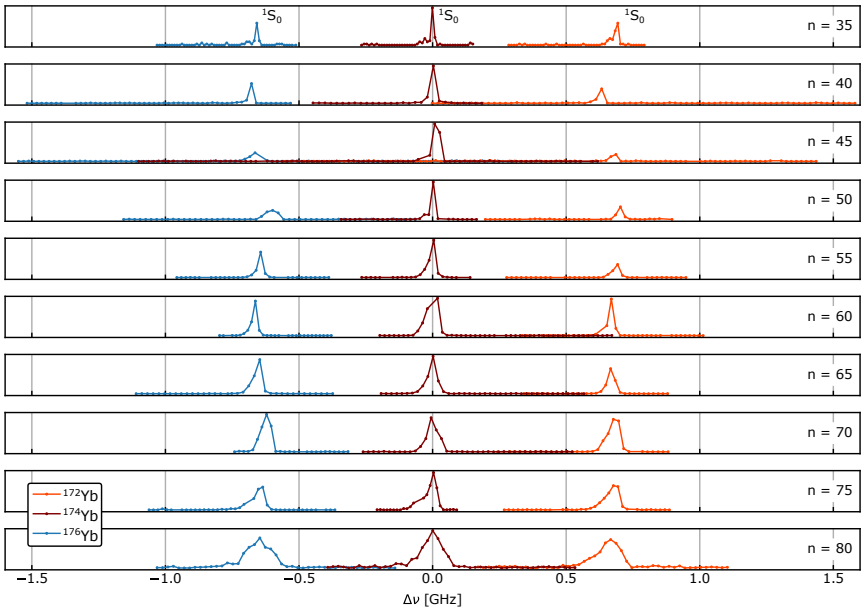

Figure 5.8.: Excitation spectra of $6sns\,^1S_0$ Rydberg states of bosonic Yb isotopes. Excitation frequencies are given relative to the corresponding transition in ^{174}Yb.

In figure 5.9, spectra of transitions to $6snd\,^1D_2$ and $6snd\,^3D_2$ Rydberg states of the bosonic isotopes are presented. While it is obvious that transitions to $^1D_2$ from the intermediate $6s6p\,^1P_1$ state are allowed if standard selection rules are applied, the excitation of $^3D_2$ states is only possible due to mixing of the $^1D_2$ and $^3D_2$ channels which both have a total angular momentum of $J = 2$. As already mentioned, this mixing leads to a modification of the wavefunctions [61] which is in turn responsible for the observation of transitions between nominal singlet ($6s6p\,^1P_1$) and triplet states ($6snd\,^3D_2$). Transitions to the other triplet Rydberg states, $6snd\,^3D_1$ and $6snd\,^3D_3$, are forbidden and are consequently not observed in the spectra presented here.

Within experimental uncertainty, the measured isotope shifts in the S-spectra as well as the D-spectra are found to be independent of the principal quantum number n. This behavior confirms that SQDT provides an adequate description for the state energies as long as all relevant channels converge to the same threshold corresponding to the $6s\,^2S_{1/2}$ ground state of singly-ionized Yb^+ [7] and that in this case the excitation energies can be described by equation (5.7). This is true even for the D-states where an MQDT treatment is required to explain the observation of $6s6p\,^1P_1 \rightarrow 6snd\,^3D_2$ transitions. However, though mixing between $^1D_2$ and $^3D_2$ channels occurs the state energies are not changed since both channels converge to the same threshold corresponding to the $6s\,^2S_{1/2}$ ground state of singly-ionized Yb^+ [7].

The isotope shift $\Delta E_i(^X\mathrm{Yb}, ^Y\mathrm{Yb})$ between the isotopes ^{X}Yb and ^{Y}Yb can therefore be

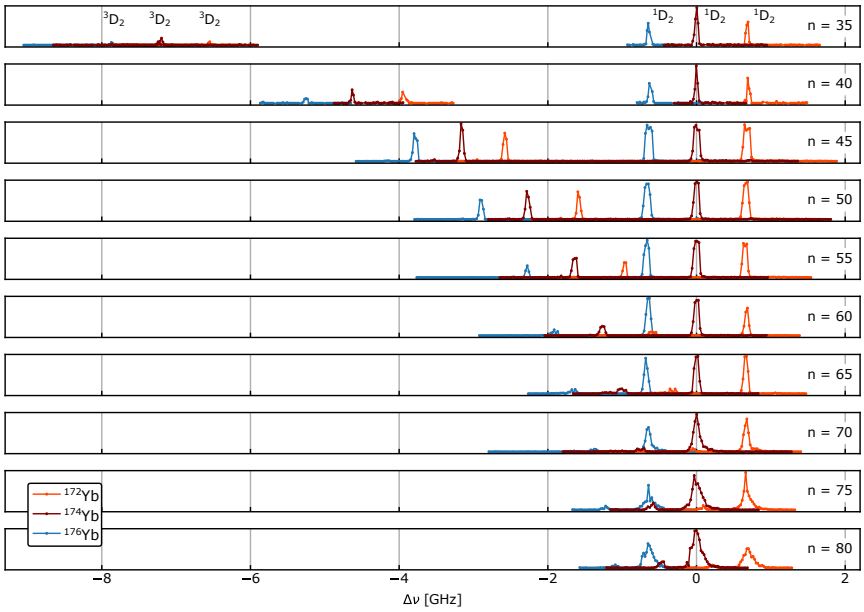

Figure 5.9.: Excitation spectra of singlet $6snd\,^1D_2$ and triplet $6snd\,^3D_2$ Rydberg states of bosonic Yb isotopes. Frequencies are given relative to the singlet-state transition in ^{174}Yb.

approximated by

$$\Delta E_i(^X\mathrm{Yb}, ^Y\mathrm{Yb}) = I_{6s}(^X\mathrm{Yb}) - I_{6s}(^Y\mathrm{Yb}) - \frac{R_X - R_Y}{(n-\mu_i)^2}\,, \tag{5.8}$$

where the difference $R_X - R_Y$ between the reduced Rydberg constants is small (about 120 MHz for isotopes with nucleon numbers differing by two). The contribution of the last term in equation (5.8) is further suppressed by the factor $(n-\mu_i)^{-2}$, resulting in an isotope-dependent contribution below 1 MHz for $n > 30$. Consequently, the measured energy differences essentially reflect the isotope shifts of the ionization energies.

Table 5.2.: Averaged isotope shifts of the bosonic Yb isotopes relative to ^{174}Yb in GHz. The measurement error for all values is ≈ 30 MHz.

Series	^{172}Yb	^{176}Yb
$6sns\,^1S_0$	0.673	-0.651
$6snd\,^1D_2$	0.674	-0.651
$6snd\,^3D_2$	0.672	-0.629

In table 5.2 the averaged isotope shifts relative to ^{174}Yb are listed, derived from the $6sns\,^1S_0$, $6snd\,^1D_2$, and $6snd\,^3D_2$ series. The excellent agreement between the different Rydberg series demonstrates the isotope independence of the quantum defect and the

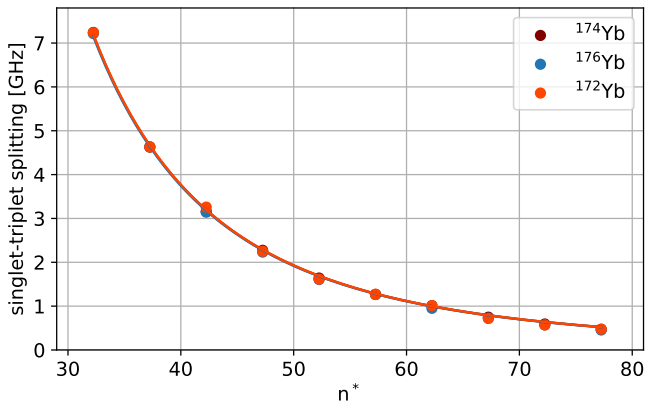

Figure 5.10.: Splitting between the $6snd\,^1D_2$ and $6snd\,^3D_2$ Rydberg states for ^{172}Yb, ^{174}Yb, and ^{176}Yb. The solid lines are fits of the form $a\,(n^*)^b$.

consistency of our measurement procedure.

The measured energy differences are plotted in figure 5.10 as a function of the effective principal quantum number $n^* = n - \mu_i$ where n^* refers to the effective principle quantum number of the corresponding triplet state and μ_i is the asymptotic quantum defect $\mu_i = 2.748627$ of the ^3D-series. The solid lines in figure 5.10 represent fits of the form $a\,(n^*)^b$ and the resulting fit coefficients are listed in table 5.3. Within experimental uncertainties the fit coefficients are isotope-independent and the fitted exponent b is close to the expected value $b = -3$ confirming the validity of an SQDT approach to describe the D-Rydberg series of the bosonic ytterbium isotopes.

Table 5.3.: Fit coefficients corresponding to fits of the form $a\,(n^*)^b$ to the fine-structure splitting presented in figure 5.9.

isotope	a [GHz]	b
^{172}Yb	296(29)	-3.06(2)
^{174}Yb	299(17)	-3.06(3)
^{176}Yb	331(17)	-3.09(1)

5.2.3.2. Fermionic Isotopes

Experimental spectra of transitions to Rydberg states in the fermionic isotopes ^{171}Yb and ^{173}Yb are shown in figure 5.11-figure 5.14. While our data for ^{171}Yb mainly confirm the results of Ref. [7], the spectra for ^{173}Yb represent to our knowledge the first extensive experimental study of Rydberg states in this isotope. In all figures, excitation energies are

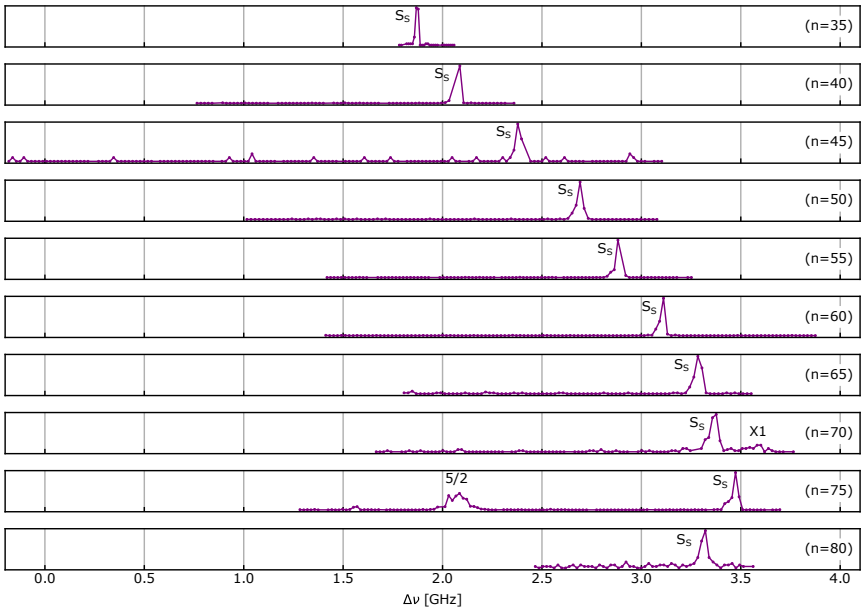

Figure 5.11.: S-Spectra of Rydberg states of fermionic ^{171}Yb. The observed lines labeled S_S correspond to singlet connected states. The line labeled $X1$ is unassigned while the line labeled $5/2$ corresponds to a D-state with $F = 5/2$. Excitation energies are given relative to the corresponding $6sns\,^1S_0$ state of ^{174}Yb.

given relative to the corresponding ^{174}Yb singlet state and the scans are labeled by the principal quantum number and angular momentum of the reference transition in ^{174}Yb. However, in figure 5.11-figure 5.14 not only the lines belonging to the target series as indicated by the scan label are observed but also additional lines which have been identified as belonging to other series or remain unassigned (labeled as X).

For ^{171}Yb, the S-states labeled S_S in figure 5.11 are identified as corresponding to the "singlet connected" levels, following the notation of Ref. [7]. The total angular momentum of the S_S series including nuclear spin is $F = 1/2$. In contrast to the bosonic isotopes, the isotope shift of the excitation energy exhibits a clear dependence on the principal quantum number n, indicating that SQDT cannot explain the observed behavior. The deviation arises from the hyperfine interaction, which strongly mixes singlet and triplet series. This is due to the fact that ^{171}Yb possesses a nuclear spin $I_{171} = 1/2$ leading to hyperfine splitting in the $6s\,^2S_{1/2}$ ground state of singly-ionized Yb^+ and thus to two energetically separated thresholds for the Rydberg series [7]. In ^{171}Yb, an avoided crossing of the S_S series is predicted around $n^* \approx 80$ [7], consistent with the onset of the observed shift reversal around $n \approx 75$ in figure 5.11.

While the S-spectra of ^{171}Yb mostly contain only a single line similar to the corresponding spectra in the bosonic isotopes, the D-spectra in figure 5.12 exhibit a much richer structure. The reason is that the nuclear spin $I_{171} = 1/2$ not only leads to two distinct

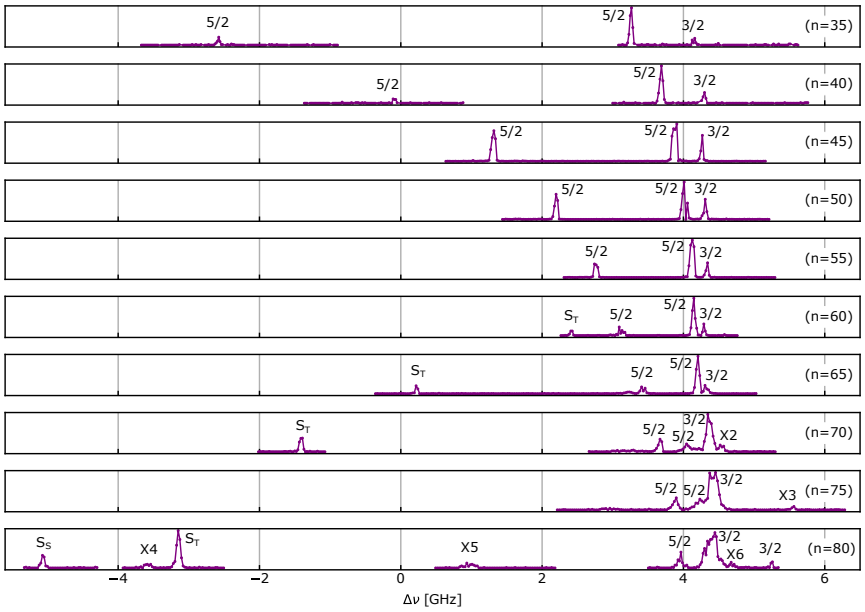

Figure 5.12.: D-Spectra of Rydberg states of fermionic ^{171}Yb. D-States are labeled by their total angular momentum F, singlet connected S-states by S_S and triplet connected S-states by S_T. Additional unassigned lines are labeled $X3 - X6$. Excitation energies are given relative to the corresponding $6snd\,^1D_2$ state of ^{174}Yb.

thresholds for the Rydberg series but also to hyperfine splitting of the Rydberg states themselves.

In general, there are four possible values for the total angular momentum of the D-states in ^{171}Yb ($F = 1/2, 3/2, 5/2, 7/2$). However, only states with $F = 3/2$ and $F = 5/2$ acquire singlet character and can thus be observed in our two-photon excitation scheme using the $6s6p\,^1P_1$ intermediate state. In figure 5.12 the lines that have been identified using the results of Ref. [7] are labeled with the corresponding total angular momentum. The agreement between our results and the MQDT model-based results of Peper et al. [7] is excellent (see Appendix). In addition to lines corresponding to D-states one singlet connected S-state (labeled S_S) and several lines corresponding to triplet-connected S-states with total angular momentum $F = 1/2$ (labeled S_T) are observed in figure 5.12. Triplet connected S-states with total angular momentum $F = 3/2$ cannot be observed with our excitation scheme since they do not acquire a singlet contribution. A few additional weak lines that cannot be assigned are labeled $X3 - X6$.

While our results for ^{171}Yb can be directly compared to the results of Ref. [7] there is no such possibility for ^{173}Yb. On the one hand there are to our knowledge no comparable experimental data available for this isotope and on the other hand the larger nuclear spin of $I_{173} = 5/2$ makes an MQDT model even more challenging. Nevertheless, it is possible to give a preliminary interpretation of the spectra shown in figure 5.13 and figure 5.14 by

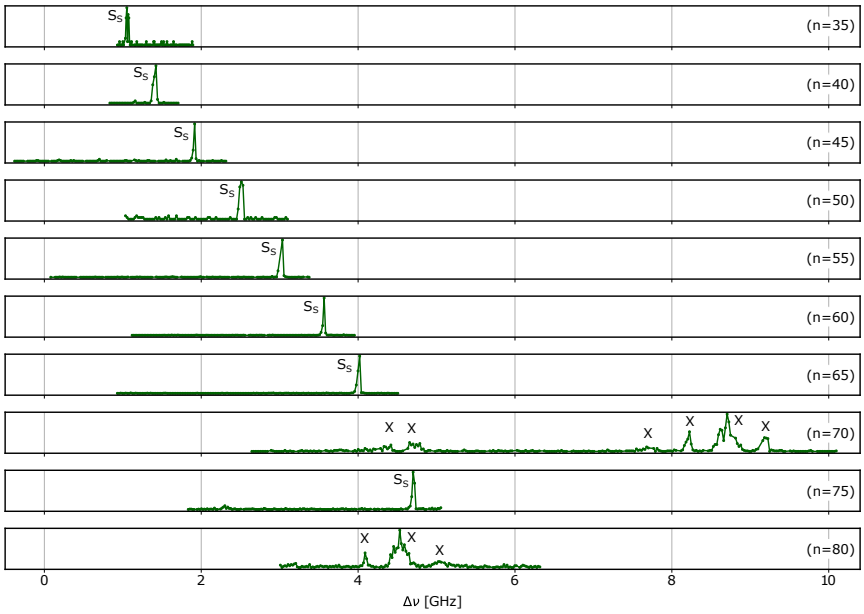

Figure 5.13.: S-Spectra of Rydberg states of fermionic ^{173}Yb. The observed lines labeled S_S are attributed to singlet connected states. The lines labeled X cannot be attributed to a specific Rydberg series. Excitation energies are given relative to the corresponding $6sns\,^1S_0$ state of ^{174}Yb.

comparing them to the spectra for ^{171}Yb.

For the S-states, the situation in ^{173}Yb is very similar to ^{171}Yb. There is one singlet connected state with $F = 5/2$ while there are now three triplet connected states with $F = 3/2, 5/2, 7/2$. In figure 5.13 the lines labeled S_S are attributed to the singlet connected S-state while for the lines labeled X an attribution is not obvious. Like in ^{171}Yb an avoided crossing seems to occur around $n \approx 75$. Of the triplet connected states, only the one with $F = 5/2$ acquires singlet character and can thus be accessed using our two-photon excitation scheme. By comparison with the results for ^{171}Yb we attribute the lines labeled S_T in figure 5.14 to these triplet connected states.

In the D-manifolds of ^{173}Yb, six different values for the total angular momentum are possible ($F = 1/2$ to $F = 11/2$) from which only four ($F = 3/2, 5/2, 7/2, 9/2$) acquire singlet character by channel mixing. Since the total angular momentum of the intermediate $6s6p\,^1P_1$ state of our two-photon excitation scheme is $F = 7/2$ only three of those ($F = 5/2, 7/2, 9/2$) can be in principle accessed. For these total angular momentum quantum numbers four (for $F = 5/2, 7/2$) or three (for $F = 9/2$) states are formed by channel mixing in each manifold and thus up to eleven lines are expected for each principal quantum number n.

In figure 5.14 eight lines are attributed to D-states which come in groups of four (highlighted in the inset o figure 5.14) which are labeled $B_1 - B_4$ and $C_1 - C_4$, respectively. At

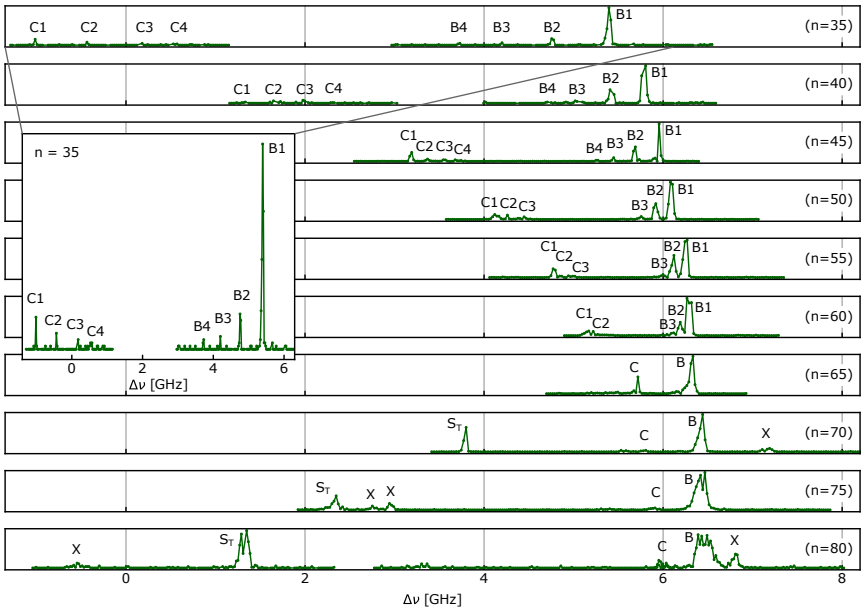

Figure 5.14.: D-Spectra of Rydberg states of fermionic ^{173}Yb. Owing to the complex level structure induced by the large nuclear angular momentum, the lines cannot be precisely assigned. However, lines labeled B and C are attributed to D-states while lines labeled S_T are most likely corresponding to "triplet connected" S-states. The lines labeled X cannot be attributed to a specific Rydberg series. Excitation energies are given relative to the corresponding $6snd\,^1D_2$ state of ^{174}Yb.

high principal quantum number both groups converge to a single line each. Considering the symmetry of states in the D-manifold of ^{173}Yb it seems appropriate to identify these two groups as belonging to a total angular momentum of $F = 5/2$ and $F = 7/2$. However it is not yet clear if this attribution is correct and why three of the accessible states (which would then be attributed to $F = 9/2$) are not observed. An extension of the MQDT model of Ref. [7] which we plan to carry out should help to clarify the attribution of the observed lines.

5.2.4. Summary

In conclusion, we have conducted a comprehensive experimental investigation of the energy spectra of Rydberg $6sns\,^1S_0$, $6snd\,^1D_2$, and $6snd\,^3D_2$ states in the range $35 \leqslant n \leqslant 80$ for five ytterbium isotopes. For the bosonic isotopes, ^{172}Yb, ^{174}Yb, and ^{176}Yb, isotope shifts of the ionization energies were determined under the assumption that single-channel quantum defect theory remains valid throughout the investigated range. The observed isotope shifts are independent of the principal quantum number confirming the applicability of SQDT and the negligible influence of configuration interaction in these systems.

For the fermionic isotopes, ^{171}Yb ($I = 1/2$) and ^{173}Yb ($I = 5/2$), hyperfine interac-

tions give rise to significant singlet-triplet mixing and complex level structures that cannot be described by SQDT alone. For ^{171}Yb, our results confirm the experimental and theoretical findings reported in Ref. [7], obtained through a combination of high-resolution spectroscopy and multichannel quantum defect theory. For ^{173}Yb, we report, to the best of our knowledge, the first systematic measurements of highly excited Rydberg states, revealing an even richer hyperfine-resolved structure.

Our results provide a comprehensive set of experimental reference data for Rydberg states of multiple Yb isotopes and form a solid basis for future modeling using multichannel quantum defect theory to extract the underlying channel couplings and to provide a consistent theoretical description of all isotopes.

5.3. Lifetime Measurements of Rydberg States

In this section, experimental investigations of Rydberg state lifetimes are presented for ^{174}Yb. These measurements are compared with theoretical predictions and thus allow to assess the influence of black-body radiation (BBR).

Compared to earlier studies on the lifetime of the bosonic isotope ^{174}Yb reported already in [1], the present experiments benefit from a significantly improved repetition rate of the experiment. This enhancement is enabled by the implementation of a newly developed frequency stabilization system based on a STCL architecture, as described in section 3.3.3.

5.3.1. Theoretical Description of Rydberg State Lifetimes

The natural lifetime of an atomic state is fundamentally limited by spontaneous decay to energetically lower-lying states. In the idealized, unperturbed case, this process is governed solely by dipole-allowed radiative transitions. "Unperturbed" in this context refers to conditions where external influences such as collisions with background gas atoms, interatomic interactions, and thermal radiation are effectively suppressed. Three conditions have to be fulfilled to approach this idealized case experimentally. First, the residual gas pressure has to be sufficiently low. Second, the atomic density also has to be able to neglect interactions between Rydberg atoms. Third, a perfectly perturbation-free environment would also imply a temperature of 0 K, eliminating any contributions from thermal photons, i.e., black-body radiation.

In the experimental setup considered here, we operate under high-vacuum conditions. Furthermore, due to the low atomic densities and short interaction times in the blue magneto-optical trap, Rydberg-Rydberg interactions are negligible and thus not considered in the lifetime modeling.

However, in our system the vacuum chamber is not cryogenically cooled and remains at ambient (room) temperature. Consequently, the surrounding environment emits a continuous spectrum of thermal radiation that can couple to the Rydberg manifold.

5.3.1.1. Natural Lifetime of Rydberg States

In the absence of external perturbations, the lifetime of an atomic state is calculated using the spontaneous decay rates of the initial state to energetically lower-lying states. For the spontaneous transition from an initial Rydberg state $|nl\rangle$ to a lower state $|n'l'\rangle$ the decay rate is given by the Einstein A coefficient [18]

$$A_{n'l',nl} = \frac{4e^2\,\omega^3_{nl,n'l'}}{3\hbar c^3}\,\frac{l_{max}}{2l+1}\,|\langle n'l'|\,r\,|nl\rangle\,|^2, \tag{5.9}$$

where $\omega_{nl,n'l'}$ is the transition frequency and the radial electric dipole matrix element is $|\langle n'l'|\,r\,|nl\rangle\,|$. The total decay rate of the initial state is obtained by summing over all energetically lower states that are dipole-coupled to the initial state

$$\Gamma_{nl} = \sum_{n'l'} A_{n'l',nl}, \tag{5.10}$$

which leads to the natural lifetime of the Rydberg state given by

$$\tau_{nl} = \frac{1}{\Gamma_{nl}} = \left[\sum_{n'l'} A_{n'l',nl} \right]^{-1}. \tag{5.11}$$

While the dipole matrix elements between neighboring states, i.e. states with similar principal quantum numbers n and n', tend to be large, the total decay is nevertheless dominated by transitions to low-lying states due to the strong frequency dependence $\omega^3_{nl,n'l'}$ in the Einstein coefficient (equation (5.9)).

The scaling behavior of the lifetime with respect to the quantum number n depends on the orbital angular momentum l. For low-l Rydberg states (such as s or p states with $\ell = 0$ and $\ell = 1$), the radiative lifetime scales as $\tau_{nl} \propto n^3$. In contrast, for high-l states approaching the circular limit $l = n - 1$, the lifetime increases significantly and follows $\tau_{nl} \propto n^5$. This scaling arises from both the dipole matrix element and the frequency dependence in the decay rate, as detailed in [18].

5.3.1.2. Black-Body Radiation

At finite temperatures, black-body radiation significantly perturbs the population dynamics of highly excited Rydberg states. In particular, the thermal radiation field induces transitions between neighboring Rydberg levels via stimulated absorption and emission processes. These transitions effectively shorten the observed lifetime compared to the idealized radiative lifetime governed purely by spontaneous decay.

The magnitude of BBR-induced depopulation increases with both the density of thermally populated photon modes and the transition dipole strength between adjacent levels. Due to the small level spacing and high dipole matrix elements in the Rydberg manifold, this effect becomes increasingly significant with increasing principal quantum number n.

To include BBR into a calculation of the Rydberg states lifetime we have to account for the mean photon occupation number in the modes of the thermal radiation field at temperature T which are given by the Bose-Einstein distribution [96]

$$\langle n(\nu) \rangle = \frac{1}{e^{h\nu/k_B T} - 1}, \tag{5.12}$$

where ν is the frequency of the mode, h is Planck's constant, and k_B is Boltzmann's constant. At room temperature, the photon occupation number in the frequency range corresponding to adjacent Rydberg transitions is several orders of magnitude higher than for optical transitions to the ground state. This was highlighted by Halter [1] and is additionally presented in [63].

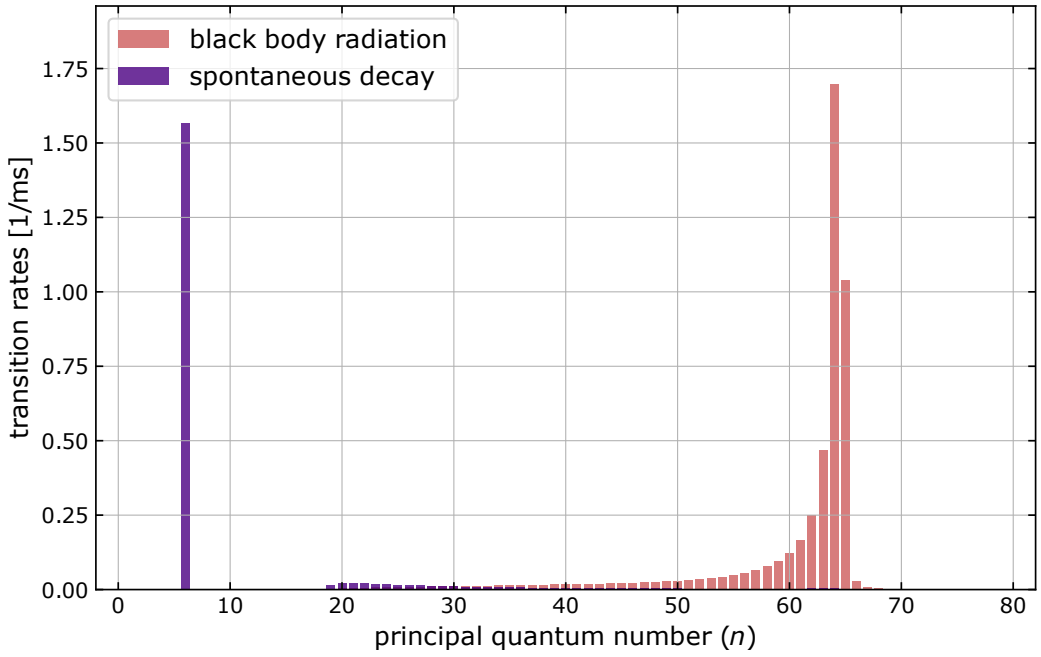

Figure 5.15.: Transition rates of the 65s Rydberg state of ^{174}Yb. Shown are the BBR-induced transition rates (pink) and the spontaneous decay rates (violet). The rates have been calculated for ^{174}Yb using the *PairInteraction* software [6]. Since the MQDT model used in the *PairInteraction* software does not yet account for all low-lying states, the spontaneous decay rates are incomplete.

Generally, the BBR-induced transition rate from an initial state $|nl\rangle$ to a final state $|n'l'\rangle$ can be written as the product of the spontaneous decay rate (equation (5.9)) and the mean photon number (equation (5.12)) [63]

$$K^{\mathrm{BBR}}_{n'l',nl} = \langle n(\nu_{nl,n'l'})\rangle \cdot A_{n'l',nl}. \tag{5.13}$$

Summing over all dipole-allowed final states yields the total BBR-induced depopulation rate of the initial Rydberg state

$$\Gamma^{\mathrm{BBR}}_{nl} = \sum_{n'l'} \langle n(\nu_{nl,n'l'})\rangle \cdot A_{n'l',nl} = \sum_{n'l'} \frac{A_{n'l',nl}}{e^{h\nu_{nl,n'l'}/k_BT} - 1}. \tag{5.14}$$

Accordingly, the effective BBR-limited lifetime becomes

$$\tau^{\mathrm{BBR}}_{nl} = \left[\sum_{n'l'} \frac{A_{n'l',nl}}{e^{h\nu_{nl,n'l'}/k_BT} - 1} \right]^{-1}. \tag{5.15}$$

Simulation results obtained using the *PairInteraction* software package [6] confirm that the BBR-induced transition rates between neighboring Rydberg states are often comparable in magnitude to the spontaneous decay rate to the ground state. These results are shown in figure 5.15 for the 65 s state as an example.

Thus, for accurate modeling of Rydberg state lifetimes in thermal environments, especially at room temperature, it is essential to include both contributions. The total effective lifetime is then given by

$$\frac{1}{\tau_{nl}^{\text{eff}}} = \frac{1}{\tau_{nl}} + \frac{1}{\tau_{nl}^{\text{BBR}}}, \tag{5.16}$$

where τ_{nl} is the natural (spontaneous) radiative lifetime and τ_{nl}^{BBR} accounts for BBR-induced transitions.

5.3.2. Experimental Procedure

To measure the lifetime of an atomic Rydberg state, the experimental sequence described in section 4.1 is employed with a minor yet important modification: a variable delay is introduced between the Rydberg excitation and the ionization pulse, as illustrated in figure 5.16.

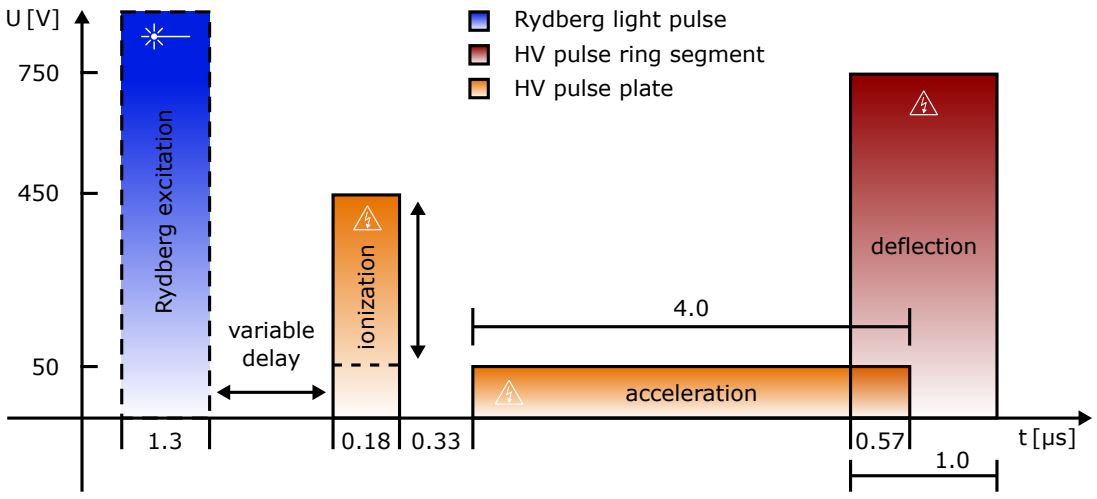

Figure 5.16.: Timing diagram of the pulse sequence used for the lifetime measurement. The variable delay between the Rydberg excitation and the HV ionization pulse allows for measurements of the atomic decay by observing the reduction in ion signal as a function of delay time. Adapted and extended from [1].

By scanning the delay time and recording the corresponding ion counts, an exponentially decaying signal is observed, reflecting decay of the Rydberg population. Exemplary measurements for the Rydberg states 65 s and 55 s are shown in figure 5.17. The data are well described by single-exponential fits without offset, yielding lifetimes of (93 ± 13) µs and (70 ± 8) µs, respectively.

It is important to note that the black-body radiation leads to significant population redistribution among neighboring Rydberg states, such that atoms initially prepared in a

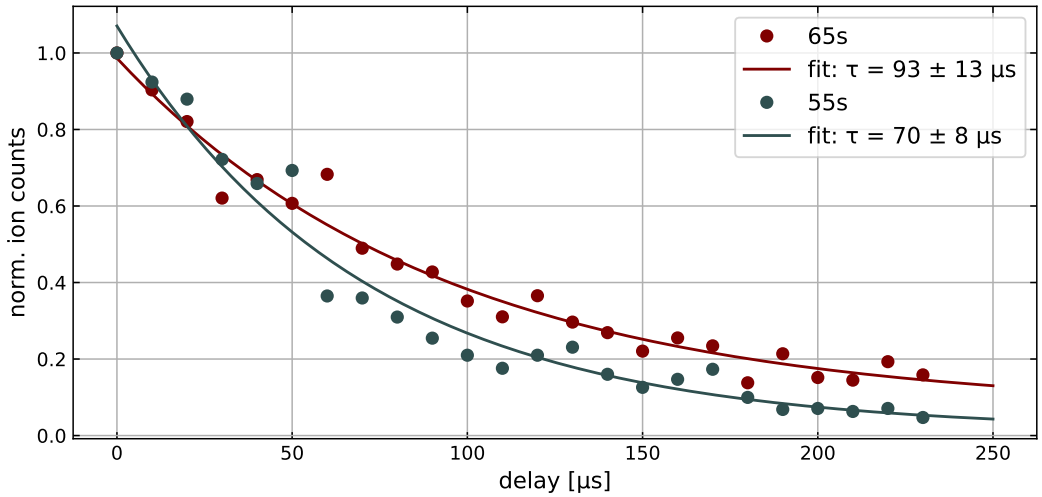

Figure 5.17.: Lifetime measurements of the Rydberg states 65 s and 55 s. The normalized ion signal is plotted as a function of the delay between the excitation and the ionization pulse. Solid lines represent exponential fits to the data.

specific target state are transferred to adjacent Rydberg states on microsecond timescales. Consequently, the BBR-limited lifetime should be understood as the effective lifetime of the entire ensemble of Rydberg states populated by BBR, rather than the intrinsic lifetime of the target state alone. In our detection scheme using electric field ionization, these BBR-induced transfers contribute to the observed signal.

5.3.3. Measurement Results for Rydberg Lifetimes

Following the procedure outlined above, the lifetimes of various states of different isotopes can be determined. Measured lifetimes of the S-states of ^{174}Yb in the range $n = 35$ to 80 are presented in figure 5.18 (blue data points). The error bars were obtained by repeatedly measuring each individual state, calculating the mean, and representing the standard deviation as the uncertainty. For higher-lying states, the uncertainties increase due to their enhanced sensitivity to perturbations, such as residual electric fields.

The corresponding theoretical values, obtained using the *PairInteraction* software described above, are shown in red. It should be noted that not all spontaneous transition rates are yet included in the model – only those shown in figure 5.18. As the developers of the software are still in the process of implementing these contributions, the theoretical values should be considered as upper limits for the lifetimes. Including the transitions to all relevant low-lying states would reduce the calculated BBR-limited lifetimes, which would likely bring the theoretical predictions into even better agreement with our experimental results.

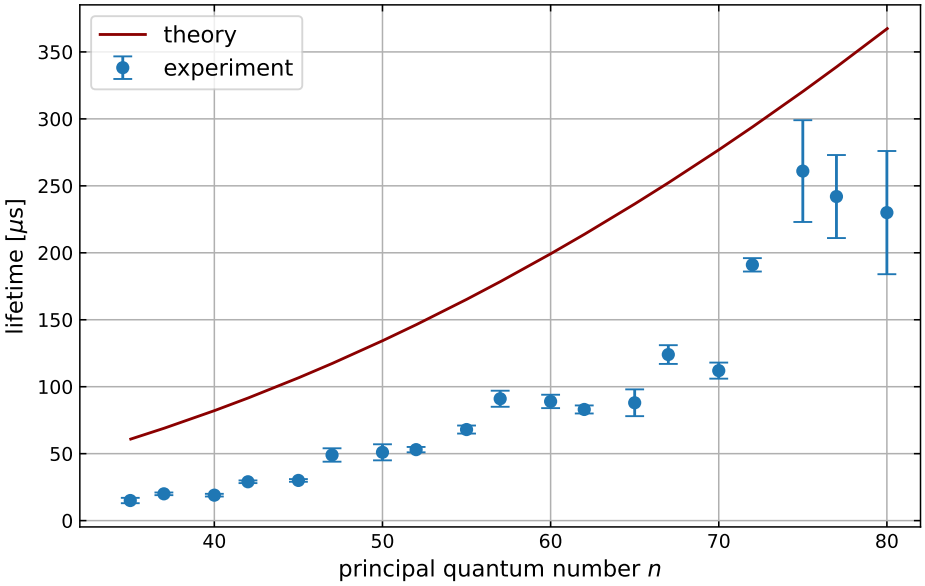

Figure 5.18.: Measured lifetimes of S-states of ^{174}Yb for effective principal quantum numbers $n = 35$–80. Experimental data are shown as blue points, with error bars obtained from exponential fits to the measured decay curves. At higher n, the uncertainties increase due to the increased sensitivity of the states to residual electric fields and other small perturbations. The theoretical lifetimes (red) are calculated using decay rates from the *PairInteraction* software [6].

6.

Rydberg-Rydberg Interactions

In the second part of this PhD project, the experimental apparatus described in chapter 3 was extended in order to enable the systematic investigation of interactions between Rydberg atoms. To this end, chapter 6 introduces the theoretical framework underlying several Rydberg-Rydberg interaction mechanisms. The experimental implementation of the extended setup within the two-stage magneto-optical trap is presented in chapter 7. Subsequently, the employed interaction detection strategies, as well as the current experimental status with respect to achievable atomic densities and interatomic separations, are discussed in chapter 8.

This chapter provides an overview of selected interaction types between Rydberg atoms, focusing on their underlying physical mechanisms, the conditions under which they arise, and their relevance for experiments. In particular, both resonant and non-resonant dipole-dipole interactions are discussed, along with interaction processes involving more than two atoms. The observable consequences of these interactions, most notably the Rydberg blockade effect, are presented and analyzed in the context of the experimental capabilities introduced in this work. Interactions between Rydberg atoms strongly depend on the specific electronic states involved, the mutual distance between the atoms, and external perturbations such as electric or magnetic fields.

The description in this chapter is based on the detailed discussions presented in [97–99].

6.1. Dipole-Dipole Interaction

Due to their strong electric transition dipole moments – especially for transitions between Rydberg states – Rydberg atoms are extremely sensitive to external electric fields. Moreover, the dipole moments associated with transitions between Rydberg states allow them to generate significant electric fields themselves that induce strong interactions with nearby atoms.

Depending on the energy structure of the involved Rydberg states, the interaction can be either resonant or non-resonant. In the resonant case, real dipole-dipole transitions occur between the atoms, which requires the participating states to satisfy an energy-matching

condition, as discussed in this chapter. On the other hand, non-resonant interactions arise from virtual transitions and manifest themselves as energy shifts (van der Waals interactions) without population transfer, making them comparatively easier to detect. Scalings and requirements for both types of interactions are discussed in the following sections.

In general, the electrostatic interaction between two point-like electric dipoles $\vec{d}_1$ and $\vec{d}_2$ separated by a vector $\vec{r}$ is given by the quantum-mechanical operator[97]

$$\hat{V}_{\mathrm{dd}} = \frac{1}{4\pi\varepsilon_0}\frac{1}{r^3}\left[\vec{d}_1 \cdot \vec{d}_2 - 3(\vec{d}_1 \cdot \hat{r})(\vec{d}_2 \cdot \hat{r})\right], \tag{6.1}$$

where $\hat{r} = \vec{r}/r$ is the unit vector along the separation axis.

6.1.1. Resonant Dipole-Dipole Interaction

A resonant or near-resonant dipole-dipole interaction occurs when two Rydberg atoms separated by a distance R, initially in the states $|r_1\rangle$ and $|r_2\rangle$, can coherently exchange their excitations, resulting in the atoms occupying the states $|r_3\rangle$ and $|r_4\rangle$

$$|r_1, r_2\rangle \longleftrightarrow |r_3, r_4\rangle . \tag{6.2}$$

This process is only energetically allowed when the Förster resonance condition is approximately fulfilled [100]

$$E_1 - E_3 \approx E_4 - E_2, \tag{6.3}$$

where E_i denotes the energy of state $|r_i\rangle$. If this condition is satisfied, the Förster defect $\Delta E = (E_3 + E_4) - (E_1 + E_2)$ is close to zero [98], and the process becomes resonant. In this regime, real population transfer between the two-atom states occurs via the dipole-dipole interaction, as illustrated in figure 6.1. In the most general case, this process involves four distinct states. When restricted to only two states in identical atomic systems, the interaction leads to an exchange of states between the two atoms.

The interaction strength for resonant processes is determined by the matrix elements of the dipole-dipole Hamiltonian, and the transition rate is directly related to the product of the transition dipole moments between the involved Rydberg states.

As the energy difference of the two state combinations yields $\Delta E \ll V_{dd}$ the potential V_{dd} can be used in first-order perturbation theory, because it couples nearly degenerate states. Using equation (6.1) the coupling strength V_{res} is then given by

$$V_{res} = \langle r_3 r_4 | \hat{V}_{\mathrm{dd}} | r_1 r_2 \rangle . \tag{6.4}$$

Using this equation one can calculate for dipole-allowed transitions the distance dependence of the coupling strength which is [99]

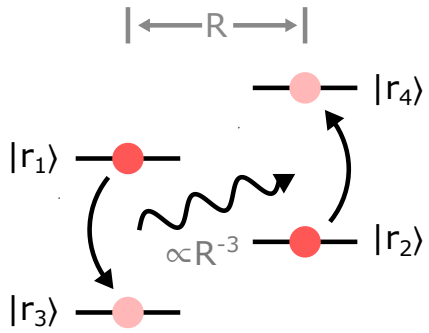

Figure 6.1.: Level scheme of interacting Rydberg states showing the general case of a resonant dipole-dipole interaction between two atoms in the states $|r_1\rangle$ and $|r_2\rangle$ at an interatomic separation R. This figure is based on the concept of [99].

$$V_{res} \sim \frac{d^2}{R^3} \sim \frac{\left(n^2 e a_0\right)^2}{R^3} = \frac{e^2 a_0^2 n^4}{R^3}, \tag{6.5}$$

resulting in a scaling of the resonant dipole-dipole interaction with the principal quantum number n and the atomic distance R as

$$V_{res} \sim \frac{n^4}{R^3}, \tag{6.6}$$

highlighting the strong increase of the interaction strength V_{res} for higher states and smaller inter-atomic distances.

Identifying suitable Förster resonances requires finding specific combinations of Rydberg levels that satisfy Eq. (6.3). In practice, this resonance condition can often be tuned by applying an external electric field, which shifts the Rydberg levels via the Stark effect (see section 2.2.1).

This tuning allows precise control over the interaction strength and character, making resonant dipole-dipole interactions a powerful tool for implementing quantum gates, creating entangled states, and studying coherent energy transport in strongly interacting Rydberg ensembles [101–103].

Nevertheless, identifying these resonant or near-resonant Rydberg transitions requires additional effort. Since we initially prepare both Rydberg atoms in the same state, the non-resonant dipole-dipole interaction, discussed in the next section, provides a natural starting point.

6.1.2. Non-resonant Dipole-Dipole Interaction

In this section, we focus on non-resonant Rydberg-Rydberg interactions, which arise from induced dipole-dipole couplings and lead to effective van der Waals potentials. These interactions play a role even in the absence of specific energy resonances and are thus always present when two atoms are sufficiently close. The non-resonant dipole-dipole

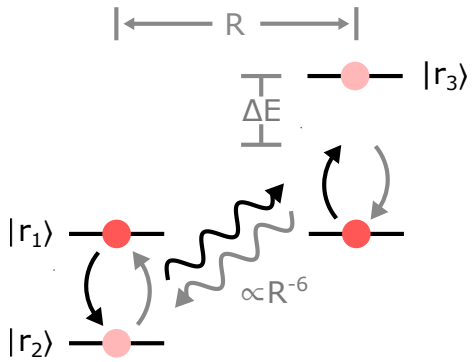

Figure 6.2.: Level scheme of interacting Rydberg states illustrating the off-resonant dipole-dipole interaction (van der Waals interaction). This figure is based on the concept of [99].

interaction can be derived using second-order perturbation theory applied to the dipole-dipole interaction Hamiltonian.

We consider two atoms at an interatomic distance R initially in the same Rydberg state $|r_1\rangle$, such that the unperturbed two-atom state is $|r_1, r_1\rangle$. The interaction between these atoms is assumed to be described by the dipole-dipole operator in equation (6.1).

Since the initial state $|r_1, r_1\rangle$ is not resonantly coupled to any final state, the dipole-dipole interaction cannot induce a real population transfer. However, transitions to other virtual pair states $|r_2, r_3\rangle$ are still possible (see figure 6.2. The rapid excitation to the virtual state, followed by its fast decay, results in a time-averaged energy shift of the initial state. Since the energy difference between the two sets of states is $\Delta E \gg V_{dd}$ in this case, there will be no energy shift in the first order.

In the second-order, the (van der Waals) energy shift can be written as

$$\Delta E_{\mathrm{vdW}} = \sum_k \frac{|\langle k|\hat{V}_{\mathrm{dd}}|r_1, r_1\rangle|^2}{E_{r_1,r_1} - E_k}, \tag{6.7}$$

where the sum runs over all intermediate two-atom states $|k\rangle = |r_i, r_j\rangle$, and $\Delta E_k = E_k - E_{r_1,r_1}$ is the energy difference between the initial state and an intermediate state.

If a single near-resonant intermediate state $|r_2, r_3\rangle$ dominates, the energy shift can be approximated as [104]

$$V_{\mathrm{vdW}}(R) \approx -\frac{|\langle r_2, r_3|\hat{V}_{\mathrm{dd}}|r_1, r_1\rangle|^2}{\Delta E} \propto -\frac{1}{R^6}. \tag{6.8}$$

This scaling results from the squared electric dipole matrix elements, leading to an effective van der Waals interaction potential of the form

$$V_{\mathrm{vdW}}(R) = -\frac{C_6}{R^6}. \tag{6.9}$$

For low-angular-momentum Rydberg states, which we consider here, C_6 typically scales with the principal quantum number as $C_6 \propto n^{11}$ (see table 1.2). This behavior arises from the rapid increase of the dipole matrix elements and the density of energy levels. As shown in equation (6.1), the dipole-dipole operator $\hat{V}_{\mathrm{dd}}$ is proportional to the square of the electric dipole moment $\vec{d}$, which itself scales as n^2 (see table 1.2). Consequently, the van der Waals interaction, being proportional to the square of $\hat{V}_{\mathrm{dd}}$, scales as $(n^2)^4 = n^8$, while the energy spacing between neighboring states scales as n^{-3}. Combining these factors yields a van der Waals coefficient $C_6 \sim n^{11}$. The resulting potential is long-ranged and always attractive when two atoms are sufficiently close.

Compared to resonant interactions, non-resonant processes are theoretically simpler to model and experimentally easier to control, as they do not require precise tuning of energy levels or the application of external electric fields. This makes them particularly suitable for initial characterization in a high-density MOT.

Furthermore, non-resonant interactions are responsible for fundamental effects such as the Rydberg blockade [100, 104] and therefore form a natural starting point for understanding and quantifying interatomic interactions in our system.

6.1.3. Additional Interactions in Rydberg Systems

In addition to the van der Waals and resonant dipole-dipole interaction further types of interactions can emerge, particularly in dense atomic ensembles or under specific geometrical and field conditions.

One such mechanism is the many-body interaction, which represents a non-trivial extension of the pairwise dipole-dipole interaction. In systems with sufficiently high atomic density, such as in single sites of an optical lattice or in tweezer arrays, the interatomic distances can become small enough that the excitation of a single atom affects not only its nearest neighbor, but also multiple surrounding atoms. In this case collective effects arise that require a genuine many-body treatment [105, 106]. One consequence in such a regime is the suppression of additional excitations in the vicinity of an already excited atom – a phenomenon known as Rydberg blockade, which will be discussed in detail in section 6.2.

Another class of special resonant interactions, mostly investigated in optical lattices is the exchange interaction, often referred to as "flip-flop process", as outlined in [107]. Here, two atoms in different Rydberg states coherently exchange their internal states through resonant dipole-dipole coupling. These interactions are inherently dependent on the relative orientation of the atomic dipole moments and the spatial arrangement of the atoms, making them highly anisotropic. Exchange processes are particularly relevant in the context of quantum spin models and coherent state transfer [107, 108].

So far we have neglected that Rydberg interactions can exhibit significant angular dependence, when atoms are excited to states with lower orbital symmetry, such as p-, d- or higher ℓ-states. In these cases, the interaction potential is no longer isotropic but varies

with the angle between the dipole orientation and the interatomic axis. This anisotropy can be exploited to engineer direction-dependent interactions, a feature that is particularly useful in the design of quantum simulators for lattice models with spatially varying couplings [109].

Under certain conditions, further interaction types may become relevant. For instance, charge-induced dipole interactions can arise in hybrid systems involving Rydberg atoms and ions or in the presence of background electric fields. Moreover, at larger distances or in high-angular-momentum states, quadrupole-quadrupole and other higher-order multipole interactions can contribute, albeit typically with reduced strength [110, 111].

Altogether, Rydberg interactions and significantly expand the possibilities for controlling and manipulating atomic ensembles. They can be used for accurately modeling many-body dynamics and for the realization of scalable quantum technologies based on Rydberg platforms.

6.2. Rydberg Blockade

The Rydberg blockade [100, 112, 113], arising from resonant or non-resonant interactions, can be described equivalently in two pictures: as an interaction-induced Stark shift of the excitation energies, or within a fully quantum-mechanical treatment based on the system Hamiltonian. We consider a situation where two atoms are close to each other and are illuminated by laser fields resonant with the ground-to-Rydberg transition. As illustrated in figure 6.3a), the excitation shall be driven by the two laser fields introduced in section 4.3. When one atom is promoted to a Rydberg state, the system is in the state $|r, g\rangle$ and a strong electric dipole moment is induced. Due to the large polarizability of Rydberg states, scaling with n^7 (see section 1.3), this dipole generates an electric field that shifts the energy levels of the neighboring atom, if the interatomic distance is sufficiently small. Consequently, the second atom is detuned from resonance and cannot be excited if $\Delta E_{\mathrm{vdW}} \geqslant \delta_E/2$ (see figure 6.3a), where δ_E is the linewidth of the Rydberg transition. This effect can be interpreted semiclassically as a Stark shift (see section 2.2.1), while in the quantum-mechanical picture it corresponds to an additional interaction term in the Hamiltonian, which modifies the eigenenergies of the two-atom system. In particular, the energy of the doubly excited state $|r, r\rangle$ is shifted by the interaction potential. As this shift depends on the interatomic distance, the influence is strong for high densities. The critical distance below which the interaction between neighboring atoms prevents simultaneous excitation is referred to as the Rydberg blockade radius R_b. The blockade radius is defined, as the distance for which the shift is larger than half of the excitation linewidth Γ_{exc} [114], which is in our case

$$R_b = \left(\frac{2C_6}{\Gamma_{\mathrm{exc}}}\right)^{1/6}. \tag{6.10}$$

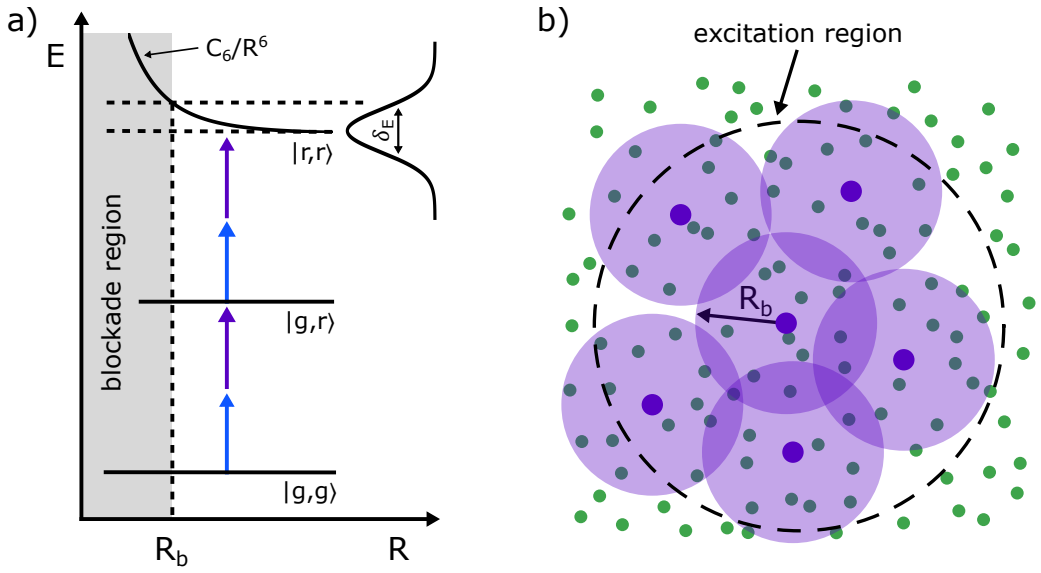

Figure 6.3.: Schematic illustration of the Rydberg blockade arising from the dipole-dipole interaction between neighboring Yb atoms. a) Energy-level diagram of two interacting atoms. For interatomic distances shorter than the blockade radius R_b, excitation of a second atom to a Rydberg state is suppressed due to the effective van der Waals potential scaling as C_6/R^6. The gray area indicates this blockade region. b) Effects of the Rydberg blockade in which only a limited number of atoms within the excitation volume can be promoted to Rydberg states, since additional excitations are suppressed inside the blockade radius. This figure is inspired by [115].

For interatomic distances larger than the blockade radius, this shift becomes negligible and excitations are again possible.

As shown in figure 6.3b, the blockade radius does not merely suppress the excitation of a single additional atom, but enforces a collective constraint that prevents multiple simultaneous excitations. Within the blockade sphere, no further atoms can be promoted to Rydberg states, effectively limiting the number of Rydberg excitations that can exist within the excitation volume. The Rydberg blockade is of central importance not only in fundamental research, where it provides unique insights into strongly interacting quantum systems, but also across a wide range of applications. It offers a robust mechanism for deterministic entanglement generation and thus constitutes a central building block for quantum information processing and quantum communication, as demonstrated in early experiments on two-qubit entanglement by Zhang et al. [116] and later in high-fidelity Bell-state generation by Maller et al. [117].

Beyond quantum gates, the blockade enables the realization of strongly correlated many-body states and the simulation of effective spin models with tunable long-range interactions [118]. Theoretical proposals and experimental progress in this direction include the

use of Rydberg-EIT systems for simulating correlated photons and spin Hamiltonians [119, 120], as well as the engineering of strongly correlated gases of Rydberg-dressed atoms [121].

7.

Implementation of the Two-Stage MOT

In order to study Rydberg-Rydberg interactions and to establish a basis for associated research fields, it is necessary to prepare atoms in a dense cloud. As discussed in this thesis (see section 7.3.2.1) and previously by C. Halter [1], the single-stage MOT operating on the broad $6s^2\,{}^1S_0 \rightarrow 6s6p\,{}^1P_1$ transition at 399 nm achieves densities corresponding to mean interatomic distances of approximately $R_{\mathrm{min}} \approx 10\,\mu\mathrm{m}$. According to simulations, interactions at this distance are expected to be negligible. Halter estimates that significant Rydberg-Rydberg interactions require interatomic separations on the order of $R_{\mathrm{min}} \leqslant 5\,\mu\mathrm{m}$. A refined analysis of the interaction stength that can be achieved in our experiment can be found in section 8.2.

To achieve such separations which correspond to atomic densities in the $10^{10}\,\mathrm{cm}^{-3}$ – $10^{11}\,\mathrm{cm}^{-3}$ range, the atomic cloud must be further compressed prior to Rydberg excitation, which is accomplished using a two-stage MOT scheme. In the first stage, atoms are loaded into a broad-linewidth MOT ${}^1S_0 \rightarrow {}^1P_1$ at 399 nm (similar to the one used in the spectroscopy experiments described in chapter 5). They are subsequently transferred to a second cooling stage at 556 nm, making use of the transition ${}^1S_0 \rightarrow {}^3P_1$ (see figure 1.1) whose natural linewidth is approximately narrower by a factor of 160. The narrow linewidth in the second-stage MOT restricts laser cooling and trapping to atoms very close to resonance, effectively reducing the capture volume. This tighter confinement increases the number of atoms within a smaller region, leading to a higher atomic density compared to a broad-linewidth MOT. Another important reason for the enhanced density in the green MOT is the low reabsorption rate of light emitted by the trapped atoms, resulting from the weak transition. Further compression in the narrow-line MOT significantly enhances the atomic density, establishing conditions favorable for the investigation of Rydberg-Rydberg interactions.

In this section the integration of the second stage MOT into our experimental apparatus is described. This includes the implementation of a new laser system for laser cooling in the second stage MOT which is described in section 7.1. The system includes a 1064 nm fiber laser and a 1112 nm fiber amplifier, discussed in detail in section 7.1.1 and section 7.1.2. The stabilization system is presented in section 7.1.3. Frequency doubling to the required

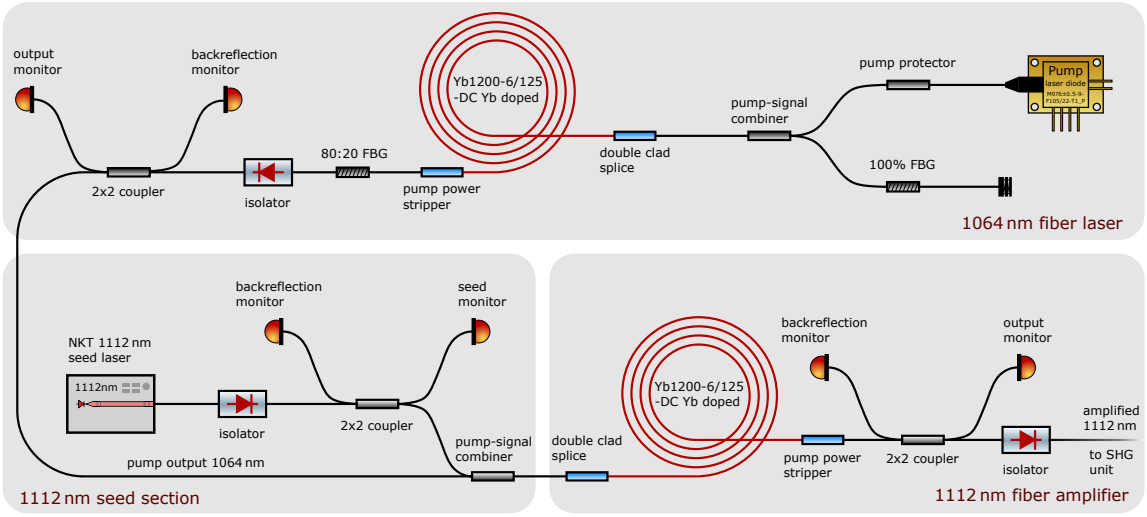

Figure 7.1.: Sketch of the home-built 1064 nm fiber laser, initially developed by E. Trede [123], and the 1112 nm fiber amplifier. The fiber laser is based on a 9 W pump laser diode at 976 nm, an active fiber, and fiber Bragg gratings. A commercial fiber laser serves as the seed source and is amplified to an output power exceeding 500 mW.

wavelength is achieved using a fiber-coupled nonlinear waveguide, described in section 7.1.4.

Following the description of the laser system, the integration of the green MOT laser system into the overall experimental sequence is outlined in section 7.2. This includes timing considerations, switching schemes, and synchronization with the preexisting MOT stages.

7.1. Green MOT Laser System

As the second part of the two-stage MOT, the green laser system operates on the ${}^1S_0 \rightarrow {}^3P_1$ intercombination transition at 555.8 nm. The system is based on a frequency-doubled and frequency-stabilized laser source at 1112 nm. To achieve this, a seed laser at 1112 nm is amplified using a fiber amplifier that is pumped by a laser at 1064 nm (see figure 7.1). The concept of this fiber amplifier is adapted from the work of Franzen et al. [122]. Building upon this idea, a custom fiber-based setup – comprising both the pump source and the amplifier – was initially developed by E. Trede [123]. However, the performance of the system was not yet sufficient for reliable use in the experiment, which necessitated further modifications. The pump diode was replaced, fiber splices were renewed, and the pump and amplifier sections were permanently connected via splicing.

7.1.1. 1064 nm Fiber Laser

A home-built 1064 nm fiber laser is used as the pump source for the amplifier. The laser system, which is sketched in figure 7.1 is based on three essential components: the new high-power pump diode[1] with an emission wavelength of 976 nm, the 5 m long (Yb1200-6/125-DC Yb doped) active fiber, and a resonator composed of two fiber Bragg gratings (FBG), described in the following. To protect the pump diode from harmful back reflections, a pump protector is employed. This passive component filters back-reflected light at 1064 nm. The pump light is coupled into the active fiber using a pump-signal combiner. Specialized splicing techniques are required to connect active and passive double cladding fibers; details on these procedures are available in [124]. The active fiber is doped with Yb^{3+} ions with optical transitions suitable for laser emission at 1064 nm. The pump light excites the ions to a higher energy level, followed by non-radiative relaxation and subsequent stimulated emission at the desired wavelength.

The laser resonator is formed by two FBGs. FBGs are fiber sections with a periodic modulation of the effective refractive index, enabling wavelength-selective reflection [125]. The reflection/transmission ratio can be tuned by adjusting the grating length and refractive index modulation depth. The first FBG, located before the active fiber (see figure 7.1), serves as a highly reflective mirror, reflecting nearly 100% of the incoming light in the signal input fiber; the small transmitted portion is dumped. The second FBG, placed after the active fiber, reflects 20% of the light back into the gain medium, while allowing 80% of the 1064 nm laser light to pass. A pump power stripper removes the residual pump light. This output is further guided through a fiber optic isolator to suppress back reflections into the laser cavity. The output then passes through a 2×2 coupler, which directs the laser beam toward the amplifier. Two monitor photodiodes are connected to the coupler for continuous monitoring both forward and backward power levels. These signals are integrated into the system's interlock mechanism, ensuring automatic shutdown in the event of excessive back reflection or undesired pulsed output above a set limit, thus protecting the laser system from damage. figure 7.2 a) shows the spectrum with the center wavelength of approximately 1063.8 nm (inset of the graph) and the current-power characteristic of the fiber laser. The laser threshold is approximately 0.65 A. Up to a power of 3.8 A, sporadic pulsing behavior is observed. To ensure stable continuous-wave operation and protect the laser, the system is operated at a current of 4.5 A, corresponding to a stable output power of 1.1 W. The measured slope efficiency is 0.28 W/A.

7.1.2. 1112 nm Fiber Amplifier

The fiber laser at 1064 nm described in the previous section is employed as the pump source for a 1112 nm fiber laser (also depicted in figure 7.1). An active fiber of approxi-

[1] M976±0.5-9-F105/22-T1-P

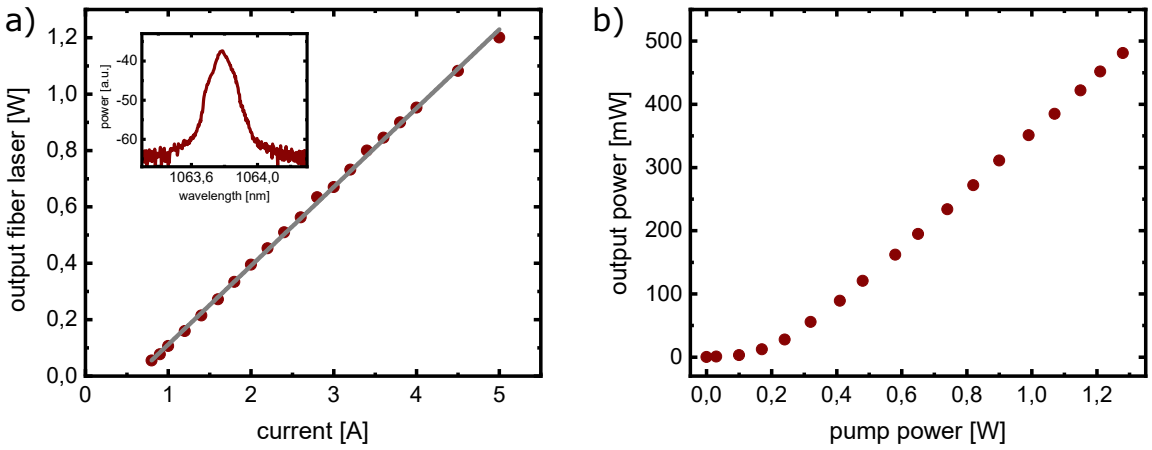

Figure 7.2.: a) Measured output power of the 1064 nm laser; the inset shows the optical spectrum. b) Output power of the 1112 nm amplifier.

mately 10.5 m length is used to generate the required power at that target wavelength. A commercial single-frequency *NKT* fiber laser[2] serves as the seed source. A 30 dB polarization independent (PI) isolator protects the seed laser from potential back reflections. The back reflection in the system and the seed signal are monitored using tow photodiodes connected to two ports of a 2×2 coupler. Pump and seed light are combined and injected into the active fiber using a pump-signal combiner. In this configuration, the Yb ions in the fiber are excited by the 1064 nm pump laser, allowing for stimulated emission at 1112 nm (see figure 7.2). Typically, Yb-doped fibers are pumped at 975 nm, where the absorption cross section is maximum. Pumping at this wavelength leads to strong amplified spontaneous emission (ASE) in the 1000 to 1060 nm range and a low gain at 1112 nm, necessitating multiple low-gain amplification stages and increasing susceptibility to photodarkening. The scheme developed in our group, using 1064 nm as the pump wavelength significantly suppresses unwanted gain outside the target wavelength. A detailed discussion can be found in [122].

The output from the active fiber requires further processing, as residual pump light must be removed from the desired 1112 nm laser signal using a pump power stripper. The amplified output and any back reflection are again monitored via photodiodes connected to the ports of an additional 2×2 coupler. To protect the system from feedback-induced damage, a second isolator – identical type to the first – is placed before the final output. The amplified 1112 nm output is then directed to both the frequency stabilization unit and the second-harmonic-generation stage, where frequency doubling to the target wavelength of 555.8 nm takes place.

[2] *NKT Photonics* Koheras ADJUSTIK

7.1.3. Frequency Stabilization using a Cavity Lock

Operating a green magneto-optical trap at 555.8 nm requires a highly stable laser frequency, typically narrower than the natural linewidth of the transition, which in this case is $\Gamma_{\text{green}} = 2\pi \times 182\,\text{kHz}$. In our system this is achieved by stabilizing the fundamental light at 1112 nm (see figure 7.3).

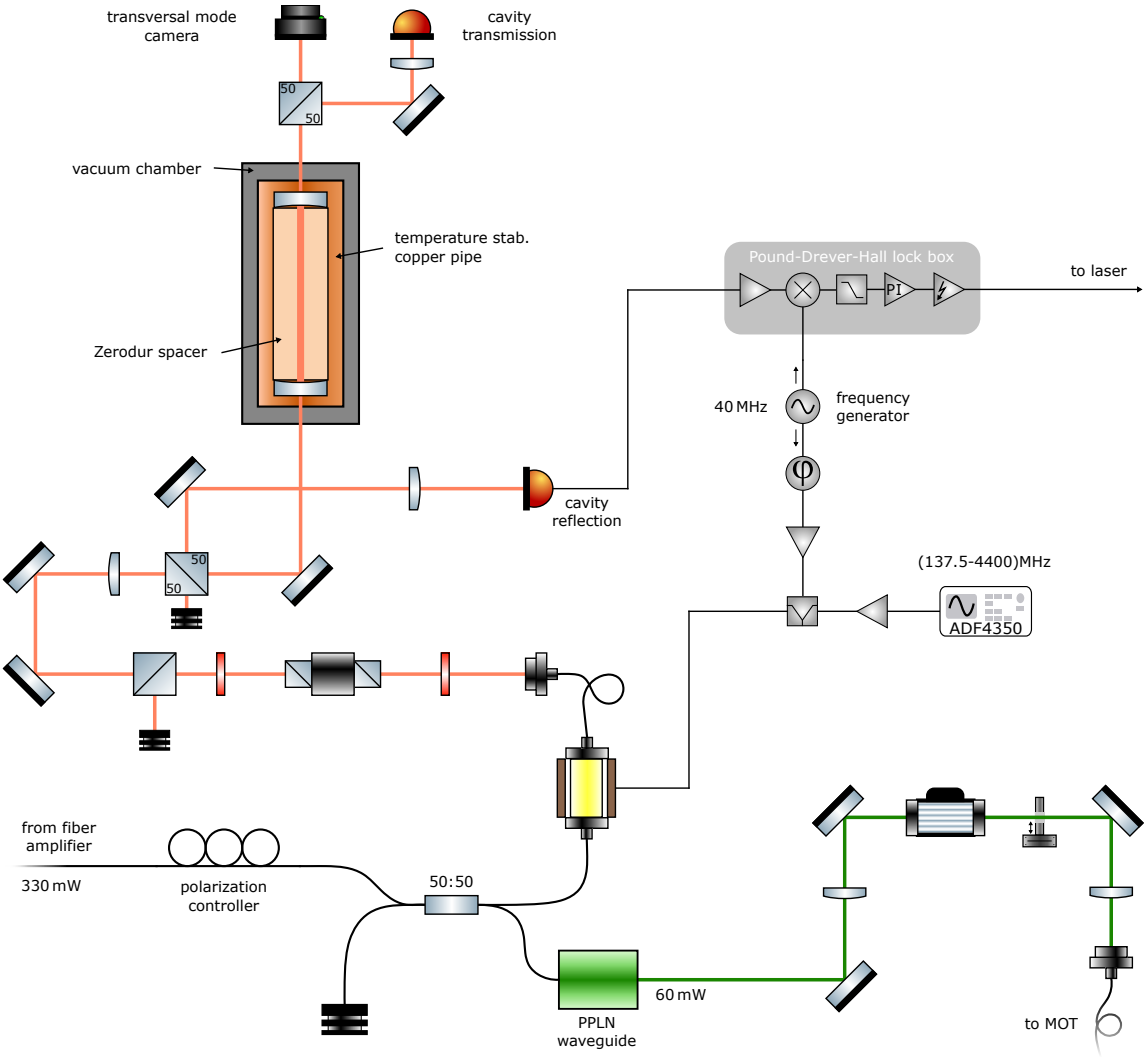

Figure 7.3.: Scheme of the setup for frequency stabilization and frequency doubling of the 1112 nm laser. At the top, the temperature-stabilized Zerodur® spacer cavity is shown, to which the 1112 nm laser is frequency-locked via an EOM. The frequency-doubled green light is guided to the MOT at the science table via a fiber and can be rapidly switched using an AOM.

The 1112 nm output of the fiber amplifier is split into two paths using a 2×2 coupler (TN1064R5A2A) functioning as a 50:50 fiber beam splitter[3]. The frequency stabilization is realized via the Pound-Drever-Hall (PDH) locking technique [126], by sending the output of one port of the 50 : 50 splitter to a highly stable reference cavity.

7.1.3.1. Intra-Vacuum Zerodur Cavity

The intra-vacuum cavity, which is used as a stable reference for the 1112 nm laser, consists of a temperature-stabilized Zerodur® spacer with a length of 105 mm, chosen for its low coefficient of thermal expansion (CTE), specified as $0 \pm 0.100 \times 10^{-6}\,\mathrm{K}^{-1}$[127]. The cavity mirrors with a reflectivity of 99.995 % at 1112 nm, yield a theoretical finesse of $\mathcal{F} = 60\,000$ and are bonded to the spacer using vacuum-compatible glue.

Long-term aging effects of the Zerodur®, as characterized in [128] result in a frequency drift of about 0.2 MHz per day, corresponding to a relative length change of $\Delta L/L = -3 \times 10^{-7}\,\mathrm{y}^{-1}$. In addition to this long-term drift, temperature-induced frequency shifts are also present. According to [85], the frequency shift due to temperature variations of the Zerodur® spacer is approximately 15 MHz/K.

The entire cavity assembly is contained within a copper cylinder, which is mounted on a temperature-stabilized copper base, serving as a thermal feedthrough into the vacuum chamber (see figure 7.3). The assembly is enclosed in a vacuum chamber to minimize environmental and thermal perturbations. This design follows the implementation described in [128]. In practice, a typical daily frequency drift of around 5 MHz is observed, which correlates with ambient laboratory temperature fluctuations. This drift is consistent with a temperature change of the spacer of about 0.3 K. This drift is routinely compensated by optimizing the performance of the green MOT.

7.1.3.2. Pound-Drever-Hall Lock

The temperature stabilized reference cavity is employed as the frequency reference required for PDH locking [126, 129, 130]. The upper section of figure 7.3 illustrates the experimental implementation of the lock. Phase modulation in the gigahertz range is applied to the 1112 nm light using a fiber-coupled electro-optic modulator (EOM)[4]. The modulation frequency is generated by a synthesizer board[5] in combination with a broadband amplifier.

In addition, a low-frequency signal at 40 MHz is generated using a commercial frequency generator. Both the high-frequency and the low-frequency signals are applied simultaneously to the EOM to create first- and second-order modulation sidebands (sidebands of

[3] Although less than half of the power is required for the locking path, the second-harmonic generation crystal has a maximum input power of 200 mW. Due to the threshold for pulsing of the fiber laser, reducing the total output power is not feasible.

[4] JENOPTIK Optical Systems GmbH, Phase Modulator PM1170

[5] Analog Devices, EVAL-ADF4350EB2Z

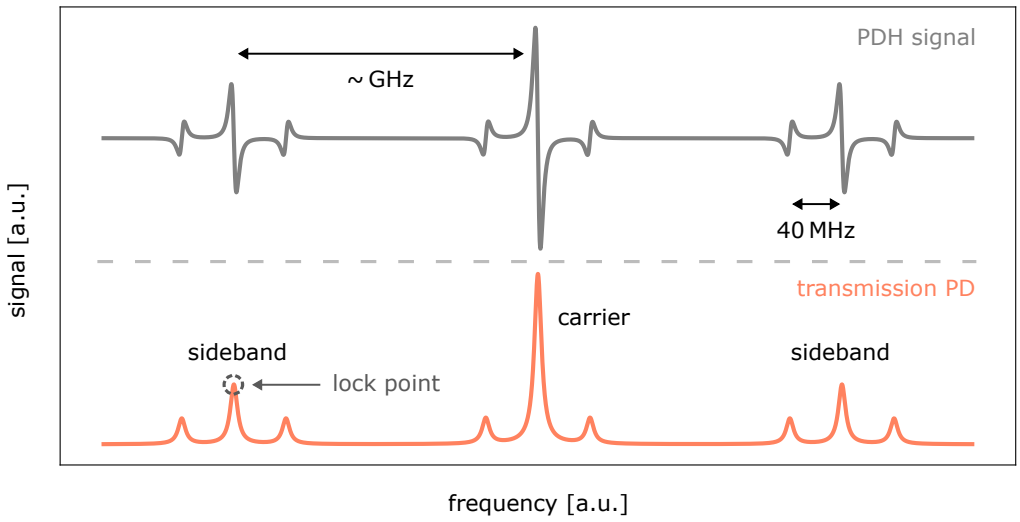

Figure 7.4.: Schematic representation of the Pound-Drever-Hall sideband-locking scheme. The lower graph illustrates the photodiode signal detecting the cavity transmission, while the upper graph shows the corresponding dispersive PDH error signal derived from the cavity reflection signal. The GHz-spaced sidebands used to shift the locked laser frequency, as well as the additional 40 MHz sidebands required for implementing the sideband lock, are indicated.

sidebands). This configuration enables frequency locking of the laser while preserving the ability to tune its frequency – realizing a shiftable locked laser.

The modulated output of the fiber EOM is sent through a free-space optical isolator to suppress back-reflections from the cavity. The beam then passes through a 50:50 beam splitter cube, allowing a portion of the light reflected from the cavity to be used for generating the PDH error signal.

The transmission through the cavity is monitored using both a photodiode and a camera, enabling real-time observation of the spatial mode structure. For optimal frequency stability, the system is aligned to support the fundamental transverse electromagnetic mode (TEM_{00}).

The reflected beam from the cavity is detected using a photodiode and the output of the photodiode is superimposed with a phase-shifted reference signal to generate the PDH error signal. This signal is subsequently processed and used to drive the piezoelectric actuator of the reference fiber laser, thereby closing the feedback loop.

A schematic of the cavity transmission photodiode (PD) signal and the corresponding dispersive signal derived from the cavity reflection is shown in figure 7.4. The carrier, the primary sidebands, and the secondary sidebands are indicated. To vary the frequency of the sidebands in the gigahertz range an ADF4350-board is used.

7.1.4. SHG using a fiber-coupled Waveguide

As the starting point for generating the MOT laser beams, we use the previously described frequency-stabilized laser operating at 1112 nm. To address the narrow intercombination transition, this light must be frequency-double using an SHG crystal. The fiber amplifier (see section 7.1.2) includes non-polarization-maintaining components; as a result, the polarization state at the amplifier output is undefined and must be adjusted to satisfy the phase-matching requirements of the frequency-doubling stage. This alignment is achieved with a three-paddle fiber-optic polarization controller, which allows precise tuning of the output polarization to maximize second-harmonic generation efficiency. In addition, this controller can be used to compensate for daily polarization drifts, which typically require slight adjustment from day to day.

Frequency doubling is accomplished using a fiber-coupled, periodically poled lithium niobate (PPLN) waveguide[6], which generates the required wavelength of 556 nm via SHG.

The efficiency of the SHG process is highly sensitive to the crystal temperature and the corresponding thermal expansion of the poled layers. Optimum performance is achieved at a crystal temperature of about 38 °C.

Under optimal conditions, the SHG module achieves a conversion efficiency of 25 %, delivering an output power of approximately 60 mW at 556 nm. To enable fast switching of the green light, a free-space AOM is used in the optical path behind the SHG unit. The beam is subsequently coupled into an optical fiber for transport to the vacuum chamber. After passing through the AOM and fiber coupling stages, an optical power of 12.5 mW is available at the experiment.

7.2. Integration into the Experimental Sequence

The transition to a two-stage MOT fundamentally changes the subsequent handling of the atomic ensemble. Therefore, the extended experimental sequence adapted for this configuration is presented in this section. The general structure and timing logic of the sequence have been developed by adapting the single-stage setup previously described in chapter 4.

In the sequence for the two-stage MOT, the initial loading phase of the blue MOT remains unchanged. Immediately after this phase, both the blue MOT beams and the Zeeman slower light are switched off. Simultaneously, the green MOT beams are activated to initiate the transfer into the second-stage MOT. The goal of this step is to transfer as many atoms as possible from the blue MOT into the green MOT which operates on the narrower ${}^1S_0 \rightarrow {}^3P_1$ transition at 556 nm.

During the green MOT loading phase, the beams are detuned by $-14\,\Gamma_{\text{green}}$, where Γ_{green}

[6] NTT, PPLN SHG module

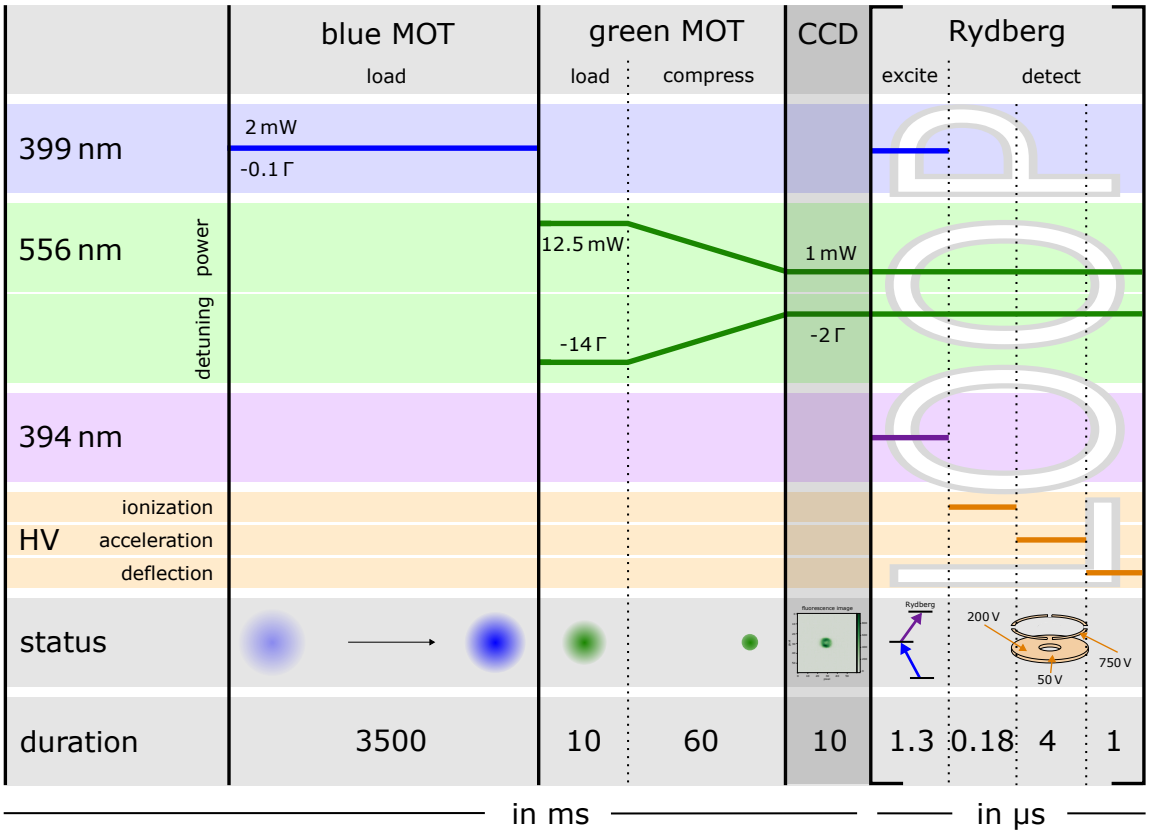

Figure 7.5.: Scheme of the experimental sequence used for the two-stage MOT and the subsequent Rydberg excitation and detection. The first-stage blue MOT is loaded into the second-stage green MOT for 10 ms. During the compression phase, the corresponding laser power is ramped down from 12.5 mW to 1 mW and the frequency detuning from $-14\,\Gamma$ to $-2\,\Gamma$. For the Rydberg excitation both the blue light and the Rydberg light are pulsed. The timing of the HV pulses in the "Rydberg" phase is the same as in figure 4.1. The figure is inspired by [131].

denotes the natural linewidth of the 556 nm transition, and the total optical power is set to 12.5 mW. This phase lasts for 10 ms. Under these conditions, approximately 5×10^5 atoms – corresponding to about ten percent of the initial population – are successfully transferred from the blue to the green MOT, providing the basis for further compression and Rydberg excitation in a denser ensemble.

This initial, low-density green MOT configuration has a lifetime of approximately 2 s. However, since the experiment aims to operate in the high-density regime, the MOT is compressed in the subsequent step of the sequence, as illustrated in figure 7.5. Over the course of the next 60 ms, both the power and detuning of the green MOT beams are ramped: the power is decreased from 12.5 mW to 1 mW, and the detuning is simultaneously reduced from $-14\,\Gamma$ to $-2\,\Gamma$. Reducing the laser power decreases the scattering force, allowing the

atoms to cool further, while decreasing the detuning draws the trapped atoms closer to the trap center. Both adjustments are performed via the green MOT AOM, depicted in figure 7.3.

This compression procedure increases the atomic density significantly, reaching peak values of up to $8 \times 10^{10}\,\mathrm{cm}^{-3}$ – almost two orders of magnitude higher than the density in the first-stage MOT. Note that the magnetic field remains constant throughout the entire measurement sequence, including the green MOT phase[7].

It is important to note that the frequency of the green light can be controlled in two ways: either via the EOM using the ADF4350 software, as described in section 7.1.3, or via the green MOT AOM. In the context of the compression sequence, the AOM is used, as it can be directly controlled via the *Cicero* sequencer without interfering with the cavity lock.

For the Rydberg excitation in the green MOT, the same excitation pathway is employed as in the single-stage MOT configuration (see chapter 4). This approach is advantageous, as it does not require additional laser sources. The same optical setup is used, specifically the blue MOT beams, which serve both as cooling in the "blue MOT" phase and Rydberg excitation light in the "Rydberg" phase.

The primary difference in this configuration lies in the timing control of the blue light: to avoid reheating the atomic ensemble, the blue MOT beams must be pulsed during the Rydberg excitation phase, using the blue MOT AOM. This is achieved using the same output channel of the fast pulse generator as for the Rydberg AOM. The duration of the excitation pulse remains unchanged at 1.3 µs.

The ionization and detection scheme also remains identical to the one described in section 4.3. Notably, it is not necessary to switch off the green MOT light during the Rydberg step. Due to the significantly higher scattering rate of the blue transition, its effect dominates the atom-light interaction during excitation, effectively suppressing any influence of the green light.

7.2.0.1. Repetition Limits in the Green MOT

In contrast to previous measurements performed in the single-stage (blue) MOT – where the Rydberg excitation sequence was repeated up to 100 times to enhance the signal-to-noise ratio – such an approach is not viable in the green MOT. As shown in figure 7.6, the number of atoms remaining in the green MOT rapidly decreases with the number of Rydberg excitation cycles. When the excitation sequence is repeated more than 25 times, fewer than 50 % of the atoms remain trapped.

Lifetime measurements of the compressed green MOT (see section 7.3.2.2) demonstrate that over a duration of 4 ms – corresponding to 20 excitation cycles with a per-cycle dura-

[7] To further reduce the atomic temperature in the green MOT, this magnetic field could be adjusted during this phase.

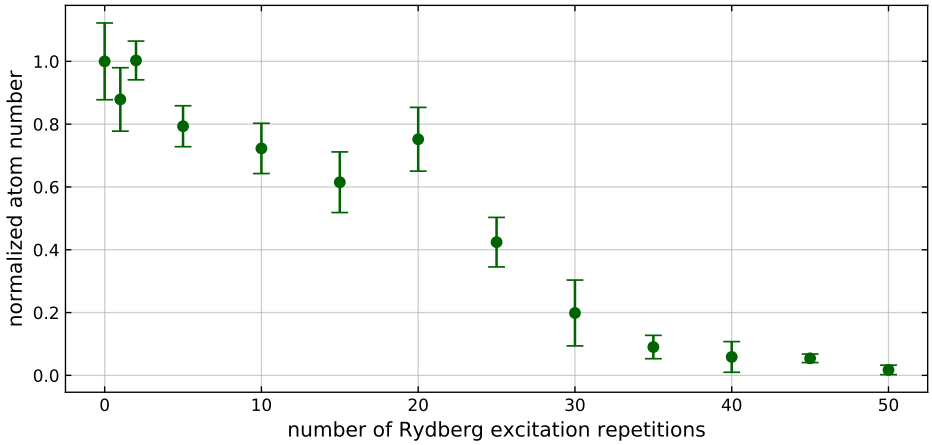

Figure 7.6.: Normalized atom number in the green MOT as a function of the number of repetitions of the Rydberg excitation sequence. The atom number is averaged over three measurements and normalized to the mean atom number without excitation. A clear reduction in atom number is observed with increasing repetition count, indicating cumulative loss due to repeated exposure to resonant blue light. Error bars represent the standard deviation of the individual measurements.

tion of 200 µs – no significant atom loss is observed in the absence of Rydberg excitation light. This indicates that the observed losses are not due to the finite MOT lifetime, but rather stem from the repeated exposure to resonant blue MOT light during the excitation sequence. This effect is expected, given the substantially higher photon scattering rate compared to the green-MOT transition at 556 nm. Thus, repeated interaction with the blue cooling light results in significant heating and a reduction in the atomic density, ultimately degrading the favorable conditions established by the second-stage (green) cooling.

To mitigate this issue while still obtaining a sufficient ion signal, a compromise was adopted and the number of Rydberg excitation repetitions was limited to 20. This approach provides an optimum balance between maintaining the integrity of the green MOT and achieving an adequate signal-to-noise ratio.

7.3. Characterization of the Two-Stage MOT

This chapter provides a detailed characterization of the second stage of the two-stage MOT, which operates on the narrow intercombination line $^1S_0 \rightarrow {}^3P_1$ at 556 nm. This stage plays a crucial role in increasing the atomic density, which is a prerequisite for the future investigation of strong dipole-dipole interactions between Rydberg atoms. High-density samples are required to reach the interaction regime where phenomena such as

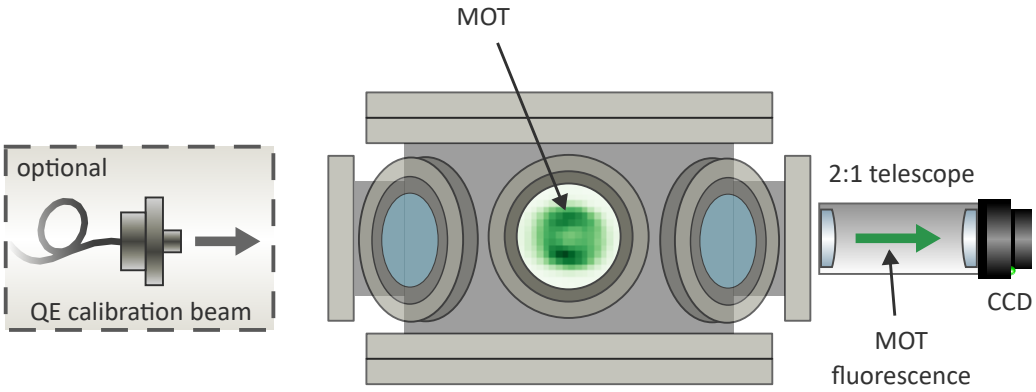

Figure 7.7.: Scheme of the fluorescence imaging system, including the 2:1 telescope and the CCD camera. Optional laser beams can be directed through the chamber onto the camera for QE calibration. The imaging system is used for fluorescence detection of both the green and the blue MOT. Note that the chamber in this figure is rotated by 90° relative to the side view of figure 3.1.

Rydberg blockade [113, 132] or collective excitation dynamics [106] can be observed, as discussed in chapter 8.

This characterization includes a systematic comparison of atom number, spatial density profiles, and ensemble temperature between both MOT stages, providing insight into the efficiency and performance gains achieved through the implementation of the second cooling stage. These quantities are key parameters for estimating the suitability of the system for further experiments involving Rydberg interactions.

The measurements described in this chapter were performed using a CCD camera to record fluorescence images of the trapped atoms, as depicted in figure 7.7. The acquired images were analyzed using a Python script, which was created as part of this work, including important specifications of the used experimental setup. The program performs image preprocessing, background correction, and fits the atomic distribution using appropriate models to extract the relevant physical quantities. The structure and core functionality of this analysis tool are briefly outlined in the following.

7.3.1. Data Analysis Methods

The starting point for the data analysis is the CCD camera's fluorescence image of the MOT. For our imaging technique, two images are recorded: one image containing atoms and a background image without atoms. In a first step, this background image is subtracted to remove stray light and offset signals. Subsequently, the total pixelsum of the corrected image (see figure 7.8) is calculated, providing a measure proportional to the number of photons detected by the camera.

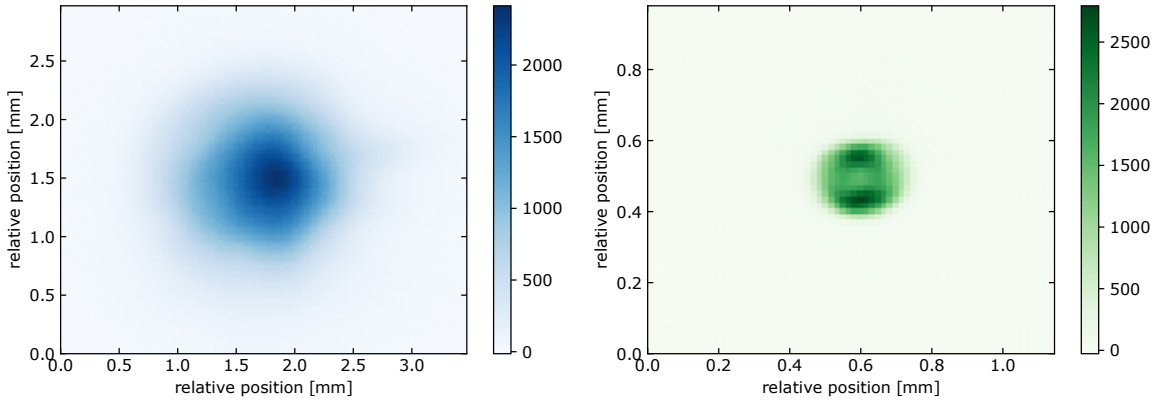

Figure 7.8.: Fluorescence images of the blue MOT (left) and the compressed green MOT (right), shown with background noise subtracted. The significantly smaller size of the green MOT is clearly visible. Note that in real space the edge length of the green MOT image is a factor of 3 smaller than that of the blue MOT.

Quantum Efficiency of the Imaging System To determine the actual number of incident photons, the quantum efficiency (QE) of the CCD camera must be known. The quantum efficiency of the camera is defined as the ratio between the detected pixelsum and the actual number of incident photons. To determine the QE, the camera is illuminated with a fraction of the laser light used in the experiment. As part of the imaging system, a telescope is directly connected to the camera via a lens tube mounted in front of one of the vacuum chamber windows (see figure 7.7). Consequently, the QE measured in this configuration corresponds to the effective QE of the entire detection system, including one vacuum window, the telescope, and the camera itself – i.e., all components located between the atoms and the detector.

In our setup, the laser used for QE calibration enters the chamber from the opposite side, passing through a second window, which is depicted on the left side of figure 7.7. This second window, however, is not part of the optical path between the atoms and the camera. Since the vacuum windows are uncoated, each surface introduces a reflectivity loss of approximately 4 % resulting in a total transmission loss of 8 %, which is taken into account in the analysis.

Knowing the laser Power P, the exposure time t_{exp} and the wavelength λ, the QE can be calculated via

$$QE = \frac{\text{pixelsum}}{N_{ph}}, \tag{7.1}$$

where the number of incident photons N_{ph} is given by

$$N_{ph} = \frac{P \cdot t_{exp}}{E_{ph}}, \tag{7.2}$$

and the photon energy is

$$E_{ph} = \frac{h \cdot c}{\lambda}. \tag{7.3}$$

Substituting the above relations yields

$$QE = \frac{\text{pixelsum} \cdot N_{ph} \cdot h \cdot c}{P \cdot t_{exp} \cdot \lambda}. \tag{7.4}$$

Applying this method, the QE was determined for both MOT stages, resulting in $QE_{blue} = 0.05$ and $QE_{green} = 0.06$.

7.3.1.1. Atom Number

The atom number in the MOT can be determined from the pixelsum of the fluorescence image, the QE of the detection system, the scattering rate Γ, and the correction factor a_{angle} accounting for the solid angle under which photons are collected (see figure 7.9).

The scattering rate for a two-level system is described by the Lorentzian function [40]

$$\Gamma = \frac{\gamma}{2} \cdot \frac{s_0}{1 + s_0 + \left(\frac{2\delta}{\gamma}\right)^2}, \tag{7.5}$$

where γ denotes the linewidth of the transition, $s_0 = I/I_{sat}$ is the saturation parameter defined by the ratio of the laser intensity to the saturation intensity, and δ is the laser detuning from resonance. Under typical operation conditions of the blue first-stage MOT, where the saturation parameter is on the order of unity and δ_{blue} is the detuning of the blue MOT, the scattering rate reduces approximately to

$$\Gamma_{blue} \approx \frac{\gamma_{blue}}{10}. \tag{7.6}$$

This provides a useful rule of thumb for estimating the photon scattering rate without detailed knowledge of the exact laser parameters. For the blue MOT with $\gamma_{blue} = 2\pi \times 29\,\text{MHz}$, this corresponds to a scattering rate of approximately

$$\Gamma_{blue} \approx \frac{\gamma_{blue}}{10} = 1.8 \times 10^7\,\text{s}^{-1}. \tag{7.7}$$

In contrast, the green MOT transition with $\gamma_{green} = 2\pi \times 180\,\text{kHz}$ features a much lower saturation intensity, resulting in a saturation parameter $s_0 \gg 1$ under typical experimental intensities. Consequently, the denominator in equation (7.5) is dominated by s_0, and the scattering rate approaches its maximum value

$$\Gamma_{green} \approx \frac{\gamma_{green}}{2} = 5.7 \times 10^5\,\text{s}^{-1}. \tag{7.8}$$

The solid angle correction factor quantifies the fraction of emitted photons that reach the detector. Under the simplifying assumption of isotropic (spherical) emission, this fraction can be determined by evaluating the ratio between the area of the first lens of the imaging system, A_{lens}, and the surface area of a sphere, A_{sphere}, with a radius equal to the distance

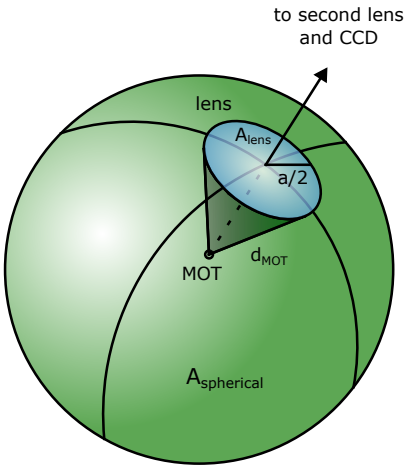

Figure 7.9.: Schematic representation of the fluorescence light emitted by the MOT, modeled as a spere centered at the MOT. A surface area $A_{\text{spherical}}$ intersects the first lens of the telescope with area A_{lens} and is imaged onto the CCD camera. The distance between the MOT and the first lens is $d_{MOT} = 14\,\text{cm}$ and the lens diameter is 2.54 cm.

between the MOT and the telescope. This distance is given by $d_{MOT} = 14\,\text{cm}$, and the diameter of the telescope´s first lens is $a = 2.54\,\text{cm}$. An illustration of this concept is shown in figure 7.9. The resulting solid angle correction factor is

$$a_{angle} = \frac{A_{lens}}{A_{spherical}} = \frac{\pi \cdot \left(\frac{a}{2}\right)^2}{4\pi \cdot d_{MOT}^2} = \left(\frac{a}{4\,d_{MOT}}\right)^2 = 0.00206. \tag{7.9}$$

Using this correction factor, the total number of atoms can be calculated from the pixelsum of an image as

$$N_{atoms} = \frac{\text{pixelsum}}{QE \cdot a_{angle} \cdot \Gamma \cdot t_{exp}}. \tag{7.10}$$

7.3.1.2. Size and Density

The size of the MOT is determined by assuming a Gaussian density distribution and correspondingly performing a Gaussian fit to the one-dimensional projections of the fluorescence signal, recorded with the CCD camera, onto the horizontal and vertical axes, as shown in figure 7.10. The fit function is given by

$$f(x) = a \cdot e^{-\frac{(x-b)^2}{2 \cdot c^2}}, \tag{7.11}$$

where a is the amplitude, b denotes the center position and c corresponds to the Gaussian width. The extracted value of c is used to quantify the spatial extent of the MOT in each direction.

With the obtained width parameters and the calculated atom number, the spatial density distribution of the MOT can be determined. Following the description in [40], the three-dimensional Gaussian density distribution is given by

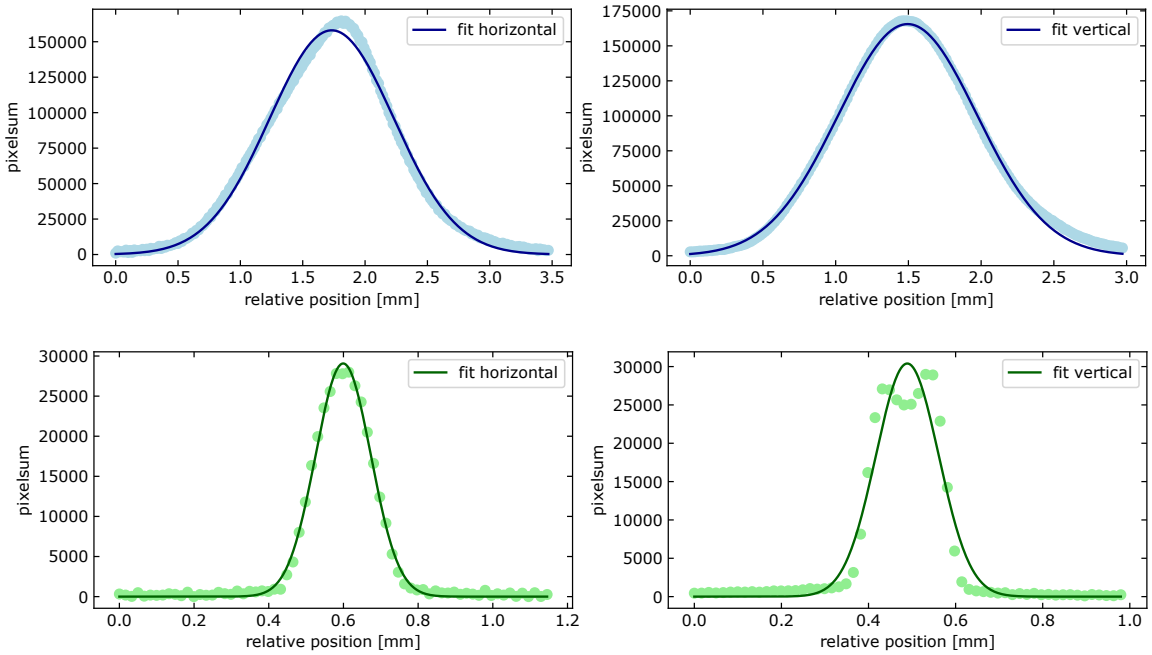

Figure 7.10.: Pixelsum projections of the CCD fluorescence images for the blue MOT (top) and green MOT (bottom), shown along the horizontal and vertical axes. The spatial width of each MOT is extracted by fitting a Gaussian function to the corresponding 1D projection data. Note the different scales of the x-axis.

$$n(x,y,z) = \frac{N_{atoms}}{(2\pi)^{3/2}\sigma_x\sigma_y\sigma_z} \cdot e^{-\left(\frac{x^2}{2\sigma_x^2}+\frac{y^2}{2\sigma_y^2}+\frac{z^2}{2\sigma_z^2}\right)}, \tag{7.12}$$

Where N_{atoms} is the total number of trapped atoms and σ_x, σ_y and σ_z denote the Gaussian width of the atomic cloud along the respective spatial directions.

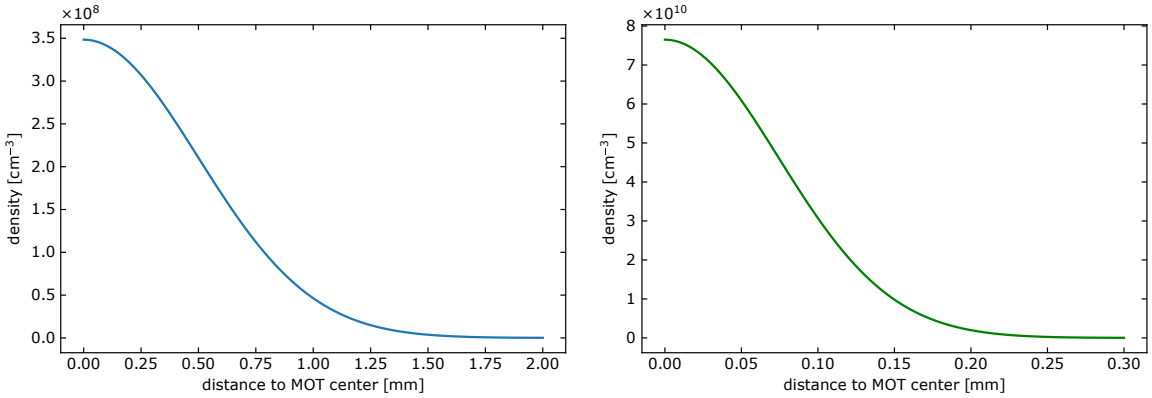

Figure 7.11.: Fit of the radial density distribution of the blue (left) and green (right) MOTs along the horizontal direction, starting from the MOT center at $z = 0$. The peak density for the first stage MOT is $3.5 \times 10^8\,\mathrm{cm}^{-3}$ and for the second stage $0.8 \times 10^{11}\,\mathrm{cm}^{-3}$.

Assuming radial symmetry in the horizontal plane ($\sigma_x = \sigma_y = \sigma_r$), the expression simplifies to

$$n(r,z) = \frac{N_{atoms}}{(2\pi)^{3/2}\sigma_r^2\sigma_z} \cdot e^{-\left(\frac{r^2}{2\sigma_r^2}+\frac{z^2}{2\sigma_z^2}\right)}. \tag{7.13}$$

The integration over z or, respectively, r, yields the fit functions employed in figure 7.10 to determine the MOT width along the corresponding direction. A representative fit of the radial density distribution at the center of the cloud ($z = 0$) is shown in figure 7.11. The maximum density is attained at the center of the trap ($x = 0$, $y = 0$, $z = 0$) and is given by

$$n(r,z)_{max} = \frac{N_{atoms}}{(2\pi)^{3/2}\sigma_r^2\sigma_z}. \tag{7.14}$$

The characterization results of the atom numbers and densities are presented in section 7.3.2.1.

7.3.1.3. Time-of-Flight Temperature Measurement

Among the various techniques for determining the temperature of a MOT, the time-of-flight (ToF) method [38] is particularly advantageous because it provides direct and model-independent access to the velocity distribution of the atomic cloud. In this method, the thermal expansion is quantitatively extracted from fluorescence images recorded after controlled free-expansion times, as implemented in our experiment.

The experimental sequence described in section 4.2 is applied with only minor modifications. First, the atoms are loaded into the MOT, as illustrated in figure 7.12. Subsequently, a variable free-expansion time is introduced, during which both the cooling laser light and the magnetic field are switched off. During this interval, the atomic cloud expands freely. After the selected expansion time, the atoms are imaged using the MOT laser beams, while the magnetic coils remain switched off. This ensures that the atoms are not recaptured into the MOT but are solely imaged using the MOT light; otherwise, the measured spatial expansion would not accurately reflect the free expansion of the atomic cloud. The procedure is repeated for several expansion times, and for each time step the width of the cloud is extracted from the corresponding fluorescence image.

By switching off the MOT – both the cooling beams and the magnetic fields – the atoms begin to expand freely with the velocity they possess at the moment of release. Since the atomic temperature is directly related to their velocity distribution, and assuming a Gaussian velocity distribution, the equipartition theorem yields the following relation in one dimension [133]

$$\frac{1}{2}\,m\,\sigma_v^2 = \frac{1}{2}\,k_B\,T. \tag{7.15}$$

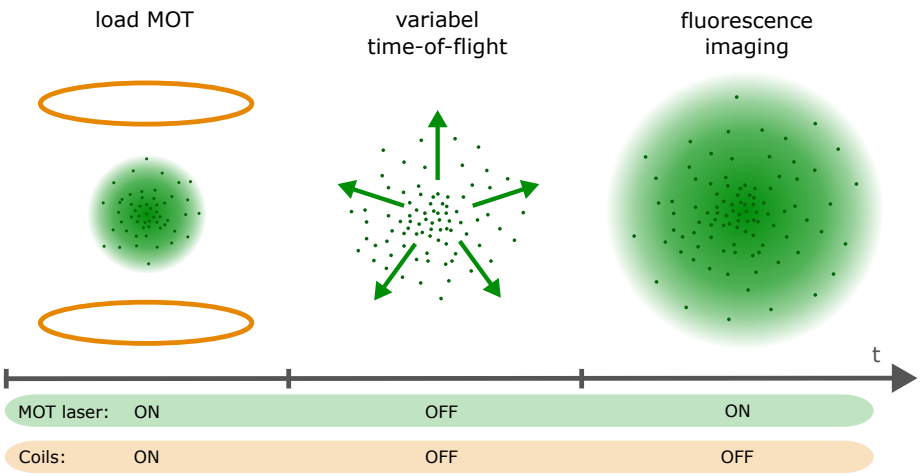

Figure 7.12.: Schematic of the time-of-flight measurement sequence. First, the MOT is loaded with the cooling laser beams and magnetic coils switched on. During the subsequent variable-duration free-expansion phase, both the lasers and magnetic fields are turned off. Finally, the MOT beams are switched on again to perform fluorescence imaging of the atomic cloud.

This leads to a temperature of

$$T = \frac{m\,\sigma_v^2}{k_B}, \tag{7.16}$$

where m is the mass of the isotope under investigation, σ_v is the width of the one-dimensional velocity distribution, and k_B is the Boltzmann constant. By measuring the width of the atomic cloud $\sigma(t)$ with the fit described in section 7.3.1.2 for different expansion times t and using the expression [134]

$$\sigma(t) = \sqrt{\sigma_0^2 + \sigma_v^2 t^2} = \sqrt{\sigma_0^2 + \frac{k_B T}{m} t^2}, \tag{7.17}$$

where σ_0 is the initial width of the atomic cloud, the velocity σ_v can be extracted and thus the temperature determined. It should be noted that the temperature may differ along different spatial axes, as the velocity is determined independently in each direction. Two representative time-of-flight measurements of the second-stage MOT are presented in figure 7.13. The width of the atomic cloud is plotted as a function of expansion time.

From the fit to the data, the corresponding temperature is determined assuming ballistic expansion. In this example, following a final laser power of 5 mW intended to reduce the atomic temperature, the horizontal and vertical temperatures were found to be (282 ± 32) µK and (386 ± 86) µK, respectively. This measurement represents a single example from a series of measurements presented in section 7.3.2.3, in which the atomic temperature was determined for several final laser powers.

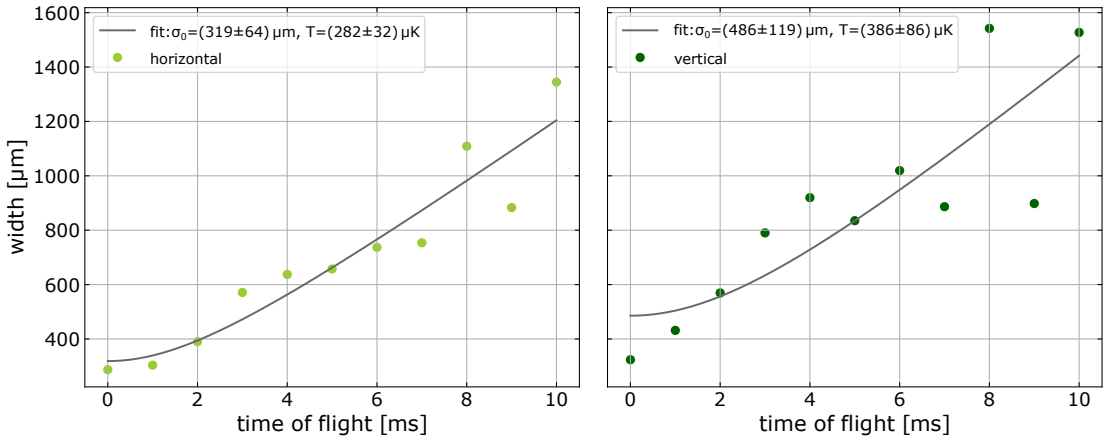

Figure 7.13.: Time-of-flight measurements of the second-stage MOT for a final laser power of 5 mW, shown separately for the horizontal (left) and vertical (right) dimensions. The fit yields the expansion velocity, which is then used to determine the corresponding temperature.

Low MOT temperatures are crucial for spectroscopy measurements as well as for Rydberg excitation and the investigation of Rydberg-Rydberg interactions. Reduced thermal motion minimizes Doppler broadening and thereby improves spectral resolution. In addition, low temperatures increase the effective interaction time with the excitation lasers and reduce inhomogeneous broadening arising from spatial intensity variations. For Rydberg-Rydberg interactions, low atomic temperatures ensure well-defined and nearly constant interatomic distances during the excitation process, which is essential for observing interaction-induced effects such as Rydberg blockade.

7.3.2. Characterization Results

This section presents the characterization results determined using the analysis methods described in the previous section.

7.3.2.1. Atom Number and Density

Following the description in section 7.3.1.1, the total atom number in the MOT can be determined using equation (7.10). A typical atom number of approximately 1×10^7 in the first-stage MOT, operating on the strong ${}^1S_0 \rightarrow {}^1P_1$ transition, has previously been reported in [1] and was independently confirmed in this work.

The atoms are subsequently transferred to the narrower second-stage MOT. However, the transfer efficiency is limited by several factors. Owing to the narrow linewidth of the 556 nm transition, the capture velocity of the second-stage MOT is approximately an order of magnitude lower, significantly reducing the number of atoms that can be

decelerated and trapped [135]. As the radiative cooling force scales with the linewidth [40], this imposes an intrinsic limitation on transfer efficiency. Insufficient pre-cooling in the first-stage MOT can result in atomic velocities exceeding the capture range of the second stage. This issue has been analyzed in similar systems [136]. Equally important, and particularly critical, is the spatial overlap between the pre-cooled atoms in the first-stage MOT and the trap center of the second-stage MOT. In the broad-linewidth MOT, the light force varies only weakly across the trapping region, so the location of the atomic cloud is primarily determined by the magnetic-field zero and the light field geometry. In contrast, as discussed in detail in [128], the radiation pressure in the narrow-line second-stage MOT becomes comparable to the gravitational force. Consequently, the equilibrium position of the atoms is shifted downward, resulting in a pronounced gravitational sag. Because this force balance occurs away from the true magnetic-field center, the narrow-line MOT exhibits a substantial vertical displacement of the atomic cloud, which depends sensitively on the detuning, intensity, and magnetic-field gradient. This gravitational sag complicates the spatial overlap between the two MOT stages, as the displaced second-stage trap center may no longer coincide with the position of the first-stage MOT.

As a result of these combined loss mechanisms, the number of atoms successfully transferred to the second-stage MOT in our experiment is reduced to typically approximately 5×10^5. Despite the lower atom number in the second-stage MOT significantly higher atomic densities can be achieved.

The atomic density is enhanced by ramping the detuning of the green MOT laser during the compression stage, as described in section 7.2. In figure 7.14 the measured peak atomic density in the second-stage MOT as a function of the initial detuning at which the atoms are transferred from the blue MOT to the green MOT is presented. In each case, the laser frequency is ramped linearly from the respective start detuning toward resonance, reaching a final detuning of $-2\,\Gamma$ within 60 ms. We found that compression is most efficient for ramping the green MOT frequency down to $-2\,\Gamma$. In the following steps of the experiment we primarily focused on increasing the density by optimizing the transfer efficiency.

As the initial detuning is increased (i.e., shifted further from resonance), the peak density first rises, reaching a maximum at a start detuning of $-14\,\Gamma$. This behavior can be attributed to the increasing capture volume from which atoms are collected and subsequently compressed.

However, beyond this optimal detuning, the peak density no longer increases as the detuning is moved further from resonance. This behavior can be attributed to the reduced restoring force of the green MOT beams at larger detunings. As a result, fewer atoms are successfully transferred into the compressed MOT phase, diminishing the overall confinement efficiency.

The peak atomic density, as illustrated in figure 7.11, reaches up to $8 \times 10^{10}\,\mathrm{cm}^{-3}$ with a typical mean density of $2 \times 10^{10}\,\mathrm{cm}^{-3}$ across the MOT volume. Compared to typical den-

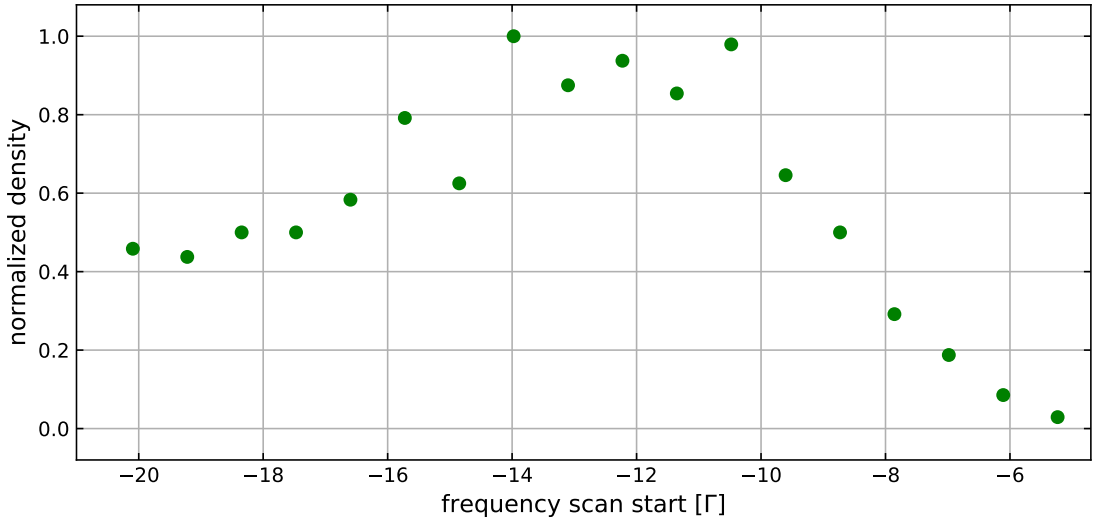

Figure 7.14.: Normalized peak atomic density in the compressed green MOT as a function of the initial detuning of the frequency ramp. The laser frequency is ramped linearly from the indicated start detuning to a fixed final detuning of $-2\,\Gamma$ within 60 ms. The highest density is observed for a start detuning of $-14\,\Gamma$, indicating optimal transfer efficiency of atoms from the blue MOT to the green MOT at this value.

sities in the first-stage MOT, this corresponds to an increase by nearly two orders of magnitude, highlighting the spatial compression and improved cooling performance achieved in the second-stage MOT configuration. This density should be high enough for a study of Rydberg-Rydberg interactions. A detailed analysis of the density and the resulting interatomic distances is presented in section 8.2.

7.3.2.2. Lifetime

In order to asses whether the lifetime of atoms trapped in the MOT influence spectroscopic measurements, it is important to determine the lifetimes in our apparatus experimentally. In general, the lifetime is determined by measuring as the the number of atoms staying in the trap region after a variable time duration for which the MOT laser beams are switched off. For the blue MOT a typical lifetime of several seconds was verified in this work.

For the green MOT, two characteristic lifetimes can be distinguished: that of the uncompressed MOT and that of the compressed MOT. The uncompressed MOT is operated at the maximum laser power of 12.5 mW with a frequency detuning of $-14\,\Gamma$. The compressed MOT is operated as described in section 7.2. During compression, the laser power is ramped from 12.5 mW to a final value of 1 mW, while the laser frequency is simultaneously ramped from $-14\,\Gamma$ to $-2\,\Gamma$. The corresponding measurements are presented in figure 7.15. The uncompressed MOT, displayed on the left, exhibits a lifetime of (1.6 ± 0.2) s. Since the

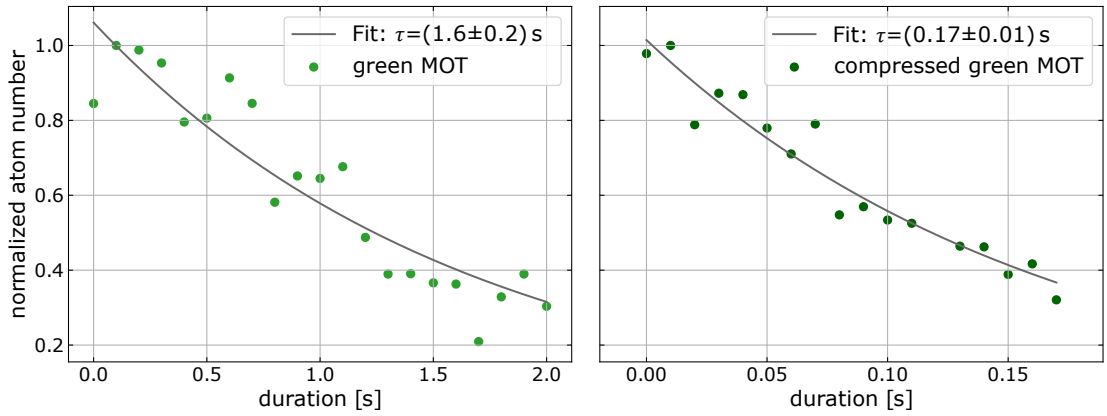

Figure 7.15.: Lifetime measurements of the green MOT operated at the maximum laser power of 12.5 mW with a frequency detuning of $-14\,\Gamma$ (left) and the compressed green MOT, with the laser power ramped from 12.5 mW to a final value of 1 mW, while the laser frequency is simultaneously ramped from $-14\,\Gamma$ to $-2\,\Gamma$ (right), showing exponential decay behavior of the atoms in the trap with fitted lifetimes of (1.6 ± 0.2) s and (0.17 ± 0.01) s, respectively.

compressed MOT is typically used to achieve higher densities and lower temperatures, its lifetime is of primary interest. As expected, the increased density leads to a significantly shorter lifetime, which is measured to be (0.17 ± 0.01) s.

This shorter lifetime is still sufficiently long for our Rydberg experiments, as these measurements operate on a microsecond timescale (see section 4.3).

7.3.2.3. Temperature

The temperature of the MOT strongly depends on experimental parameters. The fundamental lower bound for laser cooling in such systems and in the case of low intensities $s_0 \ll 1$ is given by the Doppler cooling limit [40]

$$T_D = \frac{\hbar\gamma}{2\,k_B}, \tag{7.18}$$

where γ is the natural linewidth of the cooling transition. This limit corresponds to the equilibrium temperature reached when the cooling dissipation balances the heating from photon recoil. For the transitions used in our two-stage MOT system, the Doppler limits are approximately $T_{D,blue} \approx 690\,\mu$K and $T_{D,green} \approx 4.4\,\mu$K, respectively. In practice, several effects such as laser intensity fluctuations, beam misalignment, multiple scattering of photons, and magnetic field gradients contribute to heating, so that these theoretical limits are typically not reached. For the first-stage MOT, as previously discussed, the measured temperature is on the order of 4 mK.

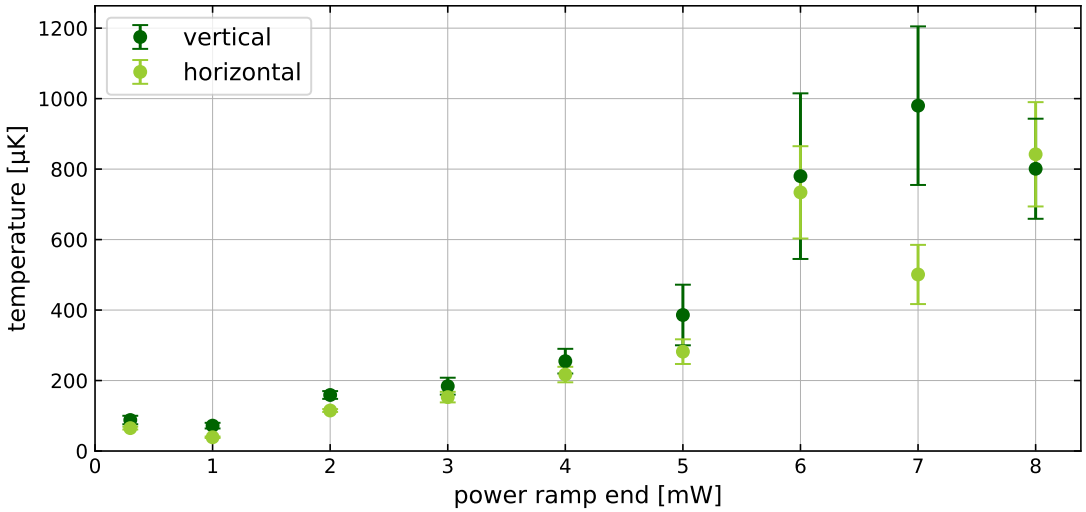

Figure 7.16.: Measured temperature of the second-stage MOT as a function of the final power of the laser ramp, starting from 12.5 mW. Lower final powers lead to reduced temperatures in both horizontal and vertical directions.

As described in [137], the MOT temperature is particularly sensitive to the total intensity of the cooling light. To systematically investigate this dependency for the second-stage MOT, we performed a series of ToF measurements while varying the final laser power in the compressed MOT. In each measurement, the total power of the MOT beams was reduced from an initial value of 12.5 mW to a variable final power.

The results are presented in figure 7.16. As expected, lower final laser powers result in lower MOT temperatures. The lowest observed temperatures were (33 ± 2) µK in the vertical direction and (21 ± 4) µK in the horizontal direction, both achieved with a final laser power of 1 mW. It is important to note that, during the compression phase of these measurements – when the laser power is ramped – the laser frequency is also ramped, as described previously in section 7.2.

Low temperatures are essential in the studies of Rydberg-Rydberg interactions, as the interatomic distances vary with atomic motion. The goal is to ensure that the Rydberg atoms move minimally during the interaction times. The measured temperatures, in the low hundred µK regime, are sufficient for these studies [138].

8.

Towards Detection of Rydberg-Rydberg Interactions in an Yb-MOT

After having discussed the general principles of Rydberg-Rydberg interactions (see chapter 6) and having presented the experimental realization of a two-stage MOT with substanially increased atomic density (see section 7.3), this chapter provides an overview of the current experimental status in our investigation of Rydberg-Rydberg interactions. The enhanced density achieved with the two-stage MOT places the system in a regime where interaction effects between neighboring Rydberg atoms are expected to become experimentally accessible.

In section 8.1, we introduce the detection strategies employed to reveal signatures of such interactions. A detailed evaluation of the conditions required for reaching the interaction regime, including excitation parameters and density considerations, is presented in section 8.2. Finally, the next steps towards interactions using this detection approach are reported in section 8.3.

8.1. Spatially Resolved Rydberg Excitation

Rather than modifying the atomic density through conventional means such as changes in magnetic field gradients or trap parameters, we pursued an alternative measurement strategy for a first detection of Rydberg-Rydberg interactions in our Yb MOT, by using that the density in the MOT is spatially varying. Our Rydberg excitation laser is coupled into the system via a fiber coupler, whose vertical position can be precisely adjusted (see figure 8.1). This setup allows us to exploit the spatial variation of the atomic density along the vertical axis of the MOT by detecting the number of atoms excited to a Rydberg state as a function of the vertical position. Due to the strong dependence of the interaction strength on the principal quantum number n, as discussed in section 6.1.2 it is expected that for high n a change in the spatial dependence of the Rydberg excitation probability could reveal the presence of interactions.

To establish a baseline, we begin by exciting to low-lying Rydberg states where, under our experimental conditions, interactions are negligible. In this regime, we perform a spatial

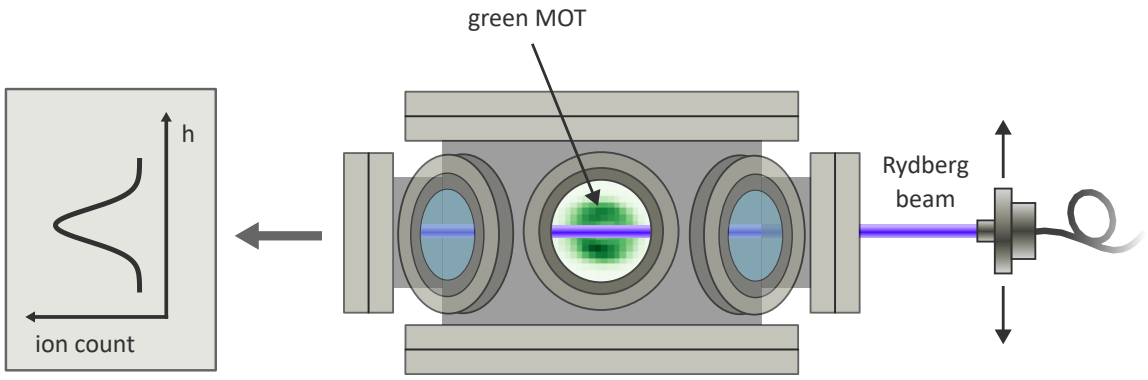

Figure 8.1.: Schematic of the experimental setup for detecting Rydberg interactions. The fiber coupler of the Rydberg excitation beam can be shifted vertically to probe different density regions of the atomic cloud. It should be noted that the chamber is shown here in a rotated orientation relative to figure 7.7. On the left, a sketch illustrates the resulting ion count as a function of the vertical position of the Rydberg beam h.

scan of the Rydberg excitation beam along the vertical axis of the MOT and subsequently follow the detection protocol outlined in section 4.3. If no Rydberg-Rydberg interactions occur, the resulting spatial excitation profile directly reflects the local atomic density. This procedure thus serves both as a reference measurement and as a calibration of the MOT size, as the integration along the excitation beam axis yields the spatial distribution of excited Rydberg atoms projected onto the scanning direction of the beam. A scheme of the experimental setup is shown in figure 8.1. On the left, a sketch illustrates the resulting ion counts as a function of the vertical position of the output coupler h.

We then repeat the measurement for higher Rydberg states where, based on our estimated densities, interactions are expected to play a role. In the absence of interactions, the excitation profile should remain unchanged regardless of the chosen Rydberg state. However, when interactions become relevant, we expect to observe a deformation of this profile – specifically, a flattening in the central, high-density region of the MOT. This effect arises due to the Rydberg blockade mechanism, which suppresses further excitations in the vicinity of an already excited Rydberg atom (see section 6.2), effectively reducing the number of Rydberg excitations in regions of high atomic density.

Figure figure 8.2 illustrates the expected modification of the spatial excitation profile arising from Rydberg-Rydberg interactions, shown as a function of the interaction strength and, consequently, the principal quantum number of the state.

While Rydberg-Rydberg interactions could not yet be clearly observed under the current experimental conditions, the method has proven effective for spatially resolving the Rydberg excitation profile and for calibrating the spatial overlap between the excitation beam and the trapped atom cloud. These initial results establish the functionality and reliability of the approach, providing a solid foundation for future measurements under conditions

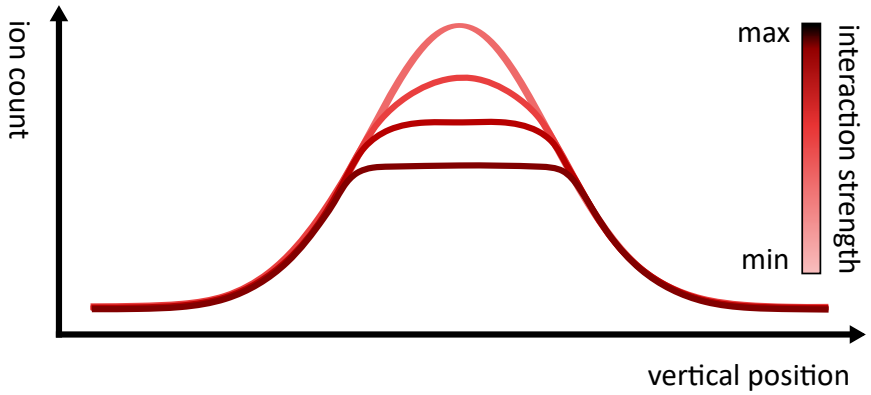

Figure 8.2.: Schematic illustration of the expected modification of the spatial Rydberg excitation profile due to Rydberg-Rydberg interactions. Darker colors correspond to stronger interactions. Increasing interaction strength leads to a Rydberg blockade effect, reducing the number of atoms excited to Rydberg states within the same volume.

optimized for observing interaction effects.

In figure 8.3 the measurement procedure was applied to the $60\,S$ Rydberg state with a Rydberg beam power of 1 mW. As this state is below the threshold at which we expect interactions, this measurement gives information about the green MOT size but not about interactions.

8.1.1. Stability of the Ion Counts

The overall stability of the detected ion signal is determined to be approximately 5 %, primarily arising from fluctuations in the atom number and variations in the Rydberg laser power. The relative uncertainty in the atom number is estimated to be about 4.5 % for the blue MOT and 3 % for the green MOT. Since the atoms are transferred to the green MOT for further manipulation, the atom number stability in this stage is of greater relevance for the ion signal.

The Rydberg laser power is found to vary by approximately 1 % over the typical timescale of a measurement cycle. Assuming linear error propagation, the combined contributions of atom number and laser power fluctuations nearly account for the total observed variation in ion signal.

Additionally, even though less significant, sources of uncertainty may include frequency drifts of the Rydberg excitation laser and timing jitter in the excitation sequence, but their influence is expected to be smaller under typical experimental conditions.

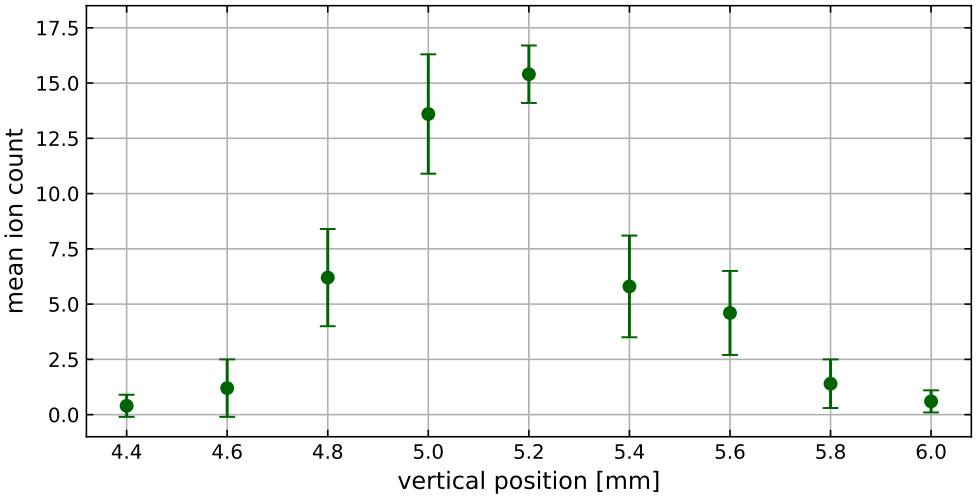

Figure 8.3.: Spatially resolved Rydberg excitation in a green MOT. The figure shows a measurement of the Rydberg excitation probability. Measurement as a function of the vertical position of the Rydberg excitation laser beam. As the beam passes through the green MOT, the ion count reflects the transverse density profile of the MOT. Error bars represent the standard deviation from multiple measurements.

8.2. Experimental Considerations

This section summarizes the experimental conditions relevant for Rydberg excitation and interaction measurements and outlines the expectations regarding the observability of interaction-induced energy shifts under our experimental conditions.

8.2.1. Effective Interatomic Distance

In the present setup, excitation to the Rydberg state is realized via the blue MOT beams driving the transition to the intermediate state, followed by the Rydberg laser coupling the intermediate state to the Rydberg state (see figure 1.1). The Rydberg laser is focused onto the atomic cloud in the two-stage MOT with a $1/e^2$ beam radius of approximately 50 µm. With the beam centered on the MOT, the laser simultaneously addresses the central high-density region and its immediate surroundings.

For a first estimate, the transverse 50 µm beam radius is considered while neglecting the elongation along the propagation axis. In figure 7.11 this area of 50 µm radius yields a minimum atomic density of $n_{min} = 6 \times 10^{10}\,\mathrm{cm}^{-3}$ within the excitation volume.

In the simplest model, the effective volume per atom is given by $V_{\mathrm{atom}} = n^{-1}$, resulting

in an average interatomic distance of

$$d = V_{\text{atom}}^{1/3} = n_{min}^{-1/3} \approx 2.6\,\mu\text{m}. \tag{8.1}$$

This value corresponds to the minimum mean distance between atoms trapped in the green MOT within the excitation volume of the focused Rydberg laser beam.

8.2.2. Excitation Probability

If all atoms in the MOT could be excited to a Rydberg state with a probability of 100 %, the interatomic distance given by equation (8.1) would give a lower limit for a blockade radius (see figure 6.3) at which interactions between Rydberg atoms could be observed. However, this would require that the Rydberg excitation reaches 100 % which is not the case under our experimental conditions. In the following we will describe the physics behind this limitation.

A quantum two-level system – such as an atom driven by a laser field – undergoes coherent oscillations between its ground and excited state at the so-called Rabi frequency. Damping of these oscillations arises from spontaneous decay, dephasing mechanisms or collisions. In the corresponding damped oscillator picture, no more than 50 % of the atoms can be transferred to the excited state in the steady-state limit.

As a consequence, the mean distance between two excited Rydberg atoms is always smaller than the value given by equation (8.1), since not all atoms trapped in the MOT can be excited to Rydberg states simultaneously. The population of the Rydberg states for the given setup is derived in the following.

To describe the quantum-mechanical interaction of light with a two-level-atom with a ground and an excited state, the Bloch equations are employed [133]. For a coherently driven two-level system with detuning Δ, the excitation probability as a function of time is

$$P_e(t) = \frac{\Omega^2}{\Omega^2 + \Delta^2} \sin^2\left(\frac{\sqrt{\Omega^2 + \Delta^2}}{2}\, t\right), \tag{8.2}$$

where Ω is the Rabi frequency and Δ the detuning.

The stationary solution of the optical Bloch equations is given by the steady-state population of the excited state [139]

$$\rho_{ee}^{\infty} = \frac{\Omega^2}{4\Delta^2 + \Gamma^2 + 2\Omega^2}, \tag{8.3}$$

where Γ denotes the decay rate of the excited state.

The Rabi frequency is defined as

$$\Omega = \frac{d\,E}{\hbar}, \qquad E = \sqrt{\frac{2I}{c\epsilon_0}}, \tag{8.4}$$

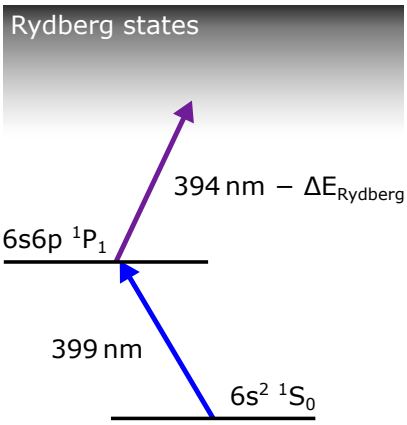

Figure 8.4.: Energy level scheme for the excitation to Rydberg states. The broad ${}^1S_0 \rightarrow {}^1P_1$ transition is employed as the intermediate state.

with transition matrix element d, electric field amplitude E, and laser intensity I. Combining both expressions yields

$$\Omega = \frac{d}{\hbar}\sqrt{\frac{2I}{c\epsilon_0}}\,. \tag{8.5}$$

As discussed previously and illustrated in figure 8.4, excitation to the Rydberg state proceeds via the intermediate ${}^1P_1$ state. The ${}^1S_0 \rightarrow {}^1P_1$ transition is driven by the blue MOT laser beams, while the subsequent excitation from the intermediate state to the Rydberg state is provided by the dedicated Rydberg excitation laser. Both laser beams are pulsed for 1.5 µs.

We first consider the case of two separate excitations, where the intermediate state becomes significantly populated and the Rydberg laser drives a single-photon transition between ${}^1P_1$ and the Rydberg state. The Rabi frequency of the first transition, driven by the back-reflected MOT beams with an intensity of $I_1 = 2I_{\mathrm{MOT}} = 280\,\mathrm{W/m^2}$, is $\Omega_1 = 2\pi \times 24\,\mathrm{MHz}$. With a lifetime of $1/\Gamma_1 = \tau_1 = 5.5\,\mathrm{ns}$ and assuming resonant excitation, the stationary excited-state population of the ${}^1P_1$ is

$$\rho_1^{\infty} = \frac{\Omega^2}{2\Omega^2 + \Gamma^2} = 29\,\%\,. \tag{8.6}$$

For the second transition from the intermediate to the Rydberg state, the focused laser has an intensity of

$$I = \frac{2P}{\pi w^2} \approx \frac{2 \times 10^{-3}\,\mathrm{W}}{\pi(50 \times 10^{-6}\,\mathrm{m})^2} \approx 2.5 \times 10^5\,\frac{\mathrm{W}}{\mathrm{m}^2}. \tag{8.7}$$

Using the *ARC* Python package [140], the reduced dipole matrix element for the transition to the Rydberg S-state is estimated to be on the order of $0.05\,ea_0$. Consequently, the

corresponding Rabi frequency is

$$\Omega_2 \approx \frac{0.05\, e a_0}{\hbar} \sqrt{\frac{5 \times 10^5\,\mathrm{W/m^2}}{c\epsilon_0}} \approx 2\pi \times 8.8\,\mathrm{MHz}. \tag{8.8}$$

For high Rydberg states, the lifetimes are typically on the order of several hundred microseconds (see section 5.3.3). Assuming $\tau_2 = 250\,\mu\mathrm{s}$, we find $\Gamma_2 \ll \Omega_2$, leading to a stationary excitation density of

$$\rho_2^\infty \approx \frac{1}{2} = 50\,\%. \tag{8.9}$$

The resulting Rydberg-state population is thus $\rho_\mathrm{R} = 0.29 \times 0.5 = 0.145 = 14.5\,\%$ of the ground state density. Consequently, the Rydberg-state population – and thus the Rydberg atom density – is reduced to 14.5 %, corresponding to a reduction by approximately a factor of seven compared to the green MOT. This yields a maximum Rydberg atom density of $n_\mathrm{R} \approx 0.9 \times 10^{10}\,\mathrm{cm^{-3}}$, which corresponds to a mean interatomic spacing of $d = 4.8\,\mu\mathrm{m}$.

Considering a two-photon excitation process, the Rydberg population density may differ slightly. The corresponding effective two-photon Rabi frequency is given by [141]

$$\Omega_\mathrm{eff} = \frac{\Omega_1 \Omega_2}{2\Delta} = \frac{2\pi \times 24\,\mathrm{MHz} \times 2\pi \times 8.8\,\mathrm{MHz}}{2 \times 2\pi \times 20\,\mathrm{MHz}} = 2\pi \times 10.6\,\mathrm{MHz}. \tag{8.10}$$

Using the stationary solution of the optical Bloch equations, and setting $|\Omega|^2 = \Omega_1^2 + \Omega_2^2$, one obtains

$$\rho_1^\infty = \frac{\Omega_1^2 + \Omega_2^2}{4\Delta^2 + \Gamma_\mathrm{m}^2 + 2(\Omega_1^2 + \Omega_2^2)} = 1.3\,\%, \tag{8.11}$$

for the population of the $^1P_1$ state. The corresponding effective scattering rate due to the virtual state is then $\Gamma_\mathrm{eff} = \Gamma_\mathrm{m} \rho_\mathrm{m}^\infty = 2\pi \times 0.38\,\mathrm{MHz}$. The resulting stationary Rydberg-state population is

$$\rho_2^\infty = \frac{\Omega_\mathrm{eff}^2}{\Gamma_\mathrm{eff}^2 + 2\Omega_\mathrm{eff}^2} \approx 50\,\%. \tag{8.12}$$

In this case the mean interatomic spacing would be $d = 3.2\,\mu\mathrm{m}$.

Because of the small detuning Δ from the intermediate state, the system exhibits a mixture of sequential and two-photon excitation pathways. In this regime, both processes can contribute, and the resulting Rydberg population must therefore lie between the limits set by the two scenarios.

8.2.3. State-Dependent Interaction Range

As previously discussed, the proximity of two atoms leads to an interaction-induced shift of their Rydberg pair energy relative to the non-interacting case. These shifts can be calculated using the open-source software *RYDCALC* [142], which is based on multichannel

quantum defect theory (see section 2.1.3) methods as described in [7]. For such interactions to be detectable, the interaction-induced energy shift must be comparable to the linewidth of the Rydberg transition. Previous measurements with our experimental setup [143] indicate typical full widths at half maximum (FWHM) of approximately 50 MHz, which defines the range required for a clear observation of interaction effects.

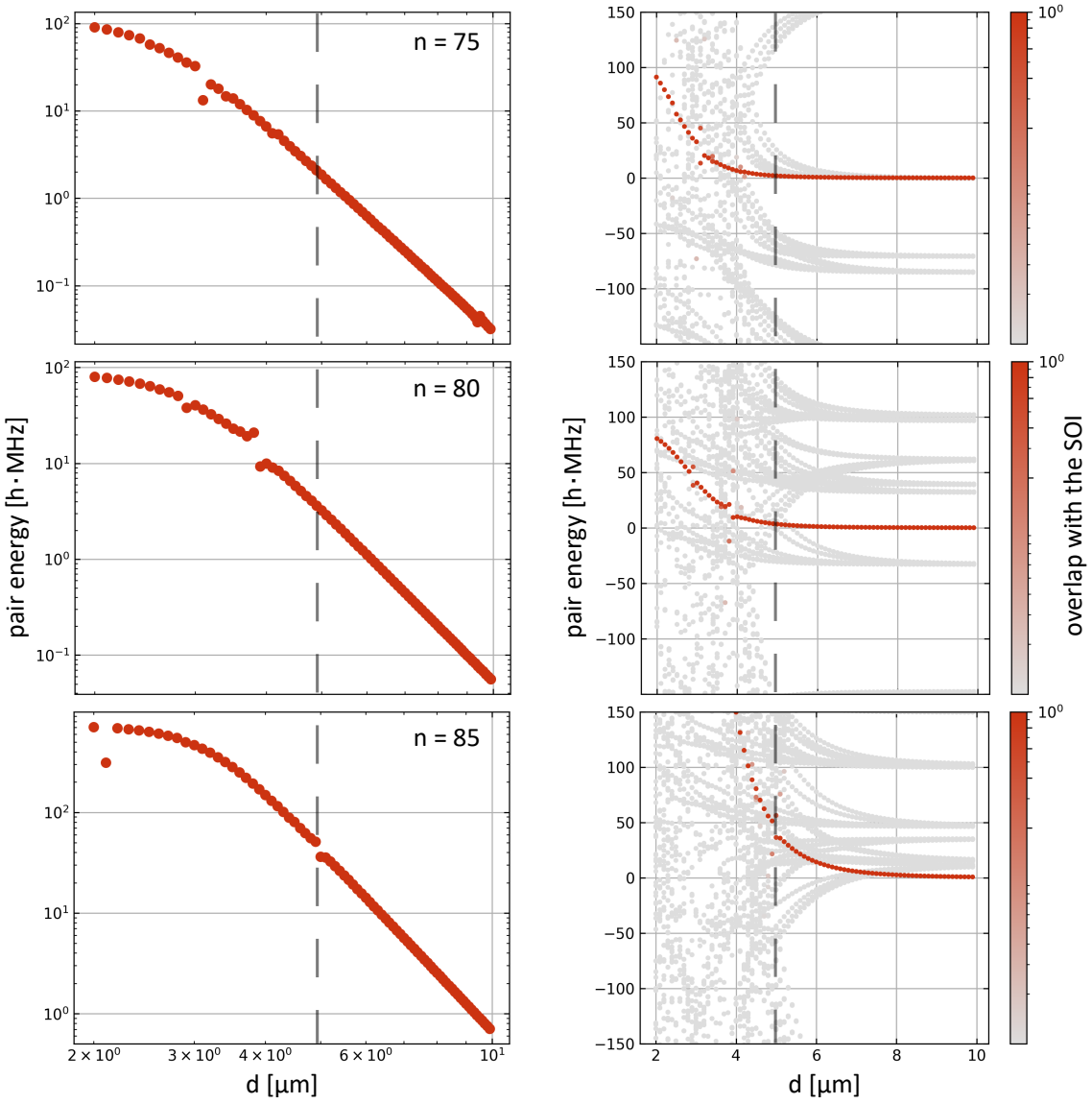

Figure 8.5.: Pair energies of two Rydberg atoms (see equation (6.7)) as a function of their interatomic distance for S-Rydberg states with $n = 75$, $n = 80$, and $n = 85$. The calculations are performed with the Python package *RYDCALC* [142]. The left panel uses a logarithmic scale, the right a linear scale. The heat map represents the overlap with the state of interest. The black dashed line marks the characteristic interatomic distance under typical conditions in a two-stage MOT.

figure 8.5 shows calculated pair energies for S-Rydberg states with principal quantum numbers $n = 75$, $n = 80$, and $n = 85$ as a function of the interatomic distance. The left panel presents the results in a logarithmic scale, while the right panel uses a linear scale. The heat map encodes the overlap with the corresponding state of interest (SOI), which in this case is the state the atoms are initially excited to. For low atomic densities – and consequently large interatomic separation – the pair interaction energy remains close to zero. As the density increases and separation decreases, the interaction energy rises. As expected for Rydberg atoms, the sensitivity to neighboring atoms grows with increasing n. This is clearly visible in the figure: the onset of the interaction induced energy shift occurs at larger interatomic distances for higher n.

While a large number of additional Rydberg pair states appear in figure 8.5 indicated in gray, their overlap with the experimentally addressed state of interest is typically much smaller. Consequently, these states are only weakly populated and mainly influence the dynamics indirectly through dipole-dipole-induced mixing. Nevertheless, their presence is crucial for an accurate description of interaction-induced energy shifts and avoided crossings.

The black dashed line indicates the expected interatomic separation of two Rydberg atoms of approximately $d = 5\,\mu\text{m}$ under the assumption of two single transition processes as described in section 8.2.2. For the $80\,S$ state, a small energy shift is apparent, but it is likely too weak to be detected. For lower-lying states, the interaction is clearly too weak to be resolved. In contrast, for the $85\,S$ state, the shift is considerably larger – on the order of the transition linewidth – indicating that the interactions should be readily observable.

Additionally, distinct resonant features appear at specific interatomic distances. These are likely signatures of Förster resonances, where near-degenerate pair states couple strongly via dipole-dipole interactions (see section 6.1). A detailed analysis of these resonances lies beyond the current scope, as we first focus on the non-resonant interactions.

8.3. Prospects for the Detection of Interactions in a Green Yb-MOT

The next step toward investigating Rydberg-Rydberg interactions is to operate the green MOT at the densities – and thus the interatomic distances – outlined in section 8.2. Under these conditions, the spatial profiles of the detected ion counts as a function of the vertical position of the Rydberg excitation beam (see Figure 8.2) can be systematically compared for different Rydberg states, in particular for states with principal quantum numbers $n \geqslant 85$.

As discussed in section 8.2.2, the achievable mean interatomic distance between two Rydberg atoms in our present experiment is $d \approx 5\,\mu\text{m}$. Furthermore, as outlined in section 8.2.3, for a Rydberg state with $n = 85$ at this interatomic distances, an energy-level

shift of sufficient magnitude to be experimentally detectable is expected.

If Rydberg-Rydberg interactions are significant, a characteristic flattening of these ion-count profiles is expected. Such a deviation from the non-interacting reference shape would provide a clear experimental signature of interaction-induced level shifts or excitation-blockade mechanisms.

Overall, the experiment is well prepared for the detection of Rydberg-Rydberg interactions. The achievable Rydberg-atom densities, the developed interaction-detection scheme, and the theoretical expectations regarding the relevant principal quantum numbers and the associated level shifts together provide a solid foundation for observing interaction effects.

9.

Outlook

This chapter aims to outline potential future directions for the experiment. Building upon the current results, one promising avenue is the further increase of atomic density combined with a reduction of the temperature, which may enable access to novel quantum regimes. Moreover, the implementation of additional trapping configurations could substantially enhance the degree of experimental control. Such extensions of the measurement capabilities would not only provide a more comprehensive characterization of the system, but also contribute to addressing unresolved challenges in the wider research context. The first part of this chapter outlines short-term objectives that are intended to enhance the current performance and stability of the experiment. The first improvement is the absorption imaging method, as described in section 9.1.1, while the second is an enhanced Rydberg excitation scheme, detailed in section 9.1.2. These immediate improvements provide the foundation for more ambitious developments, which are discussed in the second part. In this context, long-term perspectives are considered, including Förster resonance tuning via externally applied electric fields or Yb-Rydberg molecules that could significantly extend the experimental capabilities and thereby bring the setup to a new level of sophistication. Finally, potential measurement outcomes that may become achievable as a consequence of these long-term advancements are presented, highlighting the broader scientific opportunities that could emerge.

9.1. Short-Term Improvements

In this section, several short-term improvements are identified with the aim of enhancing the current performance of the experimental setup and systematically preparing the system for the planned future investigations. These measures focus on increasing experimental efficiency, improving stability and reproducibility, and enabling more precise control over relevant parameters for forthcoming studies.

9.1.1. Absorption Imaging

To enhance the detection of trapped atoms in both the one-stage and two-stage MOT, an additional imaging technique can be implemented. Until now, fluorescence imaging has been used to detect the atoms. While this method is sufficient for low atom numbers and moderate densities, it becomes increasingly inaccurate as the two-stage MOT reaches higher densities. In particular, fluorescence imaging requires a precise calibration to extract absolute densities, and in practice, the measured values often serve as estimates. In contrast, absorption imaging provides a more direct and quantitative measure of the atomic density, as the relation between the transmission of the imaging light and the atom number is well-defined. Moreover, absorption imaging allows for shorter exposure time.

The principle of absorption imaging is based on the attenuation of a resonant or near-resonant laser beam as it passes through an atomic cloud [144]. The absorption of the laser light by the atomic medium can be described by the Lambert-Beer law

$$I(x,y) = I_0(x,y)\,\exp(-\sigma\, n_{\mathrm{col}}(x,y))\ , \tag{9.1}$$

where $I_0(x,y)$ denotes the incident intensity in the absence of atoms, σ is the effective absorption cross section, and $n_{\mathrm{col}}(x,y)$ represents the column density along the imaging axis.

For a two-level system, the resonant absorption cross section is given by

$$\sigma_0 = \frac{3\lambda^2}{2\pi}\,, \tag{9.2}$$

with λ denoting the wavelength of the transition [40]. For Yb, equation (9.2) is a very good approximation, while for atoms with a more complex level structure, equation (9.2) has to be modified, in particular to account for angular momentum coupling. The column density $n_{\mathrm{col}}(x,y)$ along each pixel column of the CCD camera can then be calculated. The concept of absorption imaging involves three distinct images: the first is a dark image, taken without light or atoms. The second image captures the imaging light on the camera, but without any atoms present. The final image, the data image, is obtained with both the imaging light and the atoms. To correct for background light and the dark current of the camera, the dark image is subtracted from both the bright image and the absorption image. The resulting column density is therefore

$$n_{\mathrm{col}}(x,y) = \int n(x,y,z)\,dz = -\frac{1}{\sigma}\ln\!\left(\frac{I(x,y)}{I_0(x,y)}\right) = -\frac{1}{\sigma}\ln\!\left(\frac{I_{\mathrm{abs}}-I_{\mathrm{dark}}}{I_{\mathrm{bright}}-I_{\mathrm{dark}}}\right). \tag{9.3}$$

Integration over all columns yields the total atom number in the trap. By fitting an appropriate model to the spatial distribution of the atom number, the full density profile of the cloud can be extracted. Furthermore, by combining this method with variable expansion times of the atomic cloud, time-of-flight measurements can be performed, providing a precise determination of the temperature and allowing for a detailed characterization of

the thermal properties of the trapped ensemble. If absorption imaging is used to image optically trapped ensembles it might even allow to directly image the distribution of Rydberg excitations.

9.1.1.1. Experimental Requirements

As described above, absorption imaging requires a near-resonant laser with a beam diameter larger than the extent of the atomic trap. The required power is modest, typically not exceeding a few microwatts, and this light is largely already available on the optical table. As explained in section 3.2, the blue MOT light is switched using an acousto-optic modulator, with the first diffraction order employed for the experiment while the zeroth order is currently blocked. For absorption imaging, this existing light can be utilized by introducing an additional AOM for fine frequency tuning, shaping the beam with appropriate optics to achieve the desired profile, and coupling it into an optical fiber. The light can then be guided to the viewport opposite the CCD camera, enabling precise absorption measurements of the atomic cloud.

9.1.2. Rydberg Excitation Laser

The excitation of atoms to Rydberg states is currently implemented using the blue MOT beams to drive the transition to the intermediate state, followed by the DL Pro laser for the second photon, connecting the intermediate $^1P_1$ state to the desired Rydberg state (see section 3.3). To minimize spontaneous decay from the intermediate state, the excitation can alternatively be performed via a two-photon process in which the first excitation laser is further detuned from the$^1S_0 \rightarrow {}^1P_1$ transition. This approach reduces population of the short-lived $^1P_1$ level while maintaining coherent transfer. In this way, the number of atoms prepared in the Rydberg state of interest can be increased.

9.1.2.1. Experimental Requirements

To implement this two-photon excitation, a new laser system must be built and integrated into our apparatus. The wavelength of this laser should be close to that of the blue MOT laser but detuned from resonance by several hundred MHz to achieve the desired intermediate-state detuning. For frequency stabilization, an additional ytterbium spectroscopy setup can be employed, while an AOM allows fine tuning of the detuning. After stabilization, the laser light is coupled into an optical fiber for delivery to the experimental chamber. At the chamber, it is combined with the existing Rydberg excitation laser and spatially overlapped using an interference filter oriented at an appropriate angle. Coupling both lasers into the same fiber ensures excellent spatial overlap at the position of the trapped atoms, which is essential for maximizing the efficiency of Rydberg excitation.

This configuration not only minimizes population in the intermediate state, thereby reducing decoherence and spontaneous emission, but also allows precise control of the excitation strength and timing, which is crucial for coherent manipulation of the atomic ensemble.

9.2. Investigation of Rydberg-Rydberg-Interactions in Yb

The long-term goal of this experiment is to investigate and use interactions between ytterbium Rydberg atoms. As a basis, the preparation of the atomic ensemble has been improved by lowering the temperature and increasing the density up to $8 \times 10^{10}\,\mathrm{cm}^{-3}$ (see section 7.3). In this regime, we have developed a density-dependent Rydberg excitation and detection scheme as a first tool to probe Rydberg interactions (see section 8.1). A thorough study using this method to investigate Rydberg-Rydberg interactions in the green MOT is planned and will be carried out by a succeeding PhD student in the near future.

Once interactions have been observed, we intend to continue these studies using even denser atomic ensembles of atoms in optical dipole traps and optical lattices, which will be discussed in the following.

9.2.1. Optical Dipole Trap

A natural next step towards increasing the achievable atomic density even further and thus have direct access to the observation of interactions, is to transfer the atoms from the green MOT into an optical dipole trap (ODT) [145, 146].

The working principle of an optical dipole trap relies on the interaction between an induced dipole moment and an oscillating light field. When an atom is exposed to the electric field $\vec{E}$ of a laser, a dipole moment $\vec{d}$ is induced, governed by the complex atomic polarizability $\alpha(\omega)$ [145]

$$\vec{d} = \alpha(\omega)\,\vec{E}. \tag{9.4}$$

This phenomenon is the analogue of the static Stark effect (see section 2.2.1) for oscillating fields and is therefore referred to as the AC Stark effect. It results in a light-induced shift of the atomic energy levels, which depends on both the laser intensity and the detuning from resonance.

The potential energy of the induced dipole in the light field can be obtained by time averaging [145]

$$U_{\mathrm{dip}}(r) = -\frac{1}{2}\langle \vec{d}\cdot\vec{E}\rangle = -\frac{1}{2}\,\mathrm{Re}\big(\alpha(\omega)\big)\,|\vec{E}(r)|^2. \tag{9.5}$$

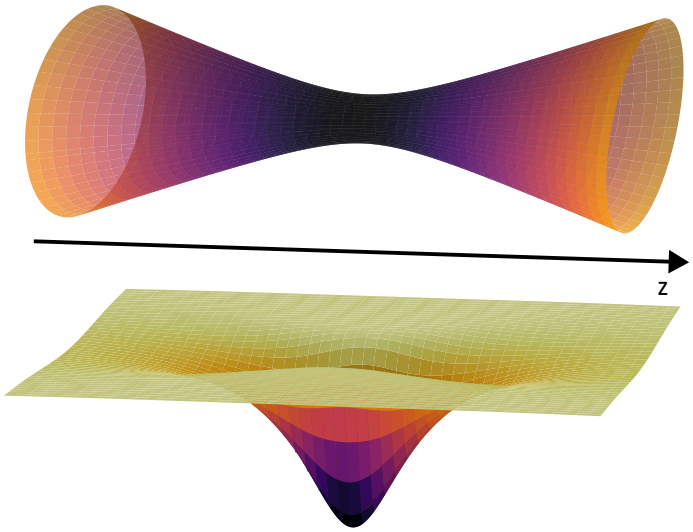

Figure 9.1.: Three-dimensional schematic representation of an optical dipole trap generated by a single focused Gaussian laser beam. The figure illustrates both the beam geometry and the associated optical potential. The lower panel shows the trapping potential along one spatial dimension, highlighting the confinement in the transverse direction. The propagation axis of the beam is indicated as the z-direction.

Using the relation between intensity and electric field amplitude, $I = 2\epsilon_0 c|\vec{E}(r)|^2$, this expression can be rewritten as

$$U_{\text{dip}}(r) = -\frac{1}{2\epsilon_0 c}\,\text{Re}\big(\alpha(\omega)\big)\,I(r). \tag{9.6}$$

The corresponding dipole force is obtained from the gradient of the potential

$$\vec{F}(r) = -\nabla U_{\text{dip}}(r) = \frac{1}{2\epsilon_0 c}\,\text{Re}\big(\alpha(\omega)\big)\,\nabla I(r). \tag{9.7}$$

Thus, the force is directly proportional to the intensity gradient of the trapping light.

For laser frequencies close to an atomic resonance, the polarizability can be expressed in terms of the natural linewidth Γ and the detuning $\Delta = \omega - \omega_0$ of the laser frequency from the atomic transition [145]

$$U_{\text{dip}}(r) \approx \frac{3\pi c^2}{2\omega_0^3}\,\frac{\Gamma}{\Delta}\,I(r). \tag{9.8}$$

For large red detuning ($\Delta < 0$), the spontaneous scattering rate is significantly reduced, minimizing heating and consequent atom loss. Simultaneously, the dipole potential becomes attractive, causing atoms to accumulate at the intensity maxima of the laser field.

The simplest geometry for an optical dipole trap is realized with a single Gaussian beam focused onto the atomic ensemble, as illustrated in figure 9.1. According to equation (9.7), the atoms are attracted towards the beam focus. This is reflected in the lower part of

the figure, which depicts the two-dimensional trapping potential across a transverse cross-section of the trap. The resulting confinement is anisotropic: strong in the transverse direction, but weak along the propagation axis due to the shallow intensity gradient. True three-dimensional confinement can be achieved by intersecting two beams which form a so-called crossed dipole trap [147], thereby generating tight trapping potentials in all spatial directions.

Such optical dipole traps enable atomic densities on the order of $10^{12}\,\mathrm{cm}^{-3}$ for a single beam and with a second beam and subsequent evaporative cooling, densities up to $10^{14}\,\mathrm{cm}^{-3}$ can be reached [148], allowing the formation of Bose-Einstein condensates of ytterbium atoms [85, 149, 150]. In this high-density regime, collective Rydberg effects become increasingly pronounced and thus more directly accessible for experimental investigation.

9.2.1.1. Experimental Requirements

Experimentally, several requirements must be fulfilled by the trapping laser. An important parameter is the wavelength, since the trap depth depends on the detuning from atomic resonances, as expressed in equation (9.8). In practice, the trap wavelength is chosen sufficiently far detuned to balance two competing requirements: achieving a deep trapping potential while keeping the rate of spontaneous photon scattering low. For ytterbium, a commonly used wavelength is 1064 nm [148, 151], while 760 nm has also been employed [152, 153].

At 760 nm, an additional and particularly important feature emerges: it coincides with a so-called magic wavelength for the clock transition between the $^1S_0$ and $^3P_0$ states [33]. Normally, different atomic states experience different AC Stark shifts due to the interaction with the laser's electric field, leading to unwanted differential shifts of transition frequencies. At the magic wavelength, however, the polarizabilities of the relevant states are identical, so that their Stark shifts cancel each other. Consequently, the clock transition remains unperturbed even if the atoms are confined in the optical dipole trap. This property is essential for high-precision spectroscopy and forms the basis for the operation of optical lattice clocks [154, 155]. In addition, triple magic wavelengths are available in two-electron atoms such as Yb [156]. At these wavelengths, the AC-Stark shifts of the ground state, the intermediate state, and the selected Rydberg state are identical.

A second key requirement is the available optical power. Since the trap depth scales with the beam intensity (see equation (9.8)), sufficient power is necessary to reach the desired confinement. Typical ODTs for Yb operate with laser powers of several watts or even tens of watts, particularly in crossed-beam geometries that demand deeper potentials [33, 148]. Nevertheless, experiments with smaller beam waists or optical tweezers demonstrate that stable trapping is also possible with only a few hundred milliwatts [54, 157]. The choice strongly depends on the experimental objectives, ranging from dense samples for evaporative cooling to single-atom control in tweezers.

Beyond wavelength and power, the laser's stability and beam quality are of fundamental importance. Frequency or power fluctuations directly translate into heating and fluctuations of the trapping potential, degrading the achievable phase-space density. Likewise, high spatial mode quality (close to TEM_{00}) is essential to achieve tight and well-defined foci, thereby ensuring a harmonic and controllable trapping potential.

For the subsequent stages of the experiment, a suitable laser source fulfilling these requirements is already available. It consists of a self-seeded tapered amplifier operating at a wavelength of approximately 760 nm, providing an output power of about 500 mW.

9.2.2. Optical Lattice

An additional and conceptually important step towards the realization of controlled many-body systems is the implementation of an optical lattice. By exploiting the existing optical resonator infrastructure (see figure 9.2a)), atoms can be localized at discrete lattice sites with separations on the order of the optical wavelength. This localization arises from the same trapping mechanism as in optical dipole traps, with atoms confined at the intensity maxima of the standing wave. This capability opens up a wide range of experimental possibilities. Most importantly, the precise control over the interatomic spacing allows one to investigate Rydberg-Rydberg interactions in a highly tunable and well-isolated environment [158, 159].

The periodic potential of an optical lattice originates from the interference of counter-propagating laser beams, typically realized by retro-reflecting a beam from resonator mirrors. In its simplest form, the resulting one-dimensional potential can be written as [160]

$$V(\vec{r}) = V_0 \sin^2(kx) \ , \tag{9.9}$$

where $k = 2\pi/\lambda$ is the laser wavenumber and V_0 denotes the lattice depth, which depends on the laser intensity and detuning via the AC-Stark effect [145]. Optical lattices can be realized in one, two, or three dimensions by combining appropriate beam geometries.

For comparison across different experimental configurations, the lattice depth is commonly expressed in units of the recoil energy,

$$E_r = \frac{\hbar^2 k^2}{2m} \ , \tag{9.10}$$

which corresponds to the kinetic energy acquired by an atom of mass m upon absorbing or emitting a lattice photon. To ensure effective confinement of atoms within the lattice sites, the lattice depth V_0 is typically chosen to be several tens of E_r. This condition guarantees that the atoms remain well localized and tunneling between neighboring sites can be controlled with high precision.

Therefore this energy scale characterizes the localization of atoms in the lattice wells and sets the fundamental scale for tunneling processes.

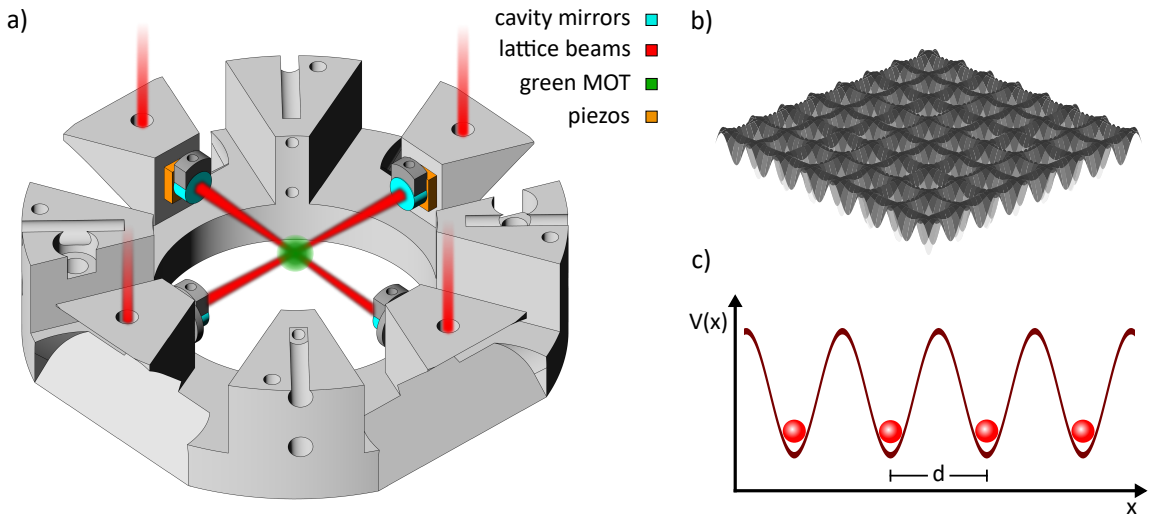

Figure 9.2.: Schematic overview of the resonator setup and the corresponding optical lattice potentials. (a) Intra-vacuum resonator configuration: two of the four cavity mirrors are mounted on piezoelectric actuators, enabling precise variation of the cavity length. Two intersecting laser beams form a two-dimensional optical lattice at the MOT position. (b) Resulting two-dimensional lattice potential. (c) One-dimensional cut through the potential, illustrating the periodic structure with lattice spacing d and a single atom localized in each potential well.

The lattice spacing d is given by half the laser wavelength, $d = \lambda/2$, due to the periodicity of the standing-wave intensity pattern (see figure 9.2c)). In a two-dimensional configuration, the superposition of two orthogonal standing waves gives rise to the periodic potential shown in figure 9.2b).

Compared to a continuous optical dipole trap, an optical lattice offers a set of discrete, well-defined trapping sites. This reduces collisional losses and decoherence, enhances reproducibility, and provides control over interatomic distances. Moreover, by tuning the lattice depth one can control the tunneling rate between neighboring sites, thereby enabling the study of coherent many-body dynamics. These features render optical lattices a versatile platform not only for controlled investigations of Rydberg interactions, but also for the quantum simulation of strongly correlated systems [49, 161–163].

9.2.2.1. Experimental Requirements

In principle, the implementation of an optical lattice requires two essential components: a stable laser source and a setup to create an optical standing wave, which in our case is a high-finesse optical resonator. For the generation of a two-dimensional lattice, two laser beams with sufficient optical power – capable of producing a lattice potential depth significantly exceeding the recoil energy – and an appropriate wavelength are required. This

ensures that atoms are well localized within the lattice sites and that tunneling between neighboring sites can be precisely controlled.

In the present setup, described in detail in chapter 3, four mirrors are already installed to provide the necessary optical access for lattice beam alignment. Since the requirements for the laser source are identical to those outlined in section 9.2.1.1, the same laser system can be employed for both purposes.

The optical resonator used in this work was originally constructed in the context of [164]. Its dielectric mirrors are optimized for operation at a wavelength of 760 nm, matching the wavelength of the laser source. The intra-cavity design offers high spatial mode stability, and one of the cavity mirrors for both resonators is mounted on a piezoelectric transducer. This configuration allows precise variation of the cavity length and enables controlled scanning of the resonance condition. In particular, the piezo actuators for both resonators (see orange elements in figure 9.2a)) provide a compact and efficient way of simultaneously tuning the cavities into resonance with the lattice laser.

9.3. Future Investigations

Once Rydberg-Rydberg interactions are established, it becomes possible to investigate and control the underlying dipole-dipole coupling mechanisms. Two experimentally accessible methods can be employed to achieve tunable interactions.

The first approach relies on Förster resonance tuning via externally applied electric fields. By adjusting the strength of the external field, the energy levels of the interacting Rydberg pair states can be shifted into or out of resonance, thereby enabling precise control over the dipole-dipole coupling strength. This technique has been successfully demonstrated, for example, by Altiere et al. [165] for rubidium atoms, where the electric field was used to sweep across Förster resonances and modulate the interaction from resonant to non-resonant regimes.

The second approach exploits state-selective light shifts induced by an additional off-resonant laser field. This laser introduces an AC Stark shift that modifies the energy separation between Rydberg pair states, allowing dynamic tuning of the interaction landscape. By carefully adjusting the laser intensity and detuning, the system can be driven from a resonant to a non-resonant coupling regime. This method was experimentally demonstrated by de Léséleuc et al. [166], providing a highly versatile mechanism for optical control of dipole-dipole interactions.

Another promising direction for future investigations lies in combining the expertise in Rydberg atom physics and the experimental capabilities of the present setup with the knowledge developed in the second experiment of our working group, which focuses on ytterbium-rubidium molecules [151]. The intersection of Rydberg and molecular physics opens the field of Rydberg molecules, a fascinating class of ultralong-range bound states

that emerge from interactions involving at least one atom in a highly excited Rydberg state.

Two principal formation pathways can be envisioned:

Rydberg-ground-state molecules. In the first scenario, a single Rydberg atom interacts with a neighboring ground-state atom. The scattering of the Rydberg electron off the neutral ground-state atom induces an attractive potential between the Rydberg ionic core and the ground-state atom, resulting in bound states at extraordinarily large internuclear separations – often on the order of hundreds of nanometers.

Experimentally, such molecules can be created by exciting ultracold atoms into Rydberg states within a dense atomic sample. If a ground-state atom lies within the spatial extent of the Rydberg electron's orbital, photoassociation resonances can drive the pair into a molecular bound state. Detection is typically achieved via field-ionization spectroscopy, where characteristic molecular signatures appear as small energy shifts relative to the atomic Rydberg lines.

These ultralong-range Rydberg molecules were first theoretically predicted by Greene et al. [167] and later experimentally observed by Bendkowsky et al. [27] in rubidium, marking the first realization of molecular binding mediated by a Rydberg electron.

Rydberg macrodimers. In the second approach, two atoms are both excited to Rydberg states. The resulting strong dipole-dipole or van der Waals interactions between the Rydberg atoms can, under specific conditions, give rise to potential wells that support bound molecular states, known as Rydberg macrodimers. These states typically occur for carefully chosen combinations of the principal and orbital quantum numbers (n, l) and can be tuned using external electric fields. In particular, electric fields can be employed to bring atomic pair states into Förster resonance, thereby enhancing the interaction strength and stabilizing the bound state.

Rydberg macrodimers were first theoretically predicted by Boisseau et al. [168] and subsequently observed experimentally by Deiglmayr et al. [111]. More recently, their properties and experimental realizations have been summarized comprehensively by Hollerith et al. [169]. These macrodimers exhibit internuclear separations on the micrometer scale, making them among the largest known diatomic molecules and an exciting platform for exploring long-range quantum interactions.

This chapter has demonstrated that, beyond establishing the foundation for exploring Rydberg-Rydberg interactions, the path is now open for further advances in Rydberg physics accessible in our experiment, promising new opportunities in the pursuit of fundamental research.

A.

Appendix

A.1. Circuit Diagram

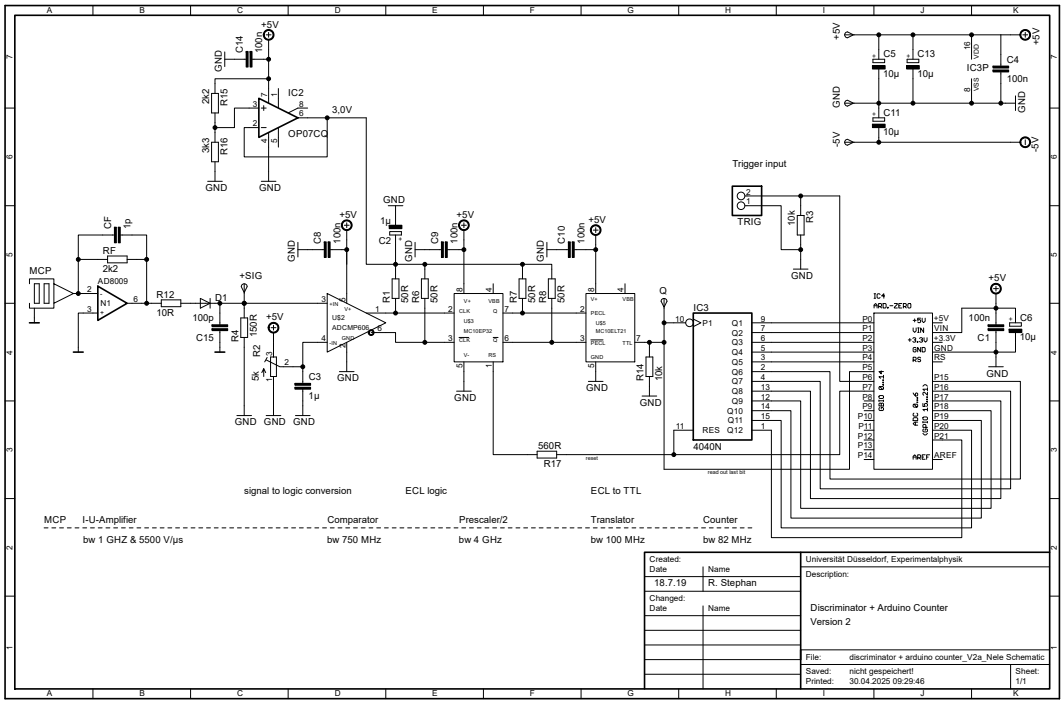

Figure A.1.: Electronic circuit diagram of the MCP-based ion counting unit.

A.2. Measured Rydberg Transition Data

In this section the energies of all measured Rydberg transitions of the different isotopes are listed. All values are given in wavenumbers $\tilde{\nu} = \nu/c = E/(hc)$ in units of cm^{-1}. The

uncertainty of the experimentally determined energies is $0,0023\,\mathrm{cm}^{-1}$ corresponding to the value of 70 MHz for the frequencies stated in the text.

Table A.1.: Energies of the S-states of the bosonic isotopes ^{176}Yb, ^{174}Yb and ^{172}Yb. The values for ^{174}Yb are taken from [89] and the values for the other t isotopes are referenced to ^{174}Yb.

n	176	174	172
35	50326.8265	50326.848499	50326.8715
40	50357.0712	50357.093890	50357.1149
45	50376.8836	50376.905462	50376.9283
50	50390.5625	50390.582791	50390.6060
55	50400.3976	50400.419329	50400.4419
60	50407.7077	50407.729587	50407.7526
65	50413.2865	50413.309647	50413.3309
70	50417.6441	50417.665460	50417.6870
75	50421.1090	50421.130458	50421.1534
80	50423.9107	50423.932196	50423.9545

Table A.2.: Energies of the D-states of the bosonic isotopes ^{176}Yb, ^{174}Yb and ^{172}Yb.

n	176		174		172	
	$^3D_2$	$^1D_2$	$^3D_2$	$^1D_2$	$^3D_2$	$^1D_2$
35	50337.5493	50337.7900	50337.5701	50337.8117	50337.5931	50337.8344
40	50363.9699	50364.1245	50363.9908	50364.1451	50364.0138	50364.1683
45	50381.5780	50381.6828	50381.5989	50381.7042	50381.6181	50381.7268
50	50393.8987	50393.9732	50393.9195	50393.9954	50393.9424	50394.0175
55	50402.8558	50402.9094	50402.8771	50402.9318	50402.8996	50402.9535
60	50409.5699	50409.6122	50409.5916	50409.6338	50409.6139	50409.6563
65	50414.7324	50414.7641	50414.7530	50414.7867	50414.7751	50414.8088
70	50418.7888	50418.8130	50418.8097	50418.8347	50418.8330	50418.8570
75	50422.0316	50422.0507	50422.0525	50422.0722	50422.0754	50422.0944
80	50424.6655	50424.6807	50424.6864	50424.7021	50424.7094	50424.7253

Table A.3.: Energies E_{exp} of the S-states of the fermionic isotope ^{171}Yb. In addition, the values E_{th} of Peper et al. [7] and the difference between the two values are listed. The first column indicates in which scan the line has been observed where the scans are labeled by the principal quantum number and angular momentum of the reference transition in ^{174}Yb. Transitions labeled "S_S" denote singlet-connected S-states, while those labeled "S_T" correspond to triplet-connected S-states. The last column contains the value of the effective principal quantum number of each state.

scan	E_{exp} [cm^{-1}]	E_{th} [cm^{-1}][7]	$E_{th}-E_{exp}$ [MHz]	label	n^*[7]
$(n = 35)$ S	50326.9109	50326.910209	-21	S_S	30.7165912
$(n = 40)$ S	50357.1635	50357.164684	35	S_S	35.7103372
$(n = 45)$ S	50376.9855	50376.985570	2	S_S	40.7045350
$(n = 50)$ S	50390.6723	50390.671919	-11	S_S	45.6991806
$(n = 55)$ S	50400.5155	50400.516695	36	S_S	50.6942249
$(n = 60)$ S	50407.8340	–	–	S_S	–
$(n = 60)$ D	50409.7143	50409.716214	57	S_T	57.2329053
$(n = 65)$ S	50413.4184	50413.418825	13	S_S	60.6845399
$(n = 65)$ D	50414.7942	50414.793977	-7	S_T	62.1351847
$(n = 70)$ S	50417.7771	50417.778142	31	S_S	65.6785389
$(n = 70)$ D	50418.7876	50418.787441	-5	S_T	67.0215248
$(n = 75)$ S	50421.2462	50421.244117	-62	S_S	70.6688628
$(n = 80)$ S	50424.0431	50424.038725	-131	S_S	75.6425488
$(n = 80)$ D	50424.5332	50424.530333	-86	S_S	76.6310624
$(n = 80)$ D	50424.5971	50424.598029	28	S_T	76.7702433

Table A.4.: Energies E_{exp} of the D-states of the fermionic isotope ^{171}Yb. In addition, the values E_{th} of Peper et al. [7] and the difference between the two values are listed. The first column indicates in which scan the line has been observed where the scans are labeled by the principal quantum number and angular momentum of the reference transition in ^{174}Yb. Transitions labeled "3/2" denote D-states with $F = 3/2$, while those labeled "5/2" correspond to D-states with $F = 5/2$. The last column contains the value of the effective principal quantum number of each state.

scan	E_{exp} [cm^{-1}]	E_{th} [cm^{-1}][7]	$E_{th}-E_{exp}$ [MHz]	label	n^*[7]
$(n = 35)$ D	50337.7257	50337.724843	-25	5/2	32.2526479
$(n = 35)$ D	50337.9204	50337.920725	10	5/2	32.2826335
$(n = 35)$ D	50337.9501	50337.950422	9	3/2	32.2871868
$(n = 40)$ D	50364.1421	50364.141606	-15	5/2	37.2524158
$(n = 40)$ D	50364.2681	50364.266902	-37	5/2	37.2819641
$(n = 40)$ D	50364.2884	50364.286299	-64	3/2	37.2865448
$(n = 45)$ D	50381.7480	50381.749055	30	5/2	42.2523037
$(n = 45)$ D	50381.8336	50381.834157	18	5/2	42.2815828
$(n = 45)$ D	50381.8464	50381.847423	29	3/2	42.2861525
$(n = 50)$ D	50394.0687	50394.069227	15	5/2	47.2522382
$(n = 50)$ D	50394.1298	50394.129706	-3	5/2	47.2813378
$(n = 50)$ D	50394.1391	50394.139148	1	3/2	47.2858856
$(n = 55)$ D	50403.0239	50403.025097	37	5/2	52.2521947
$(n = 55)$ D	50403.0693	50403.069629	10	5/2	52.2811659
$(n = 55)$ D	50403.0764	50403.076577	5	3/2	52.2856906
$(n = 60)$ D	50409.7377	50409.738747	32	5/2	57.2521625
$(n = 60)$ D	50409.7720	50409.772488	14	5/2	57.2810347
$(n = 60)$ D	50409.7769	50409.777746	26	3/2	57.2855380
$(n = 65)$ D	50414.9009	50414.900673	-7	5/2	62.2521354
$(n = 65)$ D	50414.9269	50414.926845	-3	5/2	62.2809237
$(n = 65)$ D	50414.9304	50414.930918	16	3/2	62.2854070
$(n = 70)$ D	50418.9571	50418.954678	-73	5/2	67.2521085
$(n = 70)$ D	50418.9698	50418.975377	167	5/2	67.2808137
$(n = 70)$ D	50418.9802	50418.978592	-48	3/2	67.2852759
$(n = 75)$ S	50421.1998	50421.195613	-126	5/2	70.5909944
$(n = 75)$ D	50422.2019	–	–	5/2	–
$(n = 75)$ D	50422.2138	50422.213168	-19	5/2	72.2806649
$(n = 75)$ D	50422.2198	50422.215741	-122	3/2	72.2850922
$(n = 80)$ D	50424.8340	50424.829519	-136	5/2	77.2519712
$(n = 80)$ D	50424.8490	50424.844902	-123	3/2	77.2843039
$(n = 80)$ D	50424.8772	50424.875086	-63	3/2	77.3478673

Table A.5.: Energies of unassigned transitions of the fermionic isotope ^{171}Yb. The first column indicates in which scan the line has been observed where the scans are labeled by the principal quantum number and angular momentum of the reference transition in ^{174}Yb. The labels Xn are used to identify the states in the corresponding scans.

scan	E_{exp} [cm^{-1}]	label
$(n = 70)$ S	50417.7849	X1
$(n = 70)$ D	50418.9859	X2
$(n = 75)$ D	50422.2576	X3
$(n = 80)$ D	50424.5826	X4
$(n = 80)$ D	50424.7347	X5
$(n = 80)$ D	50424.8582	X6

Table A.6.: Energies E_{exp} observed in the "S-state scans" of the fermionic isotope ^{173}Yb. The first column indicates in which scan the line has been observed where the scans are labeled by the principal quantum number and angular momentum of the reference transition in ^{174}Yb. Transitions labeled "S_S" are attributed to singlet-connected S-states, while those labeled "X" could not be attributed.

scan	E_{exp} [cm^{-1}]	label
$(n = 35)$ S	50326.8838	S_S
$(n = 40)$ S	50357.1414	S_S
$(n = 45)$ S	50376.9697	S_S
$(n = 50)$ S	50390.6664	S_S
$(n = 55)$ S	50400.5201	S_S
$(n = 60)$ S	50407.8492	S_S
$(n = 65)$ S	50413.4423	S_S
$(n = 70)$ S	50417.8110	X
$(n = 70)$ S	50417.8223	X
$(n = 70)$ S	50417.9221	X
$(n = 70)$ S	50417.9391	X
$(n = 70)$ S	50417.9554	X
$(n = 70)$ S	50417.9717	X
$(n = 75)$ S	50421.2877	S_S
$(n = 80)$ S	50424.0687	X
$(n = 80)$ S	50424.0835	X
$(n = 80)$ S	50424.1006	X

Table A.7.: Energies E_{exp} observed in the "D-state scans" of the fermionic isotope ^{173}Yb. The first column indicates in which scan the line has been observed where the scans are labeled by the principal quantum number and angular momentum of the reference transition in ^{174}Yb. Labels Bn, Cn correspond to groups of states which are apparently related, while those labeled "S_T" correspond to triplet-connected S-states. States labeled "X" could not be attributed.

scan	E_{exp} [cm^{-1}]	label	scan	E_{exp} [cm^{-1}]	label
$(n = 35)$ D	50337.7778	C1	$(n = 55)$ D	50403.0912	C1
	50337.7974	C2		50403.0934	C2
	50337.8173	C3		50403.0974	C3
	50337.8296	C4		50403.1319	B3
	50337.9357	B4		50403.1358	B2
	50337.9515	B3		50403.1403	B1
	50337.9705	B2	$(n = 60)$ D	50409.8062	C1
	50337.9917	B1		50409.8079	C2
$(n = 40)$ D	50364.2005	C1		50409.8378	B3
	50364.2111	C2		50409.8403	B2
	50364.2204	C3		50409.8436	B1
	50364.2274	C4	$(n = 65)$ D	50414.9775	C
	50364.3021	B4		50414.9977	B
	50364.3125	B3	$(n = 70)$ D	50418.9614	S_T
	50364.3255	B2		50419.0278	C
	50364.3388	B1		50419.0492	B
$(n = 45)$ D	50381.8105	C1		50419.0741	X
	50381.8166	C2	$(n = 75)$ D	50422.1503	S_T
	50381.8228	C3		50422.1642	X
	50381.8271	C4		50422.1707	X
	50381.8797	B4		50422.2686	C
	50381.8858	B3		50422.2864	B
	50381.8937	B2	$(n = 80)$ D	50424.6841	X
	50381.9032	B1		50424.7463	S_T
$(n = 50)$ D	50394.1327	C1		50424.9023	C
	50394.1375	C2		50424.9176	B
	50394.1437	C3		50424.9291	X
	50394.1873	B3			
	50394.1928	B2			
	50394.1982	B1			

Bibliography

[1] Christian Halter. “Rydberg spectroscopy in a gas of ultracold Ytterbium atoms”. PhD thesis. Heinrich-Heine-Universität Düsseldorf, 2021.

[2] Bastian Schepers. “Aufbau einer Apparatur für Experimente mit lasergekühltem Ytterbium”. Master thesis. Heinrich-Heine-Universität Düsseldorf, 2016.

[3] Vitali D. Ovsiannikov, Andrei Derevianko, and Kurt Gibble. Rydberg Spectroscopy in an Optical Lattice: Blackbody Thermometry for Atomic Clocks. Phys. Rev. Lett. 107 (Aug. 2011), p. 093003.

[4] Zhubing Jia, William Huie, Lintao Li, Won Kyu Calvin Sun, Xiye Hu, Aakash, Healey Kogan, Abhishek Karve, Jong Yeon Lee, and Jacob P. Covey. An architecture for two-qubit encoding in neutral ytterbium-171 atoms. npj Quantum Information 10.1 (2024), p. 106.

[5] Samuel Saskin. “Building Quantum Systems with Ytterbium Rydberg Arrays”. PhD thesis. Princeton University, 2021.

[6] Sebastian Weber, Christoph Tresp, Henri Menke, Alban Urvoy, Ofer Firstenberg, Hans Peter Büchler, and Sebastian Hofferberth. Tutorial: Calculation of Rydberg interaction potentials. J. Phys. B: At. Mol. Opt. Phys. 50.13 (2017), p. 133001.

[7] Michael Peper, Yiyi Li, Daniel Y. Knapp, Mila Bileska, Shuo Ma, Genyue Liu, Pai Peng, Bichen Zhang, Sebastian P. Horvath, Alex P. Burgers, and Jeff D. Thompson. Spectroscopy and Modeling of ^{171}Yb Rydberg States for High-Fidelity Two-Qubit Gates. Phys. Rev. X 15 (Jan. 2025), p. 011009.

[8] A. Einstein. Ist die Trägheit eines Körpers von seinem Energieinhalt abhängig?. Annalen der Physik 323.13 (1905), pp. 639–641.

[9] Francis W. Aston. *Mass Spectra and Isotopes*. Nobel Lecture. Dec. 1922.

[10] Igor E. Tamm and Andrei D. Sakharov. “Otchety o magnitnom termoyadernom reaktore”. *Fizika plazmy i problema upravlyaemykh termoyadernykh reaktsii*. Original in Russian; reports from 1950-1951 on toroidal plasma magnetic confinement. Izdatel’stvo AN SSSR, 1958.

[11] Jr. Spitzer Lyman. The Stellarator Concept. The Physics of Fluids 1.4 (Jul. 1958), pp. 253–264.

[12] Felix Bloch. Über die Quantenmechanik der Elektronen in Kristallgittern. Zeitschrift für Physik 52.7 (Jul. 1929), pp. 555–600.

[13] Clarence Zener. A Theory of the Electrical Breakdown of Solid Dielectrics. Proceedings of the Royal Society of London 145.855 (1934), pp. 523–529.

[14] John Bardeen and Walter H. Brattain. The Transistor, A Semi-Conductor Triode. Physical Review 74.2 (1948), pp. 230–231.

[15] Johannes Robert Rydberg. *Recherches sur la constitution des spectres d'émission des éléments chimiques*. fr. Kungliga vetenskapsakademiens handlingar 11. Kungliga Vetenskapsakademien, 1890.

[16] Niels Bohr. On the Constitution of Atoms and Molecules. Philosophical Magazine 26.153 (1913), pp. 1–25.

[17] E. Schrödinger. Quantisierung als Eigenwertproblem. Annalen der Physik 384.4 (1926), pp. 361–376.

[18] Thomas F Gallagher. *Rydberg atoms*. Vol. 3. Cambridge University Press, 2005.

[19] P. Komár, T. Topcu, E. M. Kessler, A. Derevianko, V. Vuletić, J. Ye, and M. D. Lukin. Quantum Network of Atom Clocks: A Possible Implementation with Neutral Atoms. Physical Review Letters 117.6 (Aug. 2016), p. 060506.

[20] William J. Eckner, Nelson Darkwah Oppong, Alec Cao, Aaron W. Young, William R. Milner, John M. Robinson, Jun Ye, and Adam M. Kaufman. Realizing spin squeezing with Rydberg interactions in an optical clock. Nature 621.7980 (2023), pp. 734–739.

[21] Mohammad Noaman, Donald W. Booth, and James P. Shaffer. Rydberg-Atom Sensors in Bichromatic Radio-Frequency Fields. Phys. Rev. Appl. 20 (Aug. 2023), p. 024068.

[22] Hadi Amarloo, Mohammad Noaman, Su-Peng Yu, Donald Booth, Somayeh Mirzaee, Rajesh Pandiyan, Florian Christaller, and James P. Shaffer. A photonic crystal receiver for Rydberg atom-based sensing. Communications Engineering 4.1 (2025), p. 70.

[23] Igor I. Ryabtsev, Denis B. Tretyakov, and Ilya I. Beterov. Applicability of Rydberg atoms to quantum computers. Journal of Physics B: Atomic, Molecular and Optical Physics 38.2 (Jan. 2005), S421.

[24] M. Saffman. Quantum computing with atomic qubits and Rydberg interactions: progress and challenges. Journal of Physics B: Atomic, Molecular and Optical Physics 49.20 (Oct. 2016), p. 202001.

[25] Sam R. Cohen and Jeff D. Thompson. Quantum Computing with Circular Rydberg Atoms. PRX Quantum 2 (Aug. 2021), p. 030322.

[26] Serge Haroche. Nobel Lecture: Controlling photons in a box and exploring the quantum to classical boundary. Rev. Mod. Phys. 85 3 (Jul. 2013), pp. 1083–1102.

[27] Vera Bendkowsky, Björn Butscher, Johannes Nipper, James P. Shaffer, Robert Löw, and Tilman Pfau. Observation of ultralong-range Rydberg molecules. Nature 458.7241 (2009), pp. 1005–1008.

[28] J. Farley, P. Tsekeris, and R. Gupta. Hyperfine-structure measurements in the Rydberg S and P states of rubidium and cesium. Phys. Rev. A 15 4 (Apr. 1977), pp. 1530–1536.

[29] D R Meacher, P E Meyler, I G Hughes, and P Ewart. Observations of the collapse and fractional revival of a Rydberg wavepacket in atomic rubidium. Journal of Physics B: Atomic, Molecular and Optical Physics 24.3 (Feb. 1991), p. L63.

[30] G. Raithel and H. Walther. Ionization energy of rubidium Rydberg atoms in strong crossed electric and magnetic fields. Phys. Rev. A 49 3 (Mar. 1994), pp. 1646–1665.

[31] Craig J. Sansonetti and C. J. Lorenzen. Doppler-free resonantly enhanced two-photon spectroscopy of np and nf Rydberg states in atomic cesium. Phys. Rev. A 30 4 (Oct. 1984), pp. 1805–1811.

[32] C Aman and L Holmlid. Rydberg states of caesium from a diffusion source: pulsed field ionization and lifetimes. Journal of Physics D: Applied Physics 24.7 (Jul. 1991), p. 1049.

[33] Andrew D. Ludlow, Martin M. Boyd, Jun Ye, E. Peik, and P. O. Schmidt. Optical atomic clocks. Rev. Mod. Phys. 87 2 (Jun. 2015), pp. 637–701.

[34] Guido Pagano, Marco Mancini, Giacomo Cappellini, Pietro Lombardi, Florian Schäfer, Hui Hu, Xia-Ji Liu, Jacopo Catani, Carlo Sias, Massimo Inguscio, and Leonardo Fallani. A one-dimensional liquid of fermions with tunable spin. Nature Physics 10.3 (2014), pp. 198–201.

[35] G. Audi, O. Bersillon, J. Blachot, and A. H. Wapstra. The Nubase evaluation of nuclear and decay properties. Nuclear Physics A 729.1 (2003). The 2003 NUBASE and Atomic Mass Evaluations, pp. 3–128.

[36] Bo Song, Chengdong He, Shanchao Zhang, Elnur Hajiyev, Wei Huang, Xiong-Jun Liu, and Gyu-Boong Jo. Spin-orbit-coupled two-electron Fermi gases of ytterbium atoms. Phys. Rev. A 94 (Dec. 2016), p. 061604.

[37] A. Miethke, Kozhiparambil Sajith, and A. Görlitz. Isotope dependence of ytterbium Rydberg states. Manuscript has been submitted to the Journal of Physics B. (2026).

[38] William D. Phillips. Nobel Lecture: Laser cooling and trapping of neutral atoms. Rev. Mod. Phys. 70 3 (Jul. 1998), pp. 721–741.

[39] E. L. Raab, M. Prentiss, Alex Cable, Steven Chu, and D. E. Pritchard. Trapping of Neutral Sodium Atoms with Radiation Pressure. Phys. Rev. Lett. 59 23 (Dec. 1987), pp. 2631–2634.

[40] Peter van der Straten Harold J. Metcalf. *Laser Cooling and Trapping*. Vol. 1. Springer, 1999.

[41] Alexander Batär. "Erzeugung und Charakterisierung ultrakalter Rubidium- und Ytterbiumatome - Auf dem Weg zu einem gemischten Quantengas". PhD thesis. Heinrich-Heine-Universität Düsseldorf, 2005.

[42] Robert Löw, Hendrik Weimer, Johannes Nipper, Jonathan B Balewski, Björn Butscher, Hans Peter Büchler, and Tilman Pfau. An experimental and theoretical guide to strongly interacting Rydberg gases. Journal of Physics B: Atomic, Molecular and Optical Physics 45.11 (May. 2012), p. 113001.

[43] C. L. Vaillant, M. P. A. Jones, and R. M. Potvliege. Long-range Rydberg-Rydberg interactions in calcium, strontium and ytterbium. Journal of Physics B: Atomic, Molecular and Optical Physics 45.13 (2012), p. 135004.

[44] Yu-Chi Chen, Shao-Cheng Fang, Hsuan-Jui Su, and Yi-Hsin Chen. Electric field sensing via Rydberg electromagnetically induced transparency using Zeeman and Stark effects. Journal of Applied Physics 138.9 (Sep. 2025), p. 094501.

[45] Bang Liu, Li-Hua Zhang, Zong-Kai Liu, Zheng-Yuan Zhang, Zhi-Han Zhu, Wei Gao, Guang-Can Guo, Dong-Sheng Ding, and Bao-Sen Shi. Highly Sensitive Measurement of a Megahertz rf Electric Field with a Rydberg-Atom Sensor. Phys. Rev. Appl. 18 (Jul. 2022), p. 014045.

[46] Richard P. Feynman. Simulating physics with computers. International Journal of Theoretical Physics 21.6 (1982), pp. 467–488.

[47] D. Jaksch, J. I. Cirac, P. Zoller, S. L. Rolston, R. Côté, and M. D. Lukin. Fast Quantum Gates for Neutral Atoms. Phys. Rev. Lett. 85 10 (Sep. 2000), pp. 2208–2211.

[48] M. D. Lukin, M. Fleischhauer, R. Cote, L. M. Duan, D. Jaksch, J. I. Cirac, and P. Zoller. Dipole Blockade and Quantum Information Processing in Mesoscopic Atomic Ensembles. Phys. Rev. Lett. 87 (Jun. 2001), p. 037901.

[49] Hendrik Weimer, Markus Müller, Igor Lesanovsky, Peter Zoller, and Hans Peter Büchler. A Rydberg quantum simulator. Nature Physics 6.5 (2010), pp. 382–388.

[50] P. Pillet and T. F. Gallagher. Rydberg atom interactions from 300 K to 300 K. Journal of Physics B: Atomic, Molecular and Optical Physics 49.17 (2016), p. 174003.

[51] Antoine Browaeys, Daniel Barredo, and Thierry Lahaye. Experimental investigations of dipole-dipole interactions between a few Rydberg atoms. Journal of Physics B: Atomic, Molecular and Optical Physics 49.15 (Jun. 2016), p. 152001.

[52] M. Saffman, T. G. Walker, and K. Mølmer. Quantum information with Rydberg atoms. Rev. Mod. Phys. 82 3 (Aug. 2010), pp. 2313–2363.

[53] J. P. Hague and C. MacCormick. Bilayers of Rydberg Atoms as a Quantum Simulator for Unconventional Superconductors. Phys. Rev. Lett. 109 (Nov. 2012), p. 223001.

[54] Alec Jenkins, Joanna W. Lis, Aruku Senoo, William F. McGrew, and Adam M. Kaufman. Ytterbium Nuclear-Spin Qubits in an Optical Tweezer Array. Phys. Rev. X 12 (May. 2022), p. 021027.

[55] D. Tong, S. M. Farooqi, J. Stanojevic, S. Krishnan, Y. P. Zhang, R. Côté, E. E. Eyler, and P. L. Gould. Local Blockade of Rydberg Excitation in an Ultracold Gas. Phys. Rev. Lett. 93 (Aug. 2004), p. 063001.

[56] C Halter, A Miethke, C Sillus, A Hegde, and A Görlitz. Trap-loss spectroscopy of Rydberg states in ytterbium. Journal of Physics B: Atomic, Molecular and Optical Physics 56.5 (Feb. 2023), p. 055001.

[57] David J. Griffiths and Darrell F. Schroeter. *Introduction to Quantum Mechanics*. 3rd. Cambridge University Press, 2018.

[58] B. H. Bransden and C. J. Joachain. *Physics of Atoms and Molecules*. 2nd. Pearson Education, 2003.

[59] Ugo Fano. Effects of Configuration Interaction on Intensities and Phase Shifts. Physical Review A 2.2 (1970), pp. 353–365.

[60] Gordon W. F. Drake, ed. *Springer Handbook of Atomic, Molecular, and Optical Physics*. New York: Springer, 2006.

[61] C L Vaillant, M P A Jones, and R M Potvliege. Multichannel quantum defect theory of strontium bound Rydberg states. Journal of Physics B: Atomic, Molecular and Optical Physics 47.15 (Jul. 2014), p. 155001.

[62] R. M. Potvliege. mqdtfit: A collection of Python functions for empirical multichannel quantum defect calculations. Computer Physics Communications 300 (2024), p. 109172.

[63] Stephen D. Hogan. Rydberg-Stark deceleration of atoms and molecules. EPJ Techniques and Instrumentation 3.1 (2016), p. 2.

[64] R. F. Stebbings and F. B. Dunning. *Rydberg States of Atoms and Molecules*. Cambridge, England: Cambridge University Press, 1983.

[65] A. Alijah, J. T. Broad, and J. Hinze. Stark effect and field ionisation of atomic hydrogen. Journal of Physics B: Atomic and Molecular Physics 19.17 (Sep. 1986), pp. 2617–2634.

[66] L. D. Landau. Zur Theorie der Energieübertragung. II. Physikalische Zeitschrift der Sowjetunion 2 (1932), pp. 46–51.

[67] C. Zener. Non-adiabatic crossing of energy levels. Proceedings of the Royal Society of London. Series A 137.833 (1932), pp. 696–702.

[68] B.V. Numerov. A Method of Extrapolation of Perturbations. Monthly Notices of the Royal Astronomical Society 84 (1924), pp. 592–601.

[69] Carl Runge. Ueber die numerische Auflösung von Differentialgleichungen. Mathematische Annalen 46.2 (Jun. 1895), pp. 167–178.

[70] Martin Wilhelm Kutta. Beitrag zur näherungsweisen Integration totaler Differentialgleichungen. German. Zeitschrift für Mathematik und Physik 46 (1901), pp. 435–453.

[71] M.J. Seaton. Coulomb functions for attractive and repulsive potentials and for positive and negative energies. Computer Physics Communications 146.2 (2002), pp. 225–249.

[72] M J Seaton. Quantum defect theory. Reports on Progress in Physics 46.2 (Feb. 1983), pp. 167–257.

[73] Chris H. Greene and Mireille Aymar. Spin-orbit effects in the heavy alkaline-earth atoms. Phys. Rev. A 44 3 (Aug. 1991), pp. 1773–1790.

[74] Chia-Ming Lee and K. T. Lu. Spectroscopy and Collision Theory. II. The Ar Absorption Spectrum. Phys. Rev. A 8 3 (Sep. 1973), pp. 1241–1257.

[75] Christopher L. Holloway, Joshua A. Gordon, Andrew Schwarzkopf, David A. Anderson, Stephanie A. Miller, Nithiwadee Thaicharoen, and Georg Raithel. Sub-wavelength imaging and field mapping via electromagnetically induced transparency and Autler-Townes splitting in Rydberg atoms. Applied Physics Letters 104.24 (Jun. 2014), p. 244102.

[76] Haoquan Fan, Santosh Kumar, Jonathon Sedlacek, Harald Kübler, Shaya Karimkashi, and James P Shaffer. Atom based RF electric field sensing. Journal of Physics B: Atomic, Molecular and Optical Physics 48.20 (Sep. 2015), p. 202001.

[77] Franz Schwabl. *Quantenmechanik*. 4th ed. Springer Berlin Heidelberg, 1993.

[78] John V. Prodan, William D. Phillips, and Harold Metcalf. Laser Production of a Very Slow Monoenergetic Atomic Beam. Phys. Rev. Lett. 49 16 (Oct. 1982), pp. 1149–1153.

[79] Sven Tassy. "Sympathetische Kühlung von Ytterbium mit Rubidium". PhD thesis. Heinrich-Heine-Universität Düsseldorf, 2007.

[80] Jörg Werner. "Observation of Feshbach resonances in an ultracold gas of 52Cr". PhD thesis. Universität Stuttgart, 2006.

[81] L. Ricci, M. Weidemüller, T. Esslinger, A. Hemmerich, C. Zimmermann, V. Vuletic, W. König, and T.W. Hänsch. A compact grating-stabilized diode laser system for atomic physics. Optics Communications 117.5 (1995), pp. 541–549.

[82] Nils Nemitz. "Production and spectroscopy of ultracold YbRb* molecules". PhD thesis. Heinrich-Heine-Universität Düsseldorf, 2008.

[83] T.W. Hansch and B. Couillaud. Laser frequency stabilization by polarization spectroscopy of a reflecting reference cavity. Optics Communications 35.3 (1980), pp. 441 –444.

[84] Aaron Hopf. "Frequency Stabilisation of a Rydberg Excitation Laser for the Optimization of Lifetime Measurements in Yb". Master thesis. Heinrich-Heine-Universität Düsseldorf, 2022.

[85] Tobias Franzen. "A new RbYb ultracold mixture machine - from room temperature to 2-photon-photoassociation on the intercombination line". PhD thesis. Heinrich-Heine-Universität Düsseldorf, 2022.

[86] John H. T. Burke, Ofir Garcia, K. Jeramy Hughes, Brian Livedalen, and Charles A. Sackett. Compact implementation of a scanning transfer cavity lock. Review of Scientific Instruments 76.11 (Nov. 2005), p. 116105.

[87] Aviv Keshet and Wolfgang Ketterle. A distributed, graphical user interface based, computer control system for atomic physics experiments. Review of Scientific Instruments 84.1 (Jan. 2013), p. 015105.

[88] S. E. Pollack, M. D. Turner, S. Schlamminger, C. A. Hagedorn, and J. H. Gundlach. Charge management for gravitational-wave observatories using UV LEDs. Phys. Rev. D 81 (Jan. 2010), p. 021101.

[89] H. Lehec, A. Zuliani, W. Maineult, E. Luc-Koenig, P. Pillet, P. Cheinet, F. Niyaz, and T. F. Gallagher. Laser and microwave spectroscopy of even-parity Rydberg states of neutral ytterbium and multichannel-quantum-defect-theory analysis. Phys. Rev. A 98 (Dec. 2018), p. 062506.

[90] U. Fano. Unified treatment of perturbed series, continuous spectra and collisions. J. Opt. Soc. Am. 65.9 (Sep. 1975), pp. 979–987.

[91] J Mitroy, M S Safronova, and Charles W Clark. Theory and applications of atomic and ionic polarizabilities. Journal of Physics B: Atomic, Molecular and Optical Physics 43.20 (Oct. 2010), p. 202001.

[92] V. A. Yerokhin, S. Y. Buhmann, S. Fritzsche, and A. Surzhykov. Electric dipole polarizabilities of Rydberg states of alkali-metal atoms. Phys. Rev. A 94 (Sep. 2016), p. 032503.

[93] Zhangli Lai, Shichao Zhang, Qingdong Gou, and Yong Li. Polarizabilities of Rydberg states of Rb atoms with n up to 140. Phys. Rev. A 98 (Nov. 2018), p. 052503.

[94] R. Ding, J. D. Whalen, S. K. Kanungo, T. C. Killian, F. B. Dunning, S. Yoshida, and J. Burgdörfer. Spectroscopy of ^{87}Sr triplet Rydberg states. Phys. Rev. A 98 (Oct. 2018), p. 042505.

[95] A. K. Mohapatra, T. R. Jackson, and C. S. Adams. Coherent Optical Detection of Highly Excited Rydberg States Using Electromagnetically Induced Transparency. Phys. Rev. Lett. 98 (Mar. 2007), p. 113003.

[96] Rodney Loudon. *The Quantum Theory of Light*. Oxford University Press, 2000.

[97] John David Jackson. *Classical Electrodynamics*. 3rd ed. New York: John Wiley & Sons, 1999.

[98] Sylvain Ravets, Henning Labuhn, Daniel Barredo, Lucas Béguin, Thierry Lahaye, and Antoine Browaeys. Coherent dipole–dipole coupling between two single Rydberg atoms at an electrically-tuned Förster resonance. Nature Physics 10.12 (2014), pp. 914–917.

[99] Nikola Šibalić and Charles S. Adams. *Rydberg Physics*. 2399-2891. IOP Publishing, 2018.

[100] M. D. Lukin, M. Fleischhauer, R. Cote, L. M. Duan, D. Jaksch, J. I. Cirac, and P. Zoller. Dipole Blockade and Quantum Information Processing in Mesoscopic Atomic Ensembles. Phys. Rev. Lett. 87 (Jun. 2001), p. 037901.

[101] Giuliano Giudici, Stefano Veroni, Giacomo Giudice, Hannes Pichler, and Johannes Zeiher. Fast entangling gates for Rydberg atoms via resonant dipole-dipole interaction. PRX Quantum 6.3 (2025), p. 030308.

[102] Xiao-Feng Shi. Quantum logic and entanglement by neutral Rydberg atoms: methods and fidelity. Quantum Science and Technology 7.2 (2022), p. 023002.

[103] Georg Günter, Hannes Schempp, Matthieu Robert-de Saint-Vincent, Vladimir Gavryusev, Stefan Helmrich, Christian S. Hofmann, Susanne Whitlock, and Markus Weidemüller. Observing the dynamics of dipole-mediated energy transport by interaction-enhanced imaging. Science 342.6161 (2013), pp. 954–956.

[104] Thad G. Walker and M. Saffman. Consequences of Zeeman degeneracy for the van der Waals blockade between Rydberg atoms. Phys. Rev. A 77 (Mar. 2008), p. 032723.

[105] T. Pohl, E. Demler, and M. D. Lukin. Dynamical Crystallization in the Dipole Blockade of Ultracold Atoms. Phys. Rev. Lett. 104 (Jan. 2010), p. 043002.

[106] Rolf Heidemann, Ulrich Krohn, Vera Bendkowsky, Björn Butscher, Robert Löw, Luis Santos, and Tilman Pfau. Evidence for Coherent Collective Rydberg Excitation in the Strong Blockade Regime. Phys. Rev. Lett. 99 (Oct. 2007), p. 163601.

[107] Daniel Barredo, Henning Labuhn, Sylvain Ravets, Thierry Lahaye, Antoine Browaeys, and Charles S. Adams. Coherent Excitation Transfer in a Spin Chain of Three Rydberg Atoms. Phys. Rev. Lett. 114 (Mar. 2015), p. 113002.

[108] Naveen Nishad, Anna Keselman, Thierry Lahaye, Antoine Browaeys, and Shai Tsesses. Quantum simulation of generic spin-exchange models in Floquet-engineered Rydberg-atom arrays. Phys. Rev. A 108 (Nov. 2023), p. 053318.

[109] Lin Su, Alexander Douglas, Michal Szurek, Robin Groth, S. Furkan Ozturk, Aaron Krahn, Anne H. Hébert, Gregory A. Phelps, Sepehr Ebadi, Susannah Dickerson, Francesca Ferlaino, Ognjen Marković, and Markus Greiner. Dipolar quantum solids emerging in a Hubbard quantum simulator. Nature 622.7984 (Oct. 2023), pp. 724–729.

[110] Alexander Guttridge, Daniel K. Ruttley, Archie C. Baldock, Rosario González-Férez, H. R. Sadeghpour, C. S. Adams, and Simon L. Cornish. Observation of Rydberg Blockade Due to the Charge-Dipole Interaction between an Atom and a Polar Molecule. Physical Review Letters 131.1 (Jul. 2023), p. 013401.

[111] Johannes Deiglmayr, Heiner Saßmannshausen, Pierre Pillet, and Frédéric Merkt. Observation of Dipole-Quadrupole Interaction in an Ultracold Gas of Rydberg Atoms. Physical Review Letters 113.19 (Nov. 2014), p. 193001.

[112] D. Comparat and P. Pillet. Dipole blockade in a cold Rydberg atomic sample. J. Opt. Soc. Am. B 27 (2010), A208–A232.

[113] E. Urban, T. A. Johnson, T. Henage, L. Isenhower, D. D. Yavuz, T. G. Walker, and M. Saffman. Observation of Rydberg blockade between two atoms. Nature Physics 5.2 (2009), pp. 110–114.

[114] Ningyuan Jia. “Quantum Many-Body Physics with Photons”. PhD thesis. Chicago, Illinois: The University of Chicago, 2018.

[115] C. Ates, I. Lesanovsky, C. S. Adams, and K. J. Weatherill. Fast and Quasideterministic Single Ion Source from a Dipole-Blockaded Atomic Ensemble. Phys. Rev. Lett. 110 (May. 2013), p. 213003.

[116] X. L. Zhang, L. Isenhower, A. T. Gill, T. G. Walker, and M. Saffman. Deterministic entanglement of two neutral atoms via Rydberg blockade. Physical Review A 82.3 (2010), p. 030306.

[117] K. M. Maller, M. T. Lichtman, T. Xia, Y. Sun, M. J. Piotrowicz, A. W. Carr, L. Isenhower, and M. Saffman. Rydberg-blockade controlled-NOT gate and entanglement in a two-dimensional array of neutral-atom qubits. Physical Review A 92.2 (2015), p. 022336.

[118] Y.-Y. Jau, A. M. Hankin, T. Keating, I. H. Deutsch, and G. W. Biedermann. Entangling atomic spins with a Rydberg-dressed spin-flip blockade. Nature Physics 12.1 (2016), pp. 71–74.

[119] A. V. Gorshkov, J. Otterbach, M. Fleischhauer, T. Pohl, and M. D. Lukin. Photon-photon interactions via Rydberg blockade. Physical Review Letters 107.13 (2011), p. 133602.

[120] T. Peyronel, O. Firstenberg, Q. Y. Liang, S. Hofferberth, A. V. Gorshkov, T. Pohl, M. D. Lukin, and V. Vuletić. Quantum nonlinear optics with single photons enabled by strongly interacting atoms. Nature 488 (2012), pp. 57–60.

[121] G. Pupillo, A. Micheli, M. Boninsegni, I. Lesanovsky, and P. Zoller. Strongly Correlated Gases of Rydberg-Dressed Atoms: Quantum and Classical Dynamics. Physical Review Letters 104.22 (2010), p. 223002.

[122] Tobias Franzen, Bastian Pollklesener, and Axel Görlitz. A single-stage 1112 nm fiber amplifier with large gain for laser cooling of ytterbium. Applied Physics B 124.12 (2018), p. 234.

[123] Eileen Trede. “A Fiber-Based Laser System at 556 nm for a Magnetooptical Trap with Ytterbium”. Master thesis. Heinrich-Heine-Universität Düsseldorf, 2019.

[124] Bastian Pollklesener. “Photoassociation of ultracold RbYb in an optical lattice - a quest towards absolute ground state molecules”. PhD thesis. Heinrich-Heine-Universität Düsseldorf, 2023.

[125] Biswajit Ghosh and Sanjoy Mandal. Fiber Bragg grating-based optical filters for high-resolution sensing: A comprehensive analysis. Results in Optics 12 (2023), p. 100441.

[126] Eric D. Black. An introduction to Pound-Drever-Hall laser frequency stabilization. American Journal of Physics 69.1 (Jan. 2001), pp. 79–87.

[127] SCHOTT AG. *Zerodur® - Technical Data*. 2024. URL: https://www.schott.com/de-de/products/zerodur-p1000269/downloads (visited on 05/09/2025).

[128] C. Sillus, T. Franzen, B. Pollklesener, and A. Görlitz. Active position stabilization of an atomic cloud in a narrow-line magneto-optical trap using a Raspberry Pi. Review of Scientific Instruments 92.3 (2021), p. 033204.

[129] J. I. Thorpe, K. Numata, and J. Livas. Laser frequency stabilization and control through offset sideband locking to optical cavities. Opt. Express 16.20 (2008), pp. 15980–15990.

[130] Wance Wang, Sarthak Subhankar, and Joseph W. Britton. A practical guide to feedback control for Pound–Drever–Hall laser linewidth narrowing. Applied Physics B 131.7 (2025), p. 146.

[131] Tobias Franzen. "Spectroscopy of the clock transition in ytterbium". Master thesis. Heinrich-Heine-Universität Düsseldorf, 2012.

[132] D. Jaksch, J. I. Cirac, P. Zoller, S. L. Rolston, R. Côté, and M. D. Lukin. Fast Quantum Gates for Neutral Atoms. Phys. Rev. Lett. 85 10 (Sep. 2000), pp. 2208–2211.

[133] C.J. Foot. *Atomic Physics*. Oxford Master Series in Physics. OUP Oxford, 2005.

[134] Hai chao Zhang, Peng fei Zhang, Xin ping Xu, Feng Cheng, and Yu zhu Wang. Optimized temperature measurement with time-of-flight method. Optics Communications 282.16 (2009), pp. 3278–3281.

[135] Benjamin Plotkin-Swing, Anna Wirth, Daniel Gochnauer, Tahiyat Rahman, Katherine E. McAlpine, and Subhadeep Gupta. Crossed-beam slowing to enhance narrow-line ytterbium magneto-optic traps. Review of Scientific Instruments 91.9 (Sep. 2020), p. 093201.

[136] J. Pick, R. Schwarz, J. Kruse, C. Lisdat, and C. Klempt. Compact structures for single-beam magneto-optical trapping of ytterbium. Review of Scientific Instruments 95.7 (Jul. 2024), p. 073201.

[137] S. L. Kemp, K. L. Butler, R. Freytag, S. A. Hopkins, E. A. Hinds, M. R. Tarbutt, and S. L. Cornish. Production and characterization of a dual species magneto-optical trap of cesium and ytterbium. Review of Scientific Instruments 87.2 (Feb. 2016), p. 023105.

[138] Bongjune Kim, Ko-Tang Chen, Shih-Si Hsiao, Sheng-Yang Wang, Kai-Bo Li, Julius Ruseckas, Gediminas Juzeliūnas, Teodora Kirova, Marcis Auzinsh, Ying-Cheng Chen, Yong-Fan Chen, and Ite A. Yu. A weakly-interacting many-body system of Rydberg polaritons based on electromagnetically induced transparency. Communications Physics 4.1 (2021), p. 101.

[139] Claude Cohen-Tannoudji, Jacques Dupont-Roc, and Gilbert Grynberg. *Atom-Photon Interactions: Basic Processes and Applications*. Wiley-VCH, 1998.

[140] Elizabeth J. Robertson, Nikola Šibalić, Robert M. Potvliege, and Matthew P. A. Jones. ARC 3.0: An expanded Python toolbox for atomic physics calculations. Computer Physics Communications 261 (2021), p. 107814.

[141] A. F. Linskens, I. Holleman, N. Dam, and J. Reuss. Two-photon Rabi oscillations. Phys. Rev. A 54 6 (Dec. 1996), pp. 4854–4862.

[142] Jeff Thompson and Michael Peper. *rydcalc: A Python Package for Rydberg State Calculations*. Accessed: 2025-09-26.

[143] Alexander Miethke. "Detection of Ytterbium Rydberg Atoms by Field Ionization". Master thesis. Heinrich-Heine-Universität Düsseldorf, 2019.

[144] W. Ketterle, D. S. Durfee, and D. M. Stamper-Kurn. Making, probing and understanding Bose–Einstein condensates. arXiv:cond-mat/9904034 (1999). arXiv preprint cond-mat/9904034.

[145] Rudolf Grimm, Matthias Weidemüller, and Yurii B. Ovchinnikov. Optical dipole traps for neutral atoms. Advances In Atomic, Molecular, and Optical Physics 42 (2000), pp. 95–170.

[146] K. B. Davis, M.-O. Mewes, M. R. Andrews, N. J. van Druten, D. S. Durfee, D. M. Kurn, and W. Ketterle. Bose-Einstein condensation in a gas of sodium atoms. Phys. Rev. Lett. 75 (1995), pp. 3969–3973.

[147] Shanchao Zhang, Chengdong He, Elnur Hajiyev, Zejian Ren, Bo Song, and Gyu-Boong Jo. Collective dipole oscillations of a spin-orbit coupled Fermi gas. Scientific Reports 8.1 (2018), p. 18005.

[148] Y. Takasu, K. Honda, K. Komori, T. Kuwamoto, M. Kumakura, Y. Takahashi, and T. Yabuzaki. High-Density Trapping of Cold Ytterbium Atoms by an Optical Dipole Force. Phys. Rev. Lett. 90.2 (Jan. 2003), p. 023003.

[149] Takeshi Fukuhara, Seiji Sugawa, and Yoshiro Takahashi. Bose–Einstein condensation of an ytterbium isotope. Physical Review A 76.5 (2007), 051604(R).

[150] A. Yamaguchi, S. Uetake, S. Kato, H. Ito, and Y. Takahashi. High-resolution laser spectroscopy of a Bose-Einstein condensate using the ultranarrow magnetic quadrupole transition. New Journal of Physics 12.10 (2010), p. 103001.

[151] Christian David Sillus. “Investigation of the Excited-State Potentials of Ultracold RbYb: Towards Light-Shift Spectroscopy”. PhD thesis. Heinrich-Heine-Universität Düsseldorf, 2025.

[152] J. A. Sherman, N. D. Lemke, N. Hinkley, M. Pizzocaro, R. W. Fox, A. D. Ludlow, and C. W. Oates. High-Accuracy Measurement of Atomic Polarizability in an Optical Lattice Clock. Phys. Rev. Lett. 108.15 (2012), p. 153002.

[153] Jacob P. Covey, Alp Sipahigil, and Mark Saffman. Microwave-to-optical conversion via four-wave mixing in a cold ytterbium ensemble. Phys. Rev. A 100.1 (Jul. 2019), p. 012307.

[154] C. W. Hoyt, Z. W. Barber, C. W. Oates, T. M. Fortier, S. A. Diddams, and L. Hollberg. Observation and Absolute Frequency Measurements of the $^1S_0$–$^3P_0$ Optical Clock Transition in Neutral Ytterbium. Phys. Rev. Lett. 95 (Aug. 2005), p. 083003.

[155] Z. W. Barber, J. E. Stalnaker, N. D. Lemke, N. Poli, C. W. Oates, T. M. Fortier, S. A. Diddams, L. Hollberg, C. W. Hoyt, A. V. Taichenachev, and V. I. Yudin. Optical Lattice Induced Light Shifts in an Yb Atomic Clock. Phys. Rev. Lett. 100 (Mar. 2008), p. 103002.

[156] T. Topcu and A. Derevianko. Magic wavelengths for the $nS - nP$ transitions in alkali-metal atoms. Journal of Physics B: Atomic, Molecular and Optical Physics 49.14 (2016), p. 144004.

[157] M. Schulz. “Experimental Studies on Ultracold Ytterbium Atoms”. PhD thesis. University of Innsbruck, 2002.

[158] D. Jaksch, J. I. Cirac, P. Zoller, S. L. Rolston, R. Côté, and M. D. Lukin. Fast Quantum Gates for Neutral Atoms. Phys. Rev. Lett. 85 10 (Sep. 2000), pp. 2208–2211.

[159] Antoine Browaeys and Thierry Lahaye. Many-Body Physics with Individually-Controlled Rydberg Atoms. Nature Physics 16 (2020), pp. 132–142.

[160] Immanuel Bloch, Jean Dalibard, and Wilhelm Zwerger. Many-body physics with ultracold gases. Rev. Mod. Phys. 80.3 (Jul. 2008), pp. 885–964.

[161] Immanuel Bloch, Jean Dalibard, and Sylvain Nascimbene. Quantum simulations with ultracold quantum gases. Nature Physics 8.4 (2012), pp. 267–276.

[162] D. Jaksch and P. Zoller. The cold atom Hubbard toolbox. Annals of Physics 315.1 (2005), pp. 52–79.

[163] T. Esslinger. Fermi-Hubbard physics with atoms in an optical lattice. Annual Review of Condensed Matter Physics 1 (2010), pp. 129–152.

[164] Christian Sillus. “A detector for ultracold ytterbium Rydberg atoms”. Master thesis. Heinrich-Heine-Universität Düsseldorf, 2018.

[165] Emily Altiere, Donald P. Fahey, Michael W. Noel, Rachel J. Smith, and Thomas J. Carroll. Dipole-dipole interaction between rubidium Rydberg atoms. Phys. Rev. A 84 (Nov. 2011), p. 053431.

[166] Sylvain de Léséleuc, Daniel Barredo, Vincent Lienhard, Antoine Browaeys, and Thierry Lahaye. Optical Control of the Resonant Dipole-Dipole Interaction between Rydberg Atoms. Phys. Rev. Lett. 119 (Aug. 2017), p. 053202.

[167] C. H. Greene, A. S. Dickinson, and H. R. Sadeghpour. Creation of Polar and Nonpolar Ultra-Long-Range Rydberg Molecules. Phys. Rev. Lett. 85 (2000), pp. 2458–2461.

[168] C. Boisseau, I. Simbotin, and R. Côté. Macrodimers: Ultralong Range Rydberg Molecules. Phys. Rev. Lett. 88 (2002), p. 133004.

[169] S. Hollerith, J. Zeiher, T. Ott, I. Bloch, and S. Whitlock. Ultralong-Range Interactions between Rydberg Atoms in Optical Tweezer Arrays. J. Phys. Chem. A 127 (2023), pp. 8256–8273.

[170] C. Castor, A. Miethke, B. Pollklesener, C. Sillus, V. Vogt, and A. Görlitz. Tunable External Cavity Gain Chip Laser at 1.5μm Frequency-stabilized using Sideband Locking for Molecular Spectroscopy Applications. Manuscript in preparation (2025).

[171] Many of the figures in this thesis make use of the symbols from the ComponentLibrary by Alexander Franzen. (`https://www.gwoptics.org/ComponentLibrary/`). 2023.

[172] OpenAI. *ChatGPT*. `https://chat.openai.com/`. 2025.

[173] DeepL SE. *DeepL write*. `https://www.deepl.com/write`. 2025.

Danksagung

Die Entstehung dieser Dissertation wurde von vielen großartigen Menschen begleitet, die mich immer wieder unterstützt, motiviert und inspiriert haben. Zum Abschluss möchte ich mich herzlich für all die tolle Unterstützung, die konstruktiven Anregungen und die angenehme Zusammenarbeit bedanken – ohne Euch wäre diese Arbeit nicht möglich gewesen!

- Als Erstes möchte ich mich bei Axel Görlitz bedanken – im Grunde kann man sagen für alles! Schon an meinem Probe-Studientag an der HHU konnte mich Deine unerschöpfliche Begeisterung für die Physik von diesem Studium überzeugen. Daher war für mich schnell klar, dass ich meine Bachelorarbeit in Deiner Arbeitsgruppe absolvieren möchte. Seitdem bin ich dann einfach in der AGG geblieben – über die Masterarbeit bis hin zur Promotion. Vielen Dank für die Unterstützung während dieser gesamten Zeit. Neben der Interpretation von Messdaten – und dem immer wieder notwendigen Uminterpretieren – hattest Du stets eine geeignete Idee für Herausforderungen, die im Labor aufkamen, und hast selbst beim Justieren von MOT-Strahlen geholfen, wenn es nötig war. Auch bei außerphysikalischen Themen konnte ich viel von Dir lernen. Teil Deiner Arbeitsgruppe zu sein, ist ein Privileg, um das mich viele sicher beneiden. Außerdem bedanke ich mich für das sorgfältige Korrekturlesen dieser Arbeit.

- Ich danke Priv.-Doz. Dr. Götz Lehmann für die freundliche Übernahme des Koreferats und ganz besonders für die zügige Fertigstellung des Gutachtens. Darüber hinaus möchte ich mich für häufige Gespräche auf dem Flur bedanken, die den Uni-Alltag das ein oder andere Mal freudig aufgelockert haben. Als Mentor meiner Dissertation hätte ich mich mit gutem Gefühl an Dich wenden können, wenn es notwendig gewesen wäre.

- Ein besonders großes Dankeschön geht an Ralf Stephan, unseren Techniker. Um ein ihm gewidmetes Werk unserer arbeitsgruppeninternen Musikkunst zu zitieren: "Ralf, unser Lötmeister, der Mann mit dem Plan, mit Widerständen, Platinen geht er souverän ran. Kondensatoren, OPs – kein Problem für den Mann, doch manchmal, ja manchmal geht sein Plan [...] auf, oh man. Früh am Morgen, erster Kaffee in der Hand, unser Ralf ist schon wach, während wir noch im Traumland. Reichelt oder Moser – er kennt sie alle gut. Ralf ist der Mann, der immer weiß, was er tut. Ralf

der König, der Elektronik, mit dem Lötkolben immer ikonisch. Sicherheit ist sein höchstes Gebot [...]. Er ist der Beste, das wissen wir alle. Mit jedem Projekt hebt er uns aus der Falle. Ein Meister der Schaltung, ein Freund in der Not, Ralf, unser Held, unser oberstes Gebot." Nicht nur bei Fragen zu Elektronikproblemen hattest Du stets Lösungen parat, sondern auch bei Fragen rund ums Thema Hausbau konnten wir bei einer Tasse Kaffee Ideen austauschen. Danke, Ralf, ohne Dich würde das Experiment definitiv nicht laufen.

- Die Grundlage für das gesamte Rydbergexperiment hat Christian Wallin (geb. Halter) gelegt. Vielen Dank für die gemeinsame Zeit im Labor, die gelungene Übergabe des Experiments und die vielen Besuche in verschiedenen Boulderhallen. Du hast mir die Grundlagen der Rydbergphysik gezeigt und wie man sie bändigt. Durch Deine guten Vorarbeiten konnten die verschiedensten Messungen erst gelingen.

- Damit die Rydberg-Traditionen gewahrt werden können, benötigt es natürlich auch einen Nachfolger – oder besser noch eine Nachfolgerin. Vielen Dank, Nele, dass Du den Mut hast, das Experiment fortzuführen. Schon während Deiner Masterarbeit konntest Du das Experiment eigenständig bedienen und bist mittlerweile vermutlich selbständiger, als ich es je war. Du gehst Herausforderungen strukturiert an, zum Glück mit den Schlappen im Hintergrund, und wirst das Experiment auf das nächste Level heben – da bin ich mir sicher. Stichwort: Wechselwirkungen. Ich bin froh, dass Du sowohl das Interesse für Fußball als auch, was noch viel wichtiger ist, für den Kaffeegenuss in der Arbeitsgruppe bewahrst. Super!

- Als nächstes möchte ich mich beim RbYb-Team bedanken – ehemals angeführt von Tobi und Basti, den Labor-CEOs. Ihr hattet stets ein offenes Ohr für all die aufkommenden Fragen und Probleme. Danke für gegenseitigen Katastrophentourismus und eine angenehme Laboratmosphäre mit physikalischem und musikalischem Austausch.

- Die meiste Zeit im Labor habe ich mit Christian Sillus verbracht. Moin oder watt – und herzlichen Dank, Dr. Sillus für die tolle Zeit; ich konnte sehr viel von Dir lernen. Auch wenn Du mir nicht immer zugehört hast, hatte ich doch das Gefühl, dass Du mir bei meinen Problemen helfen wolltest. Wir waren in ständigem Austausch über alles, jede und jeden – auch wenn manchmal nur über kritische Blicke. Du hast mich oft bestärkt, meinem "Gefühl" und meinem "Humor" zu vertrauen – danke fürs Aushalten. Am Ende bist Du dann doch trotz verschiedener Vorhersagen vor mir fertig geworden, was Du mehr als verdient hast.

- Ein großes Dankeschön geht an Céline Castor. Du hast an die Arbeitsgruppe ganz neue, vorbildliche moralische Maßstäbe angesetzt und diese dadurch optimiert. Unter Deiner Leitung macht der Laboralltag, die Mittagessen und jede Unternehmung neben der Uni gleich doppelt so viel Spaß. Danke für Dein Engagement, Dein häufiges

Nochmal-genauer-Drüberschauen über Dinge, die ich gerechnet, aufgebaut oder mir überlegt habe und für die unzähligen Reels. Ich bin froh, dass wir auf der gleichen Film- und YouTube-Welle surfen konnten und dadurch der Harry-Potter-Hype nicht in die Kammer des Vergessens verschwindet. Daher – Missetat begangen.

- Bedanken möchte ich mich auch bei Arne Kallweit. Wir teilen uns nicht nur einen Handschlag, sondern vor allem ein Büro – das legendäre "BDH, unser stolzes Reich. [...] Im A-Büro, da leben wir den großen Traum fort." Für Deine Unterstützung, sowohl im Labor, im Büro als auch neben der Uni möchte ich Dir hiermit gerne noch ein letztes, endgültiges Mal den Samariter-des-Tages-Orden überreichen. Deine selbstlose und begeisternde Art beruhigt und motiviert zugleich fast jeden Tag. Ich bin stolz, dass ich Tipps, Tricks und die ein oder andere Dehnübung vom wahrscheinlich schnellsten Menschen der Welt lernen konnte.

- Außerdem möchte ich mich bei allen Bachelor- und Masterstudierenden bedanken, die ich während meiner Promotion begleiten durfte. Durch die vielen spannenden Projekte habe ich nicht nur viel von Euch gelernt, sondern Ihr habt auch aktiv zu dieser Arbeit beigetragen.

- Speziell möchte ich mich noch bei Aaron Hopf bedanken. Wir haben das ganze Studium seit dem Physik-Vorkurs zusammen absolviert. Ohne Dich hätte ich wahrscheinlich keine passenden Vorlesungen belegt, könnte den Studiengangplan nicht lesen und mir würden bis jetzt noch irgendwelche Credit Points fehlen. Danke für Deine Unterstützung über das gesamte Studium und weit, sehr weit darüber hinaus. Man kann sich immer auf Dich verlassen und ich bin sehr froh, dass wir uns zufällig in der Uni getroffen haben!

- Ein besonderes Dankeschön geht an meine Freunde und meine ganze Familie. Ihr seid immer für mich da – egal, was passiert. Eure Unterstützung begleitet mich mein ganzes Leben, und ohne Euch wäre all das nicht möglich gewesen. Vielen Dank!

- Als Letztes möchte ich mich besonders bei Emma bedanken. Du hast mir während der gesamten Zeit geholfen, wenn ich mal wieder den Überblick verloren habe, und warst immer an meiner Seite – selbst dann, wenn es alles etwas chaotisch war. Du bist mein größter Rückhalt – egal, ob es super läuft oder schiefgeht. Danke, dass Du mich immer motivierst, mich zum Lachen bringst und ich nie das Gefühl habe, mit meinen Problemen alleine zu sein!

Publications

The following scientific papers involving work within this thesis have been published:

Reference [56]:
C. Halter, A. Miethke, A. Hegde, and A. Görlitz
Trap-loss spectroscopy of Rydberg states in ytterbium. in J. Phys. B: At. Mol. Opt. Phys., 56 055001, 2023.
The author contributed to the preparation of the manuscript. A reproduction of the published work can be found in section 5.1.

Reference [37]:
A. Miethke, L. P. Kozhiparambil Sajith, and A. Görlitz
Isotope dependence of ytterbium Rydberg states. [Manuscript has been submitted to the Journal of Physics B: Atomic, Molecular and Optical Physics.]
The author performed the data acquisition and analysis and prepared the manuscript. The corresponding results are reproduced in section 5.2 of this thesis.

Additional publication, to which the author contributed expertise, outside the scope of this thesis:

Reference [170]:
C. Castor, A. Miethke, B. Pollklesener, C. Sillus, V. Voigt, and A. Görlitz
Tunable External Cavity Gain Chip Laser at $1.5\,\mu$**m Frequency-stabilized using Sideband Locking for Molecular Spectroscopy** [manuscript to be submitted]
The author contributed expertise in the development of the laser system.
Insights gained from construction of the laser system described in this dissertation (see chapter 7) informed and supported the development of the laser system presented in the manuscript.

Eidesstattliche Erklärung

Hiermit versichere ich an Eides Statt, dass die vorliegende Dissertation eigenständig und ohne unzulässige Hilfe unter Beachtung der "Grundsätze zur Sicherung guter wissenschaftlicher Praxis an der Heinrich-Heine-Universität Düsseldorf" erstellt worden ist. Zur Überprüfung von Rechtschreibung, Zeichensetzung und sprachlicher Formulierung wurden KI-basierte large-language models wie ChatGPT [172] und DeepL [173] verwendet. Alle Abbildungen ohne explizite Quellenangabe wurden eigenständig erstellt.

Düsseldorf, 17.12.2025
Ort, Datum

Alexander Miethke